CONVEX MODEL-BASED SYNTHETIC APERTURE RADAR PROCESSING

by

Chad P. Knight

A dissertation submitted in partial fulfillment
of the requirements for the degree

of

DOCTOR OF PHILOSOPHY

in

Electrical Engineering

Approved:

Dr. Jacob H. Gunther Major Professor	Dr. Todd K. Moon Committee Member
Dr. Charles Swenson Committee Member	Dr. Randy J. Jost Committee Member
Dr. David G. Long Committee Member	Dr. Mark R. McLellan Vice President for Research and Dean of the School of Graduate Studies

UTAH STATE UNIVERSITY
Logan, Utah

2014

Abstract

Convex Model-Based Synthetic Aperture Radar Processing

by

Chad P. Knight, Doctor of Philosophy

Utah State University, 2014

Major Professor: Dr. Jacob H. Gunther
Department: Electrical and Computer Engineering

Synthetic aperture radar (SAR) is an attractive technology that is used in remote sensing, military, and commercial applications. SAR can be used as an imaging sensor in all weather conditions, during the day or night, and the resolution is not dependent on the distance from the target like optical sensors. SAR is a ranging instrument that operates fundamentally in a 3D environment. But unfortunately, most results of SAR sensors have been restricted to 2D imaging and interpretation by necessity.

With the advancement of contemporary fields, the promise of 3D scene reconstruction has received renewed attention. The active fulfilment of Moore's law, advances in compressive sensing, and convex optimization have provided new opportunities to pose the immensely underdetermined SAR 3D reconstruction problem in new ways that until recently were inconceivable.

Advanced SAR image formation processing can elicit more utility from the raw SAR sensor measurements. This has the potential to allow SAR to be used for new applications in remote sensing, commercially and in military applications. Unfortunately, the advanced SAR image formation processing generally comes at the cost of increased processing complexity.

In this dissertation, the SAR image formation problem is posed with additional constraints. These constraints are tantamount to incorporating prior knowledge about the scene or target of interest into the image-formation process. This helps enhance desirable targets and suppress targets that are not of interest.

The fundamental SAR and mathematical background is provided in this work prior to developing the SAR image formation model as a second order cone program (SOCP) that incorporates sparsity, aspect, and spatial regularization terms. The results are demonstrated on synthetic data, and actual SAR data.

The model developed naturally extends to any sparsely sampled SAR signal. The utility of the developed model is demonstrated by focusing on 3D scene reconstruction. Improved 3D scene reconstruction will allow remote sensing, military, and commercial SAR sensors to better identify targets, and provide improved overall scene interpretability. Improved scene interpretability is critical in many of the applications for which SAR is currently used and improved 3D reconstruction could extend SAR use to new applications.

(204 pages)

Public Abstract

Convex Model-Based Synthetic Aperture Radar Processing

by

Chad P. Knight, Doctor of Philosophy

Utah State University, 2014

Major Professor: Dr. Jacob H. Gunther
Department: Electrical and Computer Engineering

The use of radar often conjures up images of small blobs on a screen. But current synthetic aperture radar (SAR) systems are able to generate near-optical quality images with amazing benefits compared to optical sensors. These SAR sensors work in all weather conditions, day or night, and provide many advanced capabilities to detect and identify targets of interest.

These amazing abilities have made SAR sensors a work-horse in remote sensing, and military applications. SAR sensors are ranging instruments that operate in a 3D environment, but unfortunately the results and interpretation of SAR images have traditionally been done in 2D. Three-dimensional SAR images could provide improved target detection and identification along with improved scene interpretability.

As technology has increased, particularly regarding our ability to solve difficult optimization problems, the 3D SAR reconstruction problem has gathered more interest. This dissertation provides the SAR and mathematical background required to pose a SAR 3D reconstruction problem. The problem is posed in a way that allows prior knowledge about the target of interest to be integrated into the optimization problem when known.

The developed model is demonstrated on simulated data initially in order to illustrate critical concepts in the development. Then once comprehension is achieved the processing

is applied to actual SAR data. The 3D results are contrasted against the current "gold-standard." The results are shown as 3D images demonstrating the improvement regarding scene interpretability that this approach provides.

To my wife and best friend Jessie, and our zephyrean children...

Acknowledgments

I would like to thank my committee. First, Dr. Jake Gunther for his impeccable approach to life in general. Working with him has been an amazing experience. I do not believe we ever had a conversation that did not inspire me and make me believe that this effort was within my reach. I would also like to thank Dr. David Long for introducing me to radar and convincing me I had the mettle and perseverance to pursue a Ph.D. I also would like to thank Dr. Todd K. Moon, Dr. Randy J. Jost, and Dr. Charles Swenson for being excellent teachers and leaders, and serving on my committee.

Heartfelt thanks to Space Dynamics Laboratory (SDL) for providing the SDL fellowship and financial assistance required. SDL has been an excellent place to work for me while pursuing this dream. A special thanks to my colleague, Dave Madsen, for his invaluable feedback and suggestions. I would like to thank Joseph Winkler for graciously sharing his graphing software.

On a personal note, in the most reverent tone, I would like to thank my family, immediate and extended. Unfortunately for anything won, there is something lost. I realize the sacrifices my family has made so that I could pursue this effort. Thanks Mom and Dad for your example and always believing in me. Thank you Jessie, my amazing wife, and Jake, Colby, Jaycee, and Gracie who are my wonderful children. Thanks for your sacrifices and providing the motivation behind everything worthwhile that I do.

Chad P. Knight

Contents

List of Tables

List of Figures

Acronyms

SAR	synthetic aperture radar
CCD	coherent change detection
GMTI	ground moving target indicator
ROI	region of interest
SOCP	second order cone program
PRF	pulse repitition frequency
PRI	pulse repitition interval
IFA	image formation algorithm
UAV	unmanned aerial vehicles
LFM	linear frequency modulated signal
SNR	signal to noise ratio
TBP	time bandwidth product
AWG	arbitrary waveform generators
POSP	principle of stationary phase
ADC	analog to digital converters
GPS	global positioning system
INS	inertial navigation system
RCM	range cell migration
IPR	impulse response
CPI	coherent processing interval
CW	continous wave
KAIF	knowledge aided image formation
LP	linear program
MIMO	multiple input multiple output
KKT	Karush-Kuhn-Tucker
GTD	geometrical theory of diffraction

Chapter 1

Introduction

Synthetic aperture radar (SAR) is an active coherent radar imaging technology that has diverse applications. SAR can produce near-photographic quality images in all-weather conditions (clouds, day, night, etc.) as seen in Figure 1.1. This makes SAR sensors an attractive alternative to optical or infrared imaging systems, especially when all-weather day and night visualization is critical. For example, many modern aircraft employ SAR systems to visualize the runway for landing.

SAR can detect temporal changes, or changes that occurred over the time elapsed between the first and second image collection. This processing modality is called coherent change detection (CCD). Many of the changes CCD can detect are not detectable to the human eye in the visible spectrum. For example, CCD can discern if a field has been traversed or a dirt road utilized. Figure 1.2 shows an example CCD image that details the path sheep have traversed in a field during the time-lapse between collections [2].

Low-frequency SAR can also provide foliage penetration (FOPEN) to see through foliage. This allows man-made features to be identified even under dense foliage cover such as rain forests. A similar application of SAR is for mine detection in ground penetrating radar (GPR). Another very useful application of SAR is to identify moving targets and track them as is done in ground moving target indication (GMTI) [3, 4]. These types of capabilities have eminent military and remote sensing applications. It is expected, as the cost of developing SAR sensors continues to decrease, that more commercial applications will emerge that leverage the unique capabilities SAR provides.

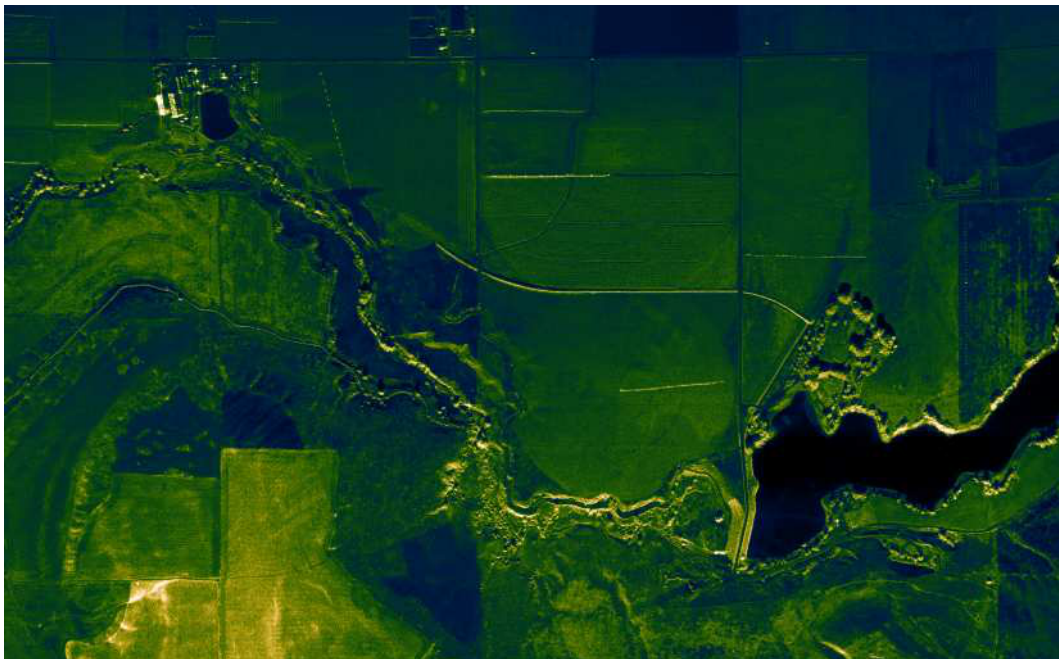

Fig. 1.1: X-band SAR image of Benson Utah.

1.1 Problem Background

Synthetic aperture radar systems naturally operate in a three-dimensional (3D) environment. Therefore, it is natural to interpret the resultant images in the 3D domain. Many features such as layover and foreshortening are naturally explained when viewed in a 3D setting [5].

The promise of 3D scene reconstruction holds several significant advantages. Some potential benefits include improved scene interpretability, better target recognition, and superior target detection. But in spite of these promises, traditionally SAR processing is limited to 2D scene reconstruction instead of 3D [5–7]. There are several reasons why SAR is rarely used for 3D scene reconstruction. First, the 3D scene reconstruction problem is almost always underdetermined with regards to the amount of data collected. It is impractical, for most imaging modalities, to collect enough data to reconstruct 3D scenes unambiguously. The time and platform resources required are generally cost-prohibitive for most missions. Secondly, the measured data has a strong angular or aspect dependence. As data is collected from diverse aspects the radar cross sections (RCS) of a target changes

Fig. 1.2: CCD results demonstrating the path sheep have traveled while grazing in a field (source Presis).

correspondingly. The angular dependence on the azimuth (θ) and elevation (ϕ) angles complicates the modeling and processing. Anisotropy violates many tacit assumptions that are used in traditional SAR imaging formation algorithms, namely that the scene is composed of isotropic reflectors.

In spite of the difficulties there has been vast improvement in 3D imaging [8–13]. The ever-increasing availability of computing power has led many to propose new processing techniques that previously would have been prohibitive due to the arduous processing requirements. Other advances in parallel fields, such as compressive sensing [14–16] and the advancement of convex optimization [17], have provided new opportunities for diverse

approaches.

Model-based processing offers potential solutions to the difficult underdetermined problem regarding 3D image formation. Mathematical models are frequently used to explain measured data by using a small numbers of unknowns compared to the vast number of unknowns in the underdetermined system.

Another benefit of model-based image formation is in regards to knowledge-aided image formation (KAIF). KAIF allows for prior knowledge of the scene globally, or on a pixel level to be incorporated into the image formation process. Model-based processing naturally allows for prior information to be incorporated into the image formation process, rather than merely as a post processing procedure.

1.2 Dissertation Problem Statement

This dissertation examines the current state of the art for SAR 2D model-based scene reconstruction and extends it by formulating the image creation process as a convex optimization problem. This formulation is done with the objective of demonstrating on actual SAR data improved interpretability for 2D scenes compared to traditional image formation algorithms like backprojection. This is accomplished by modeling the SAR reconstruction problem as a second-order cone program (SOCP). The SOCP formulation allows the isotropic model to be extended to an anisotropic model. One of the side benefits of model-based reconstruction is the inherent flexibility. This is exemplified by incorporating additional filters on the RCS magnitude. These filters are applied in aspect and spatially in order to enhance targets of interest.

The 2D model is extended to 3D. Special care is taken to formulate the problem so that the required computer resources, particularly memory and computations, allow for 3D scene demonstrations using real SAR data.

The actual demonstration of improved 3D scene reconstruction from sparsely sampled vertical aperture data is only one demonstration of the utility of the model-based processing approach for SAR. Many parallel, sparsely sampled SAR applications that can leverage an extension of this work are discussed here.

1.3 Contributions

The first contribution of this work is formulating the SAR image formation problem into a convex optimization problem that can incorporate anisotropy. The second contribution is combining spatial, and magnitude filters into the image formation process. This allows targeted features to be enhanced while suppressing nonconforming features. The third contribution is formulating the 3D model problem so that it is tractable. The reduction in problem size facilitates demonstration on actual SAR data, as opposed to only simulated theoretical results. This is of utmost importance since SAR data is well-known to be extremely difficult to model [18]. Which leads to the final accomplishment of demonstrating the SOCP model-based problem formulation utility on actual 3D and 2D scenes. This requires extensive software development and is a major accomplishment of this work.

1.4 Outline

This dissertation is outlined as follows: Chapter 2 provides the necessary radar background for SAR systems. The raw-range measurements of a radar sensor are analyzed. The necessary processing to convert these raw range-rate radar measurements into a backprojected image are specifically detailed in this chapter. The critical concepts are elucidated with simulated data, and actual SAR data is utilized to bridge concepts and demonstrate practical results.

Chapter 3 provides some detail into the fundamental assumptions that radar relies upon. The general theory of diffraction is discussed which is the basis of the isotropic point-source model. The limitations of this theory are discussed which has direct application to generation of synthetic data. The ability to generate high quality simulated data is discussed and the SAR simulator used for this effort.

Chapter 4 poses the SAR image formation problem in a linear-algebra setting and develops the spatial-domain SAR model. The intuition regarding aspect, and spatial filters is justified with actual SAR data. Prior work was examined and natural extensions of that work are described.

Chapter 5 provides the SOCP derivation by using a linear program perspective and

generalizing inequalities in convex optimization terms. The interested reader is provided references to fully understand the convex optimization terms utilized. The model developed in Chapter 4 is ultimately posed as a SOCP in diverse forms that include a model fit, as well as sparsity, aspect, and spatial regularization terms.

Chapter 6 is detailed walk-through of the processing algorithm on simulated data for a 2D scene. The objective is to fully illuminate the required steps and considerations. Intermediate results, along with the final results are discussed for completeness.

Chapter 7 provides 2D and 3D examples utilizing actual SAR data. The results are contrasted against reference images. The improvement seen for in the 3D images is the apex of this effort.

Chapter 8 provides the conclusion and summary to the results from this work. Then parallel and future applications are discussed.

Chapter 2

Radar Background

Radar sensors are ranging instruments and require a different perspective compared to visual or optical sensors when interpreting the raw data or range measurements. The objective of this chapter is to develop the background needed in order to understand the range measurements provided by a radar sensor in an intuitive manner. Common radar terminology is explained with an emphasis towards the geometrical or 3D interpretation. The 3D domain is a natural domain to develop understanding of radar operations since this corresponds to their inherent operating environment. And, for most people, the 3D environment is intuitive.

The signal processing theory required to form SAR imagery from radar range measurements is discussed in detail. SAR image formation will provide a concrete example demonstrating how the radar range rate measurements are ultimately processed to extract the signals of interest. The objective of the SAR image formation problem is generation of high quality imagery. The resultant imagery can be used for many purposes as discussed in Chapter 1.

Many of the ideas and principles used in SAR image formation can be extended to other related radar signal processing applications. Simulated radar data is utilized in order to demonstrate succinct critical concepts of SAR processing. Real radar data is utilized in order to span concepts cohesively, provide practical insight, and demonstrate comprehensive representative results.

2.1 Radar Overview

Radar sensors have broad utility from imaging, guidance systems, weather prediction and target recognition [19]. These systems can be ground-based or airborne. The back-

ground presented is inclined towards airborne radar sensors used to image the ground, such as SAR sensors. While SAR sensors are the targeted radar application, generic radar behavior is described in order to facilitate broad radar comprehension.

SAR radar sensors are generally employed on aircraft or satellite platforms. These platforms have a direction of motion that is commonly referred to as the along-track or cross-range direction. The radar sensor emits a waveform that propagates outward from the transmit antenna. The radial propagation occurs in all directions to some extent. But the range direction, commonly referred to as downrange, is defined as the radial propagation direction that aligns with the antenna boresight. The range (downrange) and along-track (crossrange) directions are shown in Figure 2.1. The emitted waveform is reflected by an object in the scene or region of interest (ROI). Part of the reflected energy travels back towards the radar sensor and is intercepted by the receive antenna. The radar sensor waits a pre-determined amount of time after the waveform transmission to commence sampling or digitizing the return signal. The delay time corresponds to the time required for the transmitted signal to reach the scene of interest and be reflected back. The sampling continues until the signal for the entire ROI is captured.

The time of each sample directly relates to the radial or range distance since the transmitted and reflected electromagnetic waves travel at the speed of light. The sampled returns contain the traditional range-rate measurements. After the sensor samples the returned waveform, the radar sensor waits as the platform continues to move forward. Then after a predefined time delay, a new waveform is transmitted and sampled again. This entire process is repeated again and again. The time delay between successive waveform transmissions is called the pulse repetition interval (PRI) or inversely the pulse rate is called the pulse repetition frequency (PRF).

The system described previously is a pulsed radar system. Continuous wave systems behave similarly and will not be discussed here. An excellent overview of the different radar systems is given in Skolnik [19].

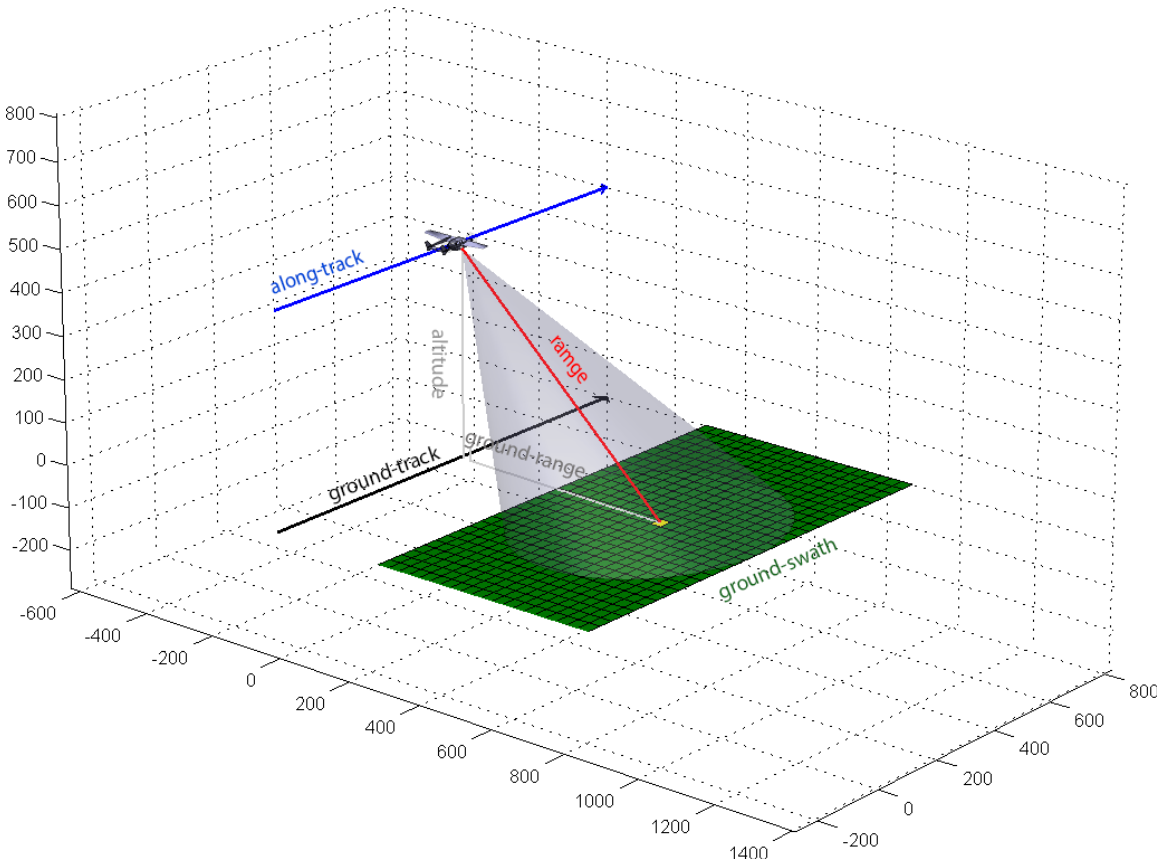

Fig. 2.1: Radar geometry and terms.

2.2 Radar Geometry

It is assumed that the platform moves very slowly compared to electromagnetic propagation and can adequately be assumed to be stationary during transmission and reception of the single radar pulse. This is generally called the *stop and hop* assumption. This supposition embodies the idea the platform stops while transmitting and receiving the radar returns. The platform then hops forward to the next PRI location and stop again while it transmits and receives another radar pulse. This behavior of stopping and then hopping provides the basis for the name.

The stop and hop assumption is assumed unless otherwise stated. The details of when the stop and hop assumption is appropriate are derived in Richards [20]. The geometry associated with a single pulse under the stop and hop assumption can be visualized as in Figure 2.2. The platform is stationary while the pulse propagates to and from the target.

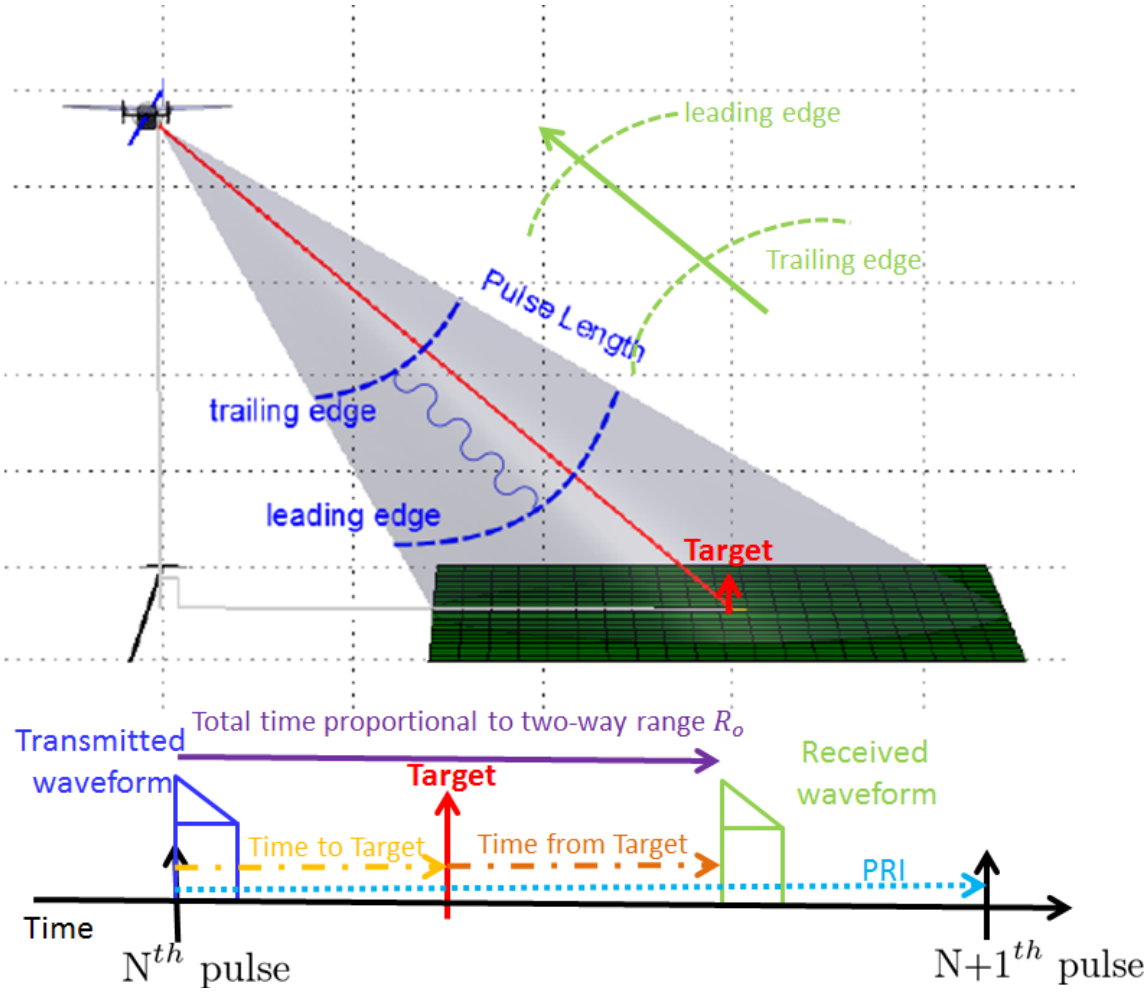

Fig. 2.2: Radar pulse timing visualization.

If the radar is looking for a target at a particular range, it will open up the receiver and start sampling the returns for a specified time period. The time period when the radar is listening is known as the range gate period, and the distance that is covered by the range gate period is the actual range gate. The time period is set to start slightly before the leading edge of the reflected pulse will return from a particular range, and turn off slightly after the trailing edge of the reflected pulse is received. By adjusting the range gate to just cover the target, the noise and clutter from the area surrounding the target is reduced. This is relatively easy to do for a point target. For a distributed target, the range gate has to be left open for a length of time that covers all the time that energy is being reflected, resulting

in a returned signal that usually incorporates extra noise and clutter. For the purposes of this discussion a point target is considered.

Generally the receive and transmit antennas are collocated as shown previously in Figure 2.1. This is referred to as a monostatic configuration. But the transmit and receive antennas can be separate physical antennas. The antennas can even be on separate platforms with diverse geometries. This is referred to as a bistatic configuration and is shown in Figure 2.3. Bistatic radar is an area of active research [21,22]. For simplicity the monostatic configuration is assumed throughout this work.

2.3 Radar Range Rate Measurment

The returns from a single PRI or pulse of data are examined initially. A single sample

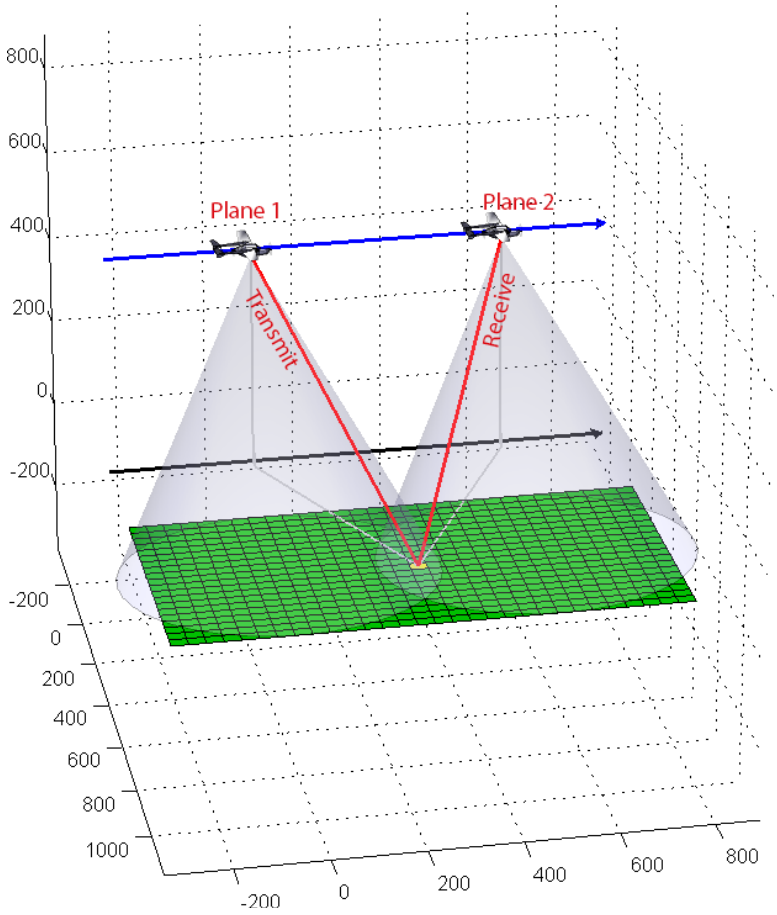

Fig. 2.3: Bistatic radar configuration.

of data is composed of many reflected measurements from distinct targets in the scene. These measurements delineate the radial distance of the reflecting targets during a given PRI. The resolution achieved, or the ability to distinguish targets, in the range dimension depends on the bandwidth of the transmitted waveform. The larger the bandwidth the finer the resolution. It is desirable for many applications to have high bandwidth so that targets in close proximity can be distinguished.

Traditional radar sensors use a rectangular shaped waveform. Radars that emit a rectangular waveform could be viewed as the canonical radar. For a rectangular waveform the bandwidth is inversely related to the pulse duration or pulse length T_P. This implies that a very short pulse length, or burst is required in order to generate signals with a large bandwidth since the bandwidth is equal to $\approx \frac{1}{T_p}$. This requires special hardware to support the large peak power requirements inherent in such a short burst.

The cost incurred financially and in size, weight, and power (SWaP) can be prohibitive when designing and building high bandwidth systems. In order to overcome this difficulty radar engineers encode the radar pulses using frequency or phase modulation. This allows for the generation of waveforms that have a much higher bandwidth than an equivalent uncoded waveform of the same pulse length T_p. Radars that encode pulses in this manner are often called pulse compression radars. This allows for radars to have a much lower peak power and attain a required transmit energy level simply by increasing the pulse length. This also allows for the use of electrical components that have a more favorable cost and SWaP.

The most common waveform used in practice for pulse compression radars is the linear frequency modulated signal (LFM) [20]. The LFM waveform is used as the principle example but waveform diversity is an active area of research [23–25] and has many interesting applications since waveforms can be optimized for specific targets or signals of interest [26]. The basic LFM signal can be represented by

$$s(t) = e^{j\pi K_r t^2}, \tag{2.1}$$

but this simple LFM signal lacks several key components that are pertinent to understanding LFM radar systems. So we define an LFM signal as the following

$$s(t) = w(t - \frac{R_0}{c})e^{j\pi K_r(t-\frac{R_0}{c})^2} \quad \text{s.t.} \quad \frac{-T_p}{2} \leq t - \frac{R_0}{c} \leq \frac{T_p}{2}, \tag{2.2}$$

since this incorporates all the critical components essential to LFM radar systems, particularly the target range R_0, pulse length T_p, and the range weighting window, or envelope factor $w(t)$, which is real-valued.

The variable t represents fast time and is referenced from the start of the pulse transmission or PRI. The terminology *fast time* infers the proportional relationship of the transmitted LFM's position to the speed of light. The variable R_0 represents the two-way range of a specific target of interest. The two-way range is the distance from the transmit antenna to the target and then from the target back to the receive antenna. It is assumed that the radar specific calibration, such as the cable delay, and the zero range delay have appropriately been incorporated. Such details are very important in practice but are overlooked in this development in order to focus on fundamental principles. Several good references that include many radar system details are Carrara et al. and Skolnik [6, 19].

The LFM waveform has a duration or pulse length defined as T_p. The variable K_r is the chirp rate and has units of Hertz per second. The variable K_r can be positive or negative. A positive value implies an up chirp that goes from lower frequency to higher frequency, whereas a down chirp denotes the opposite.

The fast time variable t is defined by the start of the PRI or pulse. The radar returns from a specific target appear at a delayed time according to the target two-way radial distance R_0. The target will then interact with the waveform proportional to the pulse length T_p. A graphical representation depicting the pulse length T_p is seen in Figure 2.2. The range window $w_r(t - \frac{R_0}{c})$ is only defined for a specific target located at a two-way distance R_0, during the relative time of $\frac{-T_p}{2}$ to $\frac{T_p}{2}$. The range window is zero outside this interval since a single targets response will only persist for the duration of the pulse length T_p.

The full derivation of the frequency response of Equation (2.2) is found in Curlander and McDonough but can be represented by

$$H(f) = W(c(f))e^{(-j\pi \frac{f^2}{K_r})} \quad \text{s.t.} \quad \frac{-T_p K_r}{2} \leq f \leq \frac{T_p K_r}{2}, \tag{2.3}$$

where a rectangle window $W(c(f))$ is a scaled version of $w(t)$ [7]. The duality of windowing in time or frequency for an LFM signal is unique. The preservation between the time and frequency can be better understood by examining the instantaneous frequency of Equation (2.1). Taking the derivative of the phase term $\pi K_r t^2$ results in $2\pi Kt$ Hz. This has an instantaneous frequency $f_i(t) = Kt$. The specification of a transmit time also uniquely denotes a corresponding transmit frequency. This underlying duality between time and frequency is the basis for the equivalence of windowing in time or in the frequency domain for an LFM waveform.

A radar sensor samples the reflected waveform at a prescribed rate defined as F_r. Then the energy from a single reflector is spread over $F_r \cdot T_p$ samples. This is shown in Figure 2.4 for a single ideal reflector. This demonstrates the return from a target with a two-way distance R_0 of 786.0 meters, where the pulse length is 5.0 microseconds, and the sample rate is 100 MHz. There are 8192 total range samples and the response from the single target spans 500 samples.

This demonstrates the results for a single discrete target, but a scene is composed of many targets. In fact, a scene is composed of continuum of targets. Fortunately, the continuous scene can be often accurately approximated by a large number of discrete scatterers. More details providing background and justification for such an approximation is detailed in Chapter 3.

This approximation allows the principal of superposition to be leveraged to generate the aggregate result for all targets. Each individual reflective target that is illuminated by the radar beam contributes to the cumulative pulse data collected. The idea of superposition, or the linearity of SAR sensors will continually be leveraged and is an underlying assumption for SAR image formation algorithms. An example of the superposition of three targets is

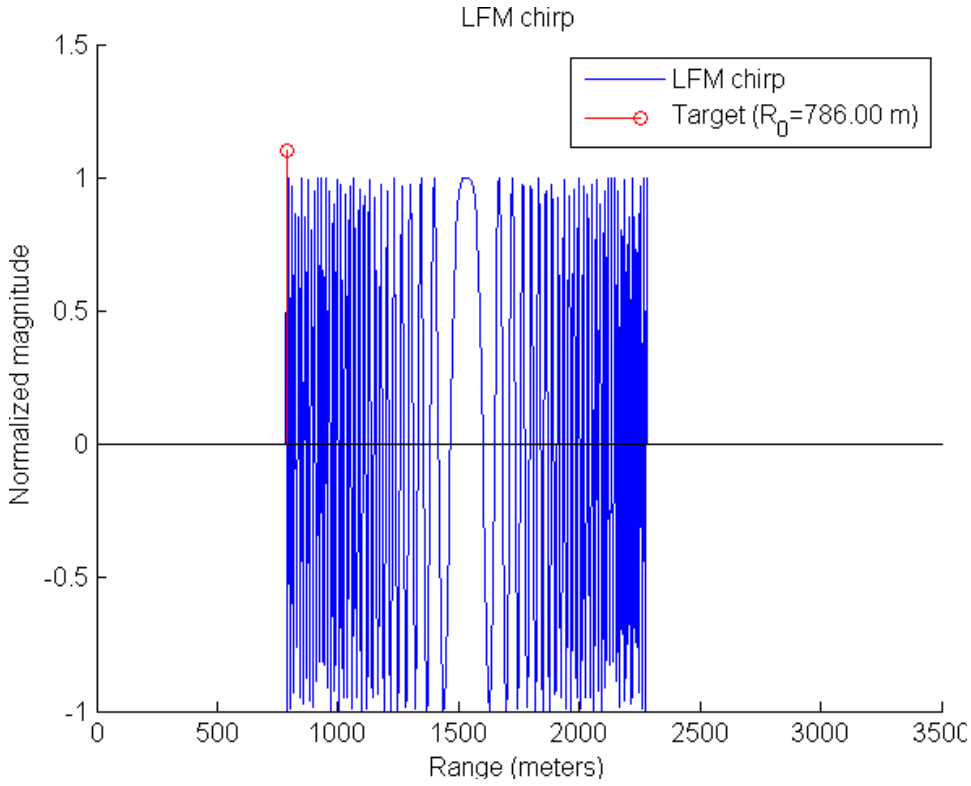

Fig. 2.4: LFM returned signal from a single ideal reflector.

graphically demonstrated in Figure 2.5.

2.4 Range Compression

With a little foresight it is easy to imagine that the inclusion of many targets in the pulse data would cause the radar returns to become difficult to interpret without additional signal processing. From a superficial perspective, a processing step is required that distinguishes range measurements. This is accomplished by matched filtering. This is a common signal processing procedure. The intrinsic details, from a stochastic process perspective, are derived in Gubner [27]. In summary a matched filter maximizes the signal-to-noise (SNR) for the radar application.

The output of a generic continuous matched filter is given by the convolution integral as

$$r(t) = \int_{-\infty}^{+\infty} s(t-u)h(u)du, \tag{2.4}$$

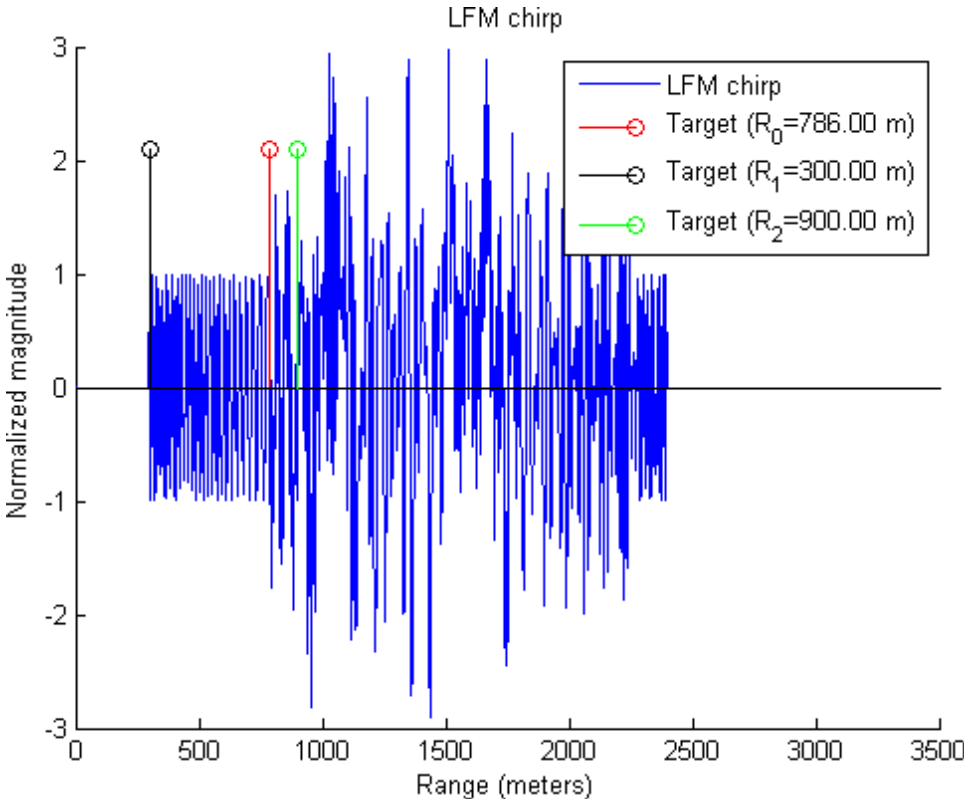

Fig. 2.5: LFM returned signal from multiple ideal reflectors.

or equivalently the generic output can be given as [28]

$$r(t) = IFFT\{S(f)H(f)\}, \tag{2.5}$$

where $S(f)$ is the Fourier transform of $s(t)$ and $H(f)$ is the Fourier transform of $h(t)$.

The matched filter is generically represented by $h(t)$ and the signal of interest is represented by $s(t)$. The specific matched filter for the LFM waveform is defined as

$$h(t) = w(-t)e^{(-j\pi K_r(-t)^2)} \quad \text{s.t.} \quad \frac{-T_p}{2} \leq t \leq \frac{T_p}{2}. \tag{2.6}$$

This is the time-reversed, complex conjugate of Equation (2.2). The results of the LFM matched filter where Equation (2.2) represents $s(t)$ and Equation (2.6) represent the LFM

matched filter can be approximated as

$$s_{mf}(t) \approx T_p \text{sinc}(K_r T_p (t - \frac{R_0}{c})). \tag{2.7}$$

The range window is assumed to be a simple rectangular window. The results are satisfying since the window in Equation (2.3) is also a rectangular window, due to the range window duality discussed previously. And the IFFT of a rectangular window is a sinc function.

The approximation in Equation (2.7) is accurate as long as the time bandwidth product (TBP) is greater than 100, allowing the principle of stationary phase (POSP) to be leveraged [29]. The signal bandwidth is equal to the chirp rate K_r (units of Hertz per second) multiplied by the pulse length T_p (units of seconds) giving bandwidth $= K_r \cdot T_p$. The TBP product is defined as the signal bandwidth times the pulse length T_p. This results in the definition of $TBP = K_r \cdot T_p^2$. But an insightful definition of the TBP is the ratio of the transmit pulse length to the *compressed* pulse main-lobe width.

For the canonical radar system mentioned previously, the TBP is equal to 1 since the bandwidth $\approx \frac{1}{T_p}$. The TBP can also be interpreted as the reduction in peak-power a compressed radar system is able to achieve compared to a canonical radar system for specified power level. The TBP for the examples given previously in Figure 2.4 and Figure 2.5 is 250. Almost all modern SAR systems have TBP well over a 1000 so generally this approximation is justified [5].

Equation (2.7) is a real function resulting in real-valued RCS. But in practice every target will have a complex reflectivity that causes the range-compressed data to be complex.

The matched filter results for three discrete point targets shown in Figure 2.5 is displayed in Figure 2.6. One observation is that most of the energy for a specific target has been localized to the particular range bin after matched filtering. The range bin location naturally corresponds to the target range. Prior to matched filtering the signal energy is spread across neighboring range bins proportional to the pulse length T_p. The term *pulse compression* generically describes this phenomenon of compressing the pulses energy to the associated range bin. Pulse compression can be accomplished in varying related procedures

besides matched filtering. The method of compression often depends on the radar mode. The details of different types of processing, such as stretch or dechirp, can be found in Skolnik [19]. Pulse compression is generally the first step in many radar processing algorithms.

The range resolution, defined by the -3dB bandwidth after matched filtering is given by

$$\phi_r = \frac{c}{2bw}, \tag{2.8}$$

for a monostatic configuration. The factor c is the speed of light, and bw is the waveform bandwidth. The factor of 2 results from the two-way wave propagation. The LFM waveforms used for previous examples had a bandwidth of 50 MHz which results in a resolution of approximately 3 meters.

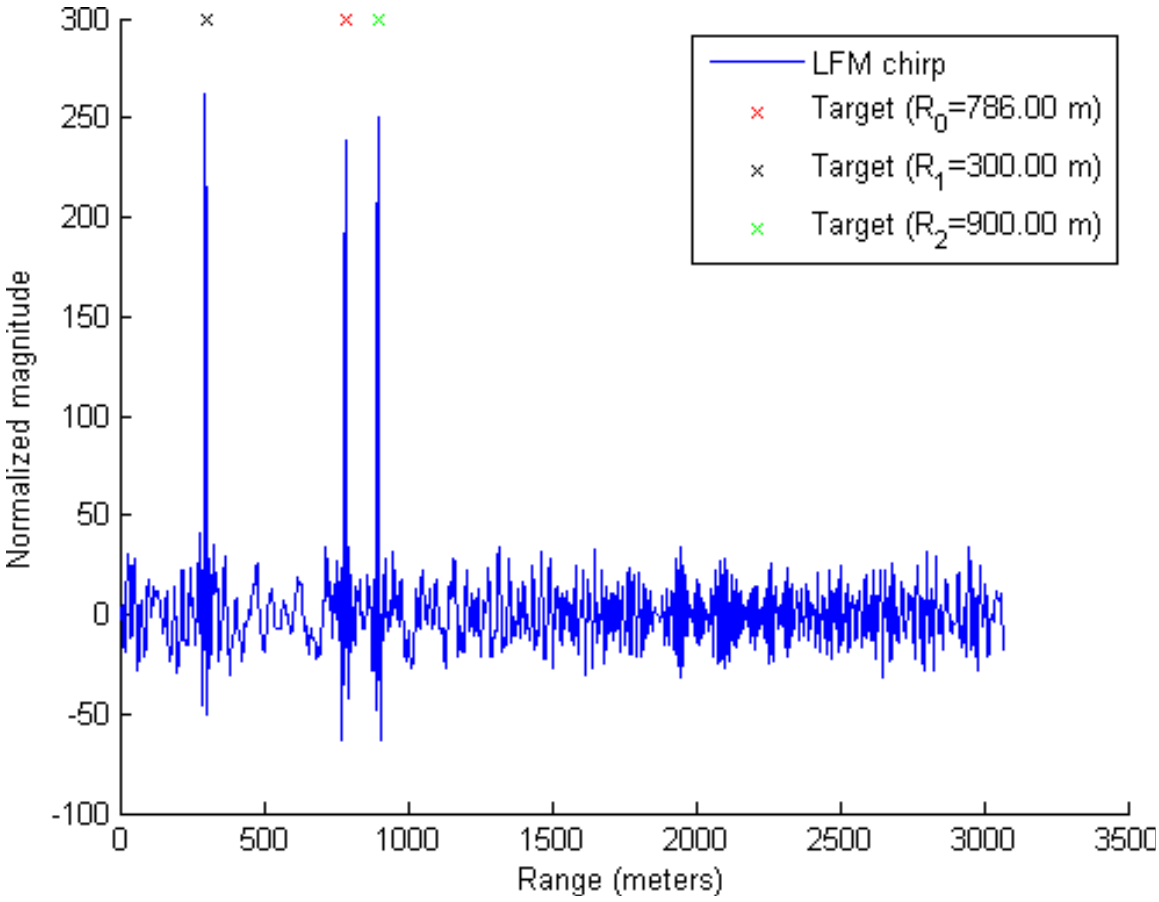

Fig. 2.6: Example LFM chirp that has been matched filtered.

2.5 Signal Modulation

A natural extension of processing a single pulse of data, as is done with pulse compression, is to extend the processing to include multiple pulses. This should be done in an efficient manner so that signals of interest are enhanced by considering multiple pulses.

Prior to proceeding it is important to cover an essential concept. The radar hardware performs a modulation and demodulation of the baseband signal, such as the LFM in Equation (2.2). This process applies a very important deterministic phase change to the signal that is critical in many coherent radar applications such as SAR, GMTI, and others. The phase change conferred by this process is often referred to as the Doppler signal. More is discussed later regarding the Doppler signal, but for now it is important to understand it is a modulation effect that it is deterministic based on a target's range.

The radar system applies the modulation by multiplying the baseband signal by a carrier frequency and low-pass filtering [28]. This translates the baseband signal, such as the LFM, to the frequency of interest. A generic representation is given by

$$x(t) = \cos(2\pi f_0 t + \phi(t)). \tag{2.9}$$

Equation (2.9) represents the actual signal that is transmitted from the radar antenna. The variable f_0 is the carrier frequency. The generic variable $\phi(t)$ represents the baseband phase or frequency encoded signal, and is often an LFM signal for pulse-compressed radars. The carrier frequency f_0 is assumed to be much higher frequency than the bandwidth of the baseband signal $\phi(t)$.

The returned signal is delayed in time by the two-way range to the reflecting target. The returned signal is also scaled in magnitude and has assimilated a target dependent phase term. The returned signal can be modeled as [30]

$$s_r(\tau,\eta) = A_0(\theta,\phi)w_r(\tau - \frac{R_0(\eta)}{c})w_a(\eta)cos(2\pi f_0(\tau - \frac{R_0(\eta)}{c}) + \pi K_r(\tau - \frac{R_0(\eta)}{c})^2 + \Psi). \tag{2.10}$$

The first factor $A_0(\phi,\theta)$ is a complex reflection term dependent on the azimuth and elevation

angles θ and ϕ due to the collection geometry. The geometrical dependence of the target $A_0(\theta, \phi)$ is almost always approximated as a constant A_0.

The second factor $w_r(\tau - \frac{R_0(\eta)}{c})$ represents a windowing function in range. It is nonzero for a specified transmit pulse length T_p during the interval $[\frac{-T_p}{2}, \quad \frac{T_p}{2}]$ relative to the two-way range $R(\eta)$ of a given target for the η^{th} pulse. The third factor $w_a(\eta)$ represents the two-way antenna gain and phase incurred due to the geometry of the η^{th} pulse and the corresponding target.

The fourth factor a cosine function has multiple phase terms. The first phase term of $2\pi f_0(\tau - \frac{R_0(\eta)}{c})$ represents the delayed carrier phase. As the platform moves from pulse η_i to pulse η_{i+1} the phase changes due to the platform translation. The extent of the change depends upon the collection geometry and the corresponding two-way distance $R_0(\eta)$. The second phase term $\pi K_r(\tau - \frac{R_0(\eta)}{c})^2$ is a delayed replica of the transmitted LFM signal. The final phase term Ψ represents a constant, unknown residual carrier phase and is generally ignored.

Upon receipt of the signal given in Equation (2.10), a process referred to as demodulation occurs. Traditional radar system might use an analog quadrature demodulation method. Many new radar systems employ direct digital conversion methods. Fundamentally, direct digital conversion and quadrature demodulation result in identical baseband signal representations. The quadrature demodulation process is examined in order to understand the final basebanded signal and is shown in Figure 2.7.

If a single pulse is examined then η is a fixed constant. The phase term $\phi(t)$ in Equation (2.9) can defined as

$$\phi(\tau) = -2\pi f_0 \frac{R_0(\eta)}{c} + \pi K_r(\tau - \frac{R_0(\eta)}{c})^2 + \Psi. \tag{2.11}$$

The phase terms on the right hand side of Equation (2.11) originate from Equation (2.10). Now substituting from Equation (2.11) to Equation (2.10) and ignoring all the magnitude

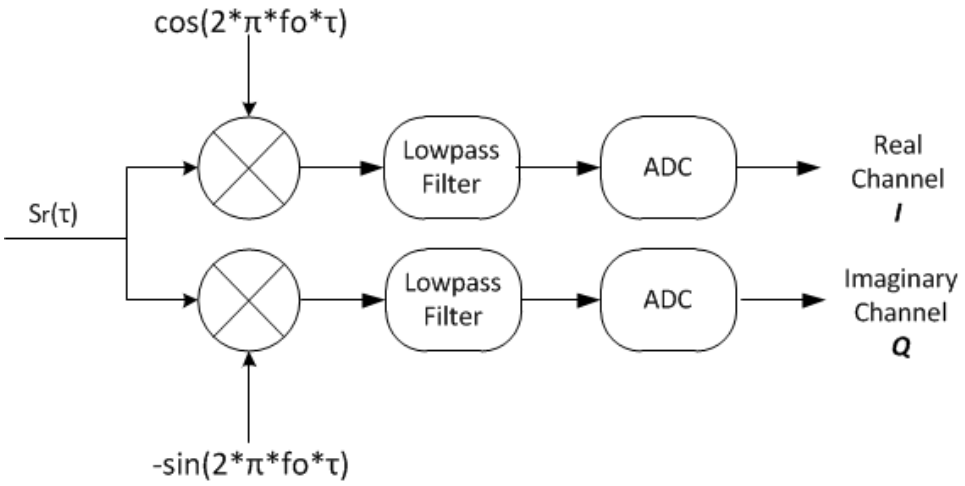

Fig. 2.7: Quadrature demodulation.

scaling parameters of Equation (2.10) condenses the equation to

$$s_r(\tau) = \cos(2\pi f_0(\tau) + \phi(\eta)). \tag{2.12}$$

The effects of quadrature demodulation on this unscaled signal in Equation (2.12) is examined briefly. The cosine path is considered first as shown in Figure 2.7. The signal at the outset is multiplied by $\cos(2\pi f_0 t)$. By leveraging the following trigonometric identity

$$\cos(\phi_1)\cos(\phi_2) = \frac{1}{2}\cos(\phi_1 - \phi_2) + \frac{1}{2}\cos(\phi_1 + \phi_2); \tag{2.13}$$

the resultant product of Equation (2.12) by $cos(2\pi f_0)$ can be written as

$$\frac{1}{2}\cos(\phi(\tau)) + \frac{1}{2}\cos(4\pi f_0(t) + \phi(\tau)). \tag{2.14}$$

The operation of low-pass filtering will remove the second cosine term on the right in Equation (2.14) leaving only the first term on the left

$$\frac{1}{2}\cos(\phi(\tau)). \tag{2.15}$$

This represent the output of the quadrature demodulation for the cosine path. Equation (2.15) can be rewritten as

$$\frac{1}{2}\cos(-2\pi f_0\frac{R_0(\eta)}{c}+\pi K_r(\tau-\frac{R_0(\eta)}{c})^2+\Psi), \tag{2.16}$$

by substituting $\phi(t)$ defined in Equation (2.9) into Equation (2.15).

A similar derivation for the sine path using the related trigonometric identify

$$\sin(\phi_1)\cos(\phi_2)=\frac{1}{2}\sin(\phi_1-\phi_2)+\frac{1}{2}\sin(\phi_1+\phi_2); \tag{2.17}$$

results in

$$\frac{1}{2}\sin(-2\pi f_0\frac{R_0(\eta)}{c}+\pi K_r(\tau-\frac{R_0(\eta)}{c})^2+\Psi). \tag{2.18}$$

The quadrature components given in Equation (2.16) and Equation (2.18) are often called the I and Q channels. They can be combined into a complex signal given as

$$\frac{1}{2}\exp(-j2\pi\frac{R_0(\eta)}{\lambda}+\pi K_r(\tau-\frac{R_0(\eta)}{c})^2+\Psi). \tag{2.19}$$

The modulation demodulation process removes the carrier phase $2\pi f_0(\tau)$ seen in Equation (2.10). But it leaves the range-dependent residual $-2\pi f_0\frac{R_0(\eta)}{c}$ term that is often written as $-2\pi\frac{R_0(\eta)}{\lambda}$ as seen in Equation (2.19). Rewriting $-f_0\frac{R_0(\eta)}{c}$ as $-\frac{R_0(\eta)}{\lambda}$ provides a natural insight. It represents the phase term imparted due to the fractional wavelengths traversed by the two-way target range R.

A critical observation is to recognize that if the relative phase change from pulse η to pulse $\eta+1$ is more than half a wavelength it cannot be resolved unambiguously. For example, if the change of phase from pulse (η) to pulse $(\eta+1)$ is 1.3 wavelengths, the phase term would be equivalent to 0.3 wavelengths and -0.7 wavelengths. But if the PRI occurred frequently enough so that all wavelength changes traverse less than half a wavelength, positive or negative, the results could be resolved unambiguously. This idea will form the basis for the required Doppler sampling or the radar PRF. The received signal in Equation

(2.10) after demodulation can be written as

$$s_b(\tau,\eta) = A_0(\theta,\phi)w_r(\tau - \frac{R_0(\eta)}{c})w_a(\eta)e^{j2\pi\frac{R_0(\eta)}{\lambda}}e^{j\pi K_r(\tau-\frac{R_0(\eta)}{c})^2}, \tag{2.20}$$

when the scaling terms are retained. This is the basebanded signal that is sampled by the radar's analog to digital converters (ADC) and stored.

The received basebanded signal s_b is then matched filter as described in Section 2.4. The matched filter is given in Equation (2.6) and the result is

$$s_c(\tau,\eta) = A_0(\theta,\phi)p_r(\tau - \frac{R_0(\eta)}{c})w_a(\eta)\exp(j2\pi\frac{R_0(\eta)}{\lambda}). \tag{2.21}$$

The factor $A_0(\theta,\phi)$ changes with azimuth and elevation, but over a limited aspect it is approximately constant. This assumption allows it to be ignored since it is a common, albeit unknown, factor for all pulses. The next factor $w_a(\eta)$ is a scaling factor from the transmit and receive antennas that is constant for the η^{th} pulse. The factor $p_r(\tau - \frac{R_0(\eta)}{c})$ represents the sinc envelope in Equation (2.7). The assumptions employed in these results are first that a rectangular window $w_r(t)$ was used and second the waveform utilized had an appropriate TBP. While almost all radar systems will have an appropriate TBP, often other windows are utilized. Some common windows are Taylor, Hamming, Hanning, or Kaiser windows. All these windows mentioned are "smoother" windows compared to the rectangular window. When non-rectangular windows are utilized, the factor $p_r(t)$ represents an approximate sinc like function.

Another elucidating perspective is gained when the duality of the LFM signal, that was discussed in Section 2.3, is considered. The time domain window $w_r(\tau - \frac{R_0(\eta)}{c})$ is approximately equivalent to applying a scaled equivalent frequency domain window $W(c(f))$ given in Equation (2.3). This gives impetus to $p_r(t)$ having a sinc like shape since the IFFT of the common windows like the Taylor, Hamming, Hanning, and Kaiser window still have an approximate sinc shape.

2.6 Doppler Signal

A logical extension of processing a single pulse is to process multiple pulses simultaneously. The same principle of matched filtering applied in the range dimension can be used in the cross-range direction, also called the azimuth direction. The compression of a specific target across pulses is called azimuth compression. The azimuth direction is synonymous with the along-track or cross range direction shown in Figure 2.1. In order to understand azimuth compression, first the signal in the azimuth dimension, called the Doppler signal, is analyzed.

To develop a solid understanding of the Doppler signal used for azimuth compression a single point is simulated and processed in a strip-map configuration. In a strip-map configuration the antennas are fixed relative to the aircraft motion. The aircraft motion convolves the antennas with the scene. This is in contrast to the other common configuration called a spot-map configuration. A spot-map configuration is when the antenna is continually steered towards a specific spot on the ground or ROI. The main difference between spot and strip modes are the antenna's configuration. Often spot-mode utilizes different processing of the radar returns compared to strip-mode. But the reflected signal, prior to any signal processing, is fundamentally the same between both modes.

The simulation geometry is visualized in Google Earth™ and shown in Figure 2.8 for context. The simulation assumes that only the push-pin point labeled as the "Discrete Target" reflects energy. By focusing on a single point, it is easier to make clear the relevant concepts and not become confused with the aggregate signal composition that actual scenes produce.

For the simulation an LFM pulse was transmitted that had a bandwidth of 50 MHz. The pulse duration was 10 microseconds. The radar system acquired 4096 samples at a 100 MHz sample rate. The signal was sampled after waiting 55 microseconds or in radar terms the range-gate-delay was 55 microseconds. The aircraft traveled east at a constant velocity of 40 m/s, with the track starting at 41.16° N 113.13 ° W and stopping at 41.16° N 113.19° W.

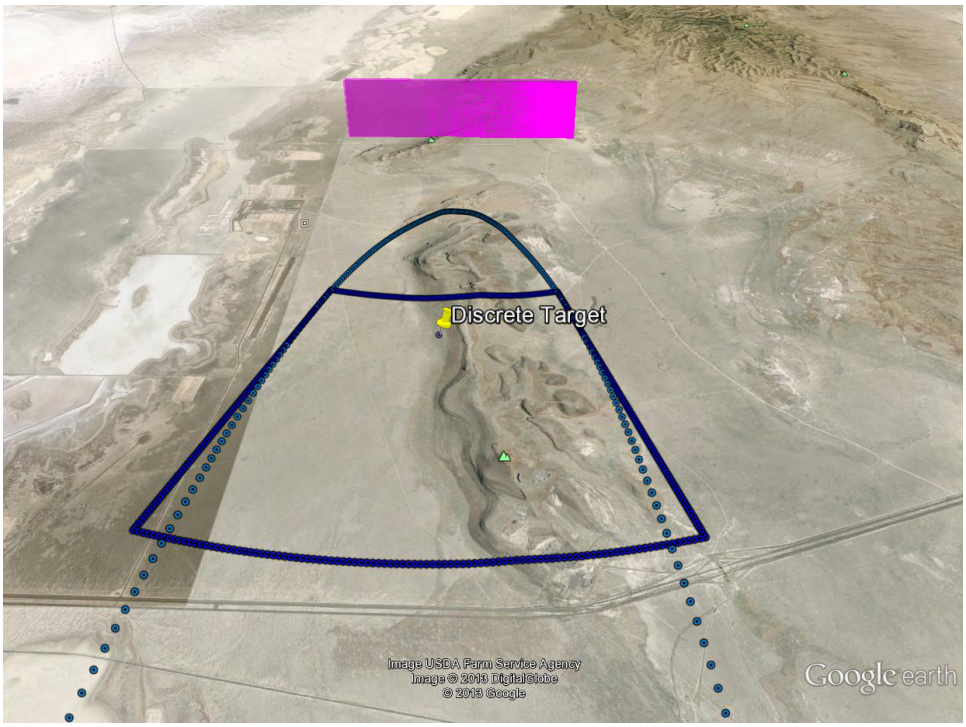

Fig. 2.8: The simulation geometry is shown in Google Earth™. The aircraft trajectory is along the top of the pink strip. The ellipsoidal beam pattern is shown in light blue and the Doppler beam pattern in dark blue. The single discrete target is shown as the yellow push-pin.

The raw data generated from a single point reflector is shown in Figure 2.9. The contrast in magnitude seen in the raw data results from the transmit and receive antenna patterns. As the target approaches the transmit and receive antenna boresight, or beam center, the signal returns increases in strength. As the target recedes from the transmit and receive antenna boresight the signal returns begin to decrease.

The first processing step done on the basebanded signal is range compression by applying a matched filter as described in Section 2.4. This localizes the point response in range as seen in Figure 2.10. The resultant range-compressed signal naturally encodes the relative target range over time. As the platform moves the changing range from the target to the platform is actually traced in the raw data and visualized in Figure 2.10 where near-range is the top and far-range is the bottom of the ordinate axis. The range decreases as the platform approaches the target and reaches a minimum when the target is perpendicular

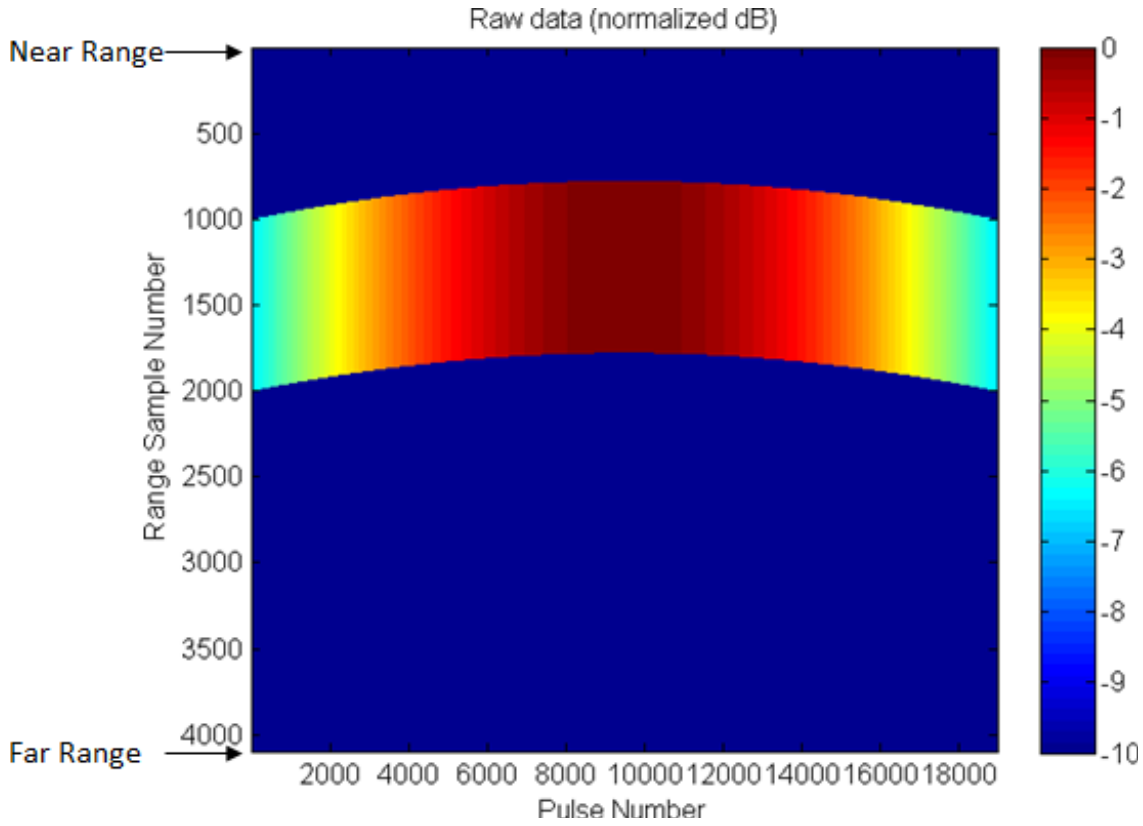

Fig. 2.9: The simulated raw SAR data.

to the flight path, then increases as the platform departs from the target. This hyperbolic shape traced by the target trajectory is often called range cell migration (RCM). The name captures the idea that a target migrates from a particular range cell, or range bin to another based on the collection geometry.

By making the assumption that the platform has constant velocity and a rectilinear flight path the target range can be computed as

$$R_0(\eta_x)^2 = R_b(\eta_b)^2 + V_p^2 \Delta_{\eta_x}^2. \tag{2.22}$$

Figure 2.11 shows such a rectilinear geometry. The term $R_b(\eta_b)$ represents the broadside distance, or the minimal distance that occurs on the η_b^{th} pulse for the rectilinear flight. The term V_p represents the constant platform velocity and the term Δ_{η_x} represents the time passed from the η_x^{th} pulse relative to the broadside pulse η_b. The distance traveled in the

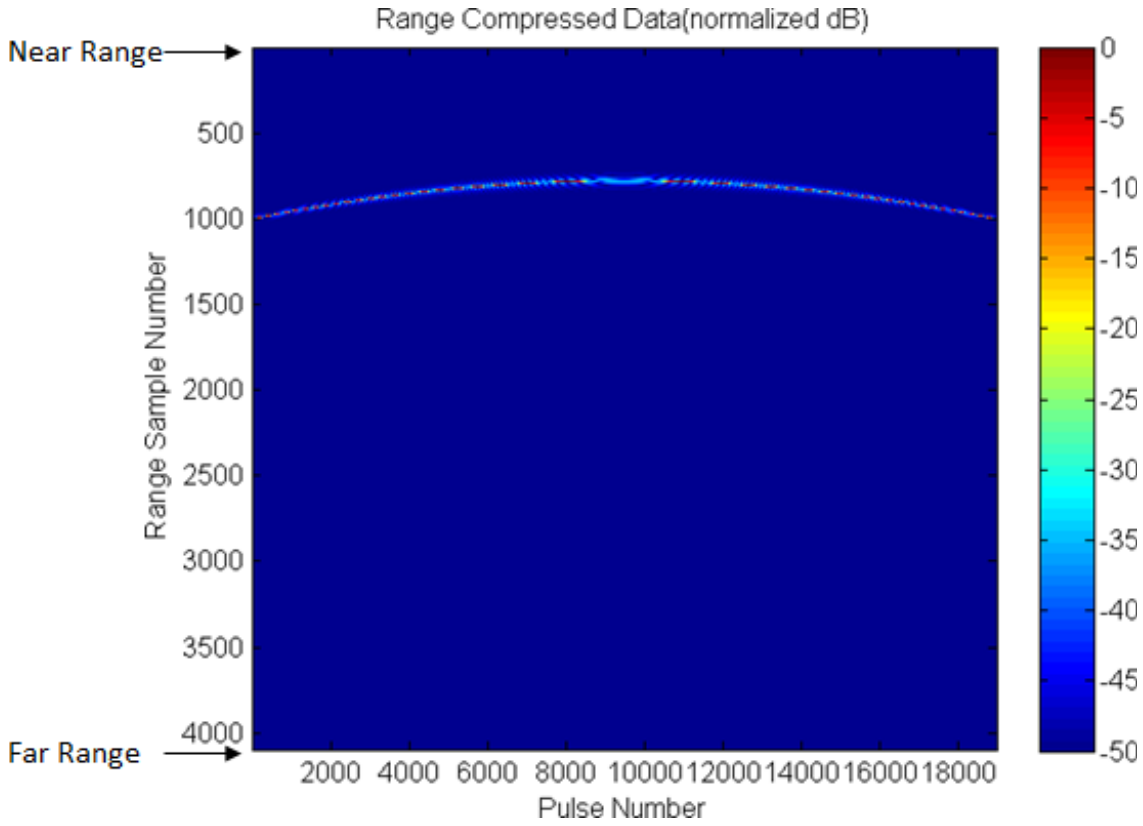

Fig. 2.10: Range-compressed data.

azimuth direction is simply the velocity multiplied by the elapsed relative time, $V_p\Delta_{\eta_x}$. The term $R_0(\eta_x)$ represents the radial distance for the $\eta_x{}^{th}$ pulse to the designated target. This representation helps understand the hyperbolic shape seen in the raw data of Figure 2.9.

The results shown in Equation (2.22) can be rearranged and written as

$$R_b(\eta_b) = \sqrt{R_0(\eta_x)^2 - V_p^2\Delta_{\eta_x}^2} = R_0(\eta_x)\sqrt{1 - (\frac{V_p^2\Delta_{\eta_x}}{R_0(\eta_x)})^2} = R_0(\eta_x)\cos(\theta). \tag{2.23}$$

The results $R_b(\eta_b) = R_0(\eta_x)\cos(\theta)$ are readily seen in Figure 2.11 geometrical by visualizing the appropriate right triangle and leveraging the Pythagorean theorem. The radial distance $R_0(\eta_x)$ from the platform to the target is the hypotenuse of the triangle. The radial distance from the target to the broadside location $R_b(\eta_b)$ forms another leg of the triangle, and the final leg of the triangle is formed by the platform displacement X_1 which is equal to $V_p\Delta_{\eta_1}$.

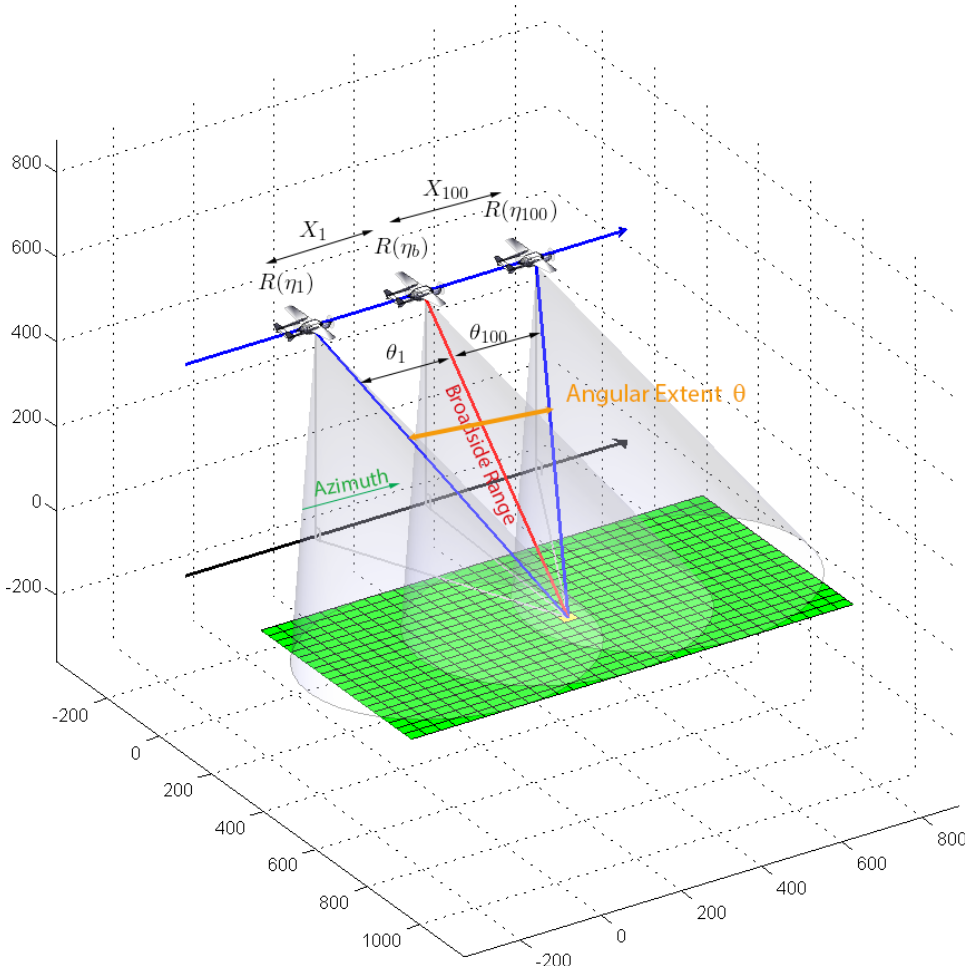

Fig. 2.11: Hyperbolic geometry.

All modern radar platforms have global positioning system (GPS) and inertial navigation systems (INS). The SAR system has knowledge of the platform position to an accuracy that is proportional to the quality of the GPS and INS systems utilized. For our simple simulation absolute positional knowledge is assumed for simplicity. But in practice, handling positional errors, especially along the radar lines-of-sight, is critical to many SAR missions and an error that needs to be analyzed [6].

For imaging radars, like SAR sensors, the target or ROI location is usually known. The knowledge of the platform pulse location and the target location allows the relative range to be computed for every pulse. Once the range is known the signal of interest for a particular target can be identified. This is possible since the radial range distance directly

relates to time as discussed in Section 2.3. The appropriate range bin, or range sample directly corresponds to a time or distance. This allows the range distance to effectively be used as a look-up parameter to select the appropriate range sample or range bin.

A simple simulation that consists of a single point located at 40.77638° N, −113.16° W with an ellipsoidal height of 1309.1260 meters is examined. The target is extracted or removed from the range-compressed data. The range-compressed data is seen in Figure 2.10. The range-compressed data exhibits the hyperbolic trajectory due to the SAR collection geometry. The range-compressed data with the target extracted is shown in Figure 2.12. The 20 range samples prior to the target range bin are removed and the 20 ranges samples after the target range bin are removed. The target range is computed for every pulse based on the geometry and then those corresponding range bins are extracted for examination.

There are several fundamental, and interesting insights to be gained by inspection

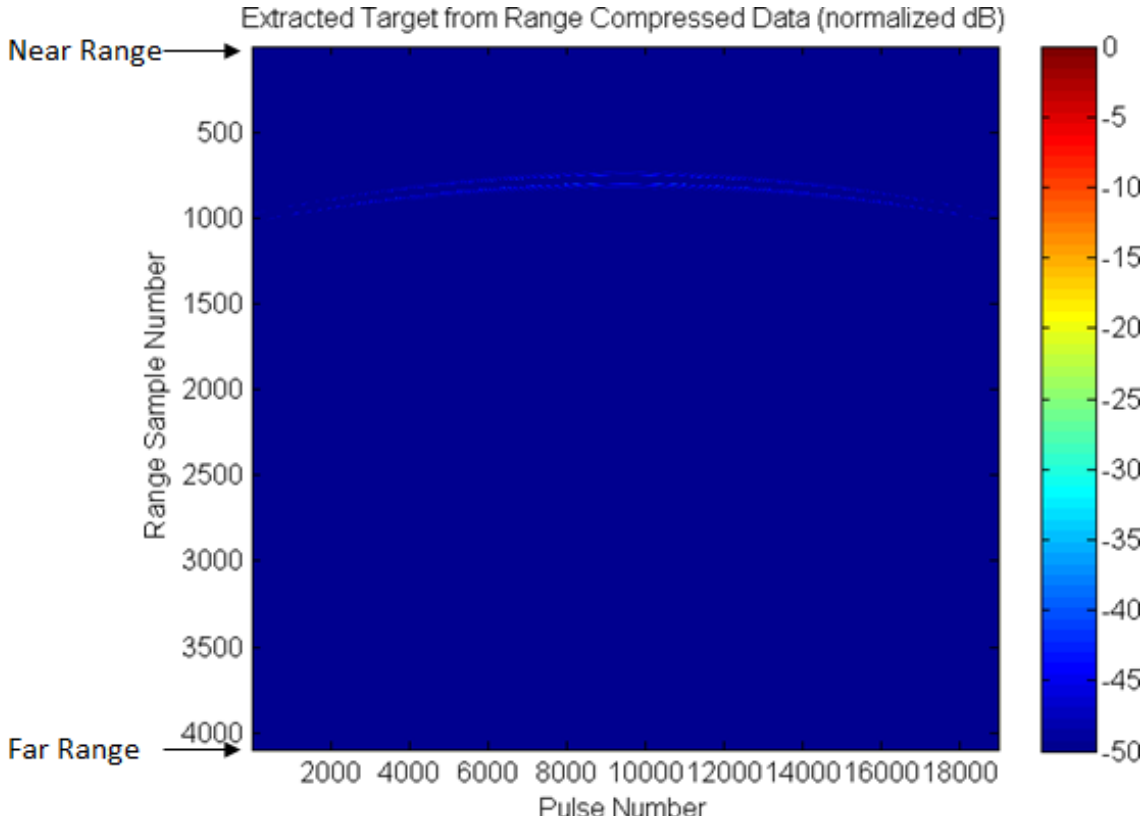

Fig. 2.12: Range-compressed data with target extracted.

of the extracted signal for a given target. The extracted signal is upsampled by 16 for visualization purposes and then displayed in Figure 2.13. The matched filter operation produces range sidelobes. As discussed in Equation (2.21) the range-compressed results has a sinc like response in range. If a rectangular window is employed the first range sidelobe is only -13dB down from the main-lobe [30]. This is generally not sufficient since weaker targets can easily be masked by bright adjacent targets. A common objective is to have the first side lobe around -35dB down. This requires smoother windows to be utilized for $w_r(\tau - \frac{R_0(\eta)}{c})$ in Equation (2.10). But a smoother window will broaden the main-lobe, compared to a rectangular window. This requires compromise since the two desirable objectives are competing [28].

The precise target range bin signal is examined, which corresponds to the white line seen in Figure 2.13 at pulse number 330. The extracted target signal is plotted in Figure

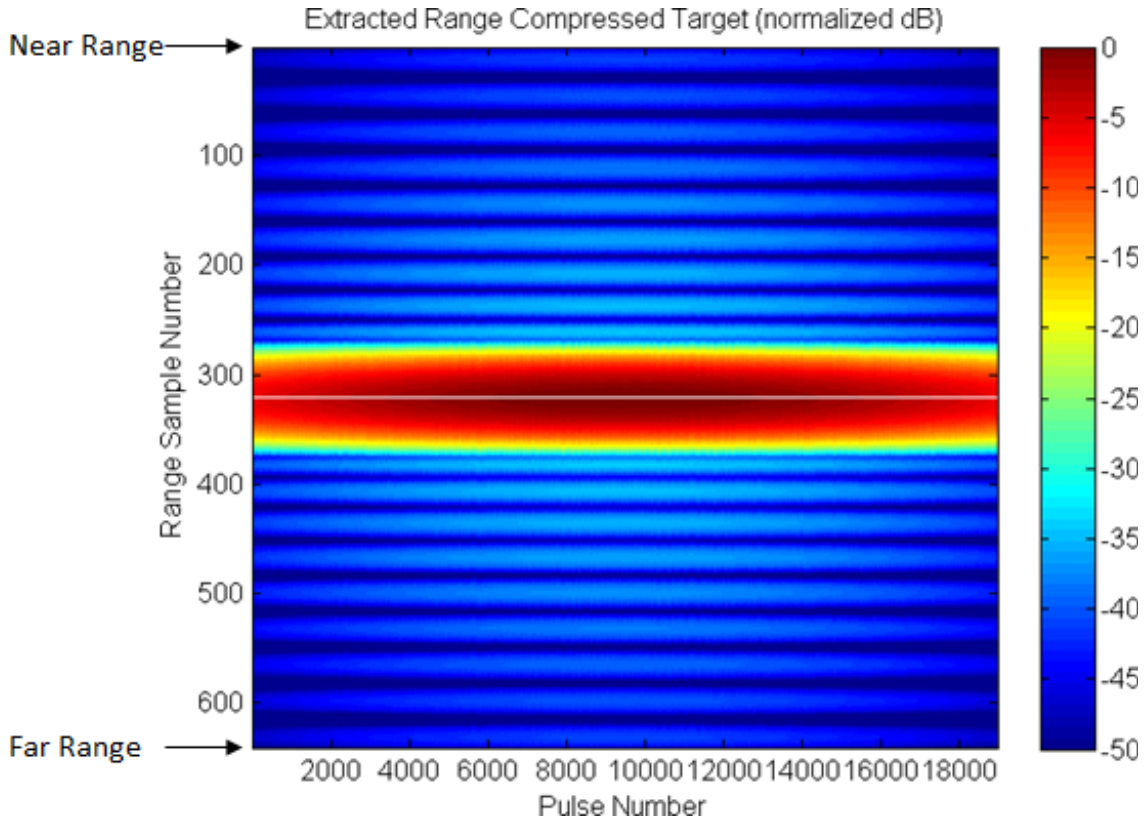

Fig. 2.13: Upsampled range-compressed target.

2.14(a), and a zoomed in view of the extracted target signal is shown in Figure 2.14(b). These plots shows the change in phase experienced by a single point for the collection geometry of a straight rectilinear flight. The change in phase for a linear flight is minimal when the target is broadside, or perpendicular to the linear trajectory. And the change in phase increases as the target is squinted relative to the broadside direction.

The phase change results from the changing motion from one pulse to the next. The rate of change is understood by considering the derivative of the position $R_0(\eta_x)\cos(\theta)$ given in Equation (2.23). The derivative of the cosine term will result in a sinusoidal term. This term is very small when the angle θ seen in Figure 2.11 is small. As the angle θ grows the rate of change will increase. It is important to realize that the angular extents, defined by θ as seen in Figure 2.11, is limited for actual systems. The angular extents are limited by the physical antenna for strip-map configuration. And for spot-map configuration the angular extent is limited by the collection geometry utilized. For our simulated strip-map configuration the antenna had a 30 degree azimuth main-lobe. This means that θ extends from -15 degrees to $+15$ degrees.

The signal experiences a frequency change. The frequency change is due to the Doppler effect. The Doppler effect is manifest when there is motion between a target and the radar.

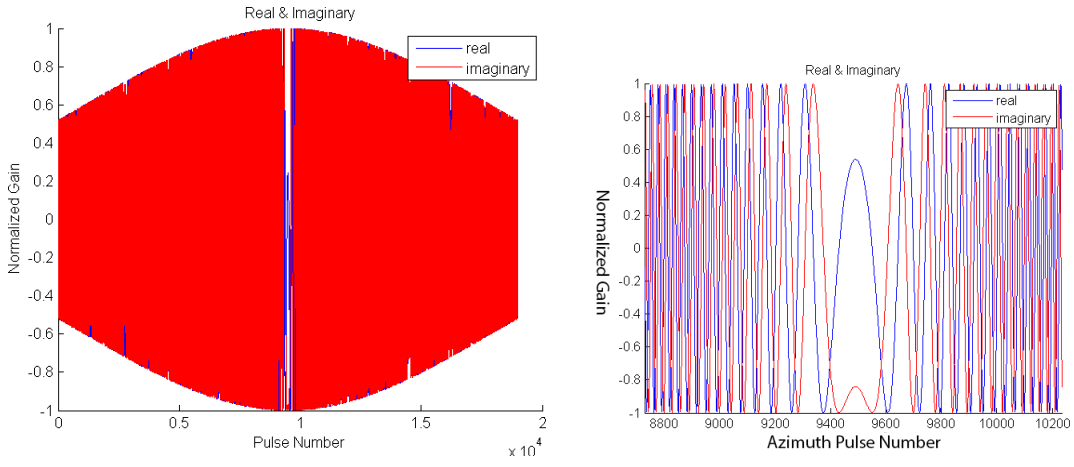

(a) (b)

Fig. 2.14: Analyzing the azimuth signal: (a) Extracted azimuth signal, (b) Extracted azimuth signal (zoomed in).

The idea of a Doppler shift is generally understood when considering an ambulance siren approaching and leaving and the corresponding change in pitch that occurs. This is the correct general idea. But the Doppler effect for radar is realized by the changing wavelength or phase from pulse to pulse of a particular target. This is in contrast to the compression and expansion of an individual wave, such as occurs with an ambulance siren.

The Doppler shift is defined as

$$f_d = \frac{2v_p}{\lambda}\cos(\psi), \tag{2.24}$$

for a monostatic radar. The term f_d represents the Doppler shift. The platform velocity is given as v_p. The angle ψ is often called the Doppler cone angle and is measured relative to the instantaneous platform velocity vector. The angle ψ can be thought of as the antenna boresight direction for SAR applications. The term λ is defined by the carrier wavelength. The Doppler bandwidth is defined as

$$f_{bw} = \frac{4v_p}{\lambda}\sin(\psi)\sin(\frac{\theta}{2}), \tag{2.25}$$

where θ represents the integration angle. In a strip-map configuration θ is equivalent to the azimuth antenna beam-width and in a spot-map configuration θ represents the angular extent defined by the geometry. The Doppler bandwidth f_{bw} provides the minimal sampling requirements or PRF in order to ensure no aliasing occurs from pulse to pulse. As discussed previously the sampling is such that the relative wavelength change never exceeds plus or minus half the wavelength from pulse to pulse.

The visualization of constant range circles with approximate hyperbolic contours of constant Doppler angle is shown in Figure 2.15. The Doppler signal follows a hyperbolic contour when the scene is flat, or has no terrain relief. And the platform has a constant velocity. The effects of terrain cause irregularities as seen in Figure 2.15. The perturbations for this image are generated by using elevation information from DTED files. The hyperbolic-like contours of constant Doppler angle can also be thought of as contours of

constant Doppler frequency.

Any target along the red hyperbolic contours shown in Figure 2.15 exhibit a common Doppler frequency. Any target located along the black radial arc resides in the same range bin, or range sample. Targets can be distinguished by considering both the Doppler frequency and the range samples. The Doppler and range contours are not smooth due to the fact that elevations is incorporated into the range and Doppler computations. For a flat scene the Doppler and range contours would be smooth.

The Doppler signal, which is a result of the modulation process described in Section 2.5 and the platform motion, resolution can be given as

$$\phi_d = \frac{v_p}{f_{bw}}, \tag{2.26}$$

which has a very similar form as the range resolution ϕ_r given in Equation (2.8). The

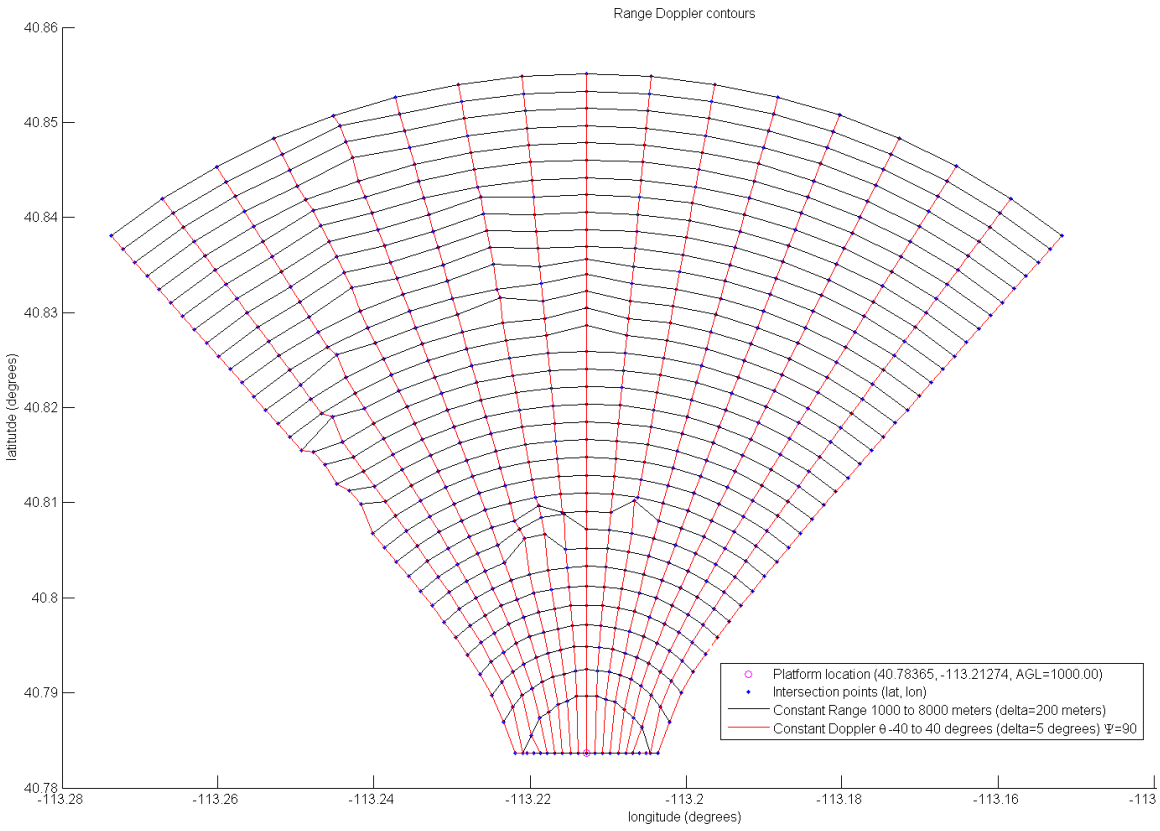

Fig. 2.15: Doppler and range contours including elevation perturbations.

simulation detailed previously in this section, used a 30 degree beam-width and had a 1GHz carrier frequency. The platform traveled at constant rate of 40 m/s. This results in an azimuth resolution of approximately 0.3 meters.

2.7 Azimuth Compression

All the components seen in the range-compressed results in Equation (2.21) can now be readily identified. The Doppler signal is given as $\exp(j2\pi\frac{R_0(\eta)}{\lambda})$ as derived in section Section 2.6. The target's RCS angular dependence $A_0(\theta, \phi)$ is ignored. It is assumed to be a constant, given by A_0. This is justified if a limited angular extent is utilized. The factor $w_a(\eta)$ is the antenna phase and weighting factor which can be measured in the lab prior to flight collections. The factor $p_r(\tau - \frac{R_0(\eta)}{c})$ represents the sinc like shape seen in Figure 2.13. This signal can be written as

$$s_c(\tau, \eta) = A_0 p_r(\tau - \frac{R_0(\eta)}{c}) w_a(\eta) \exp(j2\pi\frac{R_0(\eta)}{\lambda}), \tag{2.27}$$

and provides the basis for an azimuth matched filter.

The matched filter for a specific target R_0 and the η_{th} pulse is given as

$$h_a(\tau, \eta) = w_a(\eta) \exp(-j2\pi\frac{R_0(\eta)}{\lambda}), \tag{2.28}$$

where the term A_0 was dropped. The term A_0 adds a constant scaling and phase, but is unknown. The other term $p_r(\tau - \frac{R_0(\eta)}{c})$ is also dropped since it is assumed to be constant for a given target as shown in Equation (2.7).

A scene is composed of a grid of targets. Or in other words a grid of pixels covering the ROI to be imaged is generated. Naturally the grid spacing is related to the system resolution as defined by Equation (2.8) and Equation (2.26). Each pixel, which can be thought of as an individual target, is processed uniquely. This implies that each pixel will utilize a unique matched filter for every pulse. Equivalently, each pixel will generate a matched filter that incorporates the specific range from it to the radar. The matched filter

is generated by Equation (2.28).

Then the matched filter is multiplied by the corresponding range-compressed data. An example of simulated range-compressed data for a discrete target is visualized in Figure 2.13. The white horizontal line seen represents the "peak" target response. The peak response of the target should be utilized for the matched filtering in order to ensure quantization effects are minimal. This is accomplished by up sampling and, or interpolating the range-compressed data. The range-compressed data in Figure 2.13 was upsampled by a factor of 16. The resultant ROI grid is centered around the simulated point target. The grid is 512×512 meters. The resolution of each cell is 1 meter square. The result is displayed in Google Earth™ in Figure 2.16(a) for context. A zoomed in view of the single discrete target results generated from backprojection processing is shown in Figure 2.16(b). The results in Figure 2.16(b) appear as expected since a single discrete point was simulated.

The image formation algorithm that has been derived is called backprojection [31–33]. Backprojection processing easily could be considered the "gold standard" in SAR processing currently. It has several compelling features, compared to other common algorithms.

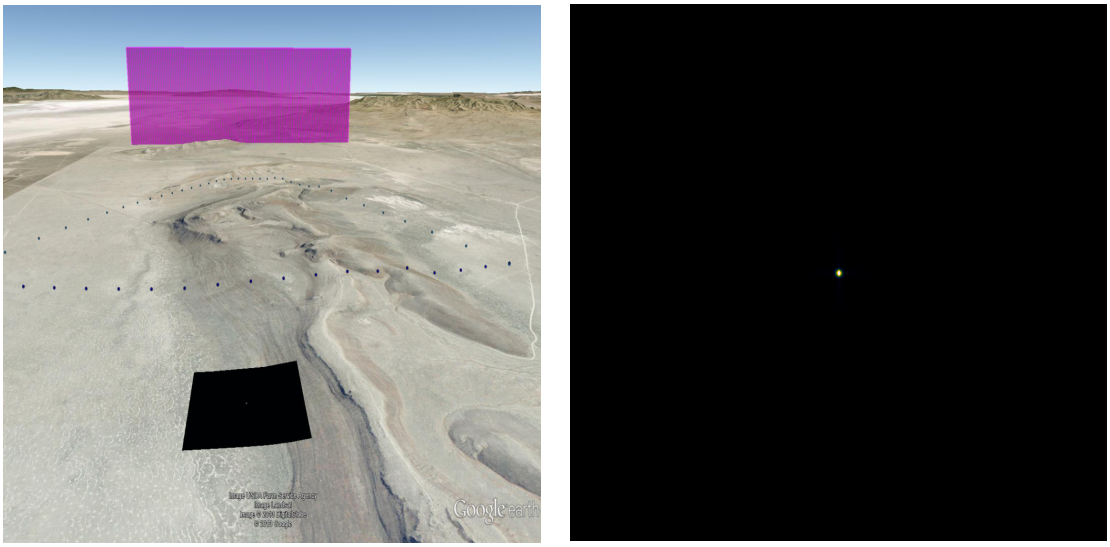

(a) (b)

Fig. 2.16: Simulated results for a discrete point: (a) Resultant image displayed in Google Earth™, (b) A zoomed in view of the resultant image showing the simulated discrete point in the center.

First, there is no assumption about the collection geometry. The flight path could have been circular, linear, zig-zag, etc. and the algorithm requires no adaptation. Second back-projection is a spatial-domain algorithm. It is natural to understand and very intuitive for most people, compared to other algorithms. The spatial domain naturally allows for non-ideal sampling which is required for specific modalities like compressive sensing, and time-sharing radar modes.

Another class of very efficient algorithms are based on processing the SAR returns in the frequency domain. Several popular frequency domain algorithms are the range Doppler algorithm (RDA), chirp scaling algorithm (CSA), and the range migration algorithm (RMA or Omega-K) [30, 34]. The main draw-back of the frequency domain algorithm is the difficulty non-ideal motion causes. The underlying difficulty is due to the ideal sampling requirements a Fourier transform imposes. This makes certain flight geometries and radar configurations problematic at best and impossible at worst. Several frequency domain algorithms also incorporate approximations that limit utility for some system configurations and, or geometries [30]. CSA and RDA both approximate the parabolic change in range, as described in Equation (2.22), with a quadratic approximation. This is a valid approximation for broadside collections when the angular extent is kept small. The main advantage of the frequency domain algorithms is speed and under certain circumstances the approximations cause no aberrant results.

Any focusing algorithm can be used as the basis for the advanced processing that is developed. But backprojection, unless otherwise specifically stated, is assumed to be the base image formation algorithm employed. The main reason backprojection is chosen is due to its general application, good performance for all collection geometries, and system modalities. The increased processing times are not problematic for this deliberation.

2.8 Synthetic Aperture Perspective

The cross-range or azimuth resolution is where SAR distinguishes itself from traditional or canonical radar systems. This is done by synthesizing a large antenna for fine cross-range resolution. In traditional antenna theory, long antennas achieve high resolution in

the corresponding "long" dimension [35]. Figure 2.17 demonstrates traditional antenna operation where all the elements radiate simultaneously. The signal is coherently summed at the target location. Or in other words, destructive and constructive interference occurs at the target, represented by the star in Figure 2.17.

After the signal coherently interacts at the target, part of the combined signal is reflected back toward the receive antenna. The receive antenna hardware applies the correct phase compensation at each individual antenna element, represented by a black box in Figure 2.17. This ensures that the signal is coherently summed in the direction of interest. The direction of interest is commonly called the angle of arrival (AoA).

This is graphically demonstrated for an ideal uniform linear array (ULA) in Figure 2.18. Each of the receive elements applies the proper phase compensation proportional to the sine of the angle θ and the relative distance "d" from a reference location [4]. This ensures that electromagnetic waves received, assuming a far-field origination, are constructively combined. This is accomplished by considering the wavelength, or phase. This idea in general is called "coherent" processing.

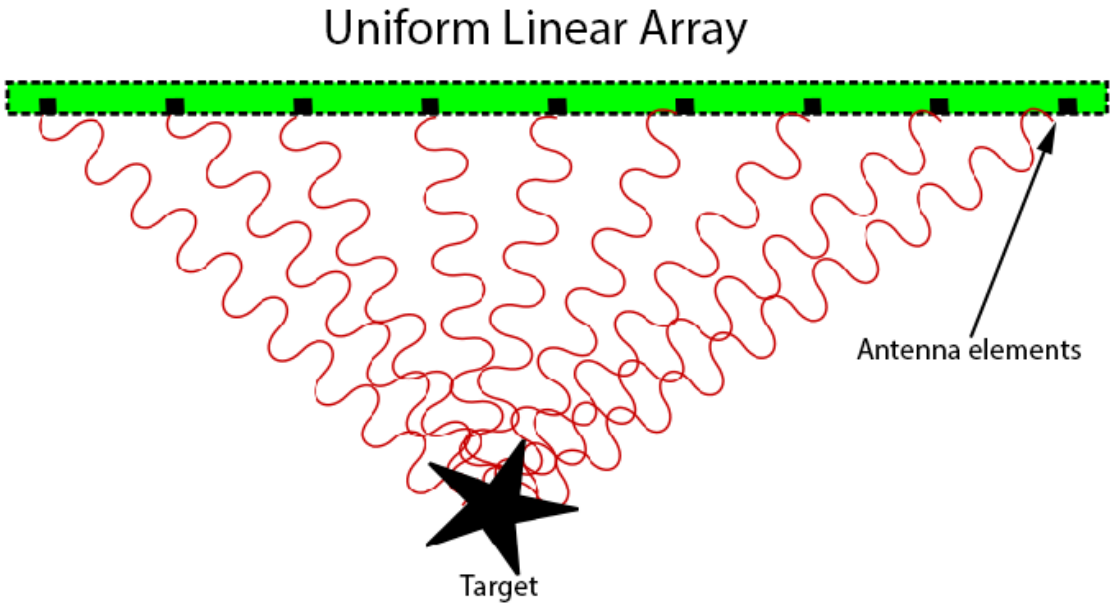

Fig. 2.17: Traditional antenna.

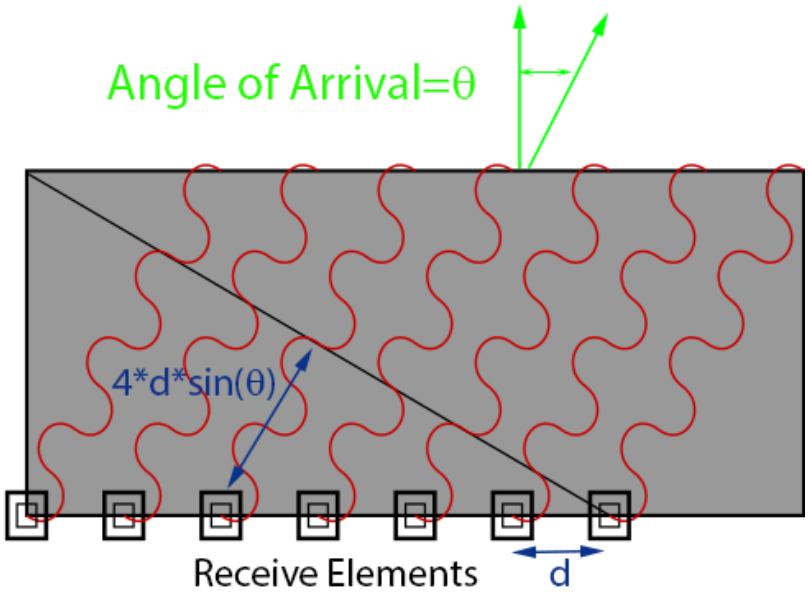

Fig. 2.18: Uniform linear array phase compensation.

SAR sensors do not actually utilize a large antenna, but synthesize a large antenna by the platform motion. The motion is generally in the horizontal plane, which is assumed for simplicity here. The extent of the angular diversity induced by the platform motion defines the aspect angle. This is often called the coherent integration angle. This is graphically shown in Figure 2.19. The SAR sensor emits a pulse and the platform motion translates the sensor to a new location and another pulse is emitted. These pulse locations are equivalent to antenna elements. This gives a logical interpretation to the *synthetic aperture radar* name.

The second critical component of a SAR system is the digital processor. With a ULA the hardware applies a phase correction that coherently sums the signal from the desired AoA, as seen in Figure 2.18. The SAR processor does exactly the same operation, but in the digital processor after the returns have been collected. The combination of the platform motion, and the coherent SAR digital processor are the key components for all synthetic aperture radar systems.

The ability to synthesize large antennas is critical since small antennas are required for most aircraft and satellite platforms. SAR provides the consummate solution. The system suffers no loss in resolution, with respect to a physical aperture or antenna, and the antenna size is small so that many platforms are feasible. In fact, a synthesized antenna has a factor of two improvement over a physical antenna of the same length. This occurs because with SAR coherent summation of the synthesized antenna elements (e.g. the pulses) occurs after the *two-way* propagation distance by the digital processor. But with physical antennas each antenna element is coherently combined at the target effectively utilizing only the *one-way* propagation distance [6].

The same principle can be applied to synthesize a large vertical or elevation aperture. A large aperture in the elevation direction would provide high vertical resolution in the scene. This would allow for 3D scene reconstruction. But the idea to synthesize apertures in both elevation and azimuth quickly becomes impractical. The platform motion, in general, does not contain large vertical components. But the platform motion naturally contains large horizontal components. In order to synthesize a vertical aperture it would require additional

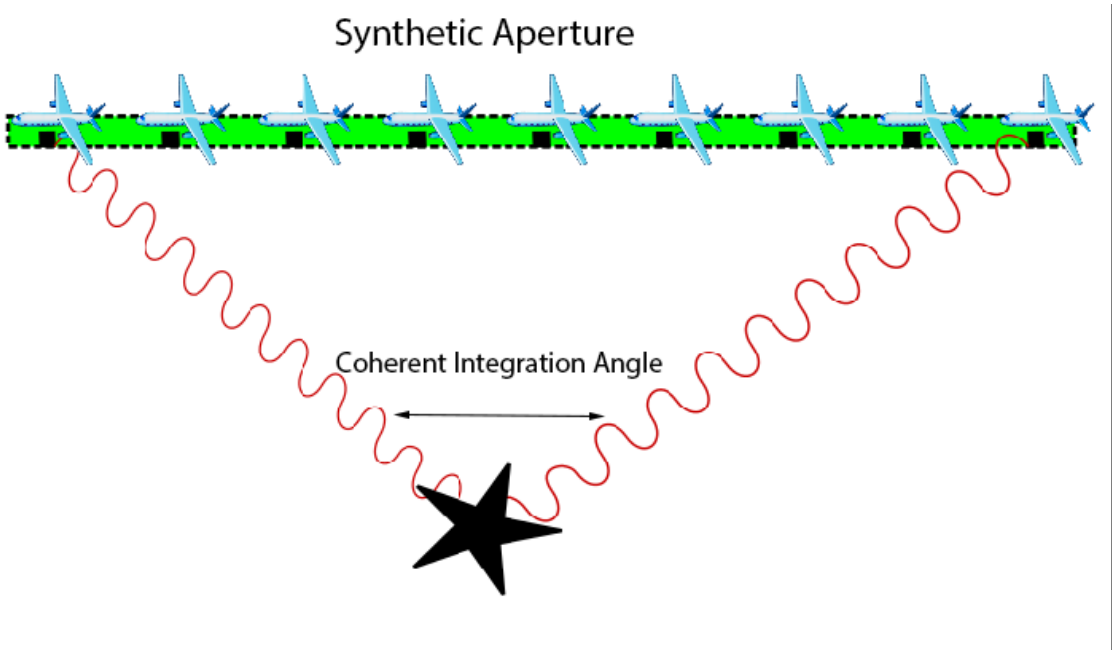

Fig. 2.19: Synthesized large antenna from platform motion.

collections for every synthetic element desired. The amount of time, platform resources, and ultimately cost becomes prohibitive. This forces most imaging modalities to have sparse elevation apertures. But the azimuth aperture, due to the co-alignment of the platform motion with the horizontal plane, can naturally be sampled at a denser rate.

2.9 Radar Background Summary

An example of the entire SAR backprojection process is shown in Figure 2.20. The collection geometry is captured and shown in Figure 2.20(a). Figure 2.20(b) shows 1024 pulses of the basebanded range-rate measurement data. Then range compression processing occurs, as detailed in Section 2.4, on the 1024 pulses resulting in Figure 2.20(c). Then the 1024 pulses are azimuth compressed. After processing all the pulses the resultant image is displayed in Figure 2.20(d).

The critical ideas presented in this section provide the background and foundation upon which the next sections will be built. The backprojection image formation algorithm was specifically derived, and examples provided on synthetic data that enlighten the critical concepts with a geometrical emphasis.

The aspiration of this chapter can be summarized with the following four objectives. The first objective is to have a general understanding of radar geometry and terminology. The second objective is to have an understanding of the range-rate measurement that is used for canonical radar systems and the corresponding range-compression processing of pulse encoded waveforms like the LFM. Third, an understanding regarding the origin of the Doppler signal. In particular, how the signal modulation process and motion induce the Doppler signal. Fourth, a general understanding of the matched filter operation applied in the azimuth direction, or across pulses is applied to the Doppler signal.

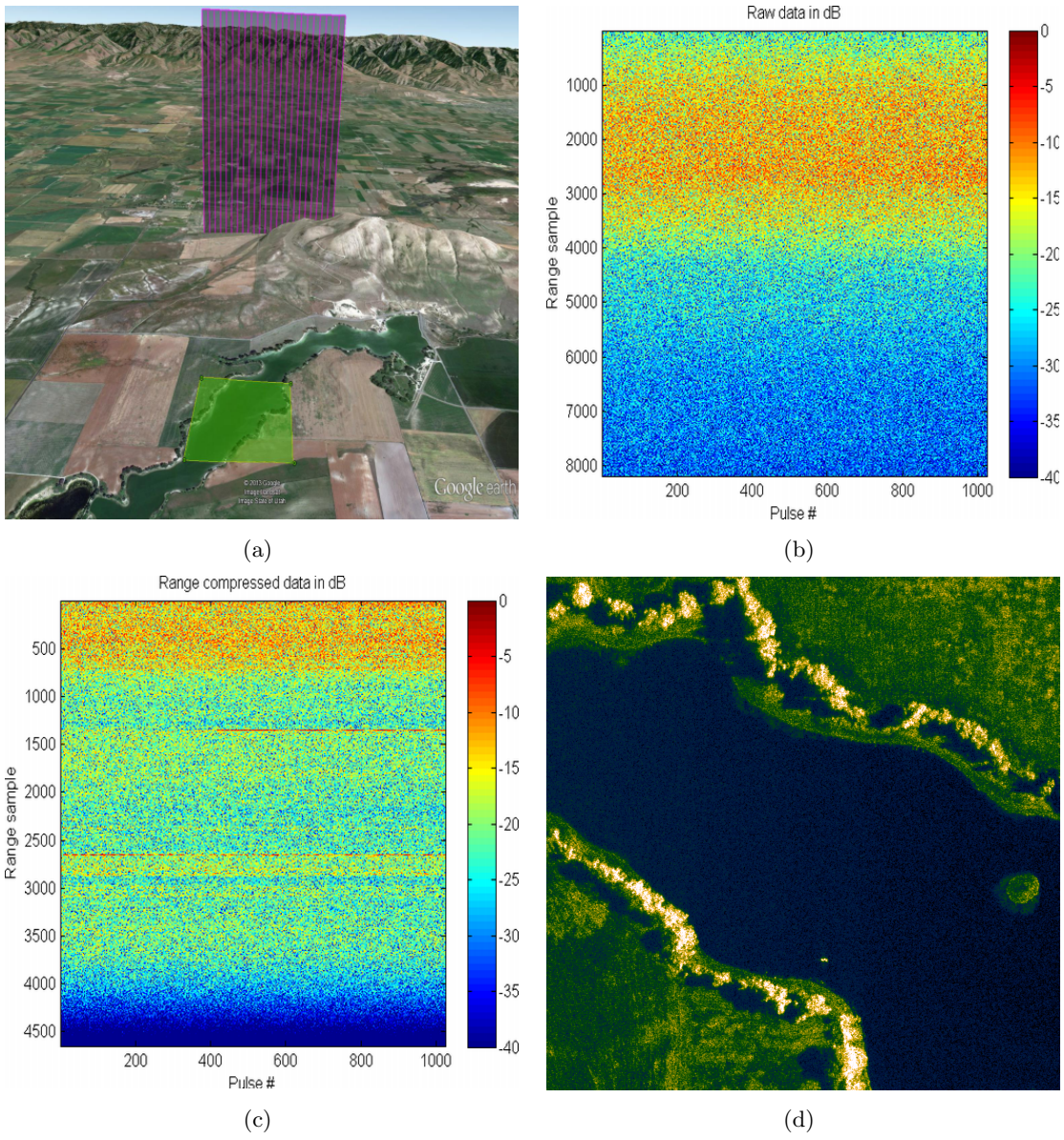

(a) (b)

(c) (d)

Fig. 2.20: Complete processing example: (a) Overview of the image collection geometry where the aircraft path is shown by the purple transparent lines and the ROI is shown in green, (b) The raw SAR data, (c) The range-compressed SAR data, (d) The azimuth compressed or backprojected resultant image for the selected ROI.

Chapter 3

Simulation

SAR simulation is a critical element for SAR development. It is economical regarding time and resources. Parameters can be changed instantly and you do not need to pay for a pilot, gas, or an aircraft to fly. SAR simulation allows for individual noise sources to be added or removed. The noise sources can be examined independently, collectively or in any combination desired. SAR simulation is very often the first step to validate new ideas and modalities that could improve SAR utility. SAR simulation helps develop intuition, which is critical for proposing new modalities and algorithms. The ability to simulate realistic SAR data is a critical tool for any SAR engineer.

But the limitations and strengths of the SAR simulation need to be understood. If the simulated SAR data does not accurately represent the complicated returns found in actual SAR data, then the results produced using simulated data are often very misleading. In this case the SAR simulation results never represent results achieved in practice. This is due often to the simplified, and unfounded assumptions that occur when simulating SAR data. In order to avoid such pitfalls, the simulation needs to resemble the complicated and random returns found in actual SAR data as much as possible.

This work uses simulated data to demonstrate the advantages of model-based processing. The simulated data is particularly important regarding theoretical performance where practical considerations can be ignored. For model-based processing, it allows for theoretical performance evaluation when the model fit is tight. Concisely put, a tight model fit means the assumed sensor behavior is modeled very accurately by the software. This is much easier to do in simulation than in practice. In practice it requires accurate calibration measurements. Most of the publically available data used in this effort, like the GOTCHA data set [36], does not provide the requisite information. But in simulation, it is trivial to

control the model fit. The simulation results provide the necessary impetus to pursue such endeavors, like model-based processing, in practice if the initial results are promising.

The emphasis of this chapter is to provide the necessary background theory and references so that two fundamental questions can be answered. First, why can SAR scenes be accurately simulated with point sources? Real scenes are composed of a continuum of reflectors. For the novice SAR practitioner it is not intuitive how a continous scene can accurately be modeled by a finite number of point reflectors. The second question is, what happens when isotropic assumptions are made for anisotropic scenes? The theoretical foundation is briefly explained so that a high-level understanding can be accomplished. The seminal works are referenced so that interested readers can pursue additional information in more depth if desired.

Lastly, the objective of this chapter is to provide insight into the general SAR simulation algorithm and software used for this effort. This provides the ability to understand the strengths and limitations of the simulated results.

3.1 Point Sources

The formal definition of the RCS is given as

$$\sigma = \lim_{R \to \infty} 4\pi R^2 \frac{|E_s|^2}{|E_o|^2}, \tag{3.1}$$

where E_o is the electric-field strength incidence on the target, and E_s is the scattered electric-field strength returned to the radar. The distance between the targets is represented by R and is assumed to tend toward infinity. The limit in Equation (3.1) is not necessary in the far field. In the far field the electric-field of the scatterers decays proportionally to the distance R. This cancels an implicit R^2 term in the denominator making the RCS independant of the range R [19].

The RCS is a ratio of the power density at the receiver compared to the incident power density at the target and has units of meters squared. This inherently assumes the same polarization is transmitted and received. To account for the polarization changes that

occur when back-scattered a *polarization scattering matrix* should be used [37]. But this important detail will be neglected for simplicity in this discussion.

An important realization regarding Equation (3.1) is that the RCS is not actually defining a physical size of the cross sectional area of the target. RCS actually defines an equivalent target area that relates the incident power at the target with the reflected power at the receiver. This means it is a fictional area that would explain the power that is reflected back to the receiver for an isotropic radiator given the power incident on the target [20].

SAR systems almost exclusively operate in the far field which is generally defined as any distance R_o greater than

$$R_o \gg \frac{2D^2}{\lambda}. \tag{3.2}$$

The term D represents the aperture size. The RCS of many simple common shapes, or ideal calibration targets have been computed from theory [38]. But in practice, there are very few known real targets that fit the solutions generated from the exact wave-equations given by Maxwell's renowned equations. Phenomenological observations provide validation to the point-scatterer response. But there is a foundation based upon electromagnetic theory that supports the point-scatterer model.

One approach that is used for electrically-small objects is the *moment of methods* (MOM). Electrically-small refers to objects that are on the order of the wave-length. MOM can handle arbitrary shapes, but has three critical drawbacks given by Knott in Skolnik [19].

- It requires large computational resources.
- It produces specific numbers for a given parameter set. The simulation must be repeated when parameters are changed. Important trends are hopefully recognized over the repeated simulations.
- It can produce spurious resonance results.

When the radiating object is large compared to the wavelength the *geometrical theory of diffraction* (GTD) is used. GTD was developed by Keller [39, 40]. This theory is a ray-tracing method that assigns a phase, and an amplitude to the reflection. GTD is based on and extends *geometrical optics* (GO). GTD extends the theory of the GO by introducing a diffraction mechanism [41]. Five advantages of GTD are given in Balanis [35] and repeated here:

- It is simple to use.
- It can be used on complicated problems that have no exact solutions.
- It provides physical insight into the radiation and scattering mechanisms from the various parts of the structure.
- It yields accurate results which compare extremely well with experiments and other methods.
- It can be combined with other techniques such as MOM.

An excellent detailed work on GTD is found in Balanis's book [41]. GTD forms the basis for the point-scatterer model. Each ray is a result of reflection and diffraction points on a target. These are what produce the individual point responses that are seen in practice. GTD provides the foundation for the point-scatterer response and also insight into how far it can be carried. GTD predicts the dispersive nature of scatterers. A dispersive scatterer does not have constant amplitude and linear phase. The returned signal is often spread-out, or dispersed compared to the incident wave and is seen in practice [42].

In summary the measured results seen in practice coincide with the predicted results expected by GTD. This allows complicated continuous targets to be modeled accurately as point sources at the appropriate locations, particularly at points of discontinuity or diffraction points. The diffraction points dominate the SAR data returns and those are represented by the discrete point sources for the modeled scene. GTD provides the theoretical foundation upon which SAR simulations rely when using point scatters to model a scene. GTD

coupled with measured data provide a strong foundation for the point-source model used for SAR simulation.

3.2 Coherency

For SAR image formation there is an assumption, often unstated, leveraged during the image formation process described in Chapter 2. The assumption is that targets reflect with a constant magnitude and phase. The constant reflection is independent of the impinging waveforms angular incidence and frequency. A reflector that exhibits such a response is called isotropic. When the actual target response $A_0(\theta, \phi)$ was approximated as A_0 in Equation (2.27) this assumption was exercised. An isotropic radiator has a frequency-and aspect-independent RCS.

A metal sphere is the device that most nearly exhibits such a response. But a metal sphere exhibits frequency-dependence regarding the returns from the creeping wave returns [19]. Over a limited frequency bandwidth it can be approximated as a constant with little error, especially in the far field. In general isotropic radiators are not readily found in nature.

All man-made objects of interest, such as cars, buildings, etc., intuitively have a strong geometrical dependence. The front of the car would reflect differently than the back, top, or side. The actual measured RCS of a B26 plane is shown in Figure 3.1 as an example [1]. The frequency was 3GHz and the figure is shown in polar format.

The RCS is clearly a function of aspect angle. Clutter simulations should exhibit the same type of behavior if realistic results are desired. Obviously, approximating the random reflectivity with a constant isotropic reflector is not very realistic and could provide misleading results when applied to actual SAR data. Clutter simulation is commonly accomplished by incorporating multiple reflectors in a single cell. The location of the point scatterers is randomly located. The magnitude distribution of the point scatterers is generated statistically based on a certain statistical distributions. Several of the most common distributions used to represent the RCS magnitude are the exponential, Chi-square of degree 2, Chi-square of degree 4, Weibull, Rice, and log-normal distributions [20]. Richards

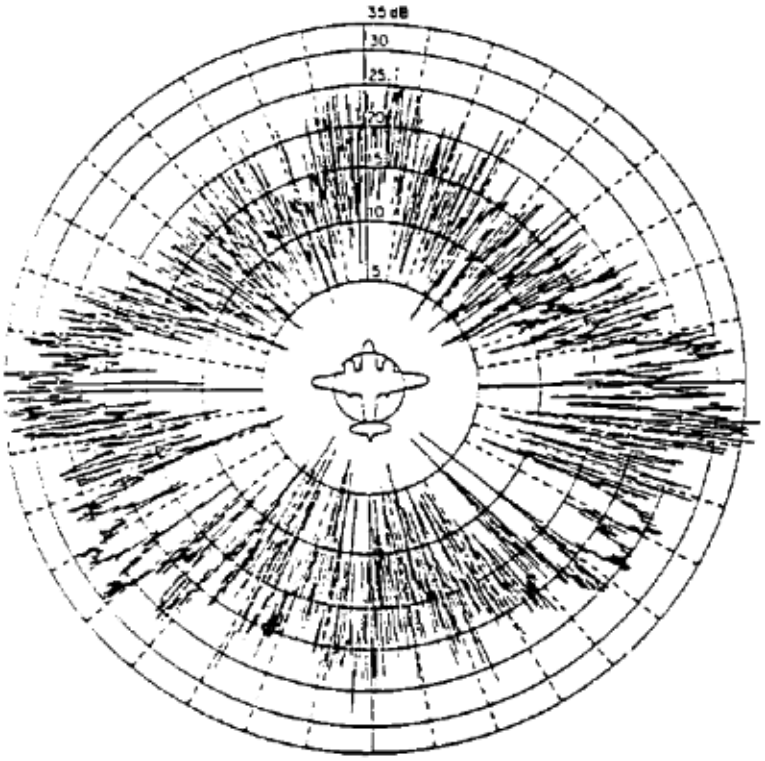

Fig. 3.1: The RCS of a B26 plane (source Ridenour [1]).

provides a good overview regarding ways to generate many of these distributions [43].

These distributions are commonly used as the background clutter. Then discrete targets of interest are superimposed on top of this background clutter. The targets of interest might be moving targets for GMTI which are injected into the raw data. This generates data that exhibits similar aspect varying decorrelation as that which is found in practice. The particular distribution used allows for controlling how fast, on average, the scene decorrelates with respect to the aspect angle.

Billingsley stated that clutter "... is a highly non-Gaussian (i.e. non-noise like), multifaceted, relatively intractable, statistical random process of which the most salient attribute was variability. The variability existed at whatever level the phenomenon was observed." This was stated after a 20-year clutter study was done [18].

In the author's opinion the ultimate test of any SAR algorithm should be on actual SAR data to ascertain the algorithm's utility. But simple simulations are ideal to develop

intuition and algorithm correctness. A simple clutter simulations is shown in Figure 3.2. The simulation is generated using 20 clutter points randomly placed in a one-meter square cell. The cell contains a single dominant clutter point shown in red can be seen in Figure 3.2(a). The aspect dependent reflectivity can be seen in Figure 3.2(b).

This cell was generated by randomly placing 20 scatterers in a cell with a single dominant scatter. The dominant scatter has an RCS that is approximately the sum of all the other scatterers. Several distributions are plotted in Figure 3.2(c) for reference.

The angular extent a target can be approximated as a constant, often referred to as correlated, is paramount. Unfortunately, the extent a target maintains correlation is extremely complicated and changes based on many factors such as frequency, geometry, background clutter, and target composition. When SAR image formation occurs, the scene is restricted to a size that in principle does not exceed the coherent limit. This idea is graphically represented in Figure 3.2(d). The simulated cell of interest is shown in Figure 3.2(a). This cell after image formation processing will be represented as a pixel. For this pixel the red line represent a nominal decorrelation of targets, which assumes a rigid target. This is given by

$$\Delta \sin(\theta) \approx \Delta\theta = \frac{c}{2Lf_c}, \tag{3.3}$$

which defines the change in angle required to decorrelate the pulse amplitude. The term L is the target length, f_c is the carrier frequency, and c is the speed of light. In Figure 3.2(d) this is represented by the red line. The green line represents a drop under 25 percent, and the black-line is the first local minimum. These results depicted in Figure 3.2 were generated by a software tool accompanying Richards' book [20].

The example in Figure 3.2 represents a single instance. Ideally, many instances would be computed. Than the statistical average could be confidently employed for the scene. The correlation limit is often subtly assumed, but has very important implications. If the coherent angular interval is too large, then information is lost. This occurs when the reflectivity changes, particularly the target's complex phase, and constructive and destructive interference occurs when combining pulses. If the coherent angular interval is too small,

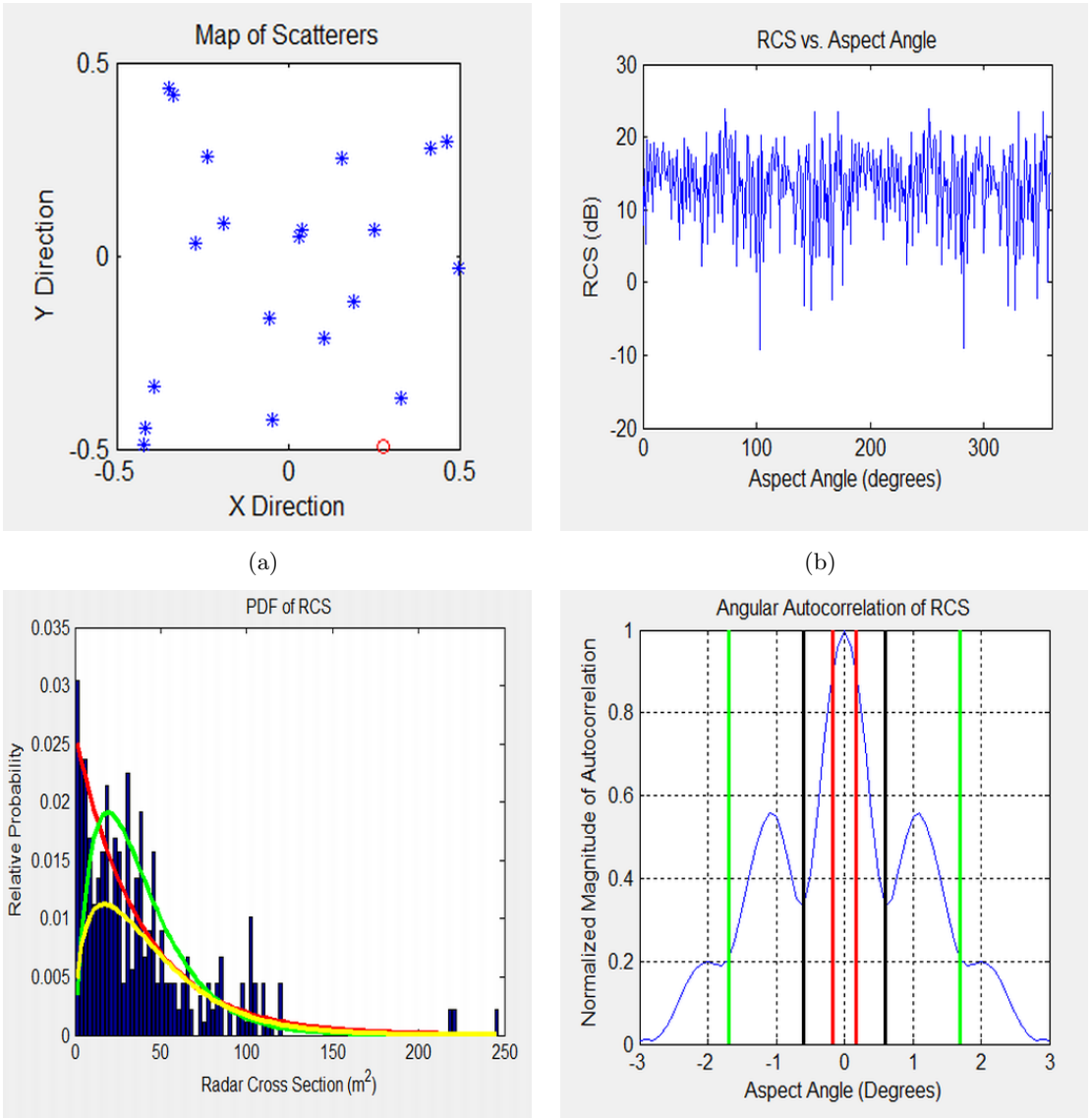

Fig. 3.2: Simulated clutter cell RCS: (a) The clutter cell spatially, (b) The clutter cell RCS vs. aspect, (c) The clutter cell RCS distribution, (d) The clutter cell RCS aspect correlation.

resolution is lost since more pulses could be coherently combined.

If SAR data is collected over a large aspect that exceeds the coherent angular interval then the SAR image formation is traditionally broken into individual images or aspects. It will be assumed that coherency is a legitimate assumption on each of the aspects or aperture images.

3.3 Simulation Software

The GTD provides the theoretical backbone for the point response modeling that is common for SAR engineers. This effort will utilize SAR simulation software. The software that is leveraged is a full time-domain simulation that employs actual 3D position and a DEM to produce accurate geometrical simulations. Several references for developing simulation software are found in the books by Jakowatz et al., Cumming and Wong, and Soumekh [5, 30, 34].

The software developed for this research employs a *graphical user interface* (GUI) that allows configuration of diverse geometries, arbitrary input/output waveforms, and other relevant parameters to quickly be changed. The simulation geometry is output in formats that can be visualized in Google Earth™. Several of these are shown for simulations to provide context. The GUI is shown in Figure 3.3.

The GUI communicates with worker-nodes via TCP. The worker-node is shown running in a Windows™ command prompt in Figure 3.4. The worker-nodes perform the actual computations. The results are generated by the worker node and sent to the GUI process and collected. This design allows for distributed processing.

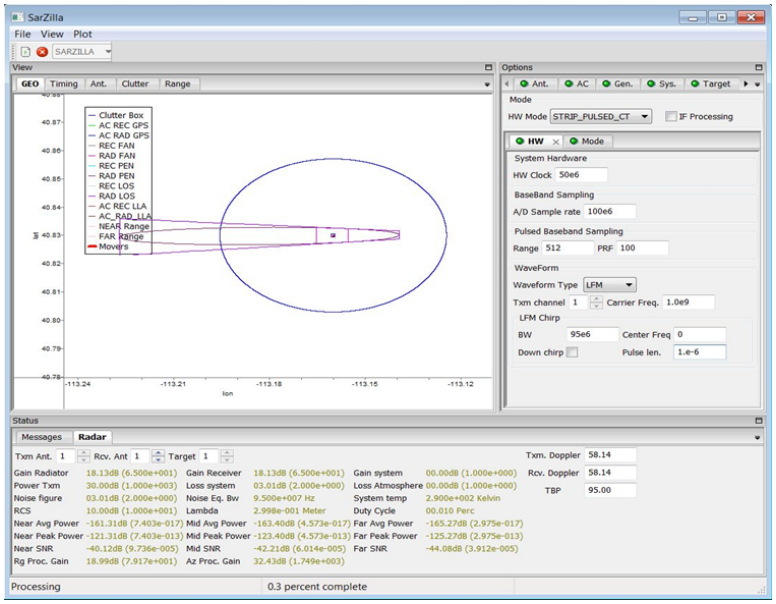

Fig. 3.3: The SAR simulation GUI.

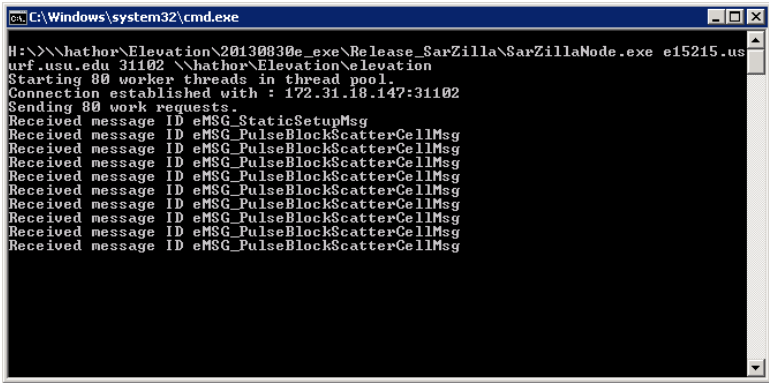

Fig. 3.4: A SAR simulation distributed worker-node.

The design easily allows for hundreds of computers to work on complicated simulations jointly. Distributed processing is critical to simulate modern SAR systems in operational situations. The simulation of SAR systems is generally much more computationally intensive than the image-formation process, especially for specific modalities like CW systems. The design incorporates fault tolerant techniques. This allows the software to gracefully handle worker-nodes coming on-line, and off-line during simulation. This is extremely important when one is parasitically borrowing computer resources from fellow colleagues and they decide they want all their computer resources.

The software generates the background clutter based on a statistical distribution. The number of clutter points in a cell is configurable. In general, 20 points or more provide excellent results so that the statistical RCS distribution of cells matches practice [20]. Several simulated examples are used to demonstrate concepts. When the objective of the simulation is to demonstrate concepts, the background clutter is often ignored and single isotropic point is employed. This is done for clarity, so the results can easily be interpreted. But when simulations are applied to generate algorithmic results the statistical properties of the clutter will be specified.

A simple example simulation is shown in Figure 3.5. The clutter is generated with 20 scatterers per one meter square. The RCS mean is 0.1 meters square. The spatial distribution is uniform over the cell as seen in Figure 3.5. The spatial distribution is always uniform but the magnitude of each individual RCS scatterer is distribution specific. For

this example, the RCS magnitude was selected to have a Chi-Square distribution with 2 degrees of freedom.

In summary, great care was taken to ensure that SAR simulations employed for this effort were of high fidelity. Actual 3D models are employed and no assumptions are employed, such as flat earth, etc. The clutter modeling has been extensive and includes many points per cell in order to replicate the aspect varying response seen in practice. These objectives have forced development of effecient simulation tools that incorporate distributive processing.

Simulation allows a controlled ideal environment which is critical for several reasons. First, individual error effects can be modeled and understand ensuring robustness. Second, improved debugging can be accomplished by injecting ideal inputs (such as a single point response) into the algorithm in order to generate intermediate results that can be visually interpreted and validated. Last, the simulation provides a reasonable understanding regarding the overall utility of the algorithm.

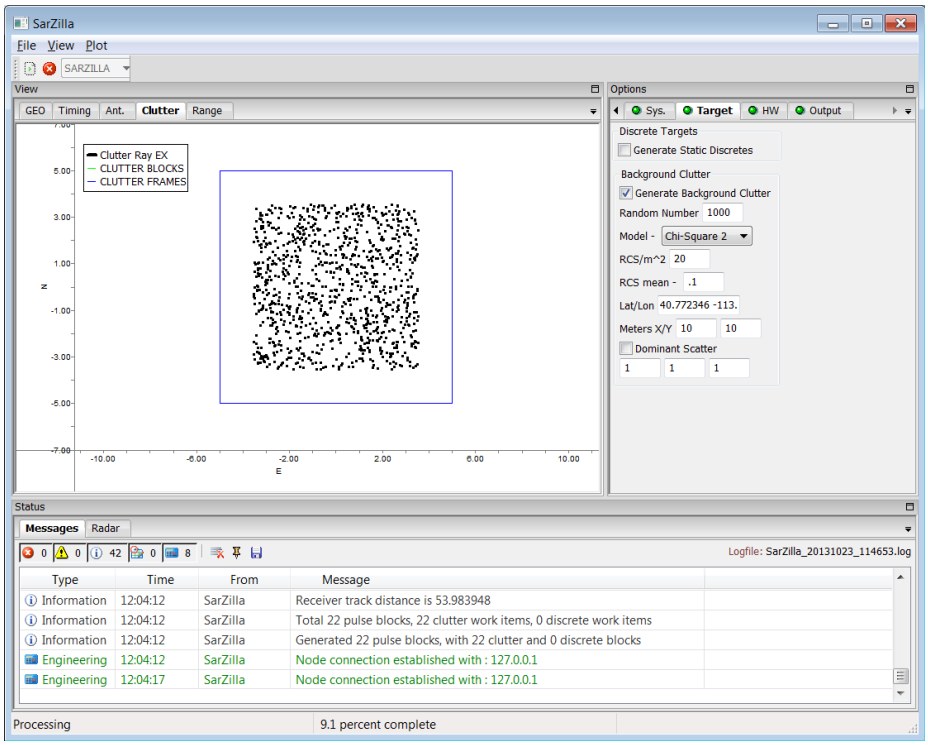

Fig. 3.5: A SAR simulation of distributed clutter showing GUI configuration.

Chapter 4

SAR Model

This chapter focuses on developing an anisotropic SAR signal model and developing a framework that incorporates the RCS magnitude and aspect into the image formation process. The work of other authors is explored, and extended. The culmination of this chapter results in an anisotropic signal model that has three critical attributes.

The first attribute of the model is robustness. SAR data is scene dependent and notoriously difficult to model [18]. The model formulation must be robust to handle model-mismatch that can occur. Ideally, the model would accurately represent the SAR system of interest. The tighter the model, or the more accurately it represents the actual system, the better the results. But when model errors are present (such as approximate antenna patterns, temperature fluctuations, imprecise position information, etc.) it is desirable to produce results that are robust. Or in other words, when model-mismatch is present the results are still "close" to the results that are produced in the ideal case with no model mismatch.

Second, the model should allow for incorporation of prior target information into the problem formulation. This should, in theory, allow for enhanced target response while suppressing legitimate features that do not exhibit the desired response. For example, it might be desirable to keep only returns that exhibit a high frequency glint-like response, and suppress all steady state or non-glint responses. A model-based formulation that allows such feature extraction could be useful for target recognition applications. And more importantly it would facilitate knowledge-aided image formation on a global scene level or on a much smaller pixel by pixel level.

Finally, the last attribute is that the model should be tractable for actual SAR data and scenes sizes of interest. This is hard to quantify, but for this work, it means that a normal

work-station computer can provide results on actual SAR data. This requires more than just theoretical modeling. It requires justifiable approximations to be considered, and leveraged where appropriate so that the problem can be tractable. The major incentive of this model-based work is to improve 3D image reconstruction. Model-based scene reconstruction in 2D is difficult and 3D is practically impossible for most problem formulations on real data.

As the signal model is developed, the advantages of model-based processing are explored, illustrated, and demonstrated with simple simulated examples. These examples illuminate critical ideas. Previous work is detailed particularly the applicable parts, including the benefits and shortcomings, that are leveraged and extended by this work.

4.1 Raw Data Model

An underlying assumption that has been prevalent is the linearity of SAR systems. A single SAR pulse is composed of all the reflected returns from each scatterer that the waveform illuminated. The returns are an aggregate sum containing each scatterer's contribution. The linearity of a *single pulse* is somewhat intuitive and, or natural. But one distinguishing feature of SAR systems, compared to traditional radar systems, is SAR systems have an extremely stable local oscillator (STALO). This means the clock does not drift over time, or from pulse to pulse. This allows us to aggregate the Doppler signal from pulse to pulse, as discussed in Section 2.6. The STALO facilitate the use of linearity, not only on a single pulse, but across pulses. The principle of linearity is often called superposition. Superposition is a common feature for linear systems [44], such as a SAR system.

The principle of superposition allows us to represent the returned SAR data using linear operations, or linear algebra. For simplicity the scene is assumed to be composed of a finite number of reflectors, represented by the stars, as shown in Figure 4.1. Representing a continuous scene with limited finite reflectors is a common practice and is a justifiable assumption for most cases as discussed in Chapter 3.

The graphical illustration in Figure 4.1 represents a scene that is uniformly modeled for simplicity. The actual spatial distribution of point reflectors, and their magnitude is scene dependent. If prior knowledge of the scene is available regarding the spatial and

intensity distribution of the scatterers, this could be incorporated into the model formulation naturally and will be discussed later, but for now no prior knowledge will be assumed.

It is important to distinguish the act of modeling the SAR data and simulating the SAR data. The forward model is trying to explain the data received from the SAR sensor. If a SAR simulator is used to generate the data it is important that the simulator is fire-walled effectively. In other words, the SAR simlator should not explicityly use the presumed SAR model. The SAR simulation should incorporate many of the best practices discussed in Chapter 3 to accurately represent SAR data as that measured in practice. Namely, there should be many point reflectors per cell to capture the aspect varying RCS phase and magnitude as seen in captured SAR data. It is assumed that the SAR data collected is restricted to a small angular extent where the response can be approximated as a constant. This small-angle assumption avoids the aspect variance seen in practice. Since aspect invariance equates to time invariance, the small-angle restriction allows SAR to be modeled as a linear time-invariant system.

A first order approximation is given by Equation (3.3) for how long a SAR scene will maintain coherence. It is important to note the coherent angular extent is frequency dependent. The longer the wavelength the longer the angular extents that can be employed, in general.

Under the assumption that the data is restricted to a small coherent aperture, it is important to realize that the simulated data was generated from many scatterers per cell, but the effective response is modeled as a single reflector. The point scatterer distribution is also a uniform random distribution whereas the modeled SAR data (or simulated data) often has a deterministic pattern. The pattern spacing is based on the system resolution and will be discussed in more detail. These are two important distinctions regarding how the SAR simulation is generated and how the data from a SAR sensor (or simulated data) is modeled. These implicit distinctions are assumed going forward, but stated explicitly here for completeness and clarity.

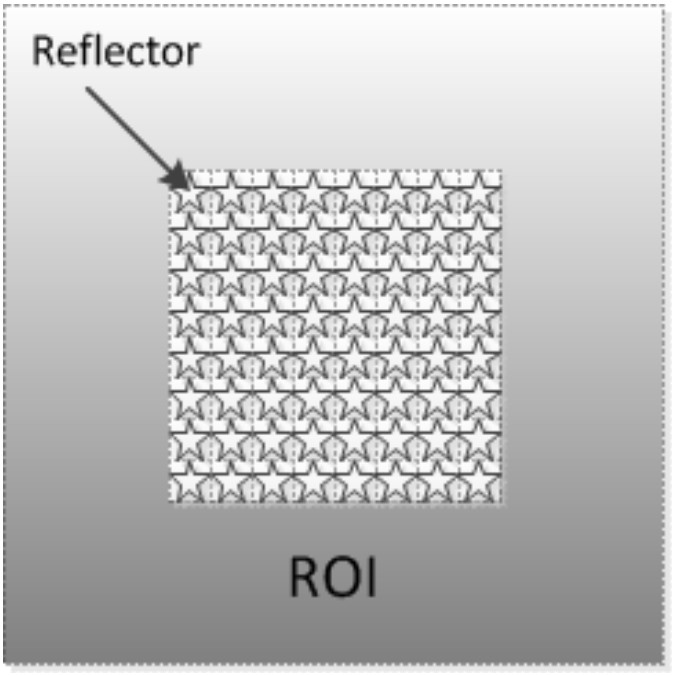

Fig. 4.1: Scene composed of a limited number of reflectors.

This model allows us to represent the returned SAR data signal as

$$y(\eta_i, \tau_k) = \sum_{j}^{N} c(\eta_i, \tau_k) x_j, \tag{4.1}$$

where η_i represents the slow-time or the i^{th} pulse number and τ_k represents the fast-time sample number k. The scene is composed of N reflectors. Each star shown in Figure 4.1 represents a unique reflector. The j^{th} reflector is given as x_j. The data sample for the η_i^{th} pulse and the τ_k^{th} sample is given as $y(\eta_i, \tau_k)$. The scalar function $c(\eta_i, \tau_k)$ internally incorporates the collection parameters needed to accurately represent the returned signal. For example, the collection geometry, the antenna pattern, and the waveform used are some of the important parameters it would require. For the LFM waveform, $c(\eta_i, \tau_k)$ could mathematically be represented as shown in Equation (2.27). It will be assumed that these parameters are known and incorporated appropriately.

By removing the summation, the equation can be equivalently written as

$$y(\eta_i, \tau_k) = C(\eta_i, \tau_k)x, \tag{4.2}$$

where the term $C(\eta_i, \tau_k)$ is a row vector and x is now a column vector where the elements in the vector x are the illuminated reflectors in the scene. The j^{th} element in the row vector $C(\eta_i, \tau_k)$ contains the j^{th} reflector's response for the η_i^{th} pulse and the τ_k^{th} sample.

A single pulse can be represented by

$$y(\eta_i) = C(\eta_i)x. \tag{4.3}$$

The sample dependence, τ_k, was removed by concatenating all the samples in the vector $y(\eta_i)$. Now $y(\eta_i)$ is a vector containing the samples for the η_i^{th} pulse. The row vectors $C(\eta_i, \tau_k)$, as given in Equation (4.2), are stacked into a matrix. The matrix has the following form:

$$C(\eta_i) = \begin{bmatrix} C(\eta_i, \tau_1) \\ C(\eta_i, \tau_2) \\ \vdots \\ C(\eta_i, \tau_M) \end{bmatrix}, \tag{4.4}$$

for the η_i^{th} pulse. The rows are composed of $C(\eta_i, \tau_1)$, $C(\eta_i, \tau_2)$, ..., $C(\eta_i, \tau_M)$ as seen in Equation (4.4). It is assumed that there are M samples collected for the η_i^{th} pulse. Now $C(\eta_i)$ is a matrix that has M rows and $C(\eta_i)$ still has N columns which represent the N reflectors that contribute to the reflected signal.

The returned signal vector $y(\eta_i)$ has a similar form where all the individual sample returns are concatenated for the η_i^{th} pulse.

$$y(\eta_i) = \begin{bmatrix} y(\eta_i, \tau_1) \\ y(\eta_i, \tau_2) \\ \vdots \\ y(\eta_i, \tau_M) \end{bmatrix} \tag{4.5}$$

The rows are composed of the individual sample returns $y(\eta_i, \tau_1)$, $y(\eta_i, \tau_2)$, ..., $y(\eta_i, \tau_M)$, as seen in Equation (4.5), generated from N modeled reflectors.

The entire collected radar data can now be represented as

$$y = Cx, \tag{4.6}$$

by simply concatenating all the pulse vectors $y(\eta_i)$, in Equation (4.3), into the vector y. The vector y is composed of the first pulse $y(\eta_1)$, then the second pulse $y(\eta_2)$ is appended, etc., and finally the last pulse $y(\eta_P)$ is appended. This is shown in Equation (4.7)

$$y(\eta_i) = \begin{bmatrix} y(\eta_1) \\ y(\eta_2) \\ \vdots \\ y(\eta_p) \end{bmatrix}, \tag{4.7}$$

where it is has been assumed that there are P pulses.

The matrix C has the form

$$C(\eta_i) = \begin{bmatrix} C(\eta_1) \\ C(\eta_2) \\ \vdots \\ C(\eta_p) \end{bmatrix}. \tag{4.8}$$

All the individual pulse response matrices, as given by $C(\eta_i)$ in Equation (4.4), are concatenated in the matrix C, where it has been assumed there are P pulses. The row dimension contains P pulses with M samples in each pulse. This gives a total of MP elements. The column dimension is still the same, and contains the N scatterers. These scatterers are represented in the vector x. The x_j^{th} reflector corresponds to the j^{th} column.

Equation (4.6) represents the ideal signal. And it is worth noting that the reflectivity has been assumed to be aspect-invariant. This is only an approximation at best for actual data and simulated data. The returned signal also contains noise. Additionally, there is thermal noise inherent in the AD process, quantization noise, and other noise sources. The noisy signal can be represented as

$$y = Cx + \nu, \tag{4.9}$$

where the term ν represents the noise vector. The term y now represents the data captured by the radar sensor. These raw radar sensor measurements are the input for any image formation processing algorithm.

The matrix C can be thought of as the isotropic raw-data simulation matrix. This idea can be understood by a simple mental illustration. Assume that only the k^{th} scatterer contributes to the results and all other scatterers do not contribute or are zero. This is graphically shown in Figure 4.2. This implies that x_k element in the vector x is the only non-zero element.

The received data y is simply a scalar value of the k^{th} column in C plus noise, under the isotropic assumption. This is readily seen by Equation (4.9). This provides intuition to why C is called the isotropic raw-data simulation matrix. Since the k^{th} column in C can be thought of as the ideal isotropic raw-data impulse response for a simple scene composed of a single scatterer located at the x_k^{th} location. Extending this idea of a simple scene to more complicated scenes is done by superposition. Complicated scenes that appear continuous can be adequately modeled by including an appropriate number of discrete points in the vector x. The number of required points will be discussed in Section 4.2.2.

A large scene may be collected by the SAR system, and only a smaller subset of the

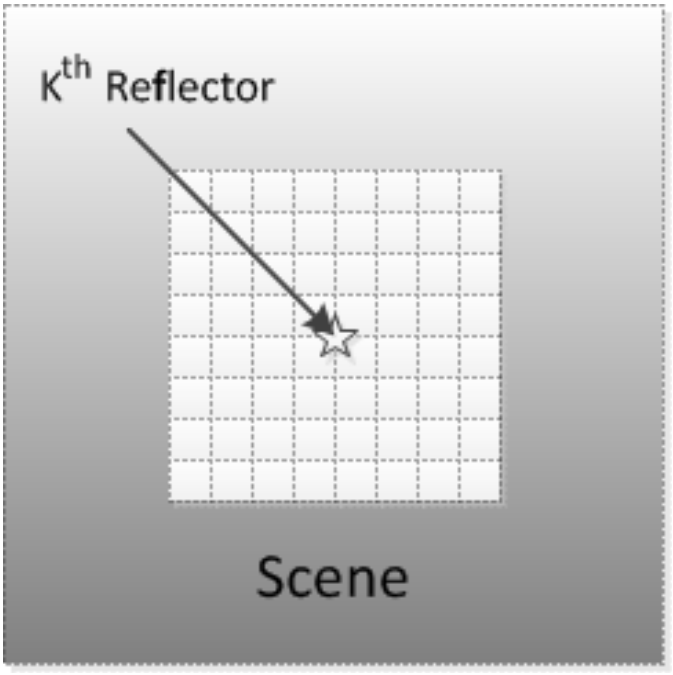

Fig. 4.2: Scene composed of a single reflector.

scene may correspond to the desired ROI. In this situation, it is desirable to reduce the collected data to the corresponding ROI only. This is done by applying the appropriate Doppler filtering and range clipping. In order to apply range clipping the raw data must be pulsed-compressed as described in Section 2.4 to localize the range response. There are different approaches to accomplish the data reduction, but all share fundamental similarities.

The general idea is illustrated in Figure 4.3. It is assumed the platform is located at the bottom of the image. The red lines correspond to near range and far range. The blue lines correspond to the Doppler signal spatial extents. The initial data captured by the SAR sensor is contained between the near, far ranges and the Doppler extents. But the ROI is represented by the black box only. In this particular case, the data can be reduced in Doppler and range to the shaded region shown in purple by the appropriate range clipping (after pulse compression) and Doppler filtering.

One common approach is called digital spot-lighting and is outlined by Soumekh and Dungan et al. for spotlight systems [34, 45]. The appropriate range and Doppler filtering reduces the raw data volume, which reduces the corresponding raw-data simulation matrix

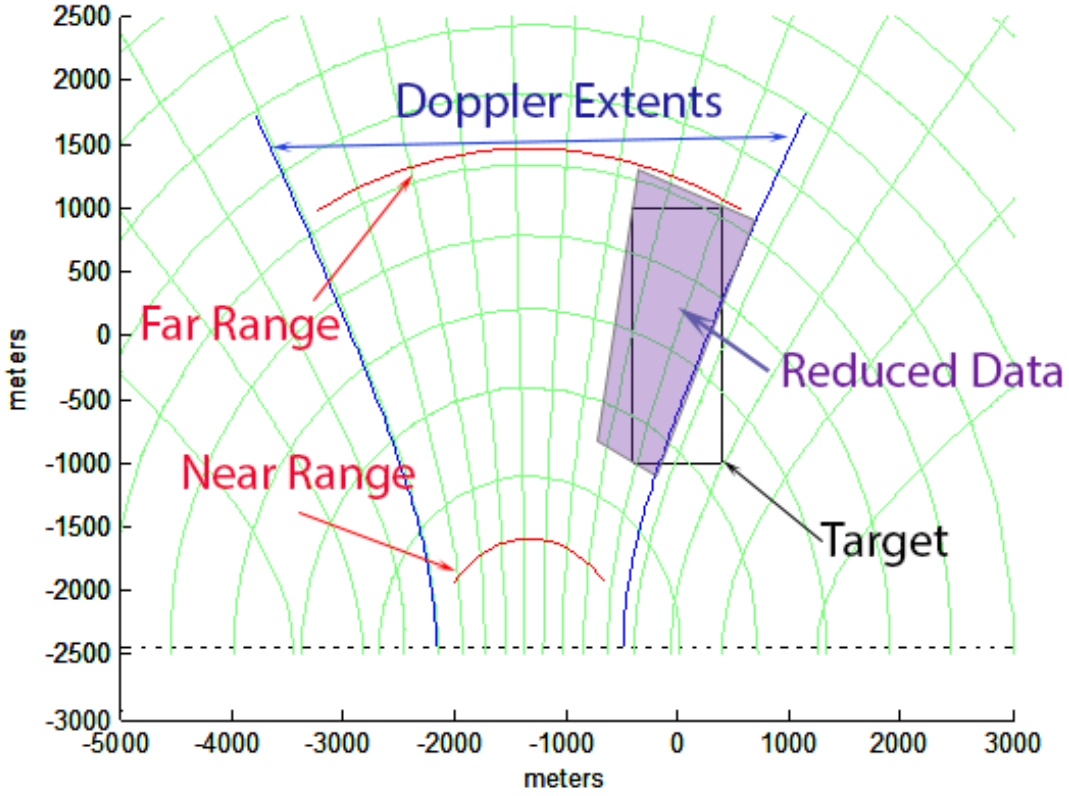

Fig. 4.3: Illustration of Doppler signal and range clipping for data reduction.

C size. The raw-data simulation matrix C size is now proportional to the ROI size. The data reduction step can be done for any system modality (strip or spot) and is often a critical step to reduce the problem size.

4.2 Focused Image Model

This section develops the *focused* SAR linear model that is the basis for the remainder of this work. The model developed and utilized is a spatial domain model. The spatial domain is an ideal domain since it is intuitive for most people and the spatial impulse response is compact. The compact spatial response allows for sparse representation. The spatial problem dimensionality is analyzed and appropriate assumptions detailed. The assumptions are critical in order to reduce the problem to a tractable size. Also, the spatial IPR response matrix is analyzed for several simulated examples to develop understanding

and familiarity.

Another advantage of the spatial domain is that the pulses can be coherently combined, assuming aspect-invariance holds, in order to improve the SNR. The improved SNR can improve estimation results. SAR imagery natively relies on the coherent combination of pulses in order to generate imagery of an appropriate SNR, or quality. The spatial domain allows the pulses to be accumulated naturally to increase the image SNR. If each individual pulse is examined, the SNR might be so low that the estimation results are very poor. But coherently combining the results allows for an adequate SNR needed for satisfactory estimation results. The ability to estimate is not a linear function of the SNR, and reaching a prescribed SNR can often dramatically improve the estimate results [46]. But the SNR cannot arbitrarily be improved by including a large number of pulses from diverse aspects, because the underlying assumption about aspect invariance is violated.

In general the impulse response (IPR) of an individual target is very diffuse in the raw SAR data, even for a single scatterer. The image formation process transforms the raw data to a compact spatial IPR. This is illustrated in Figure 4.4. A single discrete scatterer is simulated for the same geometry, but one system uses a continuous wave (CW) and the other a pulsed wave. The CW system is very diffuse in Figure 4.4(a) and the pulsed system is still diffuse in Figure 4.4(b). But in both cases the spatial impulse response is compact, seen in Figure 4.4(c) and Figure 4.4(d).

This means that fewer samples, or pixels, can be used to adequately represent the spatial IPR response, compared to the raw-data impulse response. This has important practical implications regarding overall problem tractability.

The extent a target interacts with the waveform depends on the pulse length T_p, PRF, and the collection geometry as discussed in Section 2.3. For instance a CW system has a 100 percent duty cycle or is always on verse a pulse system that might have a 10 percent duty cycle. The CW system would require many samples to represent the target or scatter whereas the pulsed system would require 90 percent fewer samples to represent the same target or scatter. This idea is illustrated in Figure 4.4 for a pulsed and CW system.

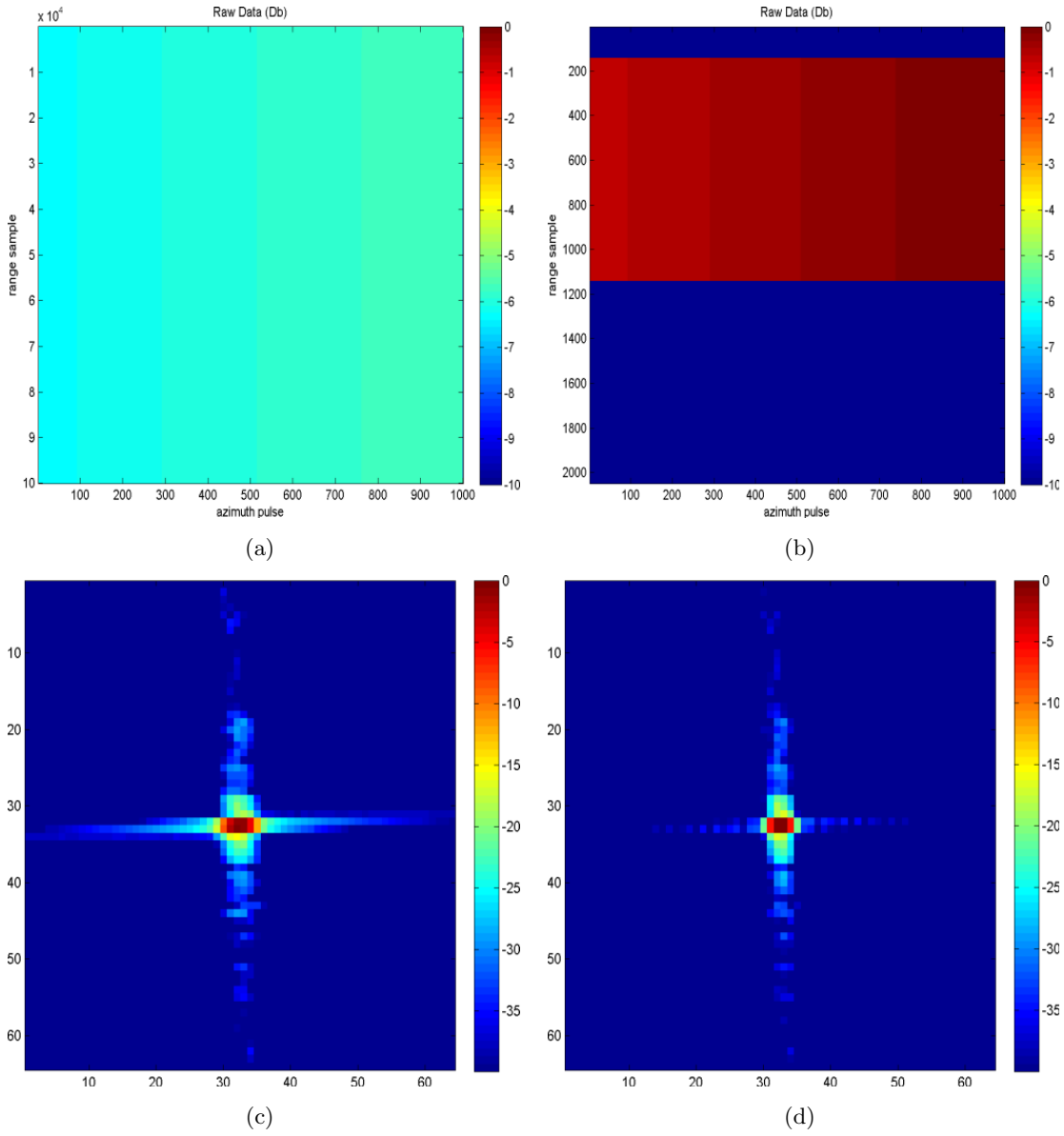

Fig. 4.4: Raw SAR data and the corresponding IPRs: (a) Raw data collected for CW mode, (b) Raw data collected for pulsed mode, (c) IPR for CW mode, (d) IPR for pulsed mode.

There is an intermediate domain which will be referred to as the pulse-compressed domain. In this domain the data has been compressed in range, but is still diffuse across pulses. But this work will focus on the most compact representation which is the spatial domain. The spatial domain abstracts the hardware and collection geometries so that an appropriate compact spatial IPR can be utilized to represent the response.

The image formation process is composed of linear operations, like matched filtering,

Fourier transforms, etc. This enables the image formation process to be represented by linear algebra in a matrix formulation. A generic image formation algorithm can be represented in matrix format as

$$b = M(\gamma)y = M(\gamma)(Cx + \nu). \tag{4.10}$$

The term γ represents the parameters the image formation algorithm requires, such as antenna patterns, pulse locations, etc., to construct an image, and the matrix $M(\gamma)$ can be thought of as a constant matrix once those parameters are fixed or provided. This is assumed going forward and $M(\gamma)$ will be written simply as M henceforth. The image formation algorithm is applied to the raw sensor measurements y resulting in an image. The image pixels represent distinct 2D or 3D spatial areas. They are mapped to the elements in the vector b. The details of the mapping (row-column order vs. column-row order, etc.) are not important, but it is important that whatever mapping is chosen must be consistently adhered to.

This allows us to generically, by matrix and vector operations, represent the image formation process. The image formation algorithm that will be leveraged for our purposes is backprojection. Equation (4.9) can be written as

$$b_{img} = My = MCx + \nu_c. \tag{4.11}$$

The term b_{img} represent the SAR image. The multiplication of the image formation matrix M to the raw data y results in a SAR image. The image b_{img} has been mapped to a vector but represents the corresponding spatial image. The noise term ν_c has also been modified by the processing, or colored. The image formation matrix M and the raw data impulse response matrix C can be combined into the *spatial impulse response* (SIPR) matrix denoted as A. This results in the following expression

$$b_{img} = Ax + \nu_c. \tag{4.12}$$

This results in a SIPR matrix A that is specific to a given flight geometry, and SAR

system hardware parameters. The generation of the A matrix is computationally intensive. It involves two expensive steps. First, the raw data for each modeled pixel is modeled or synthesized. The raw data should reflect the actual hardware system as much as possible. Next the synthesized raw data is processed by the selected image-formation algorithm to produce the spatial IPR of the pixel targeted. The spatial IPR is than stored in the appropriate column of A. The generation of the A matrix is computationally expensive, but fortunately the cost can be alleviated by distributed-parallel processing.

It is explicitly noted that the SIPR matrix models the received SAR data under the premise that the reflectivity is constant and composed of isotropic radiators. The SAR data from the sensor (or the simulated data) does not fit this assumption perfectly. The SAR data are limited so that the reflectivity can be approximated as being aspect independent. The validity of the aspect-invariant reflectivity is critical to model-based processing. It fundamentally determines the upper bounds regarding the model fit. If the SAR data are simulated they should exhibit the same aspect-invariant behavior as seen in practice. The details of how to accomplish this are explained in Chapter 3.

4.2.1 SIPR Matrix Dimensionality

The rank generated in C is a result of the "physics" native to the SAR problem. The range resolution, given in Equation (2.8), and the Doppler resolution, given in Equation (2.26) provide a basis for how close two distinct scatterers can be and still be resolved uniquely. It is actually more complicated than those simple equations portray. The phase of the two scatterers plays a role, also [5]. If the scatterers x_k and x_{k+1} are too close to each other they are not independent and appear as a single target effectively. In matrix terms, the scatterers x_k and x_{k+1} have responses that are not linearly independent. Or, put another way, the isotropic raw-data impulse response contained in column x_k and x_{k+1} are dependent.

The rank of the raw-data simulation C matrix is an excellent tool to explore the theoretical resolution intrinsically contained in the raw data [47]. In the SAR problem, the rank corresponds to the number of resolvable spatial locations, or pixels in the image. But

the isotropic raw-data simulation matrix C is a dense matrix that is often impractical to take the rank of due to the large size. But it is feasible to take the rank of the SIPR matrix A especially if several approximations are employed that will be discussed.

A graphical example of a scene with a single scatterer helps to develop intuition. The images shown in Figure 4.5 visually depict all the mathematical terms, except the noise term, found in Equation (4.12). The scene geometry is shown in Figure 4.5(a) for perspective. The SIPR response matrix A, for the particular flight geometry, is generated and shown in Figure 4.5(b). The image formed by backprojection processing is shown in Figure 4.5(c). The resultant image x is shown in Figure 4.5(d). The resultant image x shows the super-resolution capability inherent in model-based processing. There has been extensive work on 2D super-resolution methods [48], but limited work for 3D. While the results are excellent, prior to getting too excited it is important to realize that this is synthetic data. The data modeled a single reflector to demonstrate generality. The model used is also a very tight fit to the data. The only difference was the azimuth antenna pattern was ignored in the model, and incorporated in the raw data.

There was an approximation employed in the generation of the matrix A that should be justified and discussed. The discussion will focus on a 2D IPR, but can be extended naturally to a 3D IPR.

In truth, the IPR of a scatterer is infinite spatially. But in practice, the response can be truncated to some desired accuracy with minimal degradation. The truncated response is justifiable since there is an inherent dynamic range and noise level that limits the SAR system fundamentally. It might be appropriate to only keep the first N side-lobes for a given application. This corresponds to using a truncated spatial response. The truncated spatial window is centered on the scatterer or pixel of interest.

The IPR inside the windowed area often contains many small, almost zero values. Often the values are only significant along the cardinal directions of range and azimuth (in 2D). Another justifiable approximation is to only model, or keep pixels that are above a prescribed threshold, say -50 dB. This means the spatial impulse response of every pixel is

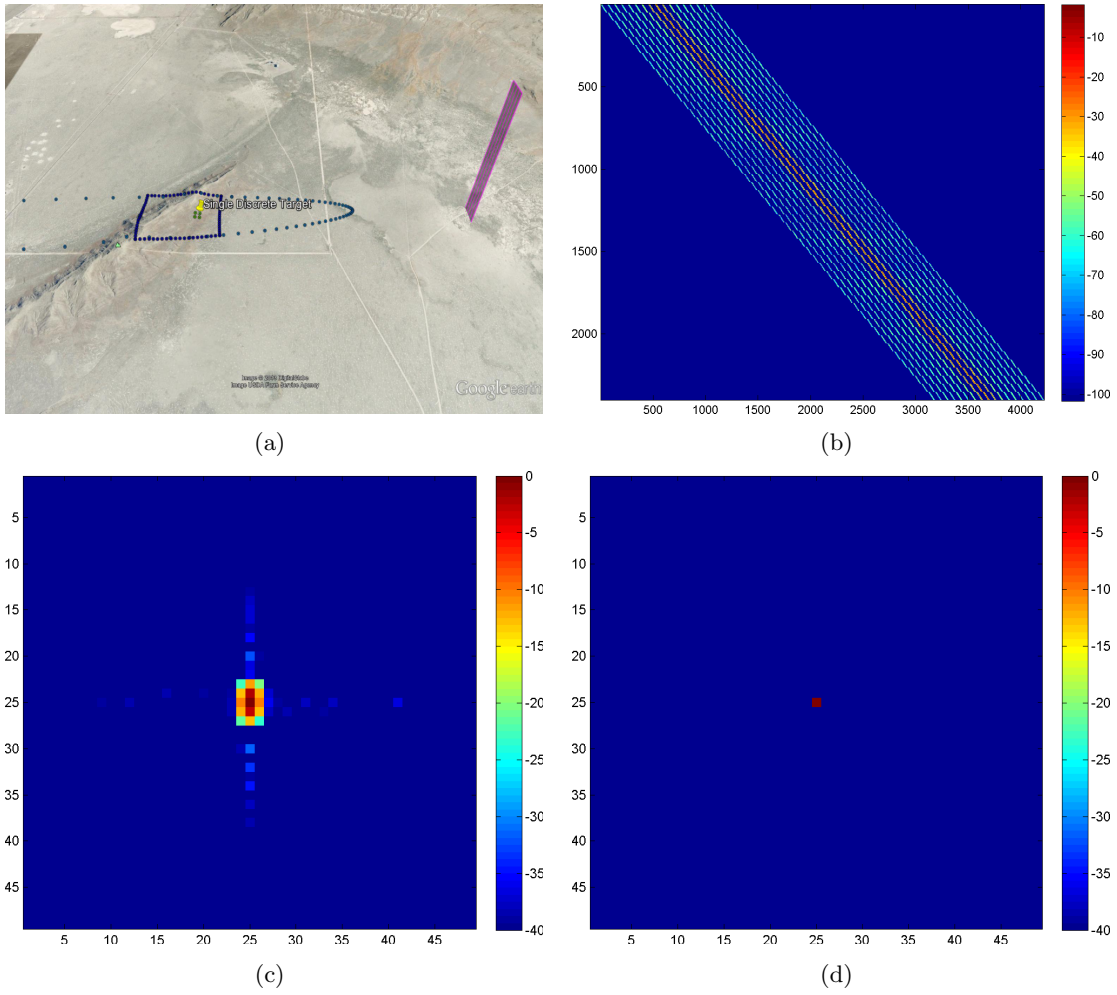

Fig. 4.5: Simulated point and the SIPR matrix with results: (a) Simulated image collection geometry, (b) SIPR A matrix, (c) SAR backprojected image denoted as the b_{img} vector, (d) Super resolved scene denoted as the x vector.

first, spatially truncated. And second, a threshold is applied where pixels are kept only if they are above the prescribed threshold. These two approximations were employed in the generation of the SIPR matrix A shown in Figure 4.5(b).

The spatial truncation of the IPR, and selection of the ROI define the problem dimensionality. For simplicity a simple 2D ROI is selected that has N columns and rows as shown in Figure 4.6. The ROI defines the area where an accurate or low-variance estimate of the scene reflectivity is desired. The IPR size is selected next. The IPR should include all the data that "significantly contributes" for each pixels IPR. The spatial IPR defines the area

of "significant contributions" for each pixel. The IPR is generically selected to be $2K+1$ by $2K+1$ in Figure 4.6. The term K can conceptually represent half the IPR.

The P^{th} pixel IPR is highlighted in Figure 4.6 portraying a boundary condition. The P^{th} pixel's spatial IPR augments the ROI size and produces a new $N+2K$ square image size. The new size generated will be referred to as the data-size. It is called the data-size because this defines the required data dimensions, or image b_{img}, that is needed. Any pixel that significantly contributes to the IPR of a pixel in the ROI should be included as data, or an input. This will ensure that a low-variance estimate of the ROI reflectivity can be achieved.

Finally the model must represent the data being utilized. This requires that each pixel in the data-size image be modeled. This is depicted for another boundary condition for the M^{th} pixel, which is located in the data-size region shown in Figure 4.6. The P^{th} pixel's spatial IPR augments the data-size and defines the final $N+4K$ square image size. This will be referred to as the model-size. The name given implies that this size is required to accurately model the data, or input image b_{img}.

In summary, the input image b_{img} is a vector that contains all the pixels defined by the data-size. The estimated image x is a vector that contains all the pixels defined by

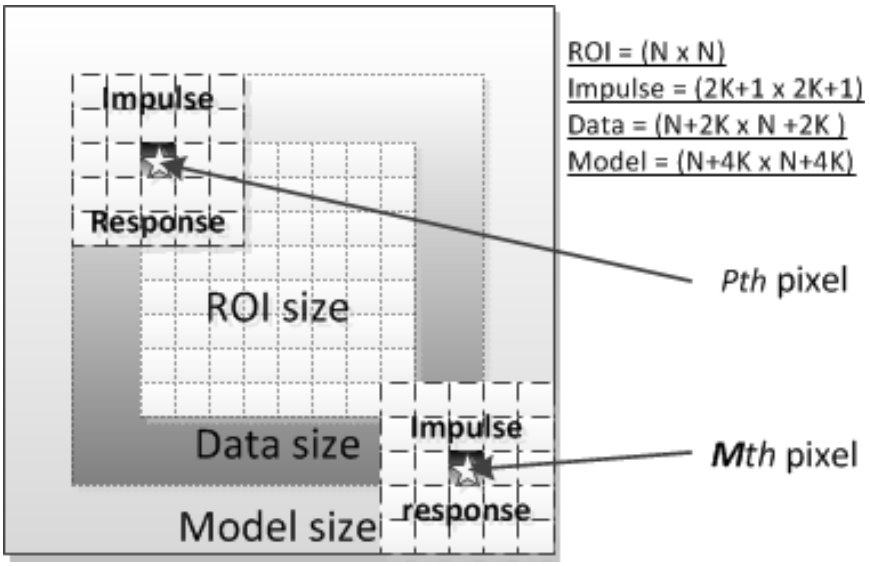

Fig. 4.6: The model, data, and ROI sizes for a 2D scene.

the model-size image. But only the components of x that are in the ROI are low-variance estimates. The selection of a ROI and an appropriate IPR define the corresponding data-size and model-size which will be used for model-based processing. This definitions always ensure that the equation shown in Equation (4.12) is a set of underdetermined equations. This is due to the fact that there are more pixels to estimate in the model-size image than there are pixels contained in the data-size image which always leads to a fat-matrix, or an underdetermined system of equations.

4.2.2 SIPR Matrix Rank

One of the benefits of model-based SAR processing is formulating the problem using linear algebra. This allows leveraging all the well-established tools, methods, and framework developed for such problems. The SIPR matrix A, when viewed through linear algebra, captures the theoretical scene resolvability. The scene resolvability can be extracted by examining the rank of the SIPR matrix A. The SIPR matrix is assumed to be wide, or underdetermined with the dimensions of m by n. The definition of the data-size and the model-size, as described previously, naturally define a SIPR matrix A that is fat, or underdetermined. This implies there are many possible solutions that are consistent with the data. The system is always underdetermined since the spatial IPR is effectively convolved with the scene as described in Section 4.2.1.

A simple example that examines the rank of the SIPR matrix A is useful to highlight the utility it provides. This example examines the rank of simulated data. The two collections have identical hardware settings. The simulation is centered at X-band, 10.0 GHz. The waveform leveraged is an LFM that has 95 MHz of bandwidth and uses a 1.0 microsecond pulse. The data-size of the scene selected is 65 meters square with 1 meter square pixel postings. The spatial impulse response is 17 meters square with 1 meter pixel postings, also. This implies that the scene ROI is 49 meters square, and the scene model-size is 81 meters square.

Since the hardware settings are identical, the objective of this simulation is to examine how sinusoidal flight perturbations affect scene resolvability. Both flights follow an ideal

circular path. But the second flight incorporates small periodic flight perturbations in the vertical and horizontal axis. The platform position oscillates in a sinusoidal pattern 10 meters vertically and horizontally. The oscillation repetition distance is 10 meters, or every 10 meters the platform traverses the sinusoidal motion resets. Such perturbations are unrealistic for a traditional system. But such effects could be accomplished with conformal antennas. Conformal antennas are embedded in the aircraft structure. It is difficult to quantify how the perturbations, in theory, affect the scene resolvability, and if they provide value that is worth pursuing further in practice. For simplicity the scene is only composed of a single reflector in order to observe the spatial IPR behavior.

Figure 4.7 shows the simulated results. The resultant images, b_{img} are shown in Figure 4.7(a) and Figure 4.7(b). It is interesting to note how the periodic motion spreads the spatial impulse response. This would classically be considered bad for a 2D image since the periodic motion induces strong side-lobes. The SIPR matrices are shown in Figure 4.7(c) and in Figure 4.7(d). The SIPR matrix of Figure 4.7(d) shows the large side-lobe effects due to the periodic motion, when compared to Figure 4.7(c). These matrices contain the theoretical spatial impulse response for every pixel in the model-size scene. The positional motion was incorporated into their generation, along with the hardware settings.

The final images in Figure 4.7(e) and Figure 4.7(f) show the singular values of the A matrices on a $10\log_{10}$ scale. If the assumption is made that a singular value of -20 dB or greater equates to pixel resolvability than the flight with periodic motion has more "resolvable" pixels than the traditional flight. It in fact has approximately 500 more resolvable pixels. The result are not surprising. One would expect that the flight with diverse aspects would have more information.

But this leads to new thinking regarding side-lobes and traditional windowing or apodization. It is well known that windowing suppresses side-lobes at the expense of broadening the main-lobe. But in model-based reconstruction windowing might not be required, and in fact it is not required for tight models. The side-lobes actually provide additional information that can be leveraged in model-based reconstruction. When there is model

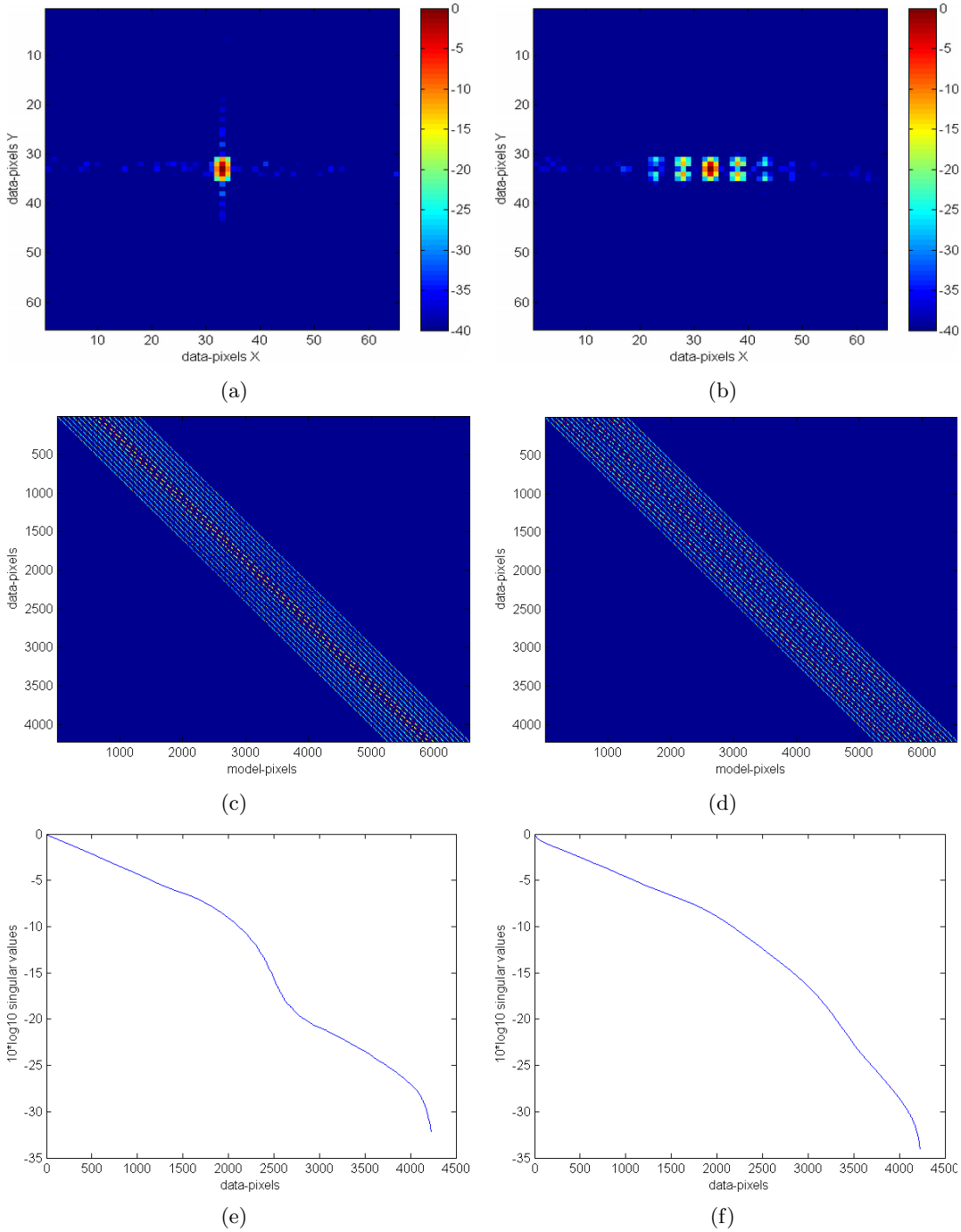

Fig. 4.7: Simulated collection geometry examining the SIPR matrix rank: (a) Traditional circular collection b_{img} image, (b) Sinusoidal circular collection b_{img} image, (c) Traditional circular collection A matrix, (d) Sinusoidal circular collection A matrix, (e) Traditional circular collection A matrix singular values, (f) Sinusoidal circular collection A matrix singular values.

mismatch it becomes a more complicated trade-space that will not be examined for this work.

The simple previous example only focused on motion. But the SIPR matrix A provides a systematic way to evaluate the theoretical gains from diverse arbitrary waveforms, diverse phase-centers, random motion, random sampling patterns, etc. Each of the attributes could be examined independently or collectively. Most of the configurations specified do not have exact closed form solutions, but the SIPR matrix A allows the trade-space to be explicitly analyzed. This example analyzed a 2D example, but 3D is where model-based reconstruction is particularly relevant. It is also important to realize that this applies for SAR data where aspect independent reflectivity can be assumed.

In practice, it is desirable to model the scene at a slightly higher fidelity than the SAR system resolution. This ensures the system resolution is not reduced due to the modeling. But it results in a wide SIPR A matrix that has a rank less than the row dimension. There are many solutions to such a system. There exists a *right-nullspace* denoted as $N(A)$ and a *left-nullspace* denoted as $N(A^T)$ for such a system. But modeling the scene at a much higher resolution does not provide additional resolvability. The resolvability or rank, as previously mentioned, is determined by the "physics" of the SAR collect. Over-modeling has some detrimental effects since it requires more resources to process.

One final advantage about model-based processing will briefly be mentioned here and talked about in more detail later. Compressive sensing is a new exciting area of research [14,15]. Model-based processing naturally extends itself to compressive sensing and in some form is required in order to apply compressive sensing.

4.3 Prior Work and Heuristics

This section focuses on incorporating prior information into the model-based SAR image reconstruction. Often the SAR scene has been collected previously and prior information is known. And there always is the current data collected b_{img} which provides scene dependent information. A natural inclination would be that incorporation of prior target information, at some level, would provide enhanced results or target detection.

This section will focus on prior work that has leveraged such heuristics in model-based SAR image reconstruction. The original works that initially incorporated such heuristics into the image formation process will be examined and briefly explained. The shortcomings of those works, that this work extends, are specifically noted in order to provide the motivation for this work.

4.3.1 Regularization and Spatial Smoothness

Underdetermined problems, such as seen in Equation (4.12), traditional employ some form of regularization [17]. One of the first papers that applied model-based processing with a regularization term to SAR was done by Cetin and Karl [49]. One of the particular challenges faced by Cetin and Karl was extending the regularization problem to complex SAR data. The phase of SAR data, in a seminal paper by Munson et al., was shown to be spatially uncorrelated [50]. This implies that little, if anything, can be gained from the phase of pixels in close proximity, but the magnitude of the surrounding pixels does provide additional information, that in many cases can be beneficial. However, this makes regularization problems challenging since the regularization term is applied to the magnitude of the complex values. Cetin and Karl proposed an iterative approach that minimized the following related cost function.

$$J(x_c) = \|Ax_c - b_{img}\|_2^2 + \lambda_1^2 \|x_m\|_k^k + \lambda_2^2 \|Gx_m\|_k^k \quad \text{s.t.} \quad x_m = |x_c| \tag{4.13}$$

The magnitude term x_m is related to the absolute value of the complex term x_c. The matrix G incorporates the spatial correlation factor into the image formation process. For example, it might be desirable to have a smooth, speckle free image. This implies that a smooth solution should be favored. Or equivalently, non-smooth solutions should be penalized. This could be accomplished for a 2D image by incorporating a 2D highpass filter. The frequency response of such a filter, the 3x3 Laplacian filter, is shown in Figure 4.8. A unique spatial filter could be applied to each pixel if desired. The matrix G generically represents this.

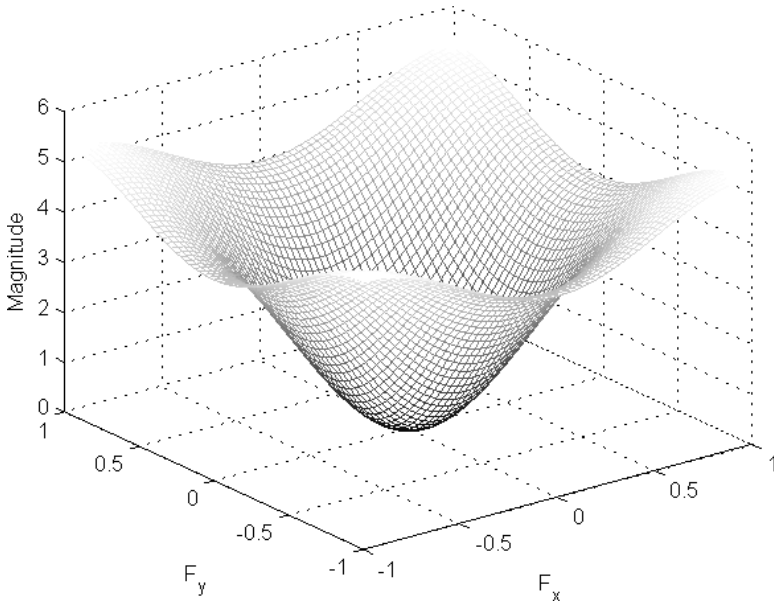

Fig. 4.8: Spatial response of G matrix.

Cetin and Karl solved the problem in Equation (4.13) by an interactive quasi-newton approximate method with ideas borrowed from half-quadratic regularization [51]. The smoothness term encourages smooth solutions. This provided natural scene segmentation and speckle reduction in the image-formation process.

Several short-comings of this approach are noted. First, this approach relied on non-standard solvers. This implies that leveraging commercial solvers is not an option. It is important to leverage commercial solvers since developing efficient solvers, and maintaining them is generally an entire career in and of itself. Second, the problem is non-convex. This has several negative ramifications. The problem solution could get stuck in a local minimum and is dependent on the initial starting value. And additionally non-convex problems are, in general, more difficult to solve. Third, the problem, as formulated, becomes intractable for large 2D scenes, and 3D scenes are all but impractical.

But there are two important contributions that are captured in this paper. First, Cetin and Karl applied regularization to the SAR image formation problem. There recently has been renewed interest in model-based SAR processing due to compressive sensing applications [16, 52], and for the inherent ability to provide super-resolution. Second, Cetin and

Karl specifically leveraged the RCS spatial correlation in his problem formulation. Spatial correlation in image processing is commonly leveraged [53]. But Cetin and Karl were one of the first authors to apply that assumption, or constraint into the image formation process for SAR.

SAR images that have been multilook processed clearly manifest spatial correlation regarding the RCS. The spatial clutter variance in the SAR image is suppressed by the multilook processing [30]. This produces low-variance SAR images that are visually pleasing. An example GOTCHA image is shown in Figure 4.9. The GOTCHA data was collected contains eight circular passes around a parking lot [36]. Each collection is separated by about 0.18 degrees in elevation. The elevation angles extends from 43.7 to 45.0 degrees. The image seen in Figure 4.9 was formed by coherently processing all eight elevation circular collects into 90 non-overlapping four-degree apertures. Coherent processing was done on each of the four-degree apertures via backprojection. Then the 90 four-degree apertures were combined by multilook processing into a single image.

It is clear when the SAR scene shown in Figure 4.9 is examined that spatial correlation

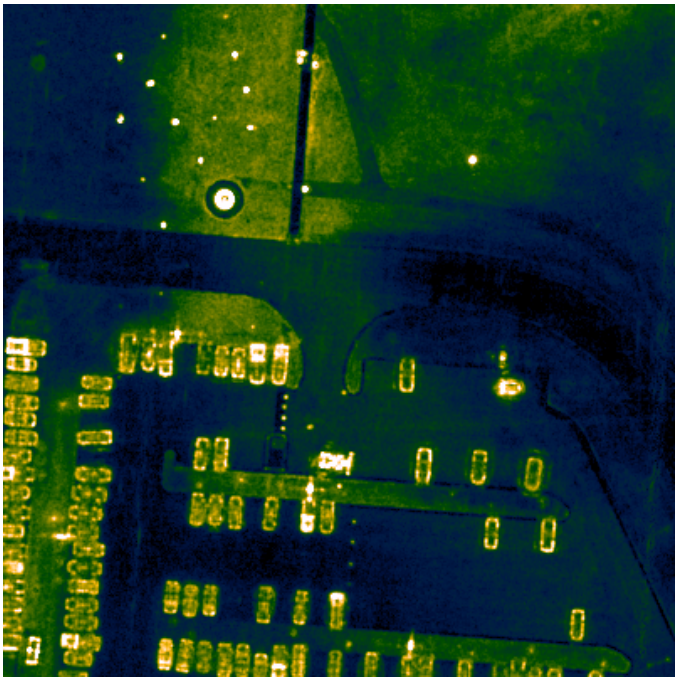

Fig. 4.9: Sample SAR scene using GOTCHA data.

definitely exists for much of the scene. While the amount of spatial correlation that exists is scene dependent, it is safe to say that for almost all SAR scenes the spatial correlation is statistical significant.

4.3.2 Aspect Correlation

SAR collections that integrate over a wide range of aspect angles hold the potential for improved resolution and foster improved scene interpretability and target detection. There has been lots of interest in processing wide-beam SAR data [54–58]. However, in practice, it is difficult to realize the potential due to the anisotropic scattering of objects in the scene for wide-aspects. The radar cross section of most objects changes as a function of aspect angle.

A key realization occurs when the phase and magnitude correlation of the RCS are examined independently. Heuristic evaluation of actual SAR data reveals that there often is a RCS magnitude correlation in aspect that exists beyond the coherent integration limits.

This is demonstrated for seven pixels selected from the GOTCHA data collect seen in Figure 4.10(c). The pixels selected have been marked with a star to help identify them. The 360 degrees of azimuth integration were divided into four-degree coherent sub-images and processed using the backprojection algorithm. Figure 4.10(a) shows the correlation of the magnitude RCS and Figure 4.10(b) shows the normalized complex RCS correlation. The correlation is computed using the selected pixel across the ninety four-degree images correspondingly.

The selected pixels demonstrate that the magnitude RCS is much smoother than the complex RCS, in general. This implies that the RCS phase often decorrelates at a different rate than the RCS magnitude across aspect. The RCS magnitude decorrelation is target-specific. The three target locations that correspond to asphalt have the lowest magnitude response, but are fairly correlated in magnitude irrespective of angle. The single pixel in the grass on the right side is similar, but has a stronger average. The strongest two returns correspond to corners of the car, and exhibit aspect dependent reflectivity. The last target, centered in the middle of the car has random behavior.

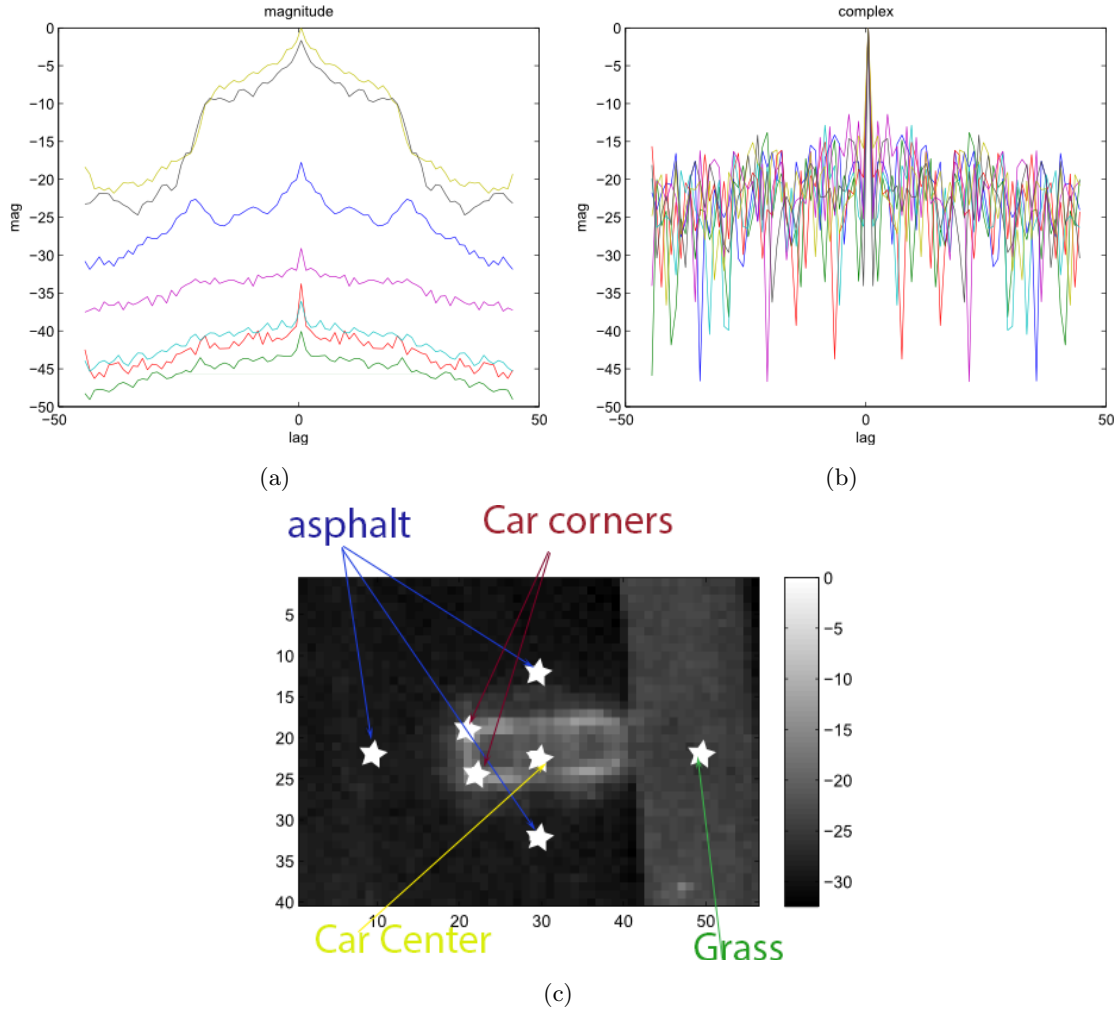

Fig. 4.10: Example of correlation in an actual SAR scene: (a) Magnitude correlation (dB), (b) Normalized complex correlation (dB), (c) Scene with seven pixels selected (white stars).

This helps develop intuition. For example, a rural scene might be fairly consistent regarding the RCS magnitude for a wide range of aspects. On the other hand, an urban scene with man-made features could exhibit glint phenomenology and decorrelate quickly due to the strong geometrical RCS dependence. The key insight is that the RCS magnitude is often correlated in aspect. This correlation can be leveraged to enhance desired features and suppress non-desired features for known target responses.

The decorrelation in aspect is often handled using multilook processing in traditional SAR image formation. This divides the scene into smaller apertures where isotropy, and

coherence are valid. This is visually shown in Figure 4.11. The full beam-width shown in red is divided into four smaller apertures shown in blue. The act of segmenting, in effect, provides a piece-wise linear model where isotropy is valid on the small individual pieces. The smaller isotropic apertures use coherent processing. While the combination of the aperture into a single image is a non-coherent operation done only on the magnitude of the image.

An actual example of real SAR data will help portray the need for multilook processing. Figure 4.12 shows actual X-band SAR data. Figure 4.12(a) shows the full 10 degree beam integration. Figure 4.12(b) and Figure 4.12(c) show unique one-degree apertures. An obvious assumption would be the image with ten times the aperture should have significantly higher resolution. This is not readily obvious. The most visually pleasing image is Figure 4.12(d) which is the multilook processed image. This is where the magnitudes from each individual 1 degree aperture are averaged together.

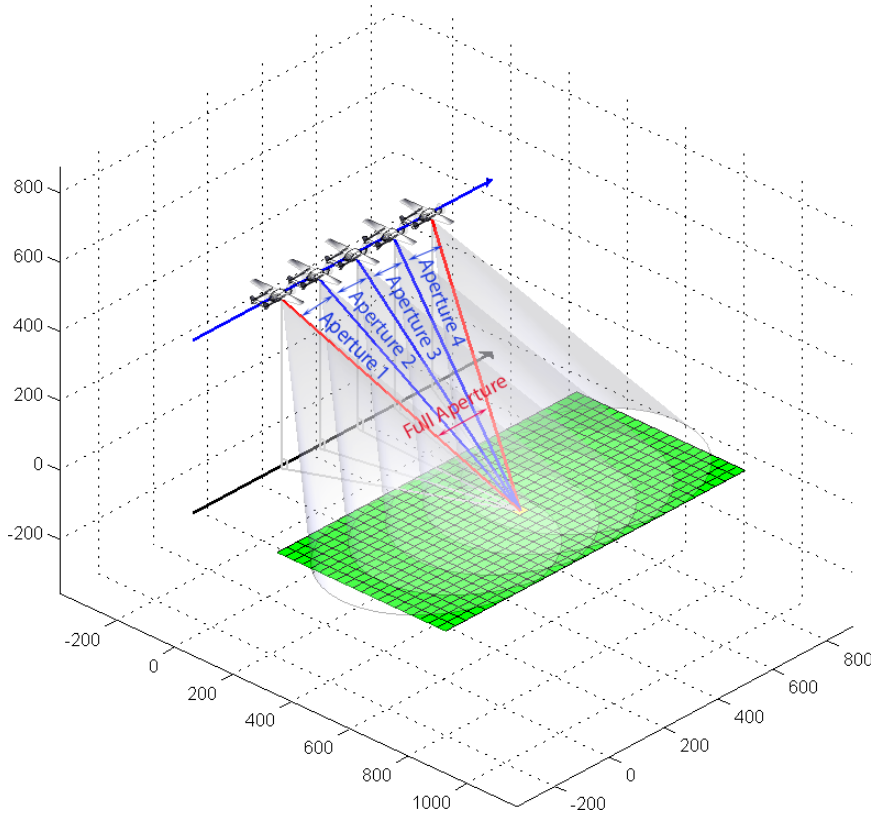

Fig. 4.11: Multilook processing done by sub-apertures.

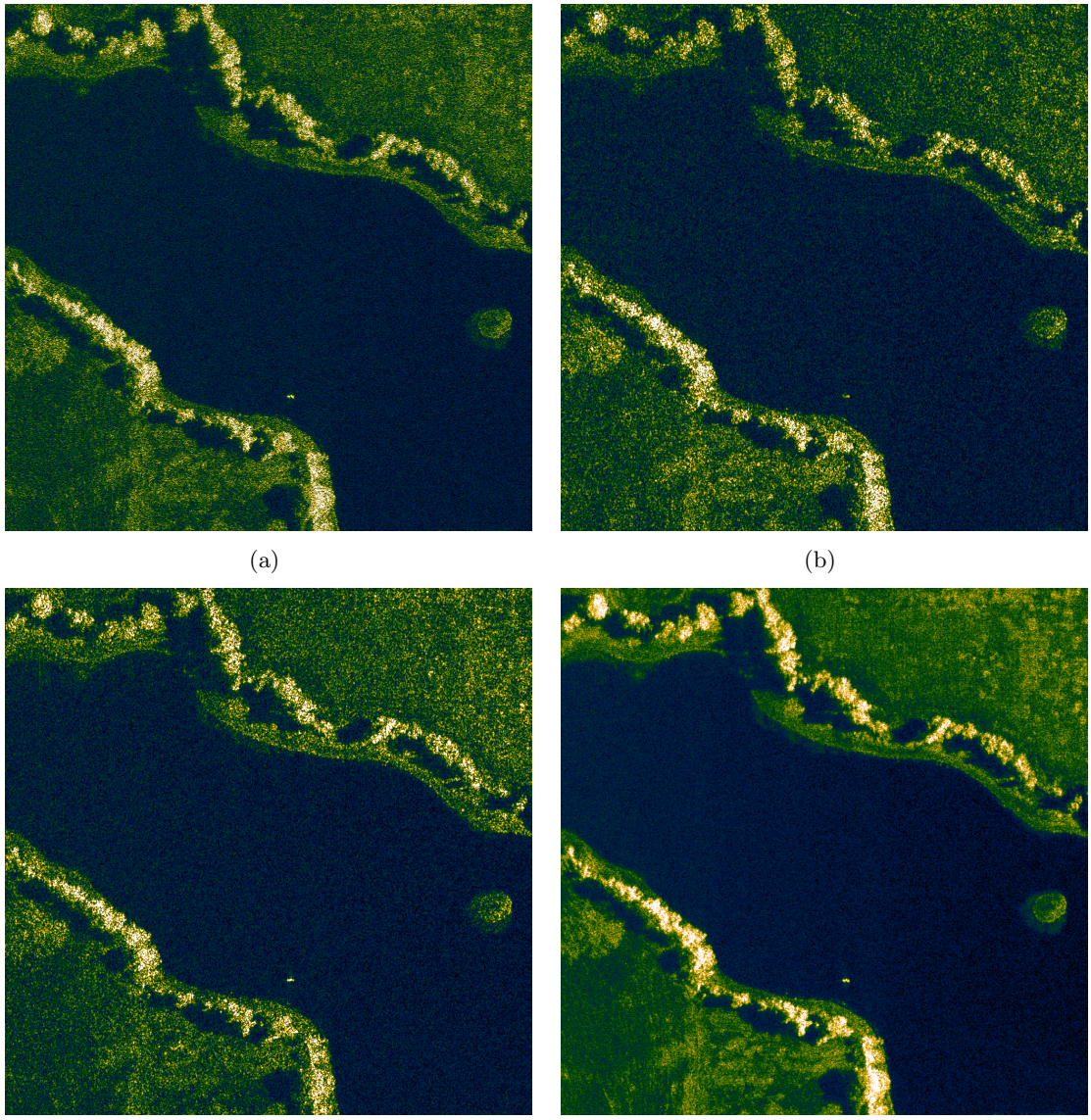

(a) (b)

(c) (d)

Fig. 4.12: SAR multilook processing example: (a) Full 10° degree aperture, (b) First 1° degree aperture, (c) Second 1° degree aperture, (d) Ten 1° degree multilook apertures combined.

In practice, the isotropic assumption, critical for coherent processing, is limited to small aspects depending on the scene content, wavelength, etc. Over wide aspects the time-varying reflectivity cannot be ignored. Coherent integration can only occur when the scene reflectivity remains constant. If the scene reflectivity begins to change with aspect than destructive interference begins to occur. This is similar to having your apple crate full

and picking up a new apple, but an existing apple falls out. The same analogy, with some imagination, could be extended to SAR. A new pulse is processed or added to the image, but the complex reflectivity has slightly changed. This causes a prior pulse to be cancelled because destructive interference occurs.

This problem becomes severe with wide-beam systems. For example it might be desirable to integrate over 30 degrees in aspect. But if the scene is only coherent over a 5 degree interval the resultant image will be restricted to a 5 degree aperture image effectively. The traditional way to accommodate such a scene is to divide the 30 degree beam into 6 separate 5 degree apertures. This, in effect, makes a piece-wise linear approximation to the time-varying reflectivity and produces improved results as seen in Figure 4.12(d). This can be represented as

$$b_{k_{img}} = A_k x_k + \nu_{k_c}, k = 1, 2, \cdots, K, \tag{4.14}$$

where the index k represents the k^{th} aperture.

This approach processes each image completely independent. The simple averaging done in multilook processing improves the image interpretability and implies that there is correlation in magnitude across the apertures. Cetin and Moses [59] were the first to propose a method to process wide-aspect SAR using a piece-wise linear model. Their model incorporated aspect magnitude correlation into the image formation process. This can be represented as

$$b_{img} = \begin{bmatrix} b_{img1} \\ \vdots \\ b_{imgK} \end{bmatrix}, \quad A = \begin{bmatrix} A_1 & & \\ & \ddots & \\ & & A_K \end{bmatrix}, \quad x = \begin{bmatrix} x_1 \\ \vdots \\ x_K \end{bmatrix}. \tag{4.15}$$

This formulation allows for joint processing across aspects.

This work was furthered by Stojanovic et al. [60]. Stojanovic et al. proposed the following SAR cost function:

$$\min_{x_1,\cdots,x_n} \sum_{k=1}^{n} \|b_k - A_k x_k\|_2^2 + \beta \sum_{i,j} \left[\sum_{k=1}^{n} |x_k(i,j)|^2 \right]^{q/2} + \alpha \sum_{i,j} \sum_{k=1}^{n-1} | \, |x_{k+1}(i,j)| - |x_k(i,j)| \, |^p. \tag{4.16}$$

The first term in this function encourages a good data fit to the observed data b_k. The second term encourages sparsity in the solution where $q \leq 1$. And the third term encourages solutions that are smooth across aspects for $p > 0$. The proposed cost function in Equation (4.16) used by Stojanovic et al. relied on a piece-wise linear isotropic assumption, also. But the aspects were jointly solved. This allowed the phase across apertures to change as needed. The correlation in magnitude could influence the results based on the weighting term α. The sparsity weighting has natural 3D application, since 3D SAR images are sparse. But sparsity could be desirable on 2D scenes. The extent sparsity is employed is controlled by the weighting β. The data fit term, is normalized to have a weighting of one.

There are several obvious areas to extend this effort. First, one extension would be to apply the results to real data, whereas only simulated results were shown. Second, the solver employed was a custom solver which suffers from performance, robustness, and maintainability when compared to commercial solvers, and this formation is inherently non-convex which has local minimum, initial starting point, and performance implications to consider.

Another generic extension would be to incorporate a matrix term into the problem formulation to generically represent the aspect filter on a pixel by pixel basis. As formulated in Equation (4.16), there is an assumption that smooth aspects are desired in the entire scene. This is implicitly incorporated by the third term in Equation (4.16), which is effectively a high-pass filter, but it would be ideal to incorporate pixel-specific aspect filters. As previously discussed and shown in Figure 4.10(c) the pixels that represent the car might employ filters that enhance the glint or high frequency response, whereas the pixels that

correspond to asphalt could incorporate filters that enhance low-pass solutions since the mean reflectivity would be appropriate.

In summary, the key idea that is incorporated into this section is jointly-processing across aspects in order to incorporate the magnitude correlation. This allows favoring solutions that exhibit a particular response across aspect. For example, solutions that have a constant magnitude across aperture could be favored, or not. This allows desirable targets responses to be enhanced, and others suppressed.

4.4 Summary of Problem Formulation

The critical ideas presented in this chapter are reviewed here for convenience and to buttress their foundational roles. Initially, in this chapter, a linear raw data model was developed in Section 4.1. The dimensionality of the raw data model was prohibitive in many respects. This led to the focused SAR linear model in Section 4.2 which reduced the model dimensions since the spatial IPR had a compact spatial representation. The utility of analyzing the rank of the SIPR matrix A was discussed regarding theoretical work and the insight provided.

Section 4.3 detailed the three main contributions that will be leverage in the remainder of this work. The first is incorporating a regularization term into the image formation processing. This is particularly useful for underdetermined systems typically encountered in the SAR image formation processing.

The second innovative ideas was incorporating a spatial magnitude term into the image-formation process. Almost all SAR scenes exhibit spatial magnitude correlation. The problem formation shown in Equation (4.13) allowed for a natural way to incorporate the spatial correlation into the image formation process.

The third related idea is jointly processing the individual apertures, or aspects. This idea is given in Equation (4.16). This allows the aspect magnitude response of known targets to be incorporated into the image formation process to enhance their response and suppress non targeted responses.

Chapter 5

Convex Model

This chapter focuses on developing a model-based convex optimization formulation of the SAR image reconstruction problem. The convex formulation naturally ensures global optimality by nature and is not sensitive to initial conditions or starting criteria. Figure 5.1 shows a convex function. The function evaluated between two points $f(x_1)$ and $f(x_2)$ is always less than the linear average of the points $tf(x_1) + (1-t)f(x_2)$ where $t \leq 1$. The power of a convex function can be summarized, admittedly this is oversimplified, by saying that local gradient information provides global information regarding where the solutions exists.

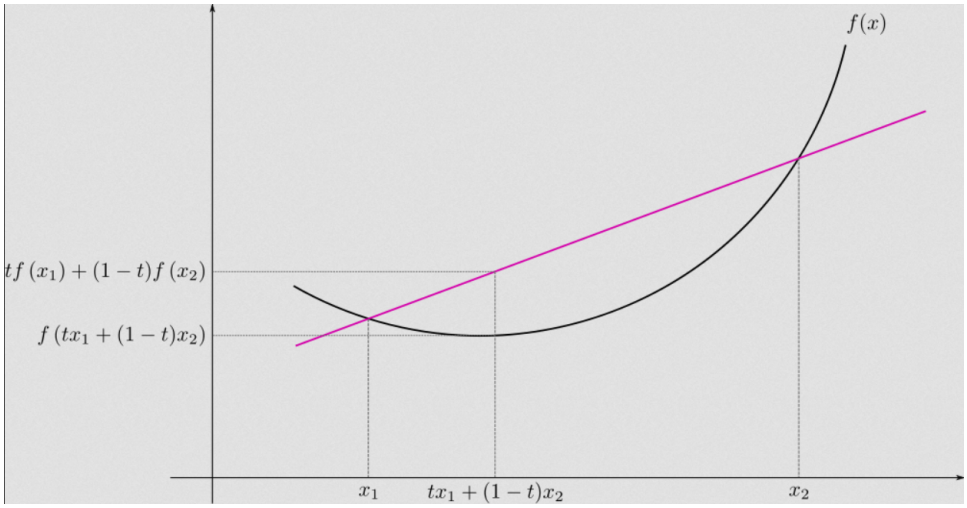

Fig. 5.1: A convex function.

Any problem formulated as

$$\begin{aligned} \underset{x}{\text{minimize}} \quad & f_o(x) \\ \text{subject to} \quad & f_i(x) \leq 0 \ \text{ for } i = 1, \ldots, m \\ & h_i(x) = 0 \ \text{ for } i = 1, \ldots, p \end{aligned} \tag{5.1}$$

can be solved by convex optimization techniques when the following conditions are met. The objective $f_o(x)$ is a convex function, and all m constraints $f_i(x)$ are convex functions. The p equality constraints $h_i(x)$ are linear functions. The inequality constraints geometrically define convex sets where the solution must reside, and the equality constraints define hyperplanes where the solutions must exist. The intersection must not be empty. The class of convex functions is a much more general class than traditional least-squares, or quadratic problems. The broader class of problems that can be represented as convex functions and the fact fast, efficient solutions can be found have made convex optimization an active area of research. The convex representation given in Equation (5.1) comes from Boyd and Vandenberghe [17].

This chapter will cover the high-level details necessary to formulate the SAR image formation problem as a *second order cone program* (SOCP) which is a convex optimization problem. The SOCP problem formulation presented can incorporate spatial magnitude constraints, and, or aspect magnitude constraints in order to accentuate desired target responses in the image formation process. The SOCP formulation also incorporates a sparsity term which is critical for underdetermined formulations. The SAR image formation problem almost always is an under-determined problem. The ability to incorporate prior knowledge into the image formation process allows for knowledge-aided image formation (KAIF). Each pixel, or scene can incorporate prior knowledge to enhance desired targets, and suppress targets that are not of interest.

The details and derivation required to fully understand convex optimization will not be provided here due to the complexity and volume of background that is required. An

excellent source is the book written by Boyd and Vandenberghe as well as the book written by Dattorro [17, 61]. The high-level convex optimization concepts used in this work that are critical to frame the SAR image formation problem as a convex optimization problem will be referenced specifically. But the details and derivation of the corresponding convex optimization terms and ideas will not be explicitly derived here. The concepts can be investigated by the interested reader in the provided references, if more details are desired.

Posing the SAR problem as a convex optimization problem allows commercial solvers to be used. Commercial solvers generally have performance that is significantly improved compared to custom solvers. Also in the author's experience, commercial solvers are much more robust. Almost all commercial solvers incorporate the critical linear algebra techniques required for rank-sensitive problems such as pivoting, refactoring, etc. [47].

Another important consideration is almost all commercial solvers support sparse matrices. This allows the SAR image formation problem to be formulated for very large problems. Due to the sparse problem structure, large problems can still be solved when sparse representations are employed, since substantially less resources are required for sparse representations. Supporting sparsity for custom solvers is not a trivial effort, and requires a lot of additional work.

5.1 Cost Function

All the terms incorporated into the cost function are designed to leverage some type of prior information about the target or scene into the image-formation, or optimization problem. This will allow targets that fit the response to be accentuated and other legitimate targets that are not of interest to be suppressed.

For example, a specified targets RCS across aspects from aperture to aperture could be persistent in magnitude. Such a response could be described as a low-pass response. Or perhaps the target RCS from aperture to aperture exhibits glint like phenomenology or a high-pass response. These responses could be specifically targeted to suppress or accentuate. The same idea extends to the spatial magnitude response.

The objective of each constraint included in the cost function is to allow the excitation

of particular desirable target responses. The model-based formulation does not restrict the results to a particular response, but provides a general approach for *knowledge-aided image formation* (KAIF) where unique response can be targeted. Often SAR scenes are collected multiple times with a particular objective in mind. But at a minimum the current collected data provides some level of scene specific information that could be leveraged.

KAIF is the objective of the model-based framework in this effort. A full-blown KAIF image formation process might allow each pixel to be classified. Then each pixel, based on the pixel classification, could incorporate the appropriate "filters" in the image formation process that elicits the desired pixel-specific response. Or maybe only a specific target in the scene is of interest and all other targets are considered "clutter." The "filters" could be tailored to the desired response.

The cost function will be derived from a basic model-fit to a more complex function that incorporates spatial and aspect magnitude correlation in this section.

5.1.1 Data Fit

The forward data model that was given in Equation (4.14) is repeated here for convenience and is given as

$$b_k = A_k x_k + \nu_k, \quad k = 1, 2, \cdots, K. \tag{5.2}$$

It is assumed that there are K apertures, and the index k represents the k^{th} aperture. It is assumed that the apertures are small enough that isotropy, or coherent processing applies. The vector b_k represents a focused SAR image in the spatial domain. But corresponding models could be applied to the pulse-compressed domain, or the raw-data domain. The image domain is ideal since the IPR is compact and will be assumed in this work. The term aperture or aspect will be used interchangeably and both terms refer to the same entity. An aperture or aspect is a single image where coherent processing was employed. For example, b_k refers to the k^{th} aperture or aspect image.

All the terms in Equation (5.2) are complex. The l^{th} pixel in the k^{th} aperture has real and imaginary components and is given as

$$b_{k,l} = b^r_{k,l} + jb^i_{k,l}, \tag{5.3}$$

$$A_{k,l} = A^r_{k,l} + jM^i_{k,l}, \tag{5.4}$$

$$x_{k,l} = x^r_{k,l} + jx^i_{k,l}, \tag{5.5}$$

$$\nu_{k,l} = \nu^r_{k,l} + j\nu^i_{k,l}. \tag{5.6}$$

It is convenient to arrange these real-valued terms as

$$b_k = M_k z_k + \nu_k \tag{5.7}$$

$$b_k = \begin{bmatrix} b^r_k \\ b^i_k \end{bmatrix}, \quad A_k = \begin{bmatrix} A^r_k & -A^i_k \\ A^i_k & A^r_k \end{bmatrix}, \quad x_k = \begin{bmatrix} x^r_k \\ x^i_k \end{bmatrix}, \quad \nu_k = \begin{bmatrix} \nu^r_k \\ \nu^i_k \end{bmatrix}. \tag{5.8}$$

This allows a wide range of commercial solvers to be used. Even solvers that do not support complex problem formulations can still be leveraged since the problem formulation has been equivalently expressed by using only real numbers.

The magnitude is a critical component of the SAR image formation problem. The magnitude is given as

$$x_{m_{k,l}} = \sqrt{(x^r_{k,l})^2 + (z^i_{k,l})^2} = |x_{k,l}|. \tag{5.9}$$

The magnitude part of the SAR imagery is what is visualized for traditional SAR images.

All the individual apertures could be estimated by solving the corresponding problem.

$$\underset{x_1,\cdots,x_K}{\text{minimize}} \ \sum_{k=1}^{K} \|A_k X_k - b_k\|_2, \tag{5.10}$$

which is equivalent to

$$\underset{x}{\text{minimize}} \|Ax - b\|_2$$

$$A = \begin{bmatrix} A_1 & & \\ & \ddots & \\ & & A_K \end{bmatrix}, \quad x = \begin{bmatrix} x_1 \\ \vdots \\ x_K \end{bmatrix}, \quad b = \begin{bmatrix} b_1 \\ \vdots \\ b_K \end{bmatrix}. \tag{5.11}$$

Considering the k_{th} aperture initially, the estimate x_k tries to fit the data b_k optimally. This is often call a model fidelity term since it tries to estimate the image x_k so the estimated results $A_k x_k$ approximates b_k. The dimension of A is $\in R_{m_a \times n_a}$.

Unfortunately, Equation (5.10) does not give robust results by simply taking the pseudo-inverse of each individual aperture. The system of equations is always underdetermined and often it has poor conditioning, as discussed in Section 4.2.2. In such cases, the pseudo-inverse results are not robust. This is illustrated by the results in Figure 5.2 for a simulated scene. The scene, or image generated by backprojection processing is shown in Figure 5.2(a). The pseudo-inverse results are shown in Figure 5.2(b). It is clear that the pseudo-inverse results in Figure 5.2(b) do not reflect the scene in Figure 5.2(a). The A matrix is given in Figure 5.2(c).

Since the problem formulation for model-based SAR image formation is underdetermined, and often not even full-row rank, the solution can be given by solving the least-norm problem [17]. The least-norm problem finds the solution that is consistent with the measurements $Ax = b$ and has the smallest norm, $\|x\|_2$. This geometrical can be understood as finding the solution x that is closest to the zero vector in Euclidean distance.

This often has the effect of spreading the energy rather than centralizing the energy, as can be seen in Figure 5.2. This is expected since the penalty function used is the l_2-norm. The l_2-norm penalizes large values of x more severely compared to smaller values of x. From a linear algebra perspective, this means that a solution would prefer to use all the linearly dependent basis at a consistent level rather than select a single basis exclusively. Now applying that interpretation to SAR, it means that linearly dependent pixels are applied at

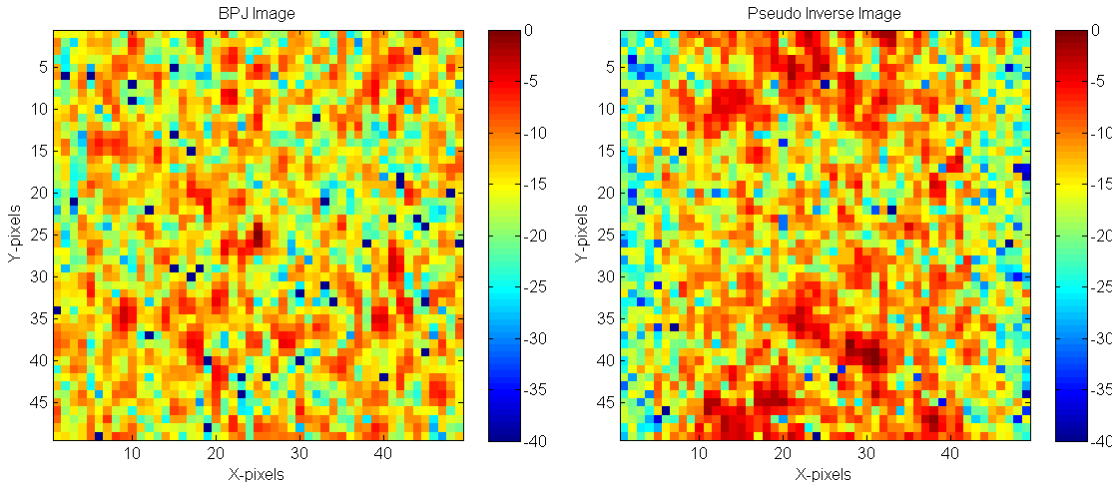

(a) (b)

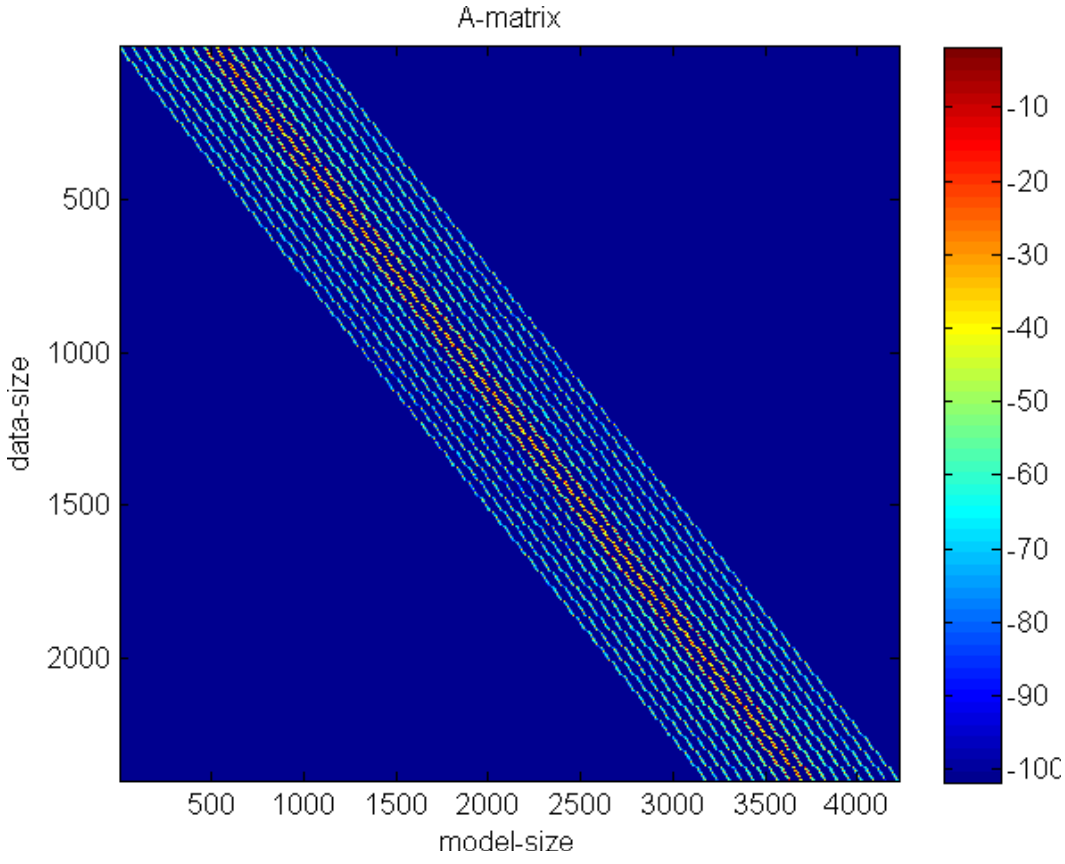

(c)

Fig. 5.2: Simulated scene applying the method of least squares: (a) Simulated scene b, (b) Pseudo-inverse solution b, (c) The SIPR matrix A.

a consistent level, rather than selecting a single pixel. This characteristic makes the standard least-norm approach generally not acceptable for model-based SAR image formation.

5.1.2 Regularization Term

A common approach to deal with underdetermined systems is incorporating a regularization term. This augments Equation (5.11) to be given by

$$\begin{aligned} \underset{x,x_m}{\text{minimize}} \quad & \|Ax-b\|_2 + \omega_m \|x_m\|_1 \\ \text{subject to} \quad & \sqrt{(x^r_{k,l})^2 + (x^i_{k,l})^2} = x_{m_{k,l}} \ \text{ for all } k,l, \end{aligned} \tag{5.12}$$

where the variable x_m is defined as

$$x_m = \begin{bmatrix} x_{m_1} \\ \vdots \\ x_{m_K} \end{bmatrix} = \begin{bmatrix} |x_1| \\ \vdots \\ |x_K| \end{bmatrix}. \tag{5.13}$$

The variable x_m is composed of all the magnitude images for the K aspects, where the l^{th} element in the k^{th} aperture is defined by Equation (5.9).

The new sparsity term $\omega_m \|x_m\|_q$ actually provides several benefits. First it penalizes solutions that have large magnitudes. This encourages x_m to be as small as possible. This counters the default behavior of the pseudo-inverse, or the l_2-norm to "smear" or spread the energy out as visualized in Figure 5.2(b). The sparsity constraint tries to concentrate the results using a minimal basis representation. Which translates in this problem case to using a minimal number of pixels. The weighting term ω_m determines the importance of the sparsity constraint compared to the data-fit term.

The variation of the weighting ω_m term traces out a Pareto optimal solution surface [17, 62]. When ω_m is zero the problem reduces to the pseudo-inverse problem and the corresponding solution. At the other extreme ω_m is so large that it is too expensive to "turn on" any pixel and the solution is zero. Between these two extreme solutions lies the solution surface, often called the Pareto surface. The exact solution is controlled by the

weighting given to ω_f between these two end points.

The second benefit the sparsity constraint provides pertains to underdetermined poorly conditioned systems. Incorporation of a sparsity term helps promote robust solutions for the SAR image formation problem. The last benefit is in respect to 3D scene reconstruction where the scene actually is sparse. The sparsity term for 3D image formation is absolutely critical. The norm used can encourage comparatively diffuse (energy spread) solutions (l_2-norm) or sparse solutions (energy concentrated) solutions (l_1-norm). The SAR image formation problem is generally always interested in sparse solutions so the l_1-norm will often be assumed for this work.

The data fit and the regularization term depend on different variables. The constraint, given as $\sqrt{(x^r_{k,l})^2 + (x^i_{k,l})^2} = x_{m_{k,l}}$, links these two variables so that they are not independent. Unfortunately, this is a non-convex constraint. Fortunately, it defines the boundary of a collection of second order convex cones (SOCP) [63,64]. In order to proceed as a convex formulation, the equality constraints are relaxed and formulated as inequalities.

$$x_{m_{k,l}} \geq \sqrt{(x^r_{k,l})^2 + (z^i_{k,l})^2} = |x_{k,l}|. \tag{5.14}$$

The solution is now optimized over these cones.

5.1.3 Aspect Term

Unfortunately, Equation (5.12) has another problem. The k^{th} image, or aperture, is processed independently of all the other apertures. It is decoupled from all the other image aspect results. This does not allow embedding prior information into the image formation process. It is desirable to leverage the aspect dependent magnitude correlation in the image formation processing to facilitate KAIF.

By augmenting the cost function in Equation (5.12) with a new term the formulation can be written as

$$\begin{aligned} \underset{x,x_m}{\text{minimize}} \quad & \|Ax-b\|_2 + \omega_f \|Fx_m\|_p + \omega_m \|x_m\|_1 \\ \text{subject to} \quad & \sqrt{(x^r_{k,l})^2 + (x^i_{k,l})^2} = x_{m_{k,l}} \ \text{ for all } k,l, \end{aligned} \tag{5.15}$$

or as

$$\begin{aligned} \underset{x,x_m}{\text{minimize}} \quad & \|Ax-b\|_2 \\ \text{subject to} \quad & \sqrt{(x^r_{k,l})^2 + (x^i_{k,l})^2} = x_{m_{k,l}} \ \text{ for all } k,l \\ & \|Fx_m\|_p \leq \varepsilon_1 \\ & \|x_m\|_1 \leq \varepsilon_2. \end{aligned} \tag{5.16}$$

The new term allows prior knowledge regarding the individual scenes magnitude aspect correlation to be incorporated to the image formation processing. The term F is $\in R_{m_f \times n_a}$. It is assumed it has the same column dimension as A in Equation (5.11), but possibly only a subset of pixels employ aspect "filters." This implies that $m_a \geq m_f$.

The problem defined in Equation (5.12) is re-cast in two different ways. Both problems incorporate the additional aspect constraint in slightly different ways. In the first problem in Equation (5.15), the aspect term is added to the cost function, whereas in Equation (5.16) the aspect term is incorporated as a constraint.

In the first formulation given in Equation (5.15), a weigthing term ω_f is used to regulate the importance, or cost of the aspect term relative to the data fit and sparsity term. If the weight term ω_f is set to zero than this problem reduces to Equation (5.12). At the other extreme, if the weight term is extremely high it is too costly to have any pixels enabled and the solution is zero or a constant.

The second problem formulation shown in Equation (5.16) has the aspect dependence term included as a constraint. The term ε_1 specifies the maximum contribution the aspect term can contribute. The term ε_1 has an inverse meaning compared to the weighting term ω_f in Equation (5.15). If the term ε_1 is infinity than the problem reduces to Equation (5.12), but if the term ε_1 is zero than the solution is zero or a constant.

In the author's opinion, the first problem formulation in Equation (5.15) is naturally more intuitive to interpret. This is because it incorporates a weighting of the sparsity, spatial, and aspect terms relative to the data-fit. A weighting of 0.5 on a particular term means it is weighted half as much as the data-fit term and a weighting of 2.0 on a particular term means that it has twice the weighting of the data-fit term. The relative weighting is very natural to interpret. In the second approach knowledge about the particular problem scaling is generally required for the second formulation, given in Equation (5.16), in order to give relative weightings. Both problems trace out the same Pareto solution surface.

To illustrate a simple example of the general structure contained in F, it is assumed that the aspect magnitude is correlated from aperture to aperture, or smooth in aspect. This implies the cost function should penalize non-smooth functions. A very simple way to accomplish this is to give F a high-pass filter. High-pass solutions, or non-smooth solutions, are penalized. Under these assumptions a simple representation of F could be given by

$$F = \begin{bmatrix} -I & I & & & & & \\ I & -2I & I & & & & \\ & \ddots & \ddots & & & & \\ & & & I & -2I & I & \\ & & & & -I & I \end{bmatrix} = \begin{bmatrix} -1 & 1 & & & & & \\ 1 & -2 & 1 & & & & \\ & \ddots & \ddots & & & & \\ & & & 1 & -2 & 1 & \\ & & & & -1 & 1 \end{bmatrix} \otimes I. \quad (5.17)$$

The frequency response is shown in Figure 5.3. This shows that high-pass solutions receive little attenuation. This means that high-pass solutions are expensive when incorporated into the cost function, because a high-pass solution is not suppressed. Conversely, a low-pass solution, or smooth solution is comparatively cheap since the results are suppressed.

The p norm is used in Equation (5.15) and Equation (5.16). It is assumed that this is the l_1-norm or the l_2-norm. Each of these norms assumes an underlying statistical distribution of the results of $\|Fx_m\|$. If there is a Gaussian distribution then the l_2-norm is optimal, whereas if there is a Laplacian distribution, the l_1-norm is optimal.

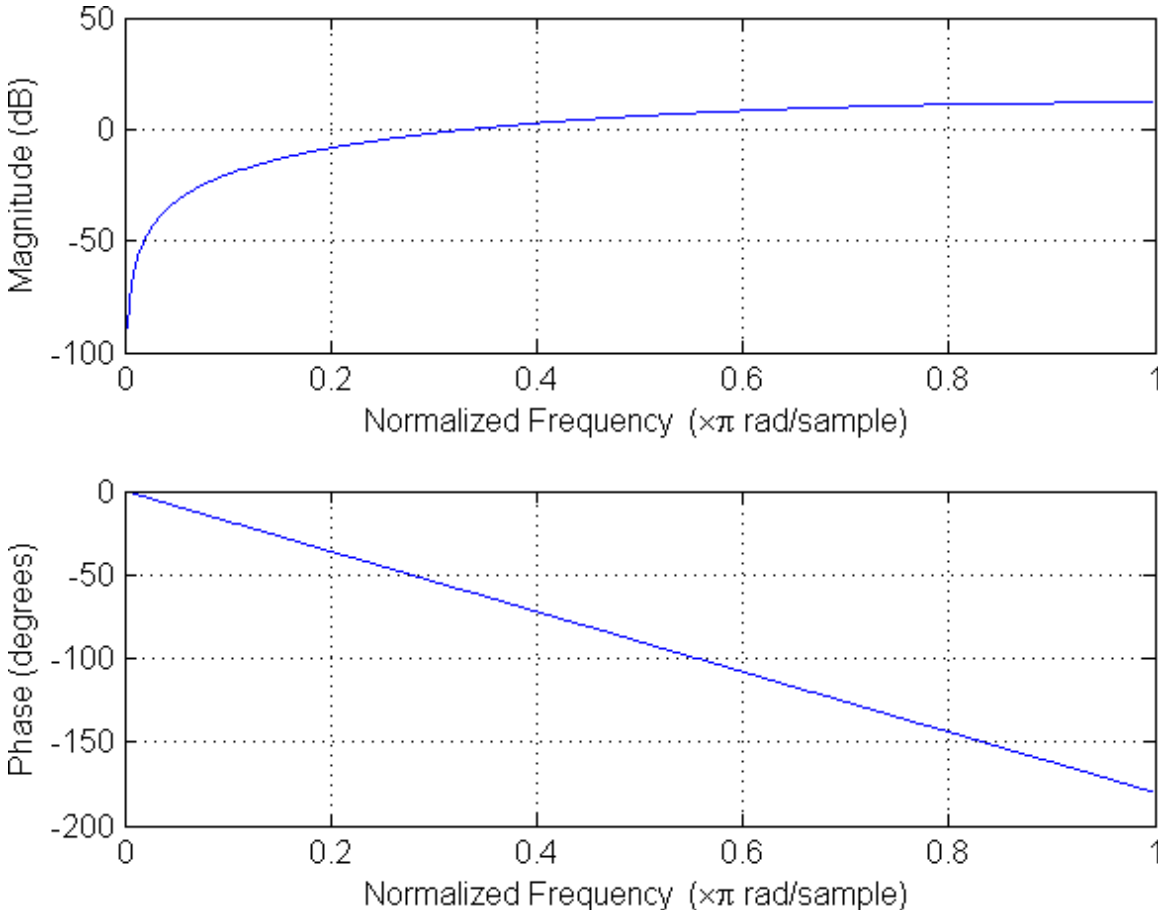

Fig. 5.3: Frequency response of the aspect filter F using [-1 2 -1].

A simple graphical example will help demonstrate the structure of the F matrix. This is shown in Figure 5.4. The scaling on the imagery is done solely to accentuate the structure present in each image. The matrix A is composed of three apertures and is shown in Figure 5.4(b). Each aperture, or image is circled in red. The columns of A contain the truncated IPR of the modeled pixels.

The aspect filter matrix F is shown in Figure 5.4(a). The matrix F has a specific structures that is dependent on the number of taps used to filter the magnitude of the reflectivity. Assuming a constant N taps are used in the aspect filter than the matrix F would have $N-1$ minor diagonal components. The diagonal components would be offset from the main diagonal since they represent a pixel in a separate aperture. In Figure 5.4 N is equal to three apertures giving the matrix the tri-diagonal form that is seen.

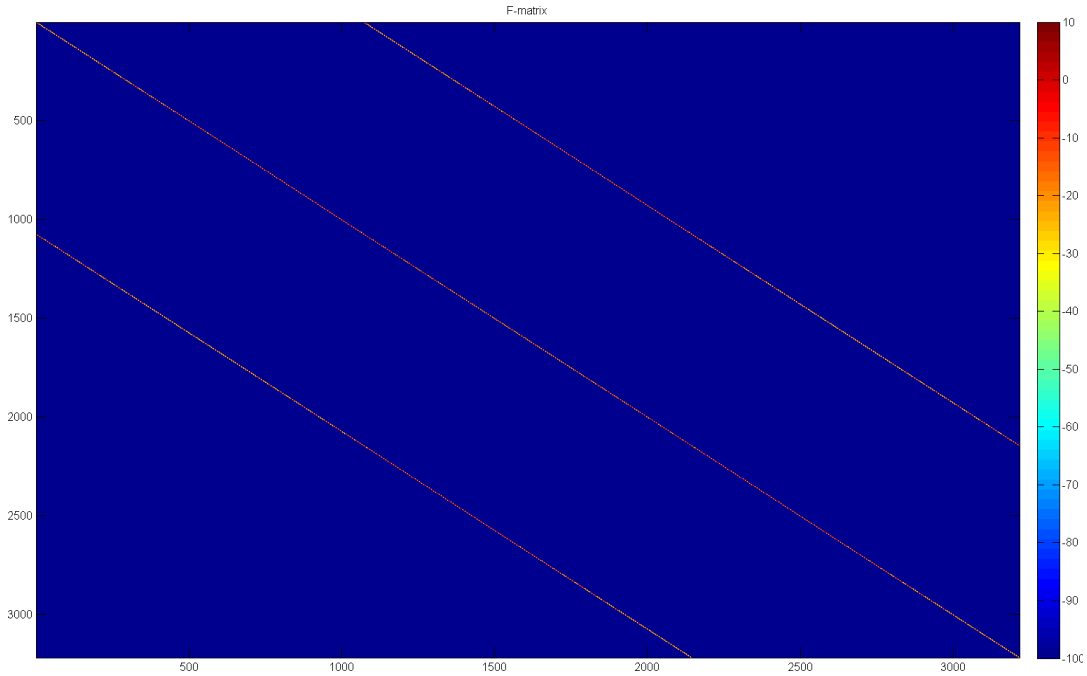

(a)

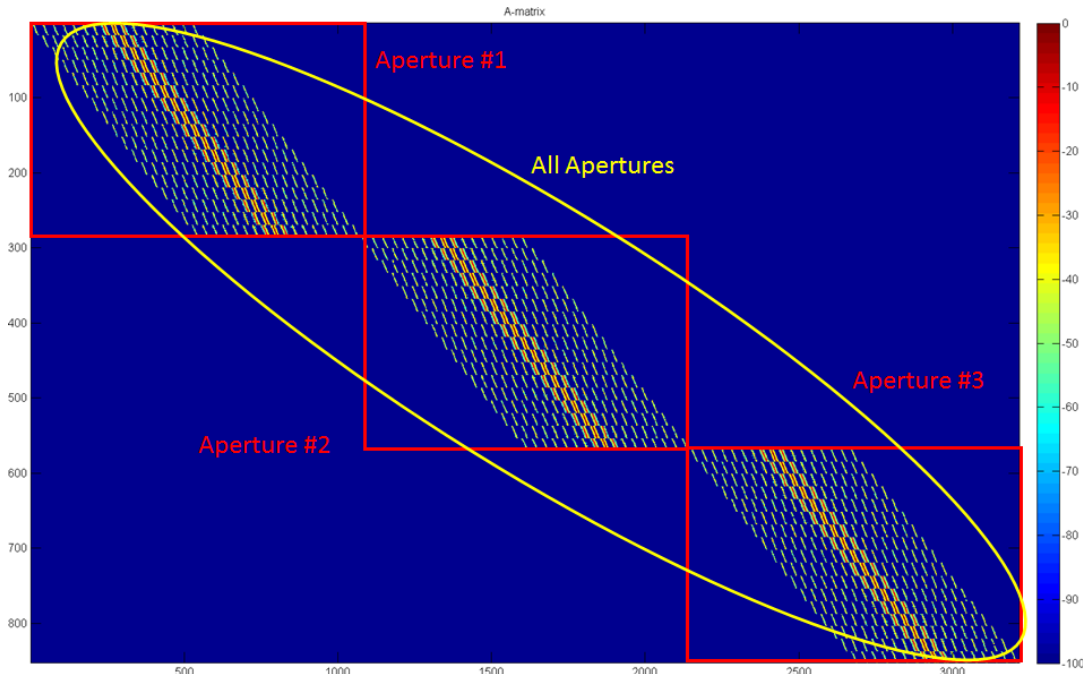

(b)

Fig. 5.4: Aspect matrix G and SIPR matrix A example: (a) Example aspect filter matrix F, (b) Example A matrix composed of three apertures.

5.1.4 Spatial Term

The last term that will be included in the problem formulation is a spatial smoothness term. The final problem formulation is than given as

$$\begin{aligned} &\underset{x,x_m}{\text{minimize}} \;\; \|Ax-b\|_2 + \omega_f \|Fx_m\|_p + \omega_m \|x_m\|_q + \omega_g \|Gx_m\|_f \\ &\text{subject to} \;\; \sqrt{(x^r_{k,l})^2 + (x^i_{k,l})^2} \leq x_{m_{k,l}} \;\; \text{for all } k,l. \end{aligned} \tag{5.18}$$

The term G is a matrix that encapsulates the prior knowledge regarding the spatial RCS magnitude. The dimension of G is $\in R_{m_g \times n_a}$ which assumes that a subset of pixels could incorporate a spatial filter. This implies that $m_a \geq m_g$ where m_a is given in Equation (5.11).

A spatial filter is more intuitive than an aspect filter naturally, but it is beneficial to show the structure of the spatial filter in conjunction with multiple apertures. The visualization helps understand the structure of the G matrices. This is shown in Figure 5.5. The scaling on the imagery is done solely to accentuate the structure present in each image. The spatial filter corresponds to the same matrix shown in Figure 5.4(b) composed of three apertures.

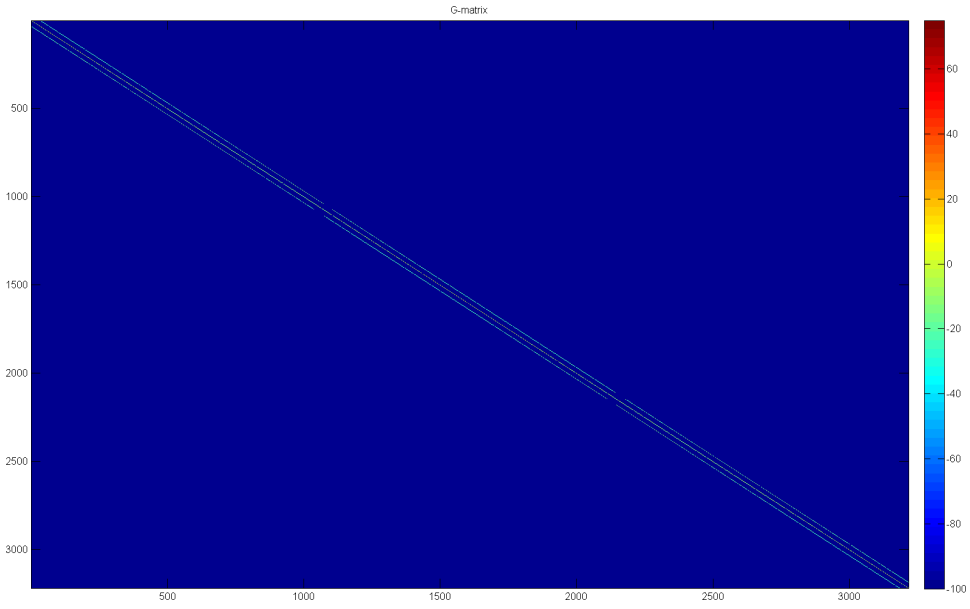

Fig. 5.5: Example spatial matrix G.

The spatial filter G is shown in Figure 5.5. This filter has taps only along the main diagonal component. This is because the spatial filter does not cross the aperture boundaries, but is applied on each individual aperture for a specified pixel. The frequency response of the filters could change upon a pixel-by-pixel bases. But the general structure would be very similar for any spatial filter G.

The spatial filters and aspect filters could be combined to produce a spatial-aspect filter that is applied to the magnitude of the reflectivity. But for simplicity, particularly for interpreting the results the two filters are kept as separate entities for this work.

This problem formulations allows us to incorporate a data fidelity term $\|Ax - b\|_2$, an aspect dependence term $\omega_f \|Fx_m\|_p$, a spatial dependence term $\omega_g \|Gx_m\|_f$, and a sparsity constraint $\omega_m \|x_m\|_q$ into the image formation problem. Solving this formulation will allow the solution to be influenced by any prior knowledge about the scene. This knowledge could be applied globally, or incorporated at a pixel-dependent level.

5.2 SOCP Formulation

This section will focus on transforming Equation (5.18) into a standard second order cone program (SOCP). A SOCP is a class of convex problems that are more general than quadratic or linear programs. A second order cone program is generically given as

$$\begin{aligned} \underset{x}{\text{minimize}} \quad & f^T x \\ \text{subject to} \quad & \|A_i x - b_i\|_2 \leq c_i^T x + d_i, \; i = 1, \ldots, m \\ & Fx = g, \end{aligned} \tag{5.19}$$

where x $\in R^n$ is the variable to be optimized over and $A_i \in R^{n_i \times n}$, and $F \in R^{p \times n}$. Constraints that have the general form of

$$\|A_i x - b\|_2 \leq c_i^T x + d, \tag{5.20}$$

are called *second-order cone constraints*. A visualization of a second order cone constraint is shown in Figure 5.6. Equality occurs when the solution resides on the cone surface.

Equation (5.20) can equivalently be given as

$$\begin{bmatrix} c^T & -1 & 0 \\ A & 0 & -I \end{bmatrix} \begin{bmatrix} x \\ t \\ s \end{bmatrix} = \begin{bmatrix} -d \\ -b \end{bmatrix}, \qquad \begin{bmatrix} t \\ s \end{bmatrix} \in K, \tag{5.21}$$

or equivalently

$$\begin{aligned} c^T - t &= -d \\ Ax - Is &= -b, \end{aligned} \tag{5.22}$$

where K is the second order cone

$$K = \left\{ \begin{bmatrix} t \\ s \end{bmatrix} \,\middle|\, \|s\|_2 \le t \right\}. \tag{5.23}$$

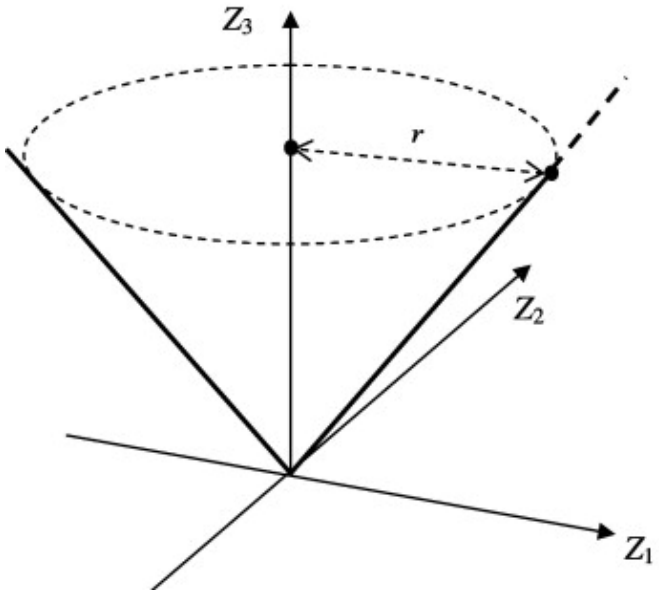

Fig. 5.6: Second order cone constraint $\sqrt{z_1^2 + z_2^2}^{1/2} \le z_3$.

This implies that the variable t defines the boundary of a second order constraint and s lives in the cone.

It is not immediately clear how the SAR image formation formulation of Equation (5.18) can become Equation (5.19) a general SOCP. The objective of the ensuing discussion is to describe the transformation required. The succeeding derivation leverages a related derivation found in Antoniou and Lu [65]. It leverages the terminology and definitions found in Boyd and Vandenberghe [17]. SOCP problem formulations have successfully been used for complex data [66].

5.2.1 Linear Program

A standard form linear program (LP) is given as

$$\begin{aligned} \underset{x}{\text{minimize}} \quad & c^T x \\ \text{subject to} \quad & Ax = b \\ & x \underset{k}{\succeq} 0, \end{aligned} \tag{5.24}$$

where the term $x \underset{k}{\succeq} 0$ is understood to be the non-negative orthant for a LP, which is a self-dual cone. The symbol "$\succeq$" or "$\preceq$" is overloaded to imply that a generalized inequality [17]. A generalized inequality constraint defines a proper cone which includes many diverse types of cone constraints. For example, the second order cone constraint given in Equation (5.20) is a proper cone and can be represented with a generalized inequality, and the component-wise non-negative constraint is a proper cone. The matrix A is $\in R^{m \times n}$. The *Lagrangian* of the LP is given as

$$L(x, \lambda, \nu) = c^T x - \sum_{i=1}^{i=n} \lambda_i x_i + \nu^T (Ax - b). \tag{5.25}$$

The Lagrangian can be thought of as augmenting the cost function with weighted sums of the constraints. It is often called a soft approximation since it penalizes solutions that are close to being feasible a lot less than solutions that are far from being feasible. It softly

approximates the ideal indicator function or "brick-wall."

The *Lagrange Dual function* of the LP given in Equation (5.25) is

$$\begin{aligned} g(\lambda,\nu) = &\quad \inf_{x\in D} L(x,\lambda,\nu) \\ L(x,\lambda,\nu) = &\quad c^T x - \sum_{i=1}^{i=n} \lambda_i x_i + \nu^T(Ax-b) \\ L(x,\lambda,\nu) = &\quad -\nu^T b + (c-\lambda+A^T\nu)^T x. \end{aligned} \tag{5.26}$$

The Lagrange dual function is defined to be the point-wise infimum of affine functions, which is intrinsically concave. The Lagrange dual function is an under-estimator, or yields a lower-bound on the optimal value for any $\lambda \succeq 0$ and ν. If the optimal value of the cost function is p^* than $g(\lambda,\nu) \leq p^*$. The solution in Equation (5.26) is only nontrivial ($g(\lambda,\nu) \neq -\infty$) when $(c-\lambda+A^T\nu)=0$, and the solution is $-\nu^T b$.

The *Lagrange dual problem* then is to find the best, or tightest estimate to the optimal value p^*. This is defined as

$$\begin{aligned} \underset{\lambda,\nu}{\text{maximize}} \quad & g(\lambda,\nu) \\ \text{subject to} \quad & \lambda \underset{k}{\succeq} 0, \end{aligned} \tag{5.27}$$

which is always a convex problem since it is maximizing a concave function with convex constraints.

This allows us to write the dual problem of Equation (5.24) as

$$\begin{aligned} \underset{\nu}{\text{maximize}} \quad & -b^T\nu \\ \text{subject to} \quad & A^T\nu - \lambda + c = 0 \\ & \lambda \underset{k}{\succeq} 0. \end{aligned} \tag{5.28}$$

This problem formulation made the equality constraint $(c-\lambda+A^T\nu)=0$, required by Equation (5.26) in order to have a nontrivial solution, explicit. It can equivalently be

written as

$$\begin{aligned} \underset{\nu}{\text{maximize}} \quad & -b^T\nu \\ \text{subject to} \quad & A^T\nu + c \underset{k}{\succeq} 0. \end{aligned} \tag{5.29}$$

The constraint has been written as a generalized inequality, but for the LP it actually represents the traditional component-wise inequality. It will become clear later why the generalized inequality representation is used.

Strong duality means the best bound of the Lagrange dual function is tight, or optimal. This means that $g(\lambda, \nu) = p^*$. Strong duality holds for convex problems under *Slater's condition*. Slater's condition implies that the convex hull is non-empty, roughly speaking [17]. This means that the dual-problem in Equation (5.28) or Equation (5.29) could be solved or equivalently the primal problem in Equation (5.24) solved. This is an important result for this effort and in general. The problem formulation might be naturally more suited for the primal or dual formulation.

5.2.2 Constrained Equivalent Problem

The general problem described in Equation (5.18) could be rewritten as

$$\begin{aligned} \underset{x.}{\text{minimize}} \quad & b_o^T x \\ \text{subject to} \quad & \|Ax_c - b\|_2 \preceq x_a \\ & \omega_f \|Fx_m\|_p \preceq x_f \\ & \omega_g \|Gx_m\|_q \preceq x_g \\ & \|S_k x_c\|_2 \preceq x_{m_k} \;\; k = 1, \ldots, n_a. \end{aligned} \tag{5.30}$$

Minimizing problem Equation (5.30) is the same as minimizing Equation (5.18) and both problems trace out the same Pareto solution surface. The new problem formulation has recast some variables. The generic variable x is now composed of additional terms where $x = [x_c \; x_m \; x_a \; x_f \; x_g]^T$.

The complex variable is now called x_c, and the magnitude of $|x_c|$ is given as x_m. The

variable x_a represents the cone variable that is associated with the data fit. The data fit variable x_a represents the fit among all K apertures as given in Equation (5.11). The variable x_a is $\in R_{1\times 1}$ since the l_2-norm is applied for the complex data fit term $\|Ax_c - b\|_2$. The variable x_f represents the cone variable that is associated with the aspect term $\omega_f\|Fx_m\|_p$. The dimension of x_f depends on the p-norm that is used.

If the norm is the l_2-norm than it also is only a single dimension, like the data fit variable x_a. If the norm is the l_1-norm it has dimension m_f, which is the number of rows in the matrix F. It is implied, when the l_1-norm is used, that each row is an independent second order cone constraint. The variable x_g relates to the spatial smoothness term $\omega_g\|Gx_m\|_q$. The same discussion regarding the q-norm leveraged applies corresponding to the dimensionality x_g will take. If the l_2-norm is used than x_g is $\in R_{1\times 1}$, otherwise if the l_1-norm is used than x_g is $\in R_{m_g\times 1}$ since it is assumed that G has m_g rows. Special care has been taken to define the variable dimensionality in order to help remove any ambiguity regarding the problem formulation that will take place later.

The matrix S_k is a selector matrix that selects the k^{th} complex components for the k^{th} cone. It is important to recognize the complex data has been aligned according to Equation (5.6) where the complex data is represented by real values. The vector e_i^T is a vector of 0's except for an appropriately placed 1 so that the product $e_k^T x_m$ yields the k^{th} element of x_m denoted as x_{m_k}. Then S_k is defined as

$$S_k = \begin{bmatrix} e_k^T & 0 \\ 0 & e_k^T \end{bmatrix}, \tag{5.31}$$

so that application of $S_k \in R_{2\times n_a}$ to the complex data $x_c \in R_{n_a\times 1}$ results in

$$S_k x_c = \begin{bmatrix} x_{c_k}^r \\ x_{c_k}^i. \end{bmatrix}, \tag{5.32}$$

where the real values $\in R_{2\times 1}$ have been selected that correspond to the complex number. The term $\|S_k x_c\|_2 \preceq x_{m_k} \quad k = 1, \ldots, n_a$ defines the n_a cones that are used to couple

the complex variable x_c and the magnitude variable x_m. The number of variables, or the dimensionality is defined by Equation (5.11).

All the cones in Equation (5.30) could be represented in a standard SOCP problem constraint given by Equation (5.19). This general formulation will be represented as $\|\tilde{A}\tilde{x} - \tilde{b}\|_2 \leq c^T\tilde{x} + d$, where the tilde is used to denote a generic variable and distinguish it from previously defined variables. The assumption is that the p-norm and the l-norm in Equation (5.30) are equal to the l_1-norm or the l_2-norm. It will be assumed, as previously mentioned, that the matrix G is $\in R_{m_g \times n_a}$ and F is $\in R_{m_f \times n_a}$ for this generic derivation.

The norm used actually changes the problem setup, or shape of $\tilde{A}$ drastically. The l_2-norm allows the aspect and spatial cone constraints in Equation (5.30) to be represented by a single second order cone constraints. For example, the aspect constraint from Equation (5.30) could be written as $\omega_f\|Fx_m\|_2 \leq x_f$ where x_f is $\in R_{1\times 1}$ or a scalar, and the spatial constraint $\omega_g\|Gx_m\|_2 \leq x_g$, where x_g is $\in R_{1\times 1}$ or a scalar.

Howerver, if the l_1-norm is used, this requires many more cone constraints. The i^{th} aspect pixel output, for the l_1-norm constraint $\omega_f\|Fx_m\|_1 \preceq x_f$ in Equation (5.30) could be written as

$$x_{f_i} \geq \omega_f\|F_i x_m\|_1 \quad \text{for all } i = 1, \ldots, m_f, \tag{5.33}$$

or equivalently for the spatial constraint in Equation (5.30) it could be written as

$$x_{g_i} \geq \omega_g\|G_i x_m\|_1 \quad \text{for all } i = 1, \ldots, m_g. \tag{5.34}$$

These constraints in Equation (5.33) and Equation (5.34) could equivalently be written as

$$\begin{aligned} -\omega_f F_i x_m \leq x_{f_i} \geq \omega_f F_i x_m \quad \text{for all } i = 1, \ldots, m_f \\ -\omega_g G_i x_m \leq x_{g_i} \geq \omega_g G_i x_m \quad \text{for all } i = 1, \ldots, m_g. \end{aligned} \tag{5.35}$$

This requires a positive and negative constraint for every pixel that incorporates a filter in aspect or spatially. This means for m_f aspect filters there will be $2m_f$ cone constraints and correspondingly for m_g spatial filters there will be $2m_g$ cone constraints. While there are

$2m_f$ aspect and $2m_g$ spatial cone constraints there are still only m_f and m_g variables that are defined correspondingly.

This can graphically be visualized, for the standard second order cone constraint, by examining Figure 5.7 and contrasting it with Figure 5.6. The absolute value $|t|$ is represented by two separate constraints, a positive and negative constraint.

The problem in Equation (5.30) can now be formulated as a generic SOCP. This problem formulation assumes the l_1-norm is used spatially and in aspect. The variable $\tilde{x}$ is defined as

$$\tilde{x} = \begin{bmatrix} x_{c_{(2n_a \times 1)}} \\ x_{m_{(n_a \times 1)}} \\ x_{a_{(1 \times 1)}} \\ x_{f_{(m_f \times 1)}} \\ x_{g_{(m_g \times 1)}} \end{bmatrix}, \tag{5.36}$$

which captures all the cone variables into a single vector $\tilde{x}$. The term x_c is $\in R^{(2n_a \times 1)}$, since it has n_a complex components, but has been defined as real valued elements given by Equation (5.8). The term $x_m \in R^{(n_a \times 1)}$ is the magnitude, which naturally has half

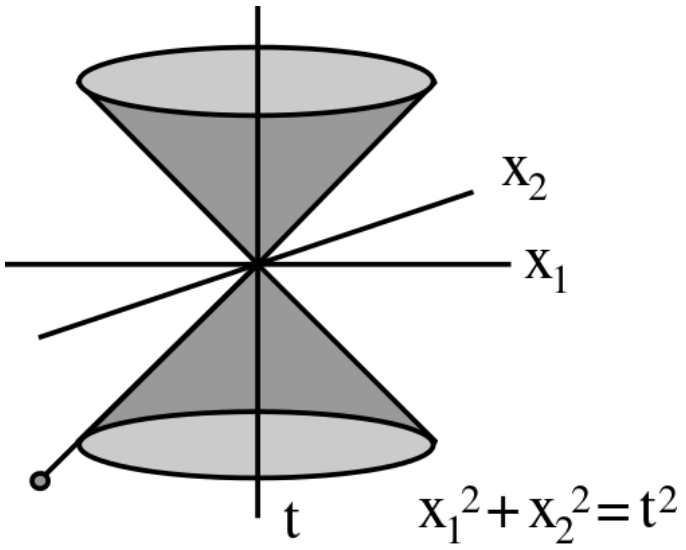

Fig. 5.7: Positive and negative second order cone constraint $\sqrt{x_1^2 + x_2^2}^{1/2} \leq |t|$.

the real components of the complex x_c. The fit term $x_a \in R^{(1\times 1)}$ since it uses an l_2-norm. Finially $x_f \in R^{(m_f \times 1)}$, and $x_g \in R^{(m_g \times 1)}$ define the number of aspect and spatial pixels that incorporate filters correspondingly assuming the l_1-norm is used for p and q. The variable x_f and x_g require two constraints, a positive and negative constraint, for all n_a pixels as discussed previously.

The variable $\tilde{b_o}$ is defined as

$$\tilde{b_o} = \begin{bmatrix} 0_{(2n_a \times 1)} \\ \omega_m \mathbf{w}_{(n_a \times 1)} \\ 1_{(1\times 1)} \\ \omega_f \mathbf{w}_{(m_f \times 1)} \\ \omega_g \mathbf{w}_{(m_g \times 1)} \end{bmatrix}, \tag{5.37}$$

which can be viewed as the global weight vector. The vector $\tilde{b_o}$ has the same corresponding dimensions as the corresponding members defined in the variable $\tilde{x}$. The vector $\mathbf{w}$ represents a generic weighting vector applied on the magnitude results and $\mathbf{w}$ is $\in R_{n_a \times 1}$. The utility of the vector $\mathbf{w}$ will be explained in more detail later, but the vectors $\mathbf{w}_{(m_f \times 1)}$ and $\mathbf{w}_{(m_g \times 1)}$ are possibly a subset of the vector $\mathbf{w}_{(n_a \times 1)}$. The aspect and spatial filters could be applied on a subset, or all of the pixels. This means that $m_f \leq m_a$ and $m_g \leq m_a$.

The matrix $\tilde{A}^T$ is given as

$$\tilde{A}^T = \begin{bmatrix} 0_{(m_f \times 2n_a)} & -F_{m_{(m_f \times n_a)}} & 0_{(m_f \times 1)} & diag(1)_{(m_f \times m_f)} & 0_{(m_f \times m_g)} \\ 0_{(m_f \times 2n_a)} & F_{m_{(m_f \times n_a)}} & 0_{(m_f \times 1)} & diag(1)_{(m_f \times m_f)} & 0_{(m_f \times m_g)} \\ 0_{(m_g \times 2n_a)} & -G_{m_{(m_g \times n_a)}} & 0_{(m_g \times 1)} & 0_{(m_g \times m_f)} & diag(1)_{(m_g \times m_g)} \\ 0_{(m_g \times 2n_a)} & G_{m_{(m_g \times n_a)}} & 0_{(m_g \times 1)} & 0_{(m_g \times m_f)} & diag(1)_{(m_g \times m_g)} \\ 0_{(1 \times 2n_a)} & 0_{(1 \times n_a)} & 1_{(1 \times 1)} & 0_{(1 \times m_f)} & 0_{(1 \times m_g)} \\ A_{(2m_a \times 2n_a)} & 0_{(2m_a \times n_a)} & 0_{(2m_a \times 1)} & 0_{(2m_a \times m_f)} & 0_{(2m_a \times m_g)} \\ S1_{(2 \times 2n_a)} & 0_{(2 \times n_a)} & 0_{(2 \times 1)} & 0_{(2 \times m_f)} & 0_{(2 \times m_g)} \\ 0_{(1 \times 2n_a)} & e1_{(1 \times n_a)} & 0_{(1 \times 1)} & 0_{(1 \times m_f)} & 0_{(1 \times m_g)} \\ S2_{(2 \times 2n_a)} & 0_{(2 \times n_a)} & 0_{(2 \times 1)} & 0_{(2 \times m_f)} & 0_{(2 \times m_g)} \\ 0_{(1 \times 2n_a)} & e2_{(1 \times n_a)} & 0_{(1 \times 1)} & 0_{(1 \times m_f)} & 0_{(1 \times m_g)} \\ \vdots & \vdots & \vdots & \vdots & \vdots \\ S{m_a}_{(2 \times 2n_a)} & 0_{(2 \times n_a)} & 0_{(2 \times 1)} & 0_{(2 \times m_f)} & 0_{(2 \times m_g)} \\ 0_{(1 \times 2n_a)} & e{m_a}_{(1 \times n_a)} & 0_{(1 \times 1)} & 0_{(1 \times m_f)} & 0_{(1 \times m_g)} \end{bmatrix}. \tag{5.38}$$

The variable $\tilde{A}^T$ has the same column dimension as the variable $\tilde{b_o}$ defined in Equation (5.37), has for a row dimension.

And the variable c will be defined as

$$c = \begin{bmatrix} 0_{(2m_f \times 1)} \\ 0_{(2m_g \times 1)} \\ 0_{(1\times 1)} \\ -b_{(2m_a \times 1)} \\ 0_{1(2\times 1)} \\ 0_{1(1\times 1)} \\ 0_{2(2\times 1)} \\ 0_{2(1\times 1)} \\ \vdots \\ 0_{m_{a}(2\times 1)} \\ 0_{m_{a}(1\times 1)} \end{bmatrix}. \tag{5.39}$$

This variable c has the same row dimension as $\tilde{A^T}$ given in Equation (5.38).

Equation (5.30) is the natural basis for this problem formulation. By grouping all the variables appropriately in $\tilde{x}$ and creating a large matrix $\tilde{A^T}$ the second order cone constraints can be leveraged to write an equivalent problem. The new variable definitions of $\tilde{b_o}$ in Equation (5.37), $\tilde{A^T}$ in Equation (5.38) and $\tilde{c}$ in Equation (5.39) are now used. The base problem in Equation (5.30) is rewritten explicitly using cone constraints as

$$\begin{aligned} \underset{\tilde{x}.}{\text{maximize}} \quad & -\tilde{b_o}^T \tilde{x} \\ \text{subject to} \quad & \tilde{c} + \tilde{A^T}\tilde{x} - \lambda = 0 \\ & \lambda \in K. \end{aligned} \tag{5.40}$$

The term $\lambda \in K$ implies that that the variable λ must reside in the cone K. This formulation is very similiar to Equation (5.28) which defines the dual problem for a standard form LP. The difference is fairly simple. Equation (5.28) uses the non-negative orthant as the cone constraint for the generalized inequality given as $\lambda \succeq 0$. The problem formulation in Equation (5.40) uses the second order cone constraint given in Equation (5.20) as the cone

constraint for the generalized inequality. The SOCP is a more generic convex optimization problem than quadratic or LP's problems. A quadratic or LP, and many other problems, can be represented as SOCPs.

The primal problem of Equation (5.40) can be written as

$$\begin{aligned} \underset{\tilde{y}.}{\text{minimize}} \quad & \tilde{c}^T \tilde{y} \\ \text{subject to} \quad & \tilde{A}\tilde{y} = \tilde{b_o} \\ & \tilde{y} \in K. \end{aligned} \tag{5.41}$$

This is very similar to the standard form LP given in Equation (5.24). There are two main differences. The first difference was previously mentioned regarding the cone definitions. A LP uses the non-negative orthant as the cone, but an SOCP uses a second order cone constraint defined in Equation (5.20) as the cone. The second difference is the primal variable definitions. The variable $\tilde{y}$ represents the primal variables for Equation (5.41) and the variable x represents the primal variables in Equation (5.24). The variable of interest for the SAR image formation problem, given in Equation (5.30), is actually the dual variables x. But the primal variable y is actually solved for in Equation (5.41).

The dual variables are often solved in conjunction with the primal variables for many modern primal-dual solvers. Otherwise, if only the primal variables are solved, then an additional step must be taken to retrieve the dual variables. The dual variables can be retrieved by solving the *Karush-Kuhn-Tucker* (KKT) conditions [17]. Most commercial solvers that solve for the primal variables will have flags that will allow retrieval of the dual variables, if desired.

If the l_2-norm is used for the p and q norms defined in Equation (5.30) then the variables $\tilde{x}$, $\tilde{c}$, $\tilde{b_o}$ and $\tilde{A^T}$ have somewhat different forms contrasted to Equation (5.36), Equation (5.39), Equation (5.37), and Equation (5.38). The new definitions are given as

$$\tilde{x} = \begin{bmatrix} x_{c_{(2n_a \times 1)}} \\ x_{m_{(n_a \times 1)}} \\ x_{a_{(1\times 1)}} \\ x_{f_{(1\times 1)}} \\ x_{g_{(1\times 1)}} \end{bmatrix}, \quad \tilde{b_o} = \begin{bmatrix} 0_{(2n_a \times 1)} \\ \omega_m \mathbf{w}_{(n_a \times 1)} \\ 1_{(1\times 1)} \\ \omega_{f_{(1\times 1)}} \\ \omega_{g_{(1\times 1)}} \end{bmatrix}; \tag{5.42}$$

$$c = \begin{bmatrix} 0_{(m_f \times 1)} \\ 0_{(m_g \times 1)} \\ 0_{(1\times 1)} \\ -b_{(2m_a \times 1)} \\ 0_{1(2\times 1)} \\ 0_{1(1\times 1)} \\ 0_{2(2\times 1)} \\ 0_{2(1\times 1)} \\ \vdots \\ 0_{m_{a}(2\times 1)} \\ 0_{m_{a}(1\times 1)} \end{bmatrix}, \quad \tilde{A}^T = \begin{bmatrix} 0_{(m_f \times 2n_a)} & F_{m_{(m_f \times n_a)}} & 0_{(m_f \times 1)} & 1_{(m_f \times 1)} & 0_{(m_f \times 1)} \\ 0_{(m_g \times 2n_a)} & G_{m_{(m_g \times n_a)}} & 0_{(m_g \times 1)} & 0_{(m_g \times 1)} & 1_{(m_g \times 1)} \\ 0_{(1\times 2n_a)} & 0_{(1\times n_a)} & 1_{(1\times 1)} & 0_{(1\times m_f)} & 0_{(1\times m_g)} \\ A_{(2m_a \times 2n_a)} & 0_{(2m_a \times n_a)} & 0_{(2m_a \times 1)} & 0_{(2m_a \times m_f)} & 0_{(2m_a \times m_g)} \\ S_{1_{(2\times 2n_a)}} & 0_{(2\times n_a)} & 0_{(2\times 1)} & 0_{(2\times m_f)} & 0_{(2\times m_g)} \\ 0_{(1\times 2n_a)} & e_{1_{(1\times n_a)}} & 0_{(1\times 1)} & 0_{(1\times m_f)} & 0_{(1\times m_g)} \\ S_{2_{(2\times 2n_a)}} & 0_{(2\times n_a)} & 0_{(2\times 1)} & 0_{(2\times m_f)} & 0_{(2\times m_g)} \\ 0_{(1\times 2n_a)} & e_{2_{(1\times n_a)}} & 0_{(1\times 1)} & 0_{(1\times m_f)} & 0_{(1\times m_g)} \\ \vdots & \vdots & \vdots & \vdots & \vdots \\ S_{m_{a}{}_{(2\times 2n_a)}} & 0_{(2\times n_a)} & 0_{(2\times 1)} & 0_{(2\times m_f)} & 0_{(2\times m_g)} \\ 0_{(1\times 2n_a)} & e_{m_{a}{}_{(1\times n_a)}} & 0_{(1\times 1)} & 0_{(1\times m_f)} & 0_{(1\times m_g)} \end{bmatrix}. \tag{5.43}$$

The main difference is a single second order cone constraint can be used instead of the $2m_f$ and $2m_g$ constraints. The l_1-norm requires a positive and negative constraint for every element in the resultant matrix-vector product Fx_m and Gx_m. The elements in the resultant matrix-vector product are given by m_f and m_g, whereas the l_2-norm requires a single constraint to represent $\|Fx_m\|_2$ and $\|Gx_m\|_2$. This reduces the dimension of $\tilde{x}$, $\tilde{b_o}$ and the column dimension of $\tilde{A^T}$ significantly for some cases.

For completeness three other problem formulations will be explicitly provided. The following problem formulations are based on Equation (5.30). Equation (5.30) incorporates sparsity, aspect, and spatial constraints, but the following formulations only incorporate a subset of those constraints. The additional problem formulation of the primal SOCP

problem is done to contrast and compare the additional capability each constraint provides and demonstrate the utility resulting from the constraint.

The first and most basic problem formulation incorporates sparsity only. This means that the spatial and aspect constraints given in Equation (5.30) are removed. The variable definitions are shown in Equation (5.44) and Equation (5.45).

$$\tilde{x} = \begin{bmatrix} x_{c_{(2n_a \times 1)}} \\ x_{m_{(n_a \times 1)}} \\ x_{a_{(1 \times 1)}} \end{bmatrix}, \quad \tilde{b_o} = \begin{bmatrix} 0_{(2n_a \times 1)} \\ \omega_m \mathbf{W}_{(n_a \times 1)} \\ 1_{(1 \times 1)} \end{bmatrix} \tag{5.44}$$

$$c = \begin{bmatrix} 0_{(1\times1)} \\ -b_{(2m_a\times1)} \\ 0_{1(2\times1)} \\ 0_{1(1\times1)} \\ 0_{2(2\times1)} \\ 0_{2(1\times1)} \\ \vdots \\ 0_{m_{a(2\times1)}} \\ 0_{m_{a_{(1\times1)}}} \end{bmatrix}, \quad \tilde{A}^T = \begin{bmatrix} 0_{(1\times2n_a)} & 0_{(1\times n_a)} & 1_{(1\times1)} \\ A_{(2m_a\times2n_a)} & 0_{(2m_a\times n_a)} & 0_{(2m_a\times1)} \\ S_{1_{(2\times2n_a)}} & 0_{(2\times n_a)} & 0_{(2\times1)} \\ 0_{(1\times2n_a)} & e_{1_{(1\times n_a)}} & 0_{(1\times1)} \\ S_{2_{(2\times2n_a)}} & 0_{(2\times n_a)} & 0_{(2\times1)} \\ 0_{(1\times2n_a)} & e_{2_{(1\times n_a)}} & 0_{(1\times1)} \\ \vdots & \vdots & \vdots \\ S_{m_{a_{(2\times2n_a)}}} & 0_{(2\times n_a)} & 0_{(2\times1)} \\ 0_{(1\times2n_a)} & e_{m_{a_{(1\times n_a)}}} & 0_{(1\times1)} \end{bmatrix}. \tag{5.45}$$

The next formulation given in Equation (5.46) and Equation (5.47) incorporates the sparsity and the spatial constraints. The variable definitions incorporating sparsity and aspect are given as

$$\tilde{x} = \begin{bmatrix} x_{c_{(2n_a \times 1)}} \\ x_{m_{(n_a \times 1)}} \\ x_{a_{(1 \times 1)}} \\ x_{g_{(m_g \times 1)}} \end{bmatrix}, \quad \tilde{b_o} = \begin{bmatrix} 0_{(2n_a \times 1)} \\ \omega_m \mathbf{W}_{(n_a \times 1)} \\ 1_{(1 \times 1)} \\ \omega_g \mathbf{W}_{(m_g \times 1)} \end{bmatrix}, \tag{5.46}$$

$$c = \begin{bmatrix} 0_{(m_g \times 1)} \\ 0_{(m_g \times 1)} \\ 0_{(1 \times 1)} \\ -b_{(2m_a \times 1)} \\ 0_{1(2 \times 1)} \\ 0_{1(1 \times 1)} \\ 0_{2(2 \times 1)} \\ 0_{2(1 \times 1)} \\ \vdots \\ 0_{m_{a(2 \times 1)}} \\ 0_{m_{a(1 \times 1)}} \end{bmatrix}, \quad \tilde{A}^T = \begin{bmatrix} 0_{(m_g \times 2n_a)} & -G_{m_{(m_g \times n_a)}} & 0_{(m_g \times 1)} & diag(1)_{(m_g \times m_g)} \\ 0_{(m_g \times 2n_a)} & G_{m_{(m_g \times n_a)}} & 0_{(m_g \times 1)} & diag(1)_{(m_g \times m_g)} \\ 0_{(1 \times 2n_a)} & 0_{(1 \times n_a)} & 1_{(1 \times 1)} & 0_{(1 \times m_g)} \\ A_{(2m_a \times 2n_a)} & 0_{(2m_a \times n_a)} & 0_{(2m_a \times 1)} & 0_{(2m_a \times m_g)} \\ S_{1_{(2 \times 2n_a)}} & 0_{(2 \times n_a)} & 0_{(2 \times 1)} & 0_{(2 \times m_g)} \\ 0_{(1 \times 2n_a)} & e_{1_{(1 \times n_a)}} & 0_{(1 \times 1)} & 0_{(1 \times m_g)} \\ S_{2_{(2 \times 2n_a)}} & 0_{(2 \times n_a)} & 0_{(2 \times 1)} & 0_{(2 \times m_g)} \\ 0_{(1 \times 2n_a)} & e_{2_{(1 \times n_a)}} & 0_{(1 \times 1)} & 0_{(1 \times m_g)} \\ \vdots & \vdots & \vdots & \vdots \\ S_{m_{a_{(2 \times 2n_a)}}} & 0_{(2 \times n_a)} & 0_{(2 \times 1)} & 0_{(2 \times m_g)} \\ 0_{(1 \times 2n_a)} & e_{m_{a_{(1 \times n_a)}}} & 0_{(1 \times 1)} & 0_{(1 \times m_g)} \end{bmatrix}. \tag{5.47}$$

This formulation is equivalent to Equation (5.30) where the l_1-norm has been used for the q norm and the aspect constraint has been removed.

The final formulation incorporates the sparsity and aspect constraints. The variable definitions are given in Equation (5.48) and Equation (5.49).

$$\tilde{x} = \begin{bmatrix} x_{c_{(2n_a \times 1)}} \\ x_{m_{(n_a \times 1)}} \\ x_{a_{(1 \times 1)}} \\ x_{f_{(m_f \times 1)}} \end{bmatrix}, \quad \tilde{b_o} = \begin{bmatrix} 0_{(2n_a \times 1)} \\ \omega_m \mathbf{w}_{(n_a \times 1)} \\ 1_{(1 \times 1)} \\ \omega_f \mathbf{w}_{(m_f \times 1)} \end{bmatrix} \tag{5.48}$$

$$c = \begin{bmatrix} 0_{(m_f \times 1)} \\ 0_{(m_g \times 1)} \\ 0_{(1\times 1)} \\ -b_{(2m_a \times 1)} \\ 0_{1(2\times 1)} \\ 0_{1(1\times 1)} \\ 0_{2(2\times 1)} \\ 0_{2(1\times 1)} \\ \vdots \\ 0_{m_{a(2\times 1)}} \\ 0_{m_{a(1\times 1)}} \end{bmatrix}, \quad \tilde{A}^T = \begin{bmatrix} 0_{(m_f \times 2n_a)} & -F_{m_{(m_f \times n_a)}} & 0_{(m_f \times 1)} & diag(1)_{(m_f \times m_f)} \\ 0_{(m_f \times 2n_a)} & F_{m_{(m_f \times n_a)}} & 0_{(m_f \times 1)} & diag(1)_{(m_f \times m_f)} \\ 0_{(1\times 2n_a)} & 0_{(1\times n_a)} & 1_{(1\times 1)} & 0_{(1\times m_f)} \\ A_{(2m_a \times 2n_a)} & 0_{(2m_a \times n_a)} & 0_{(2m_a \times 1)} & 0_{(2m_a \times m_f)} \\ S1_{(2\times 2n_a)} & 0_{(2\times n_a)} & 0_{(2\times 1)} & 0_{(2\times m_f)} \\ 0_{(1\times 2n_a)} & e1_{(1\times n_a)} & 0_{(1\times 1)} & 0_{(1\times m_f)} \\ S2_{(2\times 2n_a)} & 0_{(2\times n_a)} & 0_{(2\times 1)} & 0_{(2\times m_f)} \\ 0_{(1\times 2n_a)} & e2_{(1\times n_a)} & 0_{(1\times 1)} & 0_{(1\times m_f)} \\ \vdots & \vdots & \vdots & \vdots \\ S_{m_{a(2\times 2n_a)}} & 0_{(2\times n_a)} & 0_{(2\times 1)} & 0_{(2\times m_f)} \\ 0_{(1\times 2n_a)} & e_{m_{a(1\times n_a)}} & 0_{(1\times 1)} & 0_{(1\times m_f)} \end{bmatrix} \tag{5.49}$$

This problem is equivalent to Equation (5.30) where the l_1-norm has been used for the p norm and the spatial constraint has been removed.

5.3 Solving the SOCP

This sections proposes heuristics to solve the actual SOCP problem formulation. Unfortunately, the problem formulation becomes extremely large for 2D scene sizes of interest, and almost impractical for 3D scene sizes. A simple example will demonstrate this very succinctly. A graphical interpretation of the IPR and its effect on the data-size and model-size is given in Figure 4.6. The ROI is assumed to be a 100 pixels by 100 pixels, which is a relatively small SAR scene. The IPR size is assumed to be 17 pixels by 17 pixels. The half IPR size is 8.

The data size is 116 by 116 pixels and has 116^2 or 13,456 pixels. The model size is 132 by 132 pixels and has 132^2, or 17,424 pixels. It is assumed that there are only three distinct apertures of interest. The matrix A, as given in Equation (5.11), would have the column dimension of three times the model-pixel size of a single aperture. The row dimension

would be three times the data-pixel size of a single aperture, also. This gives a matrix that is 40,368 by 52,272. This requires 2,110,116,096 elements. The elements are complex and use double-format data types to represent. This would require around 30 Gigabytes of storage.

For perspective a simple 3D scene will be analyzed. Lets assume a smaller scene is specified with an ROI of 32 by 32 by 10 pixels for x, y, and z dimensions. The IPR is 17 by 17 by 17 pixels in x, y, and z, respectively. The data-size would be 48 by 48 by 26 and has 59,904 pixels. The model-size is than 64 by 64 by 42 and has 172,032 pixels. Again, only three apertures are assumed to be of interest. The matrix A would have the dimensions of by 179,712 by 516,096. This has 92,748,644,352 elements and would require about 1,382 Gigabytes of storage for complex double-format data types.

As can be seen the problem dimensions quickly become intractable for even relatively simple, small 2D scenes. This requires that heuristics are employed, especially for 3D that provide reasonable results and do not compromise the potential benefits that model-based processing provides.

5.3.1 Truncated IPR

Previously in Section 4.2.1, truncating the IPR was discussed. In theory, the spatial IPR is infinite, but in practice the IPR can be spatially truncated due to the noise floor contained in any SAR image due to quantization, thermal noise, positional errors, etc. Truncating the spatial IPR has several important positive ramifications. First, the IPR is sparse since a limited number of pixels significantly contribute to a selected pixel. This drastically reduces the elements that are required to be stored in memory. A sparse matrix A is shown for the forward model, as given in Equation (5.11), in Figure 5.8. There are three distinct apertures leveraged, which can be noted by the structure of the matrix.

Second, since the truncated IPR defines effectively what pixels significantly contribute to a pixel, this means large scenes can be segregated into smaller scenes. This is justifiable, and somewhat intuitive. A scene pixel in the top-left of a large scene would hardly influence a pixel in the bottom-right, per se. But there is a cascading effect that pixels have on each

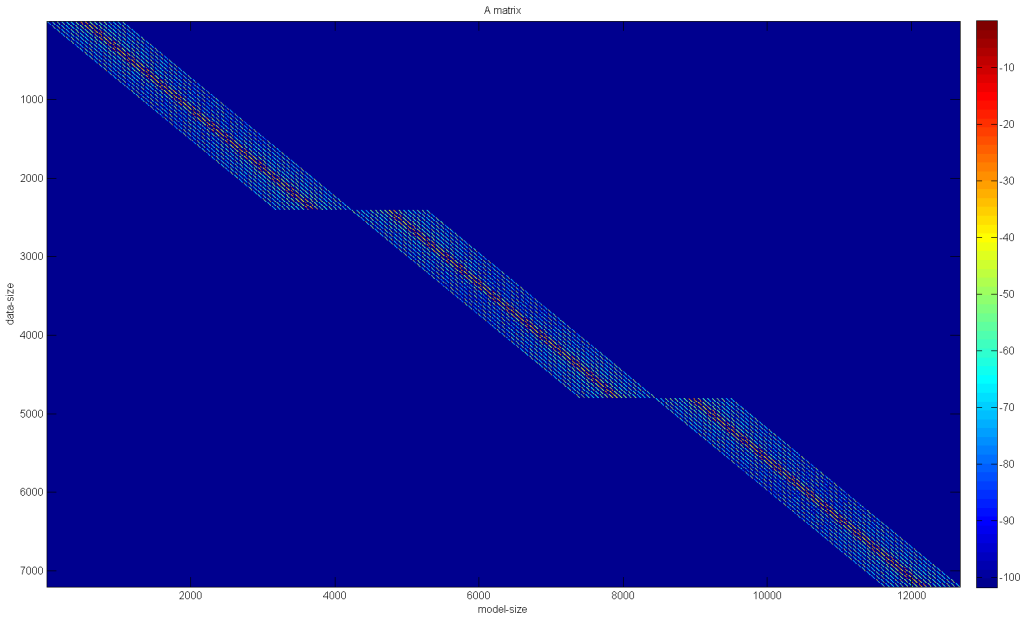

Fig. 5.8: The forward-model sparse matrix A, as in Equation (5.11) with three apertures.

other, which stems from the fact that the spatial IPR is not the ideal thumb tack response. The spatial extent a pixel is allowed to influence other pixels is limited by the truncated IPR.

Fortunately, a large ROI can be segmented into smaller ROIs and processed independently. Fundamentally, the ability to segment a large ROI into smaller ROIs has important practical ramifications. First, it allows the problem dimension to be reduced so that large scenes are tractable. This is accomplished by dividing the large problem into many smaller problems that are tractable. Second, it allows large problems to be processed in a parallel distributed manner which allows time-lines to be drastically reduced.

The IPR dimension should be considered in conjunction with the scene content, or the dynamic range of the scene reflectors, and the processing employed particularly as it relates to the ideal side-lobe levels, and fall-off in azimuth and range are very important. An example can easily illustrate this concept. A simulated scene is used with a single reflector in the center of the scene. A simplified, unrealistic scene with a single reflector centered

in the middle of the image is used to epitomize the critical considerations and is shown in Figure 5.9.

The simplified scene with a single reflector located in the middle of the center pixel is visualized in Figure 5.9(a). The truncated IPR for the center pixel is shown in Figure 5.9(b). The impulse response for the center pixel is shown for clarity as a 2D image. But the 2D impulse response for the center pixel corresponds to the appropriate column of the A matrix, as shown in Figure 5.8. The two images are than vectorized and shown side-by-side in Figure 5.9(c) for comparison purposes. The vectorized image on the left corresponds to Figure 5.9(c), or the scene. And the vectorized image from Figure 5.9(c) on the right corresponds to the truncated impulse response.

If the goal is to match the impulse response up to -50dB the truncated impulse response clearly fails. The impulse response would need to include a much larger spatial area. That is because the side-lobes do not fall off fast enough in azimuth or range. The backprojection processing employed no apodization so the first side-lobe is only about -13dB down relative to the peak in range and azimuth.

The exact same scene is reprocessed but this time a Hann window [44] is applied in range and azimuth during the backprojection processing. The results are shown in Figure 5.10. The simplified scene is shown in Figure 5.10(a). The impulse response for the center pixel is shown in Figure 5.10(b). Figure 5.10(c) shows the comparison of the ideal impulse response and the scene.

The vectorized scene shown on the left and the IPR shown on the right in Figure 5.10(c) are basically identical up to -50dB. One more similar example is shown in Figure 5.11 that visualizes the importance of having a tight model fit between the images and the IPR. The scene was processed using a Taylor window that had five approximately equal side-lobes (NBAR) at a side-lobe-level (SLL) of -35dB shown in Figure 5.11(a). But the impulse response modeling employed a Hann window in Figure 5.11(b). Figure 5.11(c) shows the comparison between the two images and the magnitude mismatch is readily apparent, not to mention the phase mismatch.

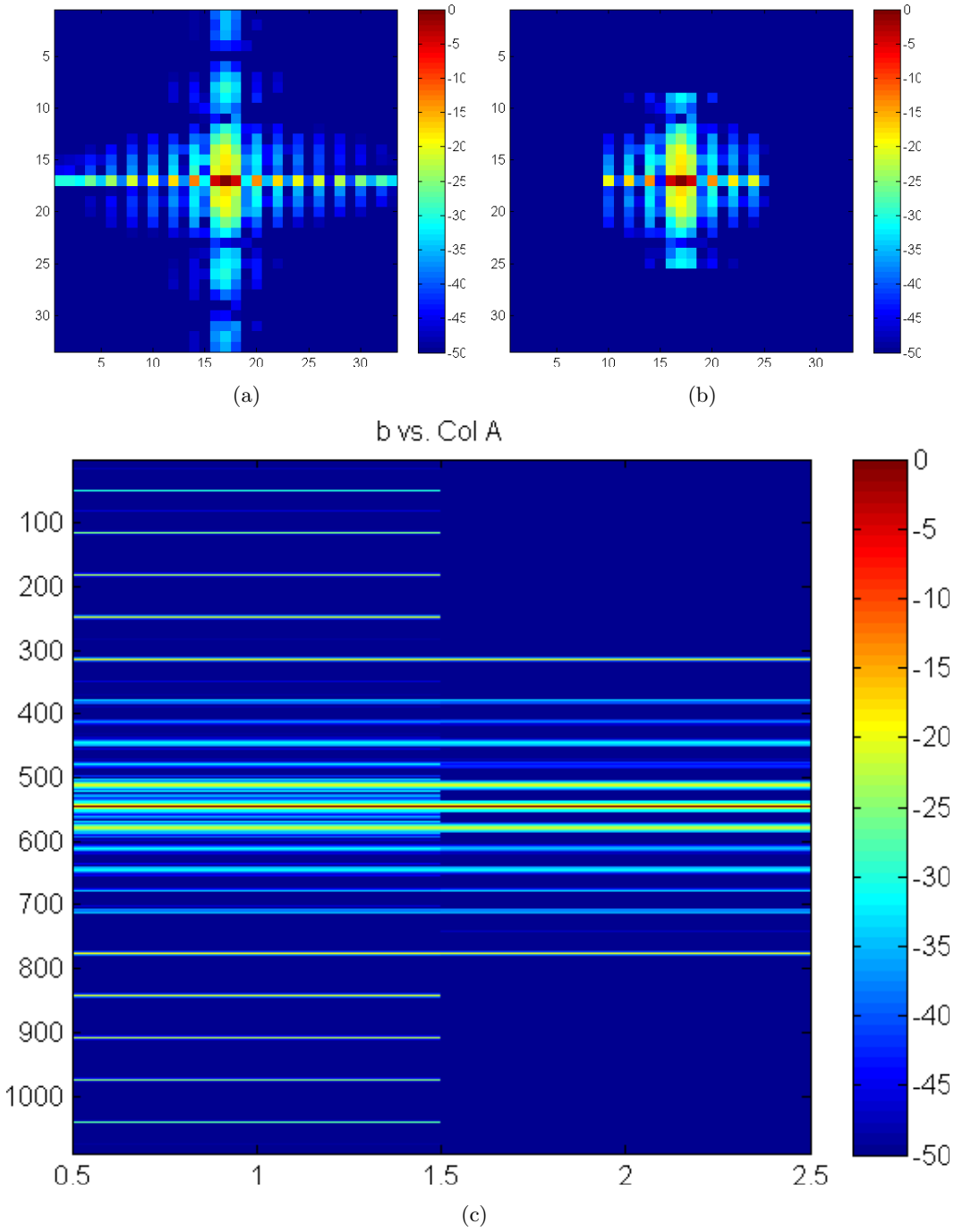

Fig. 5.9: A sparse inadequate model: (a) The scene response for a reflector located in the middle of the image processed with no windowing, (b) The truncated impulse response processed with no windowing, (c) A pixel by pixel comparison of the scene (left) and IPR (right) that fails to model adequately the spatial side-lobes.

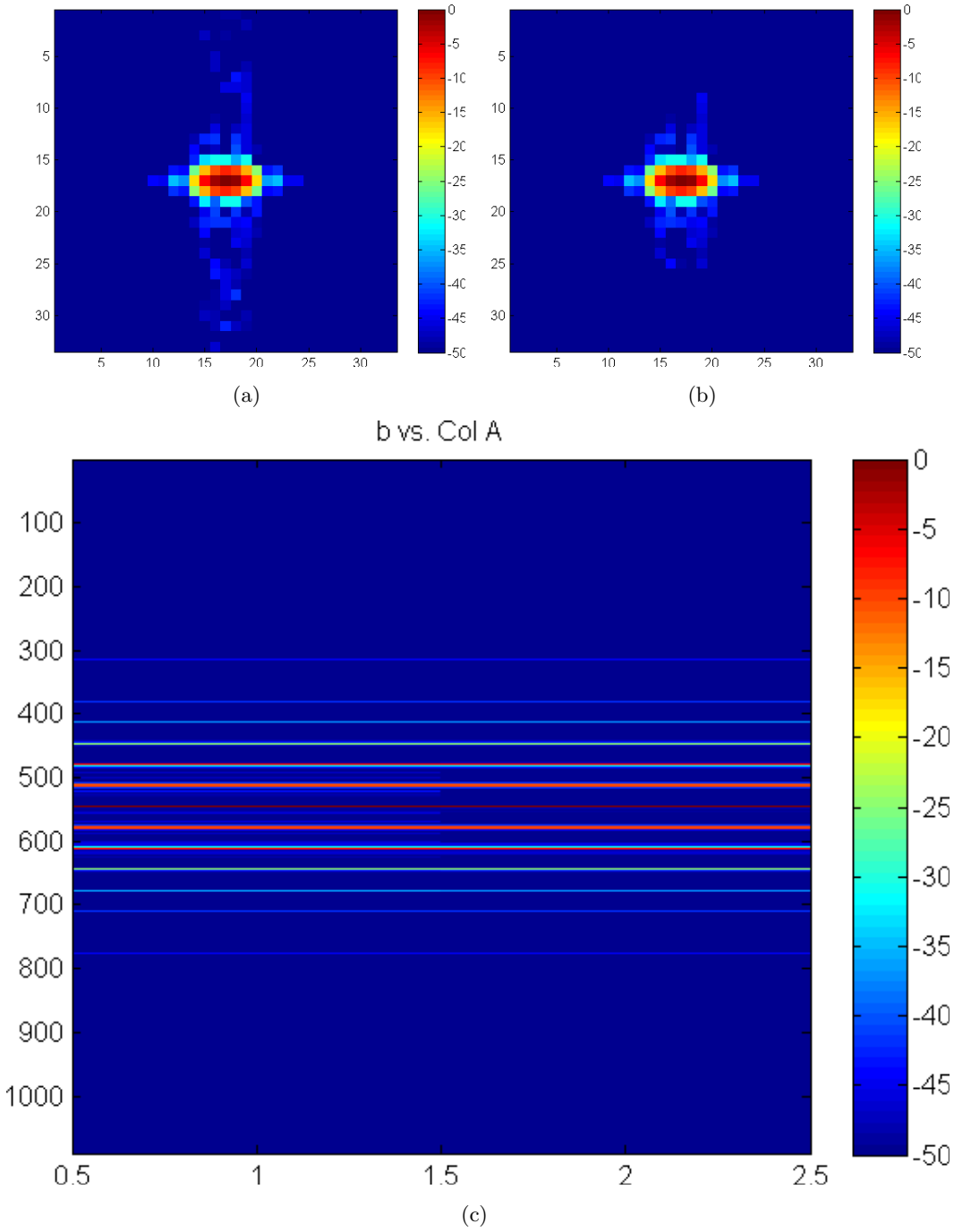

Fig. 5.10: A sparse adequate model: (a) The scene response for a reflector located in the middle of the image processed using a Hann window, (b) The truncated impulse response using a Hann window, (c) A pixel by pixel comparison of the scene (left) and IPR (right) that is almost identical.

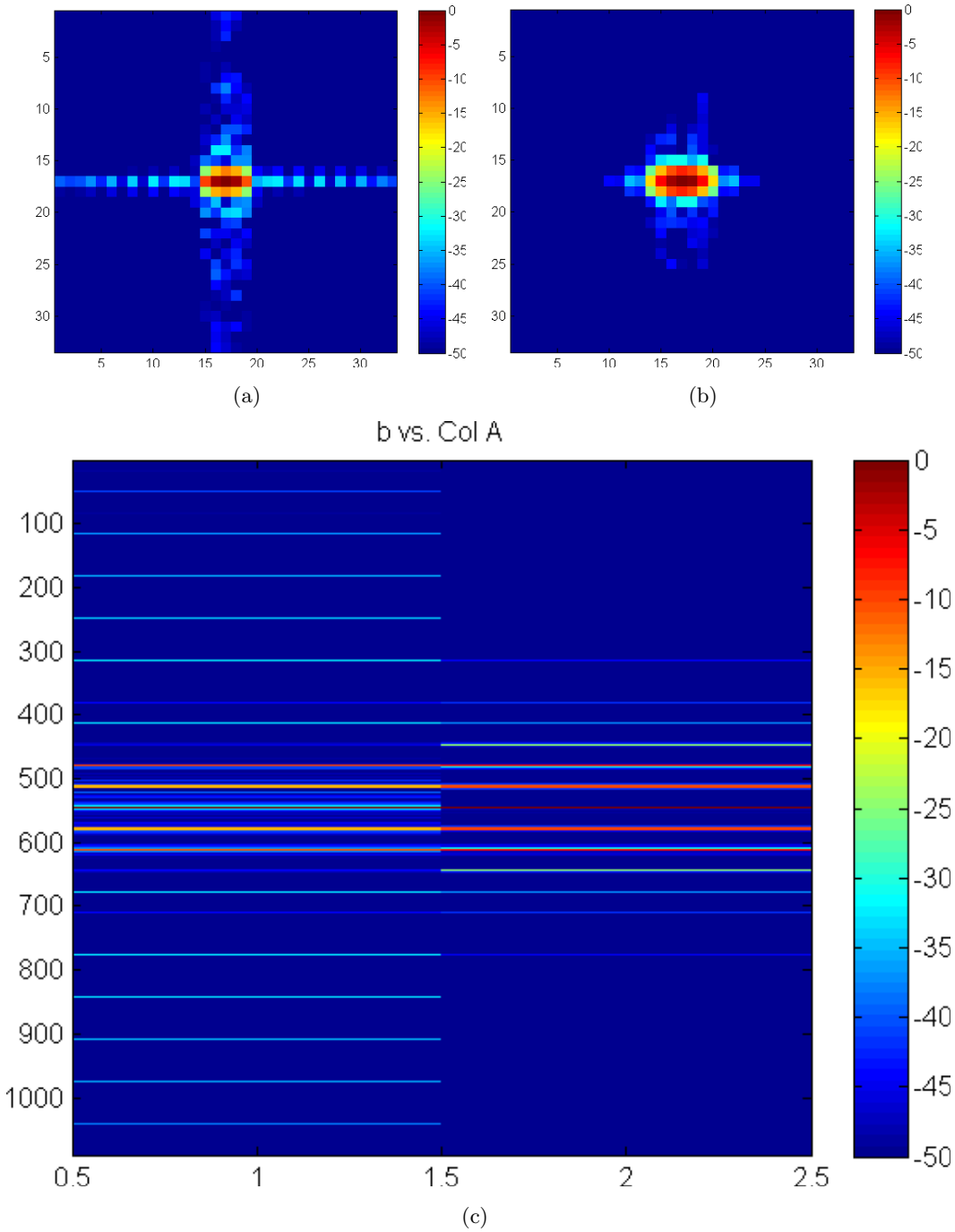

(a) (b)

(c)

Fig. 5.11: Model mismatch example: (a) The scene response for a reflector located in the middle of the image processed using a Taylor window with NBAR=5 and SLL=−35 dB, (b) The truncated impulse response using a Hann window, (c) A pixel by pixel comparison of the scene (left) and IPR (right) that has IPR mismatch.

If the scene has a large dynamic range bright targets could leave artifacts for unmodeled side-lobe levels as seen in Figure 5.9, or mismatched side-lobes as seen in Figure 5.11. Considering the scene content, the processing employed and the truncated IPR jointly is important to ensure that the appropriate approximations are used so that good results can be achieved with the model-based processing.

5.3.2 Data Masking

Another simplification that is often used is to include masks. An image mask could be used on the data, or the mask could be on the image pixels. In the generic linear algebra formulation given in Equation (5.11) the image pixels are represented by b, and the estimated pixels by x. A mask ensures that only pixels above a specified metric are preserved. A simple metric that could be applied is to examine the pixel magnitudes. Then only the pixels that surpass the metric or threshold (e.g. -40 dB) are considered legitimate or above the image noise floor and retained for model-based processing.

A mask on the term x is masking the estimated scene pixels and could be viewed as incorporating prior information into the problem to some degree. If you know that the x_i^{th} pixel represents a region that is composed of air only it can be removed with no negative effects.

The mask generated for the reflectivity term x could be generated many different ways. The choice of how a mask is generated has implications to the underlying objective, or target of interest. Two simple choices will be used mainly to mask the reflectivity x for this work, but there exists many possibilities.

The first method generates a global-mask. The global-mask is generated from all the multilook images. The resultant image has a threshold applied so that only pixels above a specified average RCS remain. A global-mask implies that the median scene content is of particular interest. An example of a global mask is seen in Figure 5.12(a) generated from the GOTCHA data for a small scene containing a vehicle.

The second mask is called a local-mask. The local-mask is generated uniquely for each individual aperture, or a small subset of apertures. The individual aperture, or the

multilook image magnitude has a threshold applied. The name implies the idea that the local reflectivity is the source of the mask. This also implies that the aspect-based RCS is the targeted objective. A local-mask is shown in Figure 5.12(b). The local-mask was generated from three multilook images. The images each contained one degree of aperture integration relative to north. The local-mask would be ideal to capture the glint information potentially for automatic target recognition applications.

It is clear that, however the mask is generated for x, it incorporates prior knowledge about the scene into the problem formulation. If no mask is used than nothing is assumed. The incorporation of prior knowledge of scene content into the image formation process is a motivating effort of this work, but masking is not a very sophisticated approach and actually is critical for another reason. The ability to mask the scene allows the problem dimensions to be reduced, which is critical for 3D scenes. This allows common computers, at the time of this writing, to tackle such problems in a reasonable time-line. If the objective is to estimate the reflectivity of a particular vehicle, as seen in Figure 5.12(a), restricting the pixels provides significant savings.

It is worth noting the important discussion regarding the problem dimensionality in Section 4.2.1. The IPR size, and the ROI define the data-size and model-size. The mask can also be used to restrict the pixels to estimate those pixels that are only contained in the ROI. This helps reduce the problem dimensionality drastically for 3D scenes, but can potentially introduce edge effects due to the model not being able to explain adequately the data used.

It is important to recognize that a mask on the input data, or b term, is not the same as a mask on x. Masking a pixel in b removes that pixel from the data. Assuming a generic formulation of $b = Ax$ seen in Equation (5.11) the removal of the b_i^{th} element means a row has been removed. This means an equation in the linear algebra formulation $Ax = b$ has been removed. If the equation is redundant, which is often the case particularly for 3D scenes, there is no real loss. Otherwise an extra degree of freedom is afforded the solution which in reality does not exist. This will degrade the solution in general.

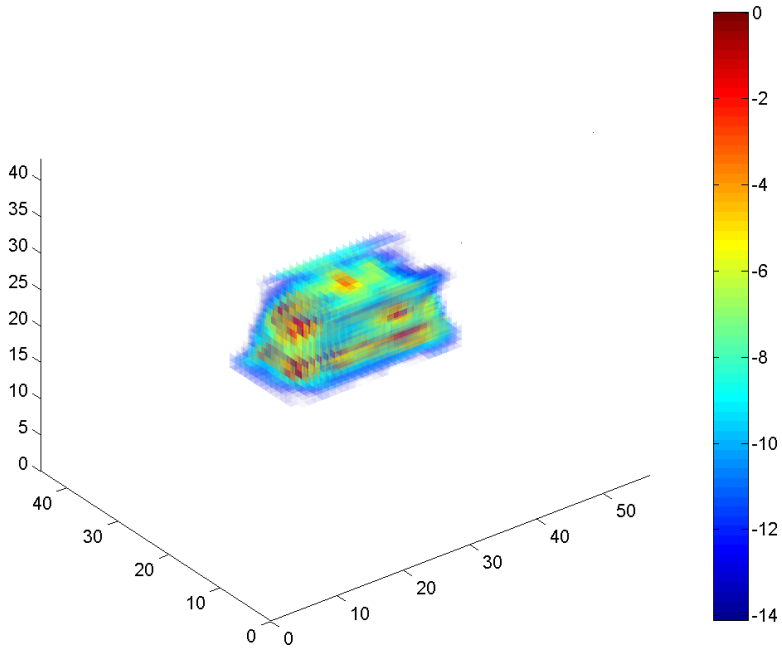

(a)

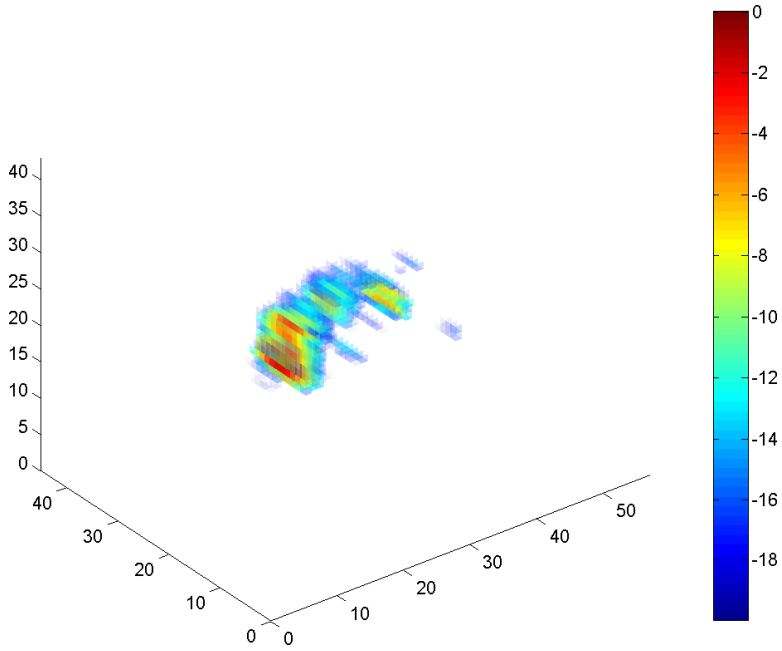

(b)

Fig. 5.12: An example of global and local masks: (a) A global mask, (b) A local mask.

The masking of the data b will not be extensively analyzed for the simple fact that most modern solvers have a preprocessing step that removes redundancy from the problem formulation. This step takes some time, but the time required is negligible in comparison

to the total processing time.

Masks provide a simple way to reduce the problem dimensionality and incorporate prior knowledge into the problem. The examples and results shown later will detail the masks incorporated, but this background discussion provides the logic behind their use.

5.4 Summary of SOCP Formulation

In summary, this chapter provides a high-level background that allows the SAR image formation problem to be formulated as a convex optimization problem. The SAR image formation cost function that incorporates sparsity, aspect and spatial constraints is developed in Section 5.1.

The details of converting the SAR image formation cost function, given in Equation (5.18), to an SOCP is provided in Section 5.2. The LP primal and dual derivation is provided since the LP derivation can be extended by using the generalized inequalities in place of the component wise inequality. The component wise or non-negative orthant cone constraint used with an LP are replaced with second order cone constraints for a SOCP.

The detailed matrix configurations are provided in Section 5.2.2 for different SAR image formation problems. The different problem formulations incorporate different constraints and utilize different norm-penalty functions. These different formulation allow for contrasting and comparing the results to demonstrate the utility each provides.

Section 5.3 discusses important practical considerations regarding solving the SOCP. The ideas discussed help formulate the SAR image formation problem, particularly for 3D, so that it is tractable or requires less resources. The two main ideas discussed are the effects of truncating the IPR in Section 5.3.1, and incorporating masks in Section 5.3.2 into the image formation problem.

Chapter 6

Algorithm

The objective of this chapter is to present all the details of the SAR image processing algorithm. This includes all the steps between receiving raw SAR sensor data to producing a model-based product. Many of these steps have been mentioned previously, but this chapter will present them in an unabridged manner. The unexpurgated presentation will help clarify any complicated details that could be glossed over. Often a statement can appear trivial, but the actual implementation can require an exorbitant amount of effort to accomplish. This chapter will detail all the processing steps to ensure comprehensive fluid understanding.

The previous chapter's definitions, background, and framework will be used as the theoretical building blocks upon which this chapter is based, but this chapter focuses on the functional steps, not the theory behind why a particular approach is chosen. Those theoretical considerations and justifications have been discussed previously and will be referenced as appropriate.

This chapter will use a synthesized example to highlight the processing steps. All the processing steps will be detailed individually. A synthetic data set is used so that particular concepts can be concisely illustrated. Synthetic data can easily be regenerated with simplified point-targets to illustrate critical ideas so that the fundamental concept can be understood.

6.1 Algorithm Overivew

The model-based processing algorithm is outlined in Algorithm 6.1. This figure defines the required steps that are required to generate the results displayed later in this chapter. The following steps will be briefly discussed and referenced to the appropriate chapters and

sections where the particular details can be found.

It is worth noting that the traditional backprojection algorithm has basically the same inputs and outputs as the model-based approach described in Algorithm 6.1, but only steps 1-3 are relevant for backprojection processing in Algorithm 6.1. In practice, the backprojection algorithm is often avoided due to its computational complexity. Unfortunately, the backprojection processing, steps 1-3, are a trivial part of the overall algorithm complexity.

Algorithm 6.1 Model-Based KAIF Processing.

Input:

GPS/IMU measurements (Ψ)
SAR sensor measurements (y)
Hardware model (antenna, waveforms, etc.) (Γ)
Target aprior knowledge (Φ)

Output:

Estimated scene x

Step 1:

Define the target or scene ROI, IPR, and resolution.

Step 2:

Reduce the SAR sensor measurements to the ROI.

Step 3:

Apply backprojection SAR image formation to the SAR sensor measurements.

Step 4:

Generate the scene masks based on prior knowledge or the backprojected image.

Step 5:

Generate the aspect and spatial RCS filters based on the target.

Step 6:

Generate the SIPR matrix leveraging the SAR hardware model and GPS measurements.

Step 8:

Formulate the primal problem.

Step 9:

Solve the primal problem and retrieve the dual variable results.

The results can then be displayed and interpreted. Often the results depend on the parameter selection or weighting. The choice of the weighting will not be addressed in the dissertation, but suffice it to say this is a nontrivial issue. Often it takes many trial runs to converge on the appropriate parameters, or weighting to produce the ideal results. This is often "OK" in a research environment since the processing can be "massaged"

until the desired results are achieved, but this causes severe practical ramifications for any time-critical applications.

Several things can be done to mitigate the effects by normalizing the data and the matrices involved, but this still leaves a lot to be desired. Several papers have attempted to address this area of concern [67, 68]. It is assumed as regularization becomes more widespread this will be an area of increased interest, particularly for the diverse data and scenes encountered with SAR sensors.

6.2 Simulation Setup

The data used was generated with the parameters found in Table 6.1. A single transmit channel was employed that used an LFM waveform. The geometry was a linear flight which can be seen in Figure 6.1. The Google Earth 3D view helps provide a geometrical overview of the collection geometry employed for the simulation. The flight line is shown in pink in Figure 6.1 and five independent aperture images will be generated from the data collection. The images extend from -2 degrees to +3 degrees relative to broadside, defined by the flight path. This particular strip-map configuration has the antenna mainlobe aligned with the broadside, which is perpenedicular to the aircraft flight path.

The scene is composed of clutter that was generated with 20 discrete points per square with a mean RCS of 0.1 m^2. There are five other discrete static points, each with an RCS of 10.0 m^2. One of the points is in the center of the image and the other four surround the center pixels. The simulated data will be referred to as SAR measurements. This will help avoid confusion later when discussing simulating the IPR, but it is understood that the SAR measurements or data used for this example is simulated and has been generated as described in Chapter 3.

6.3 Processing Steps

The processing starts with the raw range measurements collect by the SAR instrument generally, but for this case it starts with the SAR measurements generated by the SAR simulator. Model-based processing requires more input than just the SAR raw data

Table 6.1: Simulation parameters.

Parameter	**Value**
Center Frequency (f_o)	10.0 GHz
LFM Bandwidth	95.0 MHz
A/D Sample Rate (F_s)	100.0 MHz
Range Gate Delay	14.0 μs
Pulse Repetition Frequency (PRF)	600
Pulse Length (T_p)	1.0 μs
Transmit Azimuth 3dB beamwidth	10 °
Transmit Elevation 3dB beamwidth	40 °
Receive Azimuth 3dB beamwidth	10 °
Receive Elevation 3dB beamwidth	40 °
Receive Antenna pattern	Sinc
Transmit Antenna pattern	Sinc
Height Above Ellipsoid	2800 m
Linear Flight direction	East
Target lat/lon	40.85° / -113.16°
Aircraft velocity	50 m/s
Aircraft propogation	Counter clockwise
Linear integration	-2° to 5°
Clutter points	20 pts. m^2
Mean clutter	0.1 m^2

measurements. The processing, in effect, requires the ability to "simulate" the sensor that produced the data. The waveforms used, the sampling patterns employed, and hardware characteristics are known and modeled. This is the ideal situation for model-based processing.

This is often the case for traditional image formation algorithms like backprojection when high-fidelity imagery is desired. Incorporating all the parameters into the model allows for tight models which provide better results, but as will be seen later with actual SAR data, where many of these parameters are not known or available, good results can still be achieved by making commonly used assumptions.

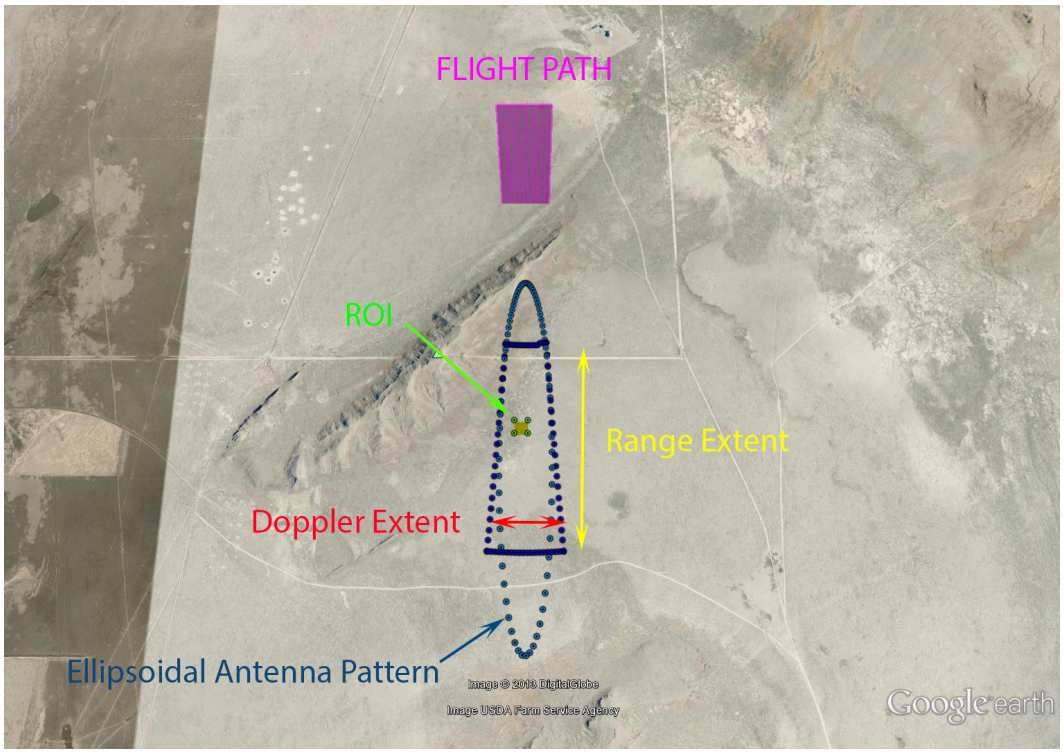

Fig. 6.1: Geometry for simulation.

6.3.1 Target and IPR Selection

After the raw sensor measurements have been acquired, the first step outlined in Algorithm 6.1 is to decide on a target's ROI and IPR. The spatial dimensions and the resolution need to be specified. The resolution naturally has a dependencies on the SAR system resolution as discussed in Section 2.4 and in Section 2.6. The other critical aspect is selecting the extent spatially of the truncated IPR as discussed in Section 5.3.1.

For this demonstration a small ROI will be analyzed that is 85 meters square. The ROI can be seen in Figure 6.1 as the small green colored square that is roughly in the center of beam. The pixel resolution is selected to be 1 m^2 since this matches approximately the transmitted waveform resolution. The IPR is truncated to include 8 pixels surrounding the center pixel. This gives a 2D IPR which is 17 pixels square. A Hann window was employed in the backprojection processing. The reduced side-lobes provided ensure the spatially truncated window is very accurate, at the cost of resolution.

Once the ROI, and the truncated IPR are defined this in turn defines the data-size,

and the model-size dimensions. This is discussed in Section 4.2.1. For this example the data-size is 101 pixels square, and the model-size is 117 pixels square. The dimensions are capture in Table 6.2.

6.3.2 SAR Measurement Reduction

The second step defined in Algorithm 6.1 is to reduce the raw sensor measurements. The raw sensor measurements can be reduced in azimuth and range so that only the data corresponding to the ROI is kept. The full data extent is visualized in Figure 6.1 with the Doppler and range extents labeled. The data extent is much larger than the ROI.

This is a critical step to reduce the problem dimensionality, by reducing the SAR measurements so that the data only corresponds to the ROI is retained. The data reduction can be accomplished by digital spotlighting, or any similar approach. This is discussed in Section 4.1 in more detail. The data reduction, in effect, band-pass filters the data in Doppler and range. The band-pass filter is centered so the frequency content that is preserved spatially corresponds to the ROI. The data reduction filtering is visualized in Figure 4.3. This step drastically reduces time-lines and resource requirements for subsequent processing steps.

6.3.3 Standard Image Formation

The third step defined in Algorithm 6.1 is to do standard image formation processing on the reduced SAR measurements or data. Backprojection processing was the processing algorithm employed for generation of the imagery, denoted by b in vector form. The back-

Table 6.2: Simulation dimensions.

Parameter	**Value**
ROI	85 x 85 meters
IPR	17 x 17 meters
Data-size	101 x 101 meters
Model-size	117 x 117 meters
Resolution	1 x 1 meter

projected images are shown as magnitude images for the five apertures in Figure 6.2. The final image shown in Figure 6.2(f) is the multilook image.

The multilook images are generated by averaging the magnitude of the 5 aperture images. Each pixel is composed of one degree of coherent integration for the specified antenna integration limits. The scene reflectivity for a single aperture is assumed to be adequately approximated as isotropic over the limited aperture. This is always assumed for traditional image formation and is discussed in more detail in Section 4.3.2. The five discrete points can be seen in Figure 6.2(f).

The background clutter exhibits the aspect dependent reflectivity seen in practice. This can be noted by inspecting the individual aperture images and noting the changing reflectivity for the background clutter. The multilook image in Figure 6.2(f) demonstrates the "smoothing" that occurs from the multilook processing. The multilook processing averages the reflectivity responses reducing the speckle variance. Once the speckle variance is reduced the persistent discrete clutter points become obvious upon inspection. In the individual aperture images the discrete clutter points are difficult to locate at best.

6.3.4 Mask Selection

Once the scene has been selected, the fourth step is to select the mask. The mask used for this example is generated using a very simple approach. Any pixel in the multilook image, seen in Figure 6.2(f) that does not exceed -30dB threshold relative to the brightest pixel is masked off, or set to zero. The results of using this mask are shown in Figure 6.3. Since this result does not have a single pixel that falls below the -30dB threshold, every pixel is enabled.

The considerations of selecting a mask are discussed in Section 5.3.2. The mask can represent any prior knowledge regarding the scene reflectivity or target. Also the mask can help reduce the problem dimensionality. This can be done by masking, or removing, pixels that are known to have zero reflectivity. This is the case for pixels below the ground or elevated too high for a known scene.

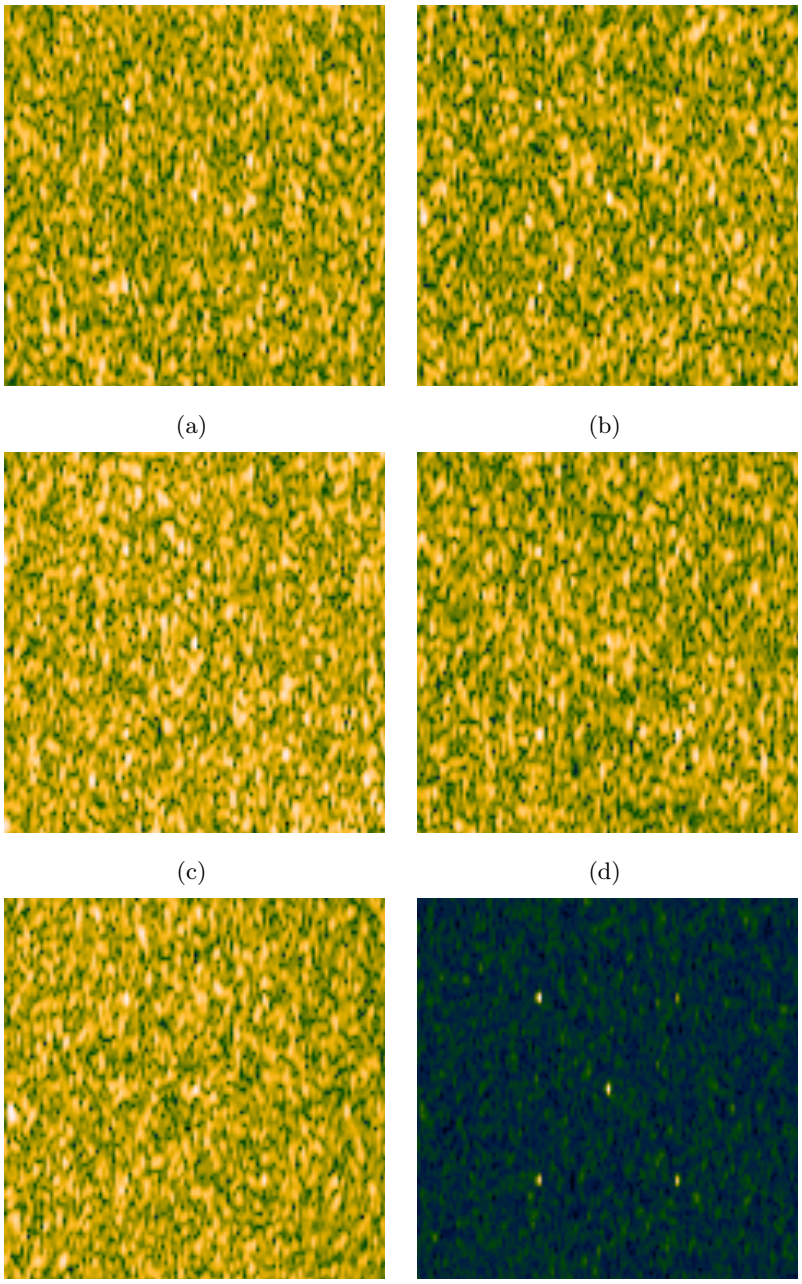

(a) (b) (c) (d) (e) (f)

Fig. 6.2: Simulated backprojected results: (a) Backprojected 1° degree aperture (-2.0° to -1.0° relative to boresight), (b) Backprojected 1° degree aperture (-1.0° to 0.0° relative to boresight), (c) Backprojected 1° degree aperture (0.0° to 1.0° relative to boresight), (d) Backprojected 1° degree aperture (1.0° to 2.0° relative to boresight), (e) Backprojected 1° degree aperture (2.0° to 3.0° relative to boresight), (f) Multilooked image from all five apertures.

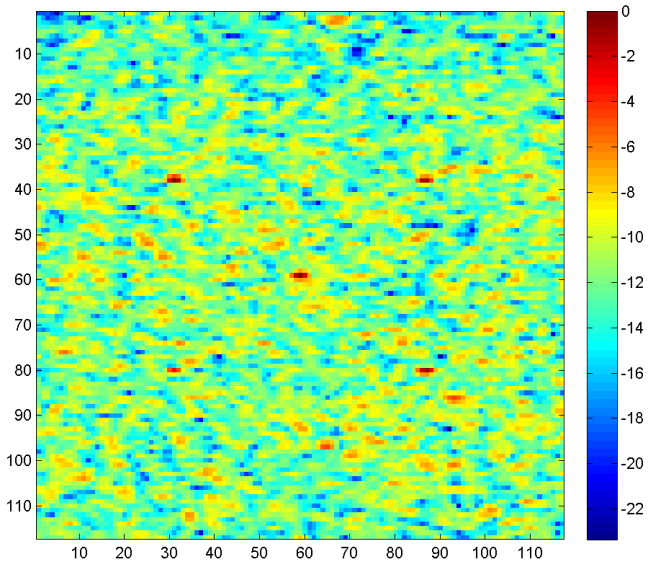

Fig. 6.3: The global mask utilized.

6.3.5 Aspect and Spatial Filter Selection

The fifth step is to select the spatial and aspect filter that will be used in the image formation processing. The optimal filter depends upon the desired objective. The justifications for incorporating an aspect and spatial filter are discussed in Section 4.3.1 and Section 4.3.2.

The aspect and spatial filter is incorporated into the optimization problem so that a plethora of responses could be targeted. The details of incorporating the aspect and spatial constraint into the optimization problem are given in Section 5.1.3 and Section 5.1.4.

For this example the results are obtained by using a very common 3x3 Laplacian spatial filter which is shown in Figure 4.8, and the default aspect filter employed is the forward-backward difference operator shown in Figure 5.3.

6.3.6 SIPR Matrix Generation

The sixth step is a very intensive processing step. This requires generating the SIPR matrix A as discussed in Section 4.2.1. The generation of the SIPR matrix requires modeling

the truncated impulse response for every pixel in the model-size image. This requires that each pixel is modeled as a single ideal-isotropic reflector that is located at the center of the pixel. The response of the reflector is synthesized for the collection. The simulated response from the pixel is, in effect, processed into an image where the size of the image is defined by the truncated IPR, which in this case it is 17x17.

The image formation processing employed on the synthesized pixel response is identical to the processing employed on the data generated by the SAR sensor. If windows where applied in the backprojected processing they need to be applied in the model synthesis. This is done for every pixel in the model size and collected in the SIPR matrix. The importance of this is discussed in Section 5.3.1 and illustrated in Figure 5.11.

This process is graphically illustrated in Figure 6.4. The image generated from the SAR sensor data is shown in Figure 6.4(a). The data in Figure 6.4(a) is simulated for this demonstrative example, as previously mentioned. The center pixel is selected to illustrate the spatial impulse response. The center pixel's impulse response is visually shown in Figure 6.4(b). This is accomplished by selecting the column of A which corresponds to the center pixel and reformatting the column vector as a 2D image for visualization.

To generate the center pixel IPR image shown in Figure 6.4(b) an identical flight that employed the same hardware, antennas, sampling, etc., was synthesized for this particular pixel. The synthesized pixel response is generated by modeling the selected pixel as an ideal-isotropic reflector and generating the appropriate simulated reflected signal for every pulse that was aggregated or used in the image formation of Figure 6.4(a).

Once all the synthesized reflected responses or pulses for the particular pixel are accumulated, the pulses are processed into an image. The image formation processing chain is identical to the image formation processing that occurred on the SAR measurements or data. This generates the ideal IPR for that pixel as illustrated in Figure 6.4(b). This response is vectorized and stored as a column of the SIPR matrix shown in Figure 6.4(c).

The center pixel is one of the 13689 pixels, in a 117x117 model-size image. Each pixel requires generating an impulse response. Figure 6.4(c) shows the SIPR matrix where each

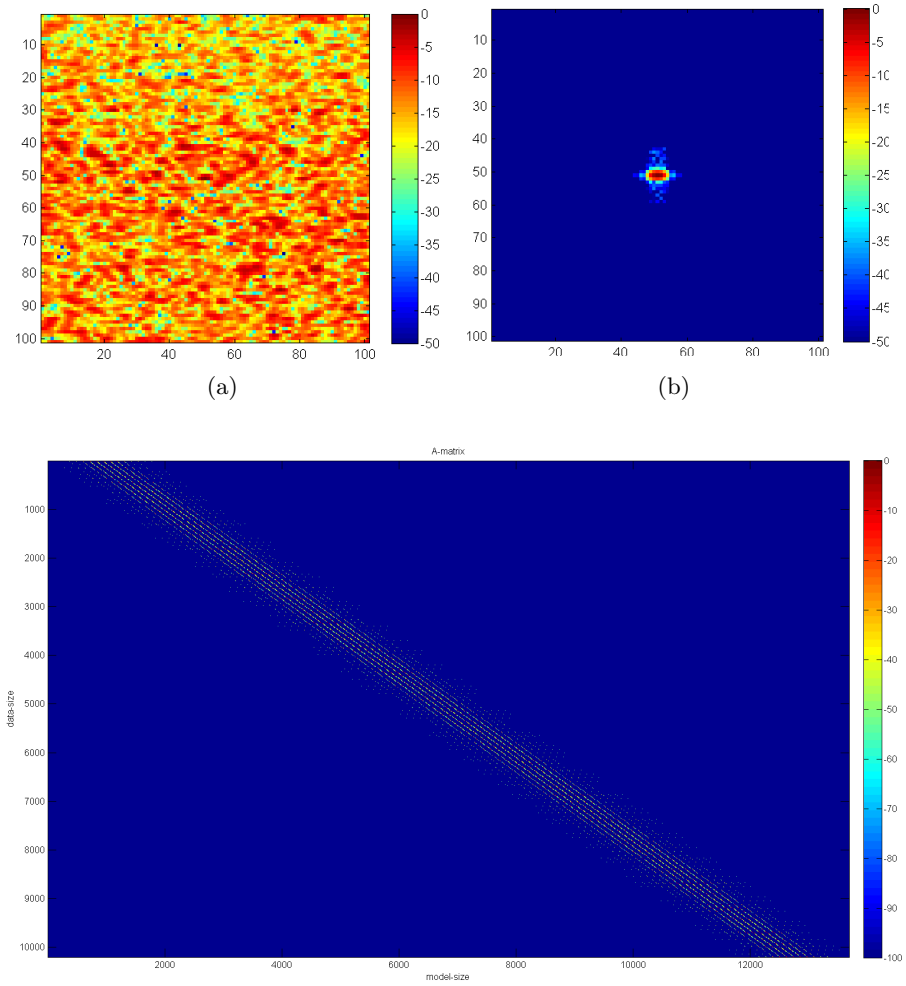

Fig. 6.4: Example visualization of the matrix A and vector b used in the problem formulation $Ax = b$: (a) Backprojected 1° degree aperture from 0.0° to 1.0° relative to boresight, this image vectorized represents the vector b; (b) Backprojected 1° degree IPR for center pixel, this image corresponds to a column of the matrix A and is shown as a 2D image for visualization purposes; (c) The full matrix A is composed of 117x117 simulated impulses.

column contains the corresponding truncated impulse response for one of the 13689 pixels. Fortunately, the impulse responses are very small spatially. The nature of the processing is ideal for parallel (CPUs and, or GPUs) and distributed processing (across computers).

The SIPR matrix leverages sparse data representation which reduces the memory utilization so that resources are not exorbitant. The reduction of the raw sensor data, and incorporation of a mask helps to reduce the processing load significantly in many cases.

6.3.7 Convex Solvers

Now that the SIPR matrix has been generated the problem can be posed as a SOCP and solved. This corresponds to steps nine and ten in Algorithm 6.1. Several convex solvers were explored by the author. Three solvers that are of particular interest will be mentioned. First, a very good introductory solver is CVX [69]. This originally used Sedumi, a semi-definite solver [70]. CVX focused on disciplined convex programing and is an excellent tool for introductory purposes. CVX has added additional support for many different commercial solvers.

Two of the most respected commercial solvers currently are Gurobi and Mosek [71,72]. Both commercial companies offer free student licenses. The other of this work tried both solvers and found them to be of similar quality regarding performance. The Mosek software was selected as the base solver. The Mosek software employed a primal-dual solver, whereas the Gurboi software employed a primal solver requiring the KKT conditions to be solved as a post step to retrieve the dual variables of interest.

Once the optimization software completes it processing the results are ready to examine and exploit. Unfortunately, As previously mentioned regularization often requires trial and error to converge on the weighting terms that provide optimal results.

6.4 Processing Results

This section displays the results of different processing configurations. The hope is that the benefits of each constraint and the effect they have on the solution can be visually analyzed and interpreted. The different problems posed in Section 5.2.2 are examined individually. The most basic form will be analyzed initially, followed by augmenting the optimization problem with additional constraints. This approach will help illustrate the benefit each constraint provides and to demonstrate the effect the constraint has on the solution.

All subsequent solutions assume the data-fit weighting term has been normalized to one, or the data-fit term has no weighting. This means all the other terms can be interpreted relative to the normalized reference weight of one given to the data-fit. The terms ω_m,

ω_g, and ω_f are the weighting values for the magnitude, spatial, and aspect terms in the optimization problem. The weighting terms applied for each optimization problem will be explicitly stated.

6.4.1 Sparsity Constraint Results

The base problem only considers the data-fit and sparsity constraint and is given in Equation (5.44) and Equation (5.45). The sparsity term can be viewed as a regularization term and the justification and advantages of a regularization term are described in detail in Section 4.3.1 and Section 5.1.2. In summary, regularization, or a sparsity constraint, is very useful for underdetermined systems.

The multilook results are shown in Figure 6.5. The weighting term used in the processing of Figure 6.5 is $\omega_m = 0.00100$. The original multilook image is shown in Figure 6.5(a) as a reference. The forward model image is given by $\hat{b} = Ax$ and is shown in Figure 6.5(b). The estimated reflectivity, given by x, is shown in Figure 6.5(c). The sparse nature is very apparent but the results are less than desirable for this particular scene. The multilook residual image resulting from $b - \hat{b}$ is shown in Figure 6.5(d).

The residual displayed in Figure 6.5(d) would correspond to the noise floor. The estimated image is then the signal component above the noise floor. This implies that the noise floor is approximately -30dB down for this particular image. The estimated image in Figure 6.5(c) in many respects looks very poor compared to the original image in Figure 6.5(a). Examination of the individual apertures are shown in Figure 6.6. All the plots use the same corresponding scale as displayed in Figure 6.5, but are not duplicated in Figure 6.6 to conserve space.

Figure 6.6(a) shows the individual aperture backprojected images. The forward-model images given by $\hat{b} = Ax$ seen in Figure 6.6(b) are almost identical upon first inspection to the reference images. The estimated aperture images seen in Figure 6.6(c) are difficult to interpret, at best. Some of the bright point-targets do appear to have been super-resolved, but that is about the only positive. The speckle variance is increased by the fact that some pixels are set to zero. The residual confirms the fact that the forward model estimated

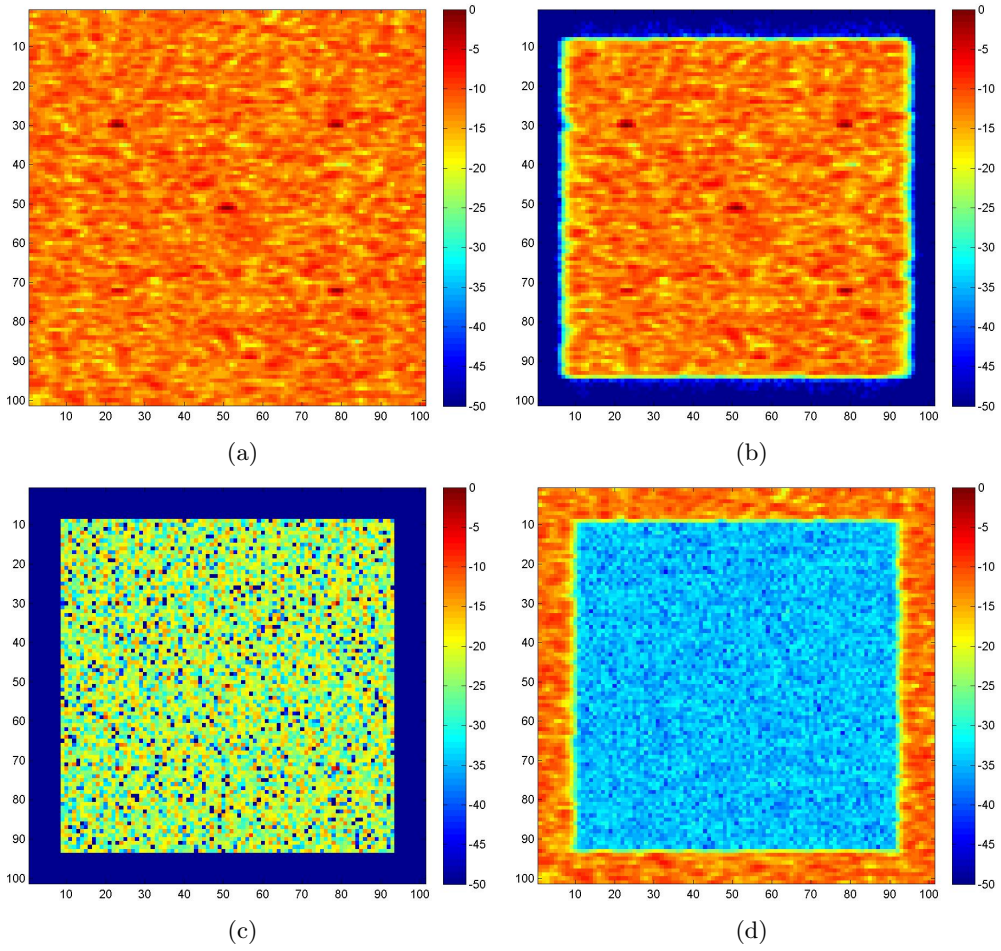

Fig. 6.5: Multilook results that employed a sparsity constraint weighted at $\omega_m = 0.00100$: (a) The default image b, (b) The estimated image $\hat{b} = Ax$, (c) The estimated x, (d) The residual image $b - \hat{b}$.

images are almost identical to the reference images up to about -30 to -35 dB.

The results displayed in Figure 6.5 and Figure 6.6 provide a high fidelity fit of the forward model images with the original images, but the estimated imagery is obviously unrealistic. The simulated scene populates every pixel with reflectors. But the estimated RCS has many pixels that have zero values. This type of behavior is expected for an underdetermined system with a sparsity constraint. There are many solutions that can fit the data, or images in this case. The sparsity constraint encourages finding the sparsest solution available.

If the weighting paramter ω_m is changed the results change in a predictable manner.

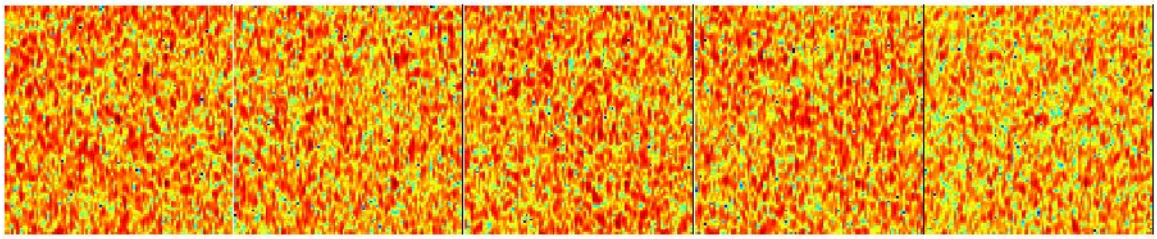

(a)

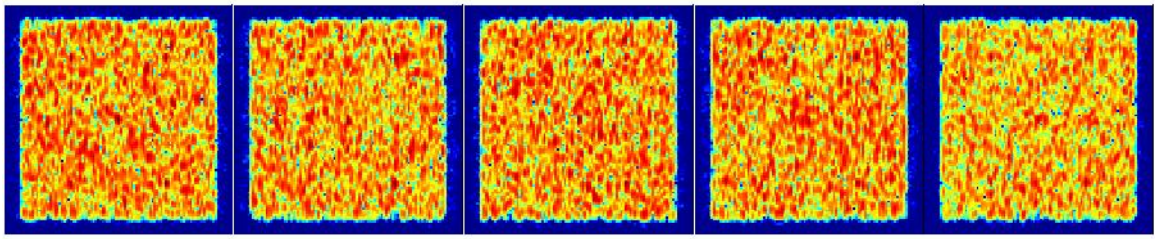

(b)

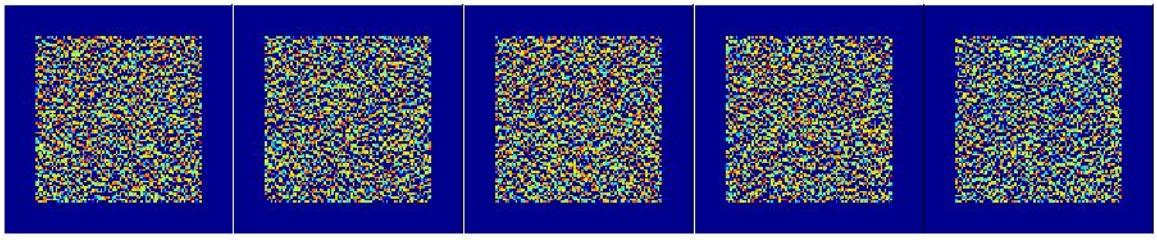

(c)

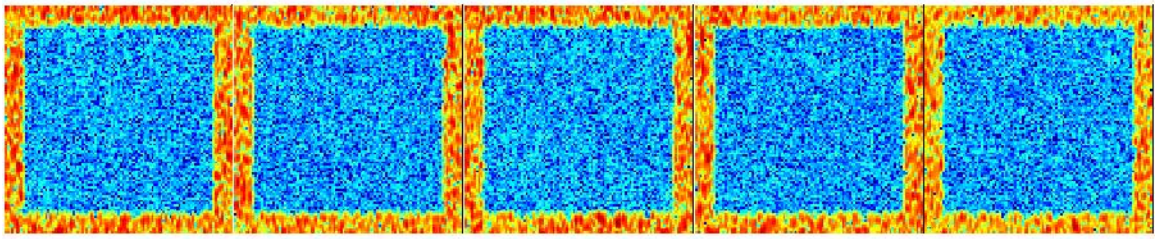

(d)

Fig. 6.6: Individual aperture results that employed a sparsity constraint weighted at $\omega_m = 0.00100$: (a) The default image b, (b) The estimated image $\hat{b} = Ax$, (c) The estimated x, (d) The residual image $b - \hat{b}$.

The multilook results for two different weighting parameters are shown in Figure 6.7. The images on the left correspond to $\omega_m = 0.00010$. This places less emphasis on sparsity, by a factor of two. This implies that the data-fit is enhanced in Figure 6.7 compared to Figure

6.5. This can be visualized by looking at the residual multilook image in Figure 6.7(c) and comparing it to the multilook image in Figure 6.5(d). The estimated image in Figure 6.7(e) exhibits less dynamic range compared to Figure 6.5(c).

The images on the right correspond to $\omega_m = 0.00050$. This has five times the emphasis

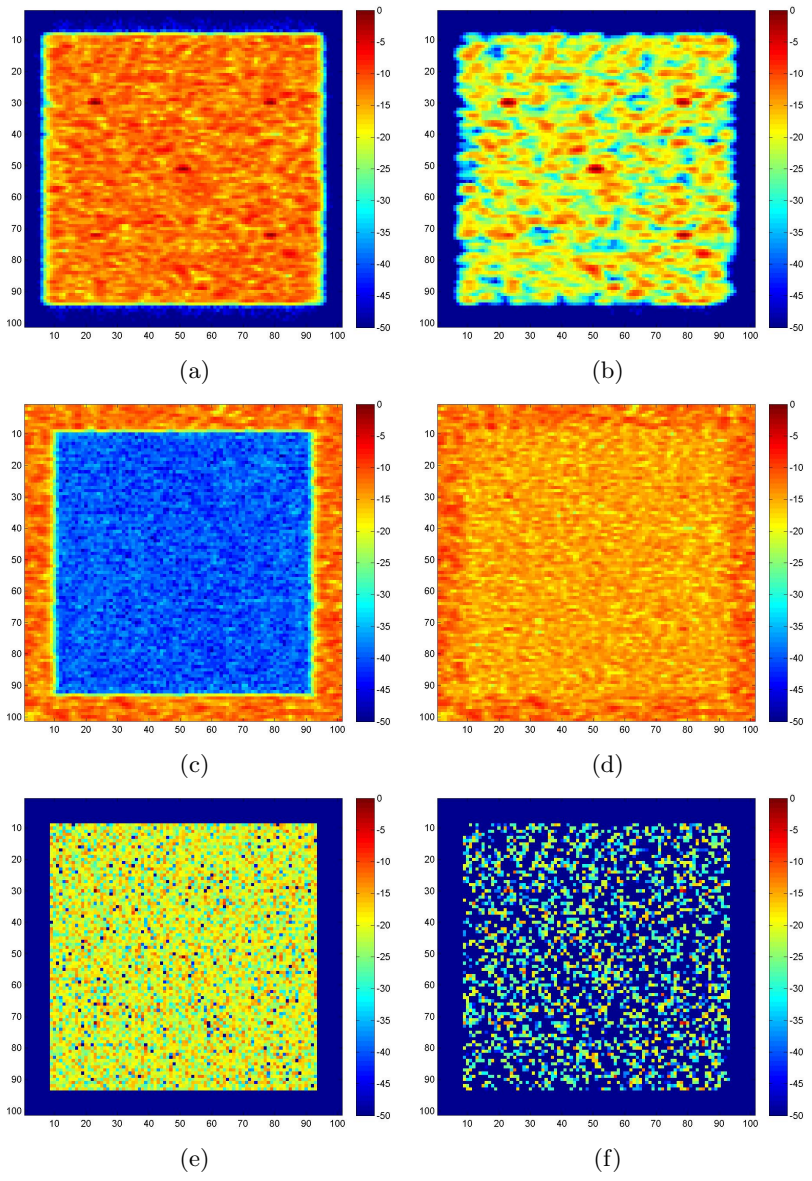

Fig. 6.7: Contrasting individual aperture results that employed a sparsity constraint weighted at $\omega_m = 0.00010$ (images on the left) and $\omega_m = 0.00050$ (images on the right): (a) The estimated image $\hat{b} = Ax$, (b) The estimated image $\hat{b} = Ax$, (c) The residual image $b - \hat{b}$, (d) The residual image $b - \hat{b}$, (e) The estimated x, (f) The estimated x.

on sparsity compared to the multilook results shown in Figure 6.5. The data-fit seen in Figure 6.7(b) does not match the default images shown in Figure 6.5(a), and it can be seen that the residual image in the ROI has a much high noise floor in Figure 6.7(d) compared to Figure 6.5(d). It is interesting to note that the estimated image in Figure 6.7(f) exhibits more dynamic range compared to Figure 6.5(c).

The optimization problem will be augmented to include additional constraints, which reduce the search space. The solution produced now must fill the additional constraints in an appropriate manner. The additional constraints can be thought of as prior knowledge, or the constraints capture the natural correlation found in practice. These constraints help find a solution, from the plethora of solutions, that is ideal or more likely.

6.4.2 Sparsity and Spatial Constraint Results

The first additional constraint that will be added is a spatial constraint. The spatial constraint tries to find solutions where the magnitude is smooth. The background and justification for such a constraint are given in Section 4.3.1 and Section 5.1.3. The need, and potential benefit of such a constraint becomes apparent when examining Figure 6.7. The detailed problem formulation is given in Equation (5.46) and Equation (5.47). The results are shown in Figure 6.8. The weighting used was $\omega_m = 0.00010$ and $\omega_g = 0.00010$ for the sparsity and spatial constraint.

These results in general show promise compared to the sparsity only results seen previously. The default backprojected multilook image is shown as a reference in Figure 6.8(a). The forward-model multilook image is displayed in Figure 6.8(b) and clearly resembles the results seen in Figure 6.8(a). The estimated multilook image given in Figure 6.8(c) has some nice traits. First, the image is much smoother. Second, the image dynamic range is increased which helps to visually separate the clutter and static points. The residual multilook image seen in Figure 6.8(d) shows an accurate fit to about -30 dB.

For the next results the data fit parameter is kept the same where $\omega_m = 0.00010$, but the spatial weighting parameter is varied. The results are shown in Figure 6.9 where the multilook images on the left had a spatial weighting of $\omega_g = 0.00100$, and the multilook

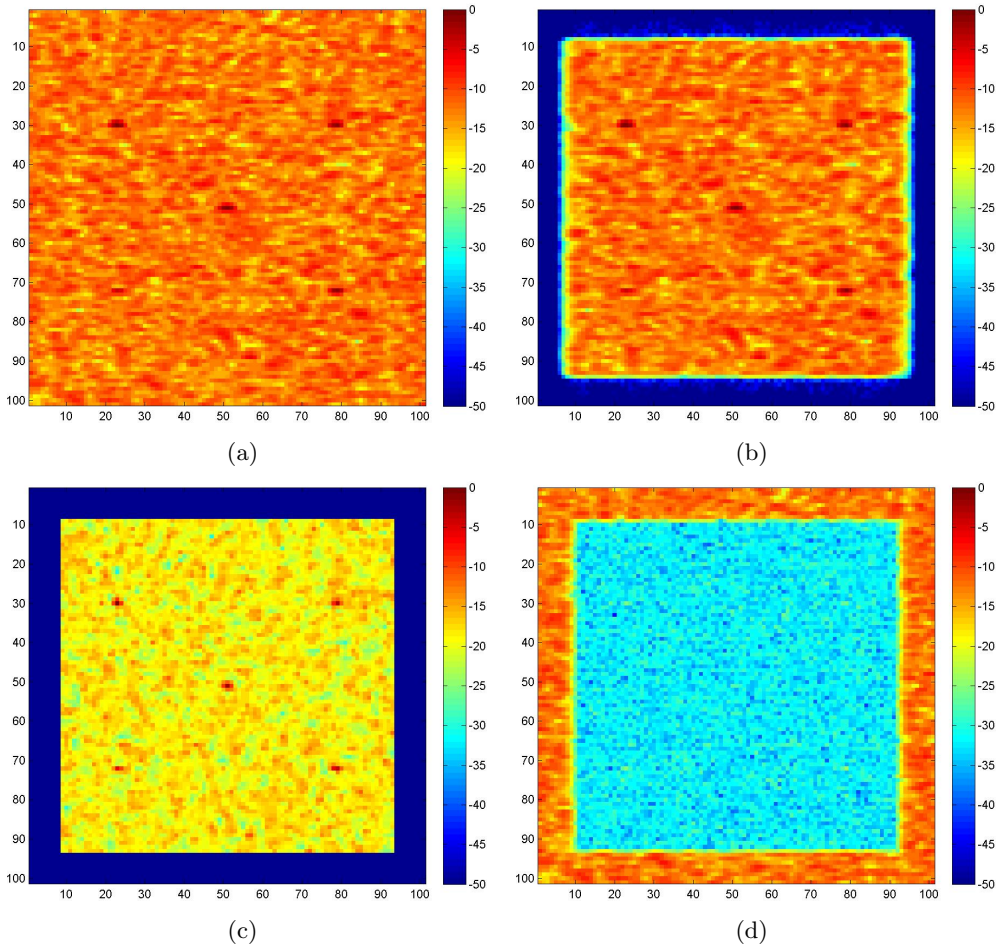

Fig. 6.8: Multilook results that employed a sparsity and smoothing constraint with weights of $\omega_m = 0.00010$ and $\omega_g = 000010$: (a) The default image b, (b) The estimated image $\hat{b} = Ax$, (c) The estimated x, (d) The residual image $b - \hat{b}$.

images on the right had a spatial weighting of $\omega_g = 0.00020$.

The results are exactly as one would expect. A heavy weighting is used for the multilook images on the left of $\omega_g = 0.00100$. The multilook images have a very smooth magnitude. In fact, the contrast is reduced. While the image is much smoother the IPR of the static targets is preserved and does not exhibit any edge effects that are common with traditional low-pass filtering. The act of incorporating the spatial constraints in the image formation process is much more complicated than just applying a "post" filter. Several advantages of incorporating post-processing operations into the image formation of SAR imagery are discussed in Onhon and Cetin which are related to this approach [73]. This is because

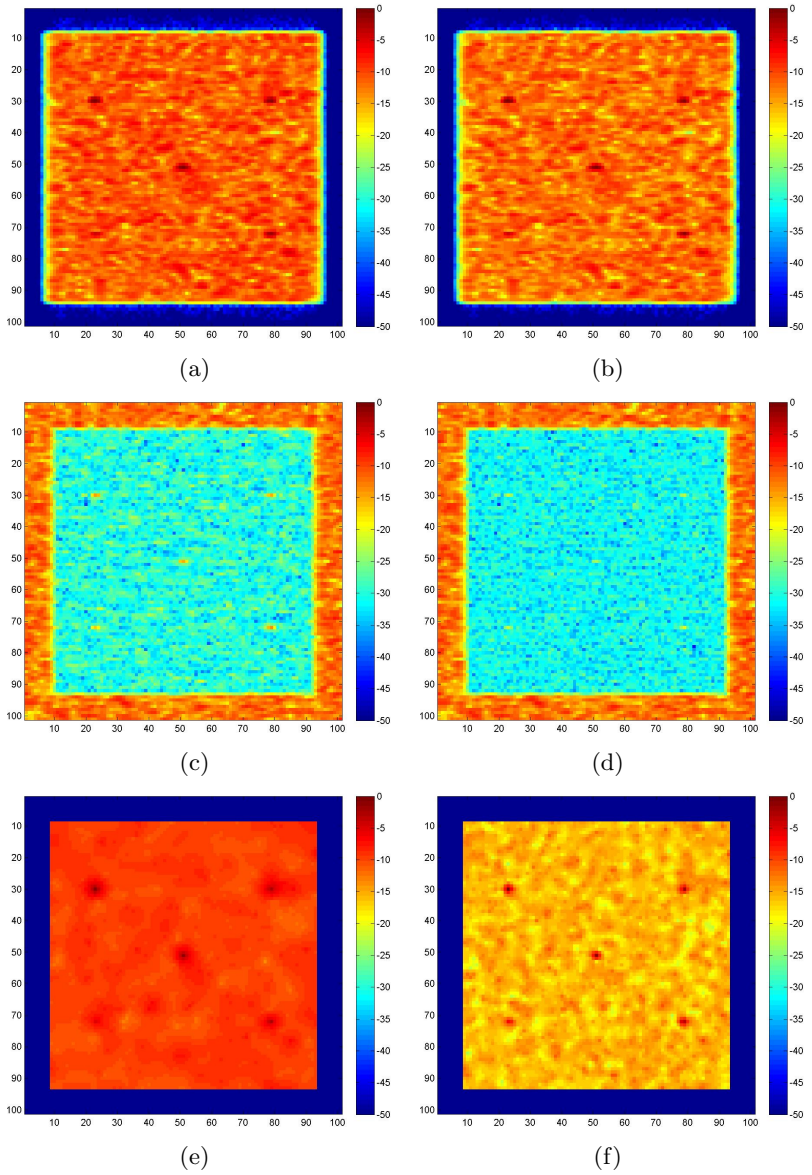

Fig. 6.9: Contrasting multilook results that employed a sparsity and smoothing constraint with weights of $\omega_m = 0.00010$ (all images), $\omega_g = 0.00100$ (images on the left), and $\omega_g = 0.00020$ (images on the right): (a) The estimated image $\hat{b} = Ax$, (b) The estimated image $\hat{b} = Ax$, (c) The residual image $b - \hat{b}$, (d) The residual image $b - \hat{b}$, (e) The estimated x, (f) The estimated x.

the data-fit term is also evaluated in conjunction with the smoothness term. The data-fit can incorporate the prior knowledge of the IPR and its corresponding side-lobes. The l_1-norm used does not penalize bright features to the extent an l_2-norm would. These benefits becomes paramount for 3D imaging, and will be discussed in more depth later

when demonstrating results for 3D.

This section displayed the results of incorporating a sparsity constraint and spatial smoothness constraint. The resultant images, that incorporated a sparsity and spatial smoothness constraint, were much easier to interpret than those that only leveraged a sparsity constraint as in Section 6.4.1. The results exhibited promise regarding over-all improved scene interpretability compared to the standard backprojected image in several aspects. The image dynamic range was often increased, and the image variance was often reduced.

6.4.3 Sparsity and Aspect Constraint Results

This section examines the results from incorporating sparsity and an aspect constraint into the optimization problem. The justification for incorporating aspect correlation, and the potential benefits are discussed in in detail in Section 4.3.2 and Section 5.1.3. In summary, the aspect constraint can be explicitly designed for a unique targets aspect dependent magnitude reflectivity.

This can target phenomenology such as glint, or the mean reflectivity response. The ensuing example is designed with an aspect filter with the intent to enhance the response of targets that have a constant magnitude reflectivity from aperture to aperture. The scene was processed with a setting of $\omega_m = 0.00050$ and $\omega_f = 0.00010$. The results are shown in Figure 6.10.

The multilook backprojected image is shown in Figure 6.10(a). The forward-model multilook image result is shown in Figure 6.10(b) and resembles the original multilook image in Figure 6.10(a) very closely upon initial inspection. The estimated multilook image is shown in Figure 6.10(c). The multilook estimated image in Figure 6.10(c) exhibits a large dynamic range compared to the original multilook image in Figure 6.10(a).

Unfortunately, Figure 6.10(c) suffers from increased speckle. Overall the estimated multilook image is more difficult to interpret than the backprojected multilook image in general due to the increase speckle. The residual multilook image seen in Figure 6.10(d)

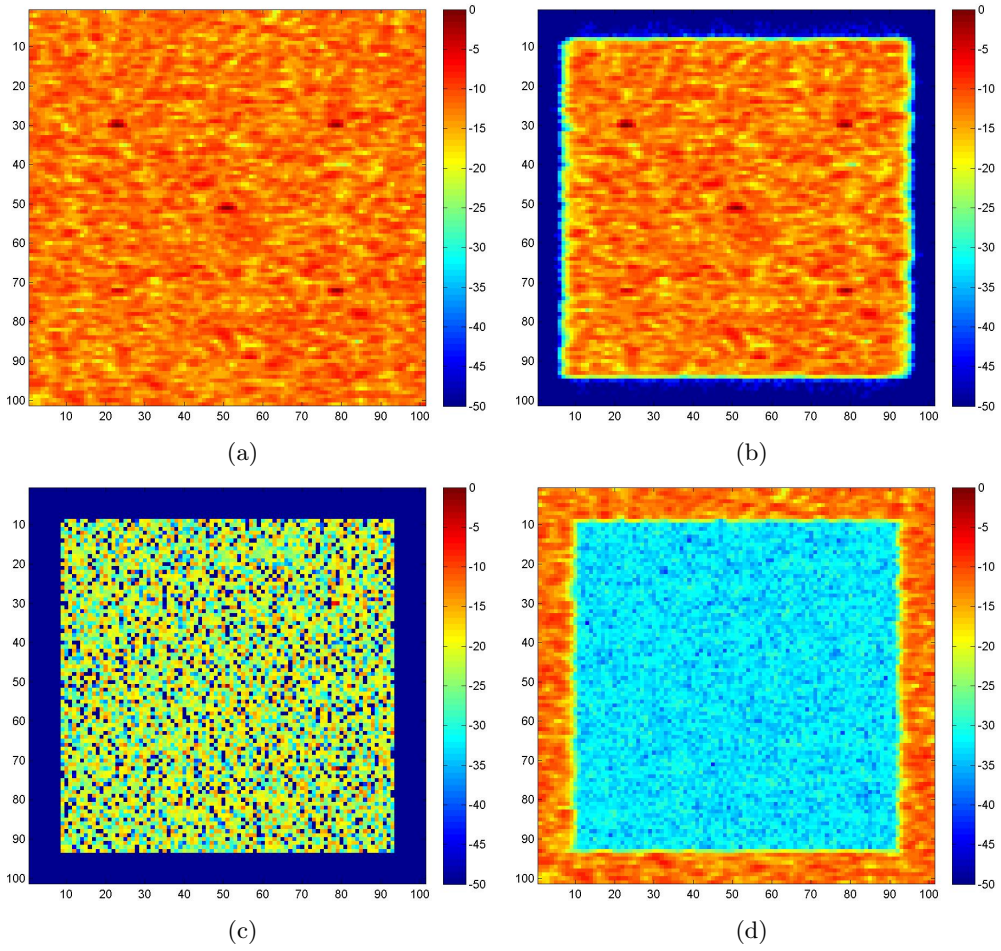

Fig. 6.10: Multilook results with a sparsity and aspect constraint with weights of $\omega_m = 0.00010$ and $\omega_f = 0.00010$: (a) The default image b, (b) The estimated image $\hat{b} = Ax$, (c) The estimated x, (d) The residual image $b - \hat{b}$.

shows that the residual error over the ROI is down about -30 to -35 dB. This confirms the original hypothesis that the forward-model matched the original image nicely.

The fundamental idea behind the aspect constraint is that targets of interest can be enhanced. In this trivial example, it does not appear readily advantageous. The benefits of the aspect filter is illustrated in Figure 6.11 and for this simple example it is assumed that the five discrete clutter points seen in Figure 6.10(a) are of the targets of interest.

The original backprojected apertures are shown in Figure 6.11(a). Since the imagery has not been multilook, the individual apertures variance is very high. The sparsity only solution is shown in Figure 6.11(b). A sparsity constraint of $\omega_m = 0.00100$ was used to

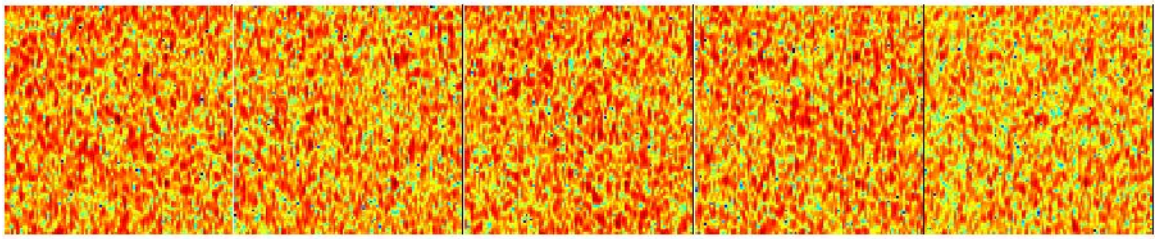

(a)

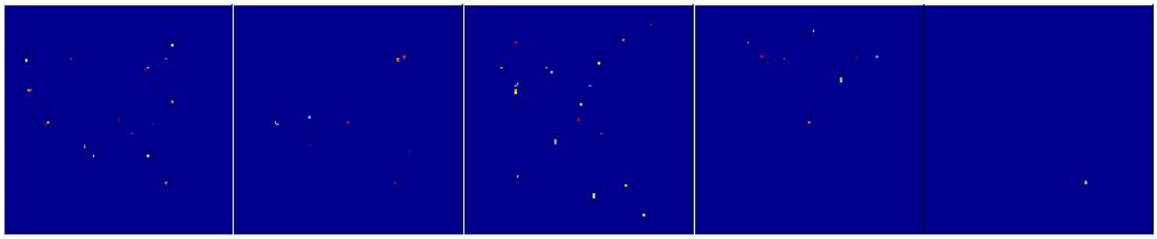

(b)

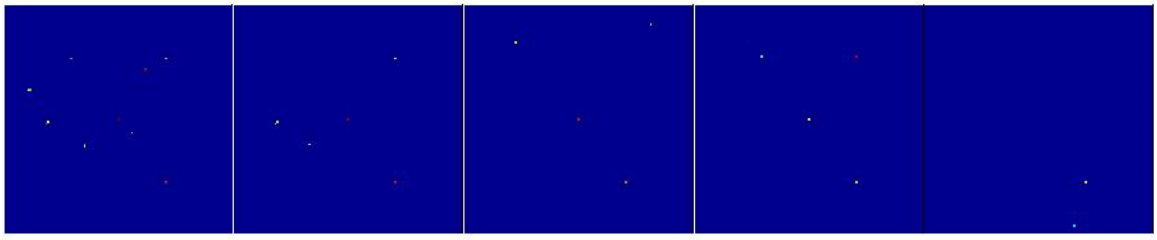

(c)

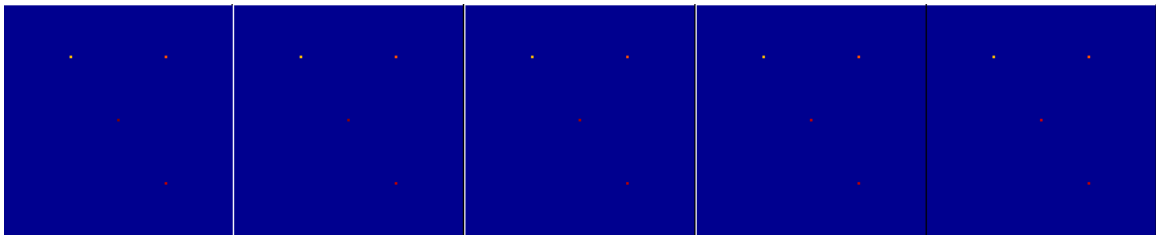

(d)

Fig. 6.11: The advantegous of an aspect filter: (a) The backprojected apertures, (b) The estimated image processed with a sparsity weight of $\omega_m = 0.00100$, (c) The estimated image processed with sparsity and aspect weights of $\omega_m = 0.00100$ and $\omega_f = 0.00010$, (d) The estimated image processed with sparsity and aspect $\omega_m = 0.00090$ and $\omega_f = 0.00090$.

form the imagery in Figure 6.11(b).

Figure 6.11(c) uses a sparsity weighting of $\omega_m = 0.00100$ and an aspect constraint of $\omega_f = 0.00010$. Figure 6.11(d) uses a sparsity weighting of $\omega_m = 0.00090$ and an aspect

constraint of $\omega_f = 0.00090$, but it is clear that Figure 6.11(c) and Figure 6.11(d) provide drastically different solutions. The difference is the result of the complex weighting intrinsically done by the optimization problem, and the details of the aspect filter incorporated.

It is important to remember the matrix formulation of the aspect filter allows for any specified filter to be incorporated into the image formation. Previously, an example of a simple aspect filter was given in Figure 5.3. The same aspect filter specified in Figure 5.3 is used in the processing for Figure 6.11(c) and Figure 6.11(d), but diverse filters could be incorporated and drastically influence the solution.

The results demonstrate the potential influence of incorporating an aspect filter into the image formation in general. The ability to target specific responses, and incorporate the neighboring aperture RCS into the solution can drastically alter the solution. While this particular result shows the ability to influence the solution, the benefits might not be readily apparent in this particular case. The advantages of an aspect filter will become more apparent when examining actual SAR data later.

6.4.4 Sparsity, Spatial, and Aspect Constraint Results

Incorporating the aspect and spatial filter into the optimization problem provides increased flexibility to accentuate targeted RCS responses. Part of the success of model-based processing depends on identifying targets with unique or distinguishable RCS magnitude. This assumes that prior knowledge about the target or scene is incorporated into the image-formation. This results will just use generic "filters" to demonstrate the fundamental capability as described in Section 5.1.3 and Section 5.1.4. But ideally, the filters would be pixel and, or target specific.

The same simulated data set is now processed with sparsity, spatial, and aspect weights of $\omega_m = 0.00050$, $\omega_g = 0.00050$, and $\omega_f = 0.00050$ correspondingly. The multilook results are shown in Figure 6.12. This particular example has a heavy emphasis on sparsity. The same sparsity weighting is used in Figure 6.7(f). The additional constraints produce an image that looks distinctly different when comparing Figure 6.7(f) and Figure 6.12(c). The image in Figure 6.12(c) is more sparse due to the additional constraints incorporated.

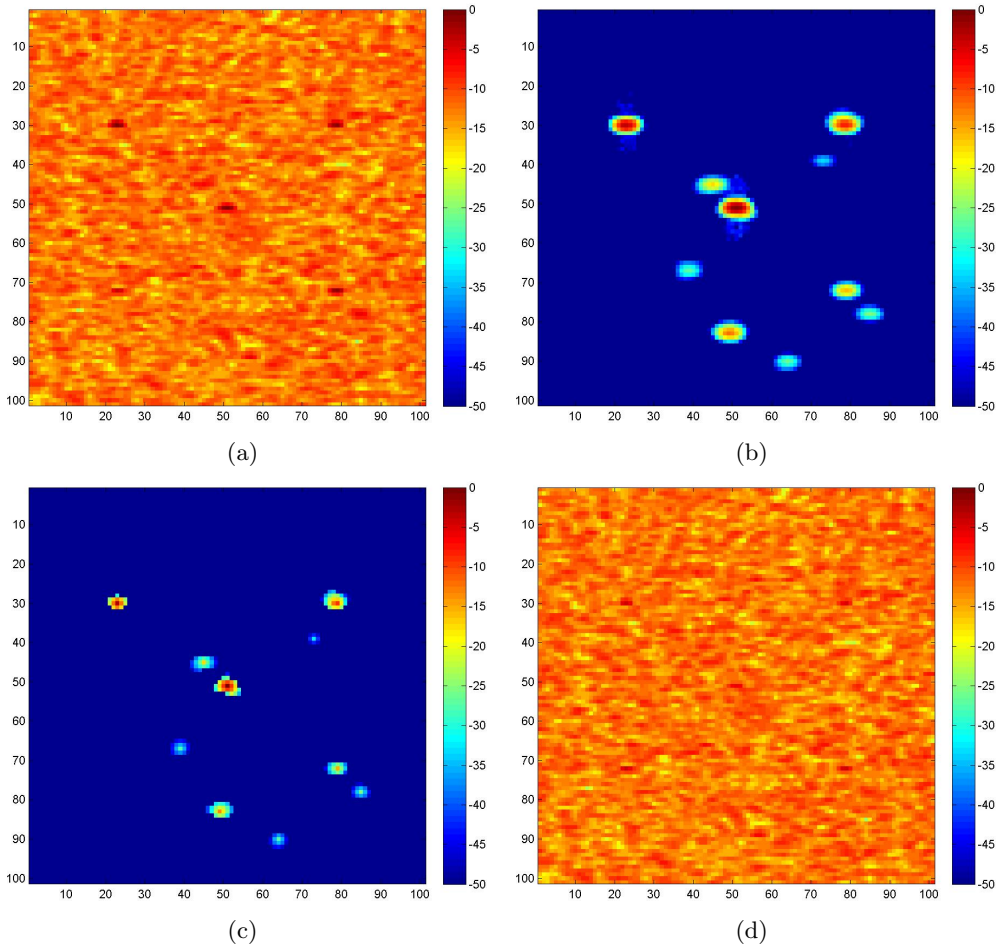

Fig. 6.12: Multilook results that employed a sparsity, spatial, and aspect constraint with weights of $\omega_m = 0.00050$, $\omega_g = 0.00050$, and $\omega_f = 0.00050$: (a) The default image b, (b) The estimated image $\hat{b} = Ax$, (c) The estimated x, (d) The residual image $b - \hat{b}$.

The original multilook image is shown in Figure 6.12(a) for reference again. The forward-model multilook image is displayed in Figure 6.12(b). The estimated multilook image is shown in Figure 6.12(c). The super-resolution capability available for model-based processing is apparent when comparing Figure 6.12(b) and Figure 6.12(c). The residual multilook image is shown in Figure 6.12(d). The residual multilook image appears to resemble the original multilook image in Figure 6.12(a). The only difference is several of the most dominant RCS features have been removed.

Several additional examples are shown in Figure 6.13 to help illustrate the individual effect the aspect and spatial constraints provide the final solution. The results on the left

have the weighting terms of $\omega_m = 0.00050$, $\omega_g = 0.00010$, and $\omega_f = 0.00050$ for the sparsity, spatial, and aspect weighting terms. The results on the left of Figure 6.13 have decreased the spatial weighting term in comparison with results shown previously in Figure 6.12.

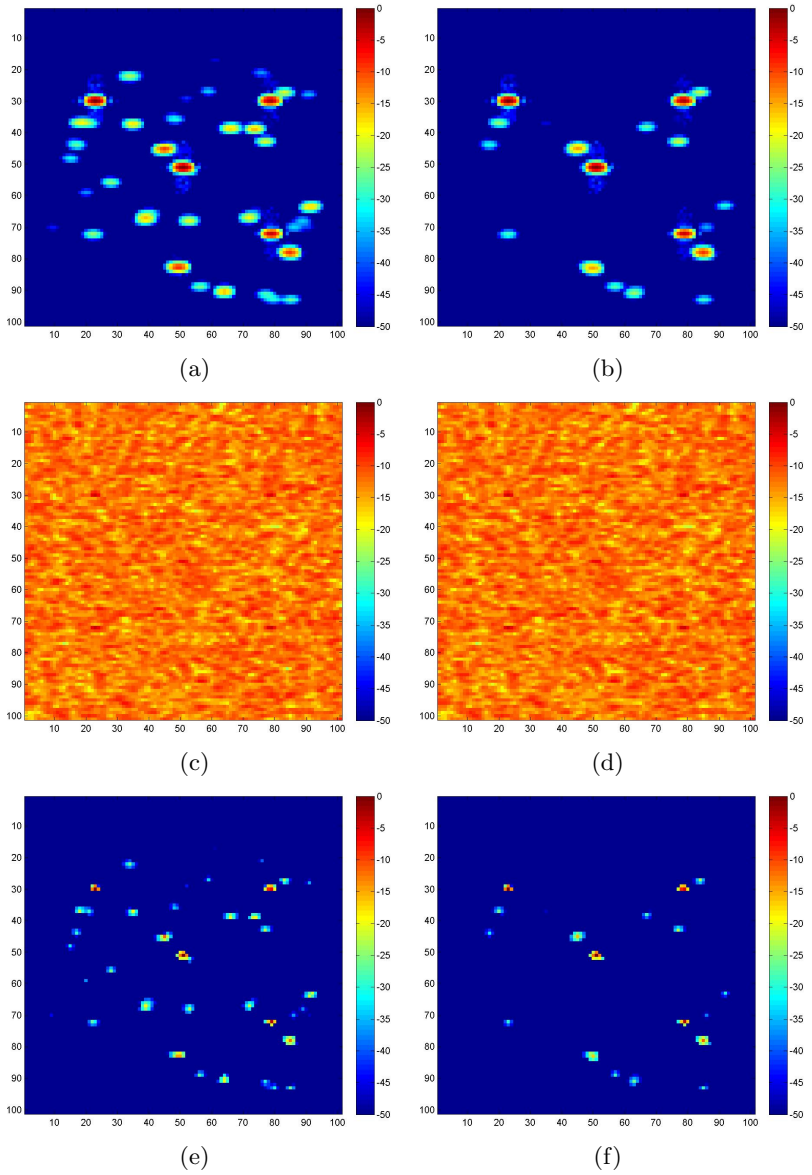

Fig. 6.13: Contrasting multilook results that employed a sparsity, spatial, and aspect constraint with weights of $\omega_m = 0.00050$ for all images. The weighting of $\omega_g = 0.00010$ and $\omega_f = 0.00050$ was used for images on the left, and the weights $\omega_g = 0.00500$ and $\omega_f = 0.00010$ was used for images on the right: (a) The estimated image $\hat{b} = Ax$, (b) The estimated image $\hat{b} = Ax$, (c) The residual image $b - \hat{b}$, (d) The residual image $b - \hat{b}$, (e) The estimated x, (f) The estimated x.

The results on the right of Figure 6.13 have the weighting terms of $\omega_m = 0.00050$, $\omega_g = 0.00500$, and $\omega_f = 0.00010$ for the sparsity, spatial, and aspect weighting terms. The aspect weighting term has been increased compared to the results displayed on the left of Figure 6.13. The increase in the aspect weighting applied to the images on the right of Figure 6.13 has the cumulative effect of selecting a subset of the pixels seen on the left in Figure 6.13. The pixels maintained though are not necessarily the ones corresponding to the largest RCS.

6.5 Summary of Algorithm

This chapter walked through a simulated example in detail to demonstrate with simulated SAR data the potential benefits each constraint provided. The results of modifying individual constraints in the optimization problem was examined primarily with the resultant images. The images graphically illustrated the effects of the corresponding constraint. The detailed background describing the justification and a detailed explanation were referenced to prior chapters where those considerations where addressed.

Since the objective was to illustrate the effect each constraint had on the optimization problem, the advantageous, in some cases, are not readily apparent. Several of the most predominant advantageous, in the author's opinion, are evident for 3D scene reconstruction and not readily apparent for 2D scenes. The ability to incorporate additional constraints into the image formation process had several observations that can be noted for 2D scenes.

First, the scene's dynamic range is often improved by incorporating a sparsity constraint. Second, the scene's spatial response could be influenced by the spatial filter incorporated. The third aspect constraint influenced the final image results by favoring RCS responses based on the particular aspect filter incorporated.

Chapter 7

Results

The emphasis of this chapter is illustrating the results achieved on actual SAR data for 2D and 3D scenes. The data employed is the GOTCHA data set [36]. The GOTCHA data set is readily available and has gained widespread use for benchmarking new algorithms by researchers. This is due to its accessibility, excellent data quality, diverse collection geometries, and excellent scene documentation and control.

The GOTCHA SAR data consists of eight circular collects. The GOTCHA sensor operated in a spot-light mode. Each of the eight collections spans the full 360 degrees in azimuth. The circular collects span 43.7 to 45.0 degrees in elevation. The collections are separated by approximately 0.18 degrees in elevation on average. Backprojected images will be used as the reference imagery to contrast the model-based processing results.

The images for this chapter are generated by coherently integrating four-degree azimuth images. This generates ninety azimuth images for the complete 360 degrees. Each azimuth image integrates all eight elevation apertures to form a single image. All 90 of the aperture images are than magnitude combined into a single multilook image. The multilook image is visualized in the succeeding images and is the basis for comparison and contrasting results. All 2D scenes have pixels that are .25 meters square and all 3D scenes have voxels that are .25 meters cubed.

The scene is composed of a parking lot consisting of well-documented diverse targets. All the targets locations and vehicle type are noted in the provided GOTCHA documentation. An optical image provided with the GOTCHA data is displayed in Figure 7.1 for background reference.

This chapter will first examine 2D processing results and then 3D processing results. The particular processing algorithm employed will be stated along with the parameter

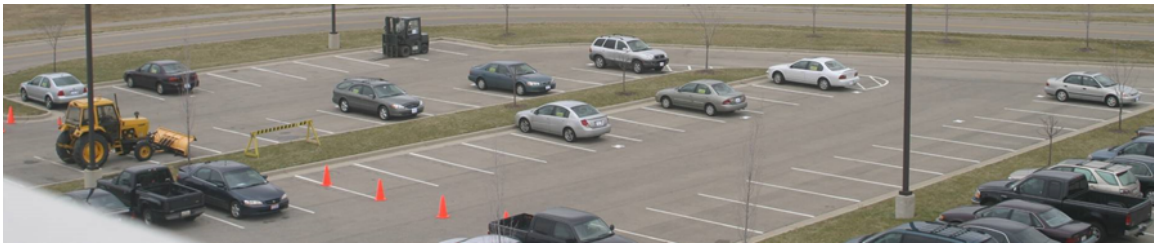

Fig. 7.1: GOTCHA data 2D scene overview.

weightings that were applied in the image formation processing. The weighting parameters will be varied to contrast the processing results. A brief summary of the results will be discussed. The main focus of the discussion will be the visual or graphical interpretation and improvements that are readily seen.

It is important to note that actual SAR data is utilized with real targets from the GOTCHA SAR sensor. Since the details of the GOTCHA SAR system are not available many assumptions are utilized. It is presumed that if the details of the GOTCHA radar sensor were incorporated into the image-formation processing the results would be improved. Despite the assumptions, improvements are readily apparent for the model-based image formation processing results demonstrated.

7.1 Results for 2D Scenes

Two targets will be examined in this section. The first target is a small scene that is composed of a single target, a Ford Taurus vehicle. The second target is a much larger scene that includes many vehicles from the parking lot. The two scenes are selected so the results of model-based processing for a scene composed of a single target can be compared with a scene composed of multiple targets.

7.1.1 2D Ford Taurus

The first 2D target examined is the Ford Taurus located in the GOTCHA data set parking lot scene. An overview of the Ford Taurus is seen in Figure 7.2. The Ford Taurus vehicle is shown in a yellow-dashed box in the optical and SAR image. The optical and

SAR images provide context and scene perspective. The SAR image is a polarimetric image generated from the GOTCHA data set using backprojection processing. A detailed image of the specific Ford Taurus used in the GOTCHA collect is provided with the GOTCHA documentation and is shown in Figure 7.2, also.

The processing results shown in Figure 7.3 utilizes only a model fidelity term and a sparsity term in the cost function. A detailed example formulation of this particular problem is provided in Section 6.4.1 along with more intermediate processing results and details.

The images shown in Figure 7.3 are displayed in a power log-scale utlizing a false color map. They have been normalized so that only pixels -20 dB relative to the max are displayed. The images are displayed in a log-scale to capture all the detail, and subtle differences between the backprojection results and the model-based image formation results. The differences are difficult to capture in the linear scale image that is often used for display. All the images have been up-sampled by a factor of three for visual aesthetics.

The image Figure 7.3(a) is the reference image generated from backprojection processing. The other images seen in Figure 7.3 result from model-based image formation processing. The sparsity weighting parameter used for the results seen in Figure 7.3(b), Figure 7.3(c), and Figure 7.3(d) is $\omega_m = 0.00100$, $\omega_m = 0.00010$, and $\omega_m = 0.00500$, respectively.

The results show some potential for automatic target recognition (ATR) where feature extraction is often critical. One feature that becomes more readily apparent is the driver and passenger side mirrors. These are the bright corner reflectors features seen on each side of the car roughly in the middle in Figure 7.3(b), but not easily noticed in the reference backprojected processed image of Figure 7.3(a).

The next processing results are derived from the same target scene with the 2D Ford Taurus. The results are shown in Figure 7.4. The results incorporate a model fit term, a sparsity term, and an additional spatial smoothness term in the cost function. A detailed consideration of this particular problem formulation is provided in Section 6.4.2 with more inspection given to detail and the intermediate processing steps. The same display prece-

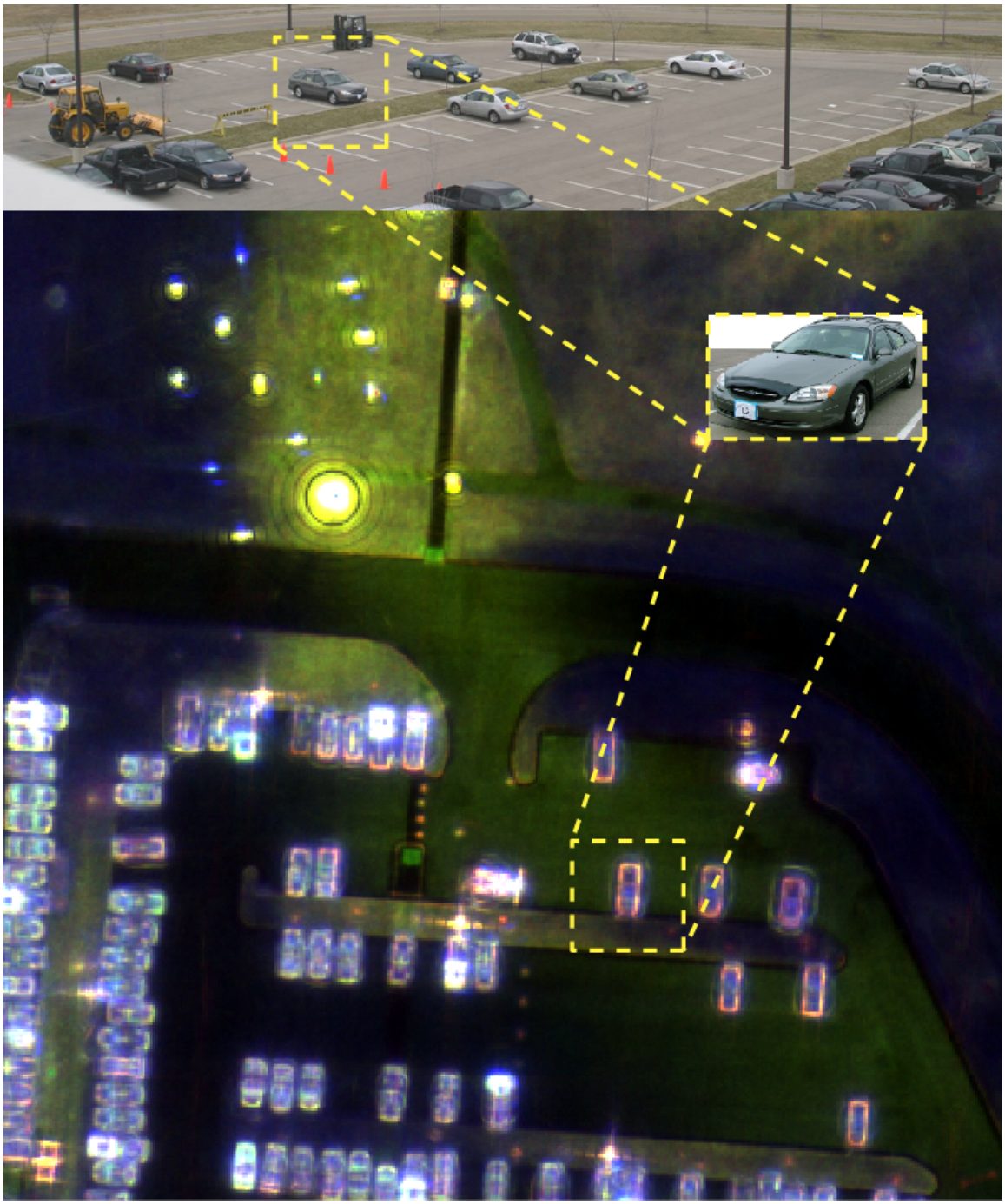

Fig. 7.2: GOTCHA data 2D scene with Ford Taurus highlighted.

dence utilized in Figure 7.3 is utilized again in Figure 7.4 with a minor difference. The difference is the log-scale in Figure 7.4 uses a display of -30 dB instead of -20 dB for more dynamic range to be displayed.

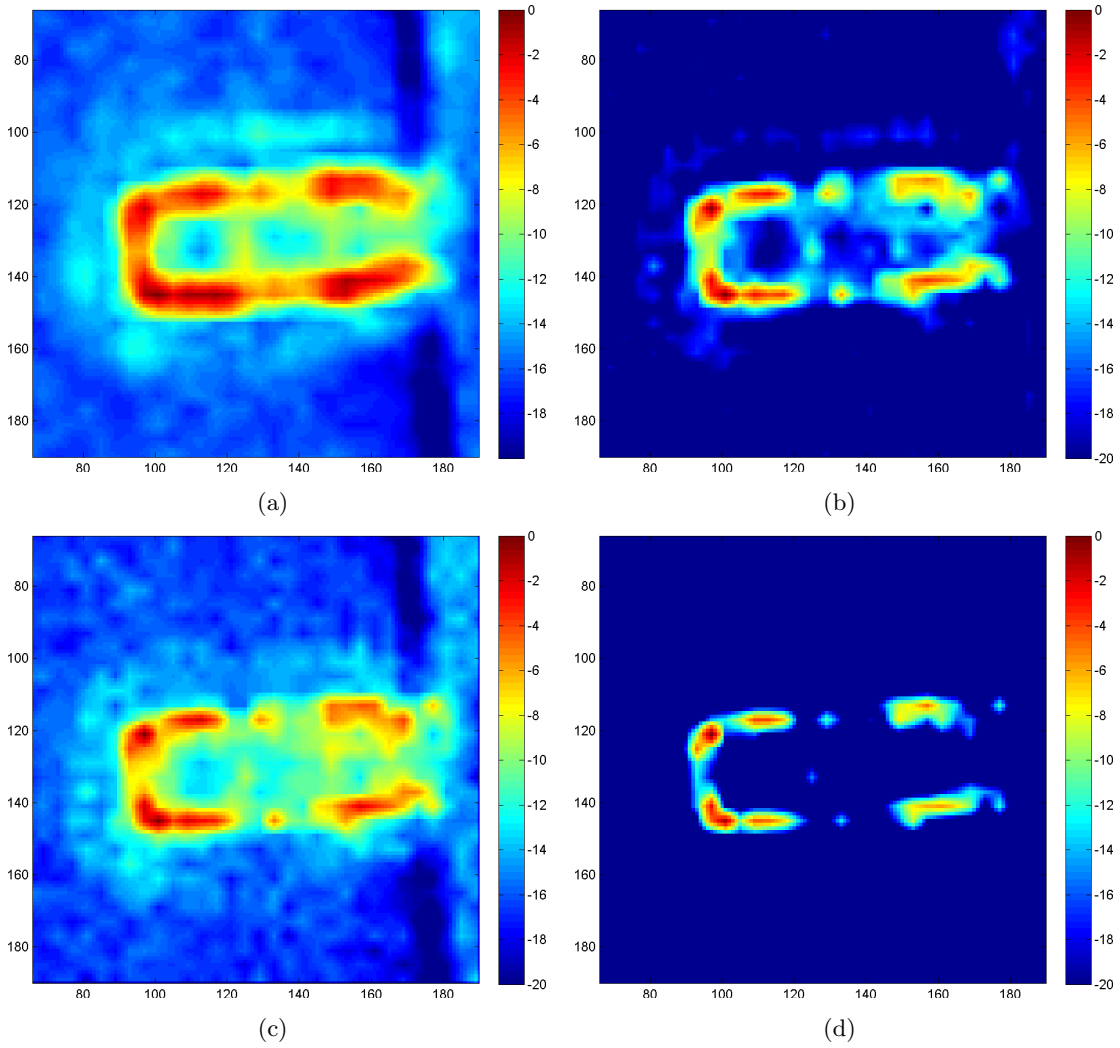

Fig. 7.3: Ford Taurus 2D processing results #1: (a) Backprojected reference image, (b) Resultant image using a weighting of $\omega_m = 0.00100$, (c) Resultant image using a weighting of $\omega_m = 0.00010$, (c) Resultant image using a weighting of $\omega_m = 0.00500$.

The sparsity and aspect weighting terms employed are given in the label of Figure 7.4. The results in Figure 7.4, in general, illustrate the advantage of incorporating a spatial term in the cost function. The scene dynamic range is often increased. The overall scene smoothness can be improved based on the weighting parameter.

The increased dynamic range and improved scene smoothness allow for improved scene segmentation. However, along with these advantages the point features, like the mirrors on the side of the car, can still be accentuated. This illustrates the advantage of incorporating

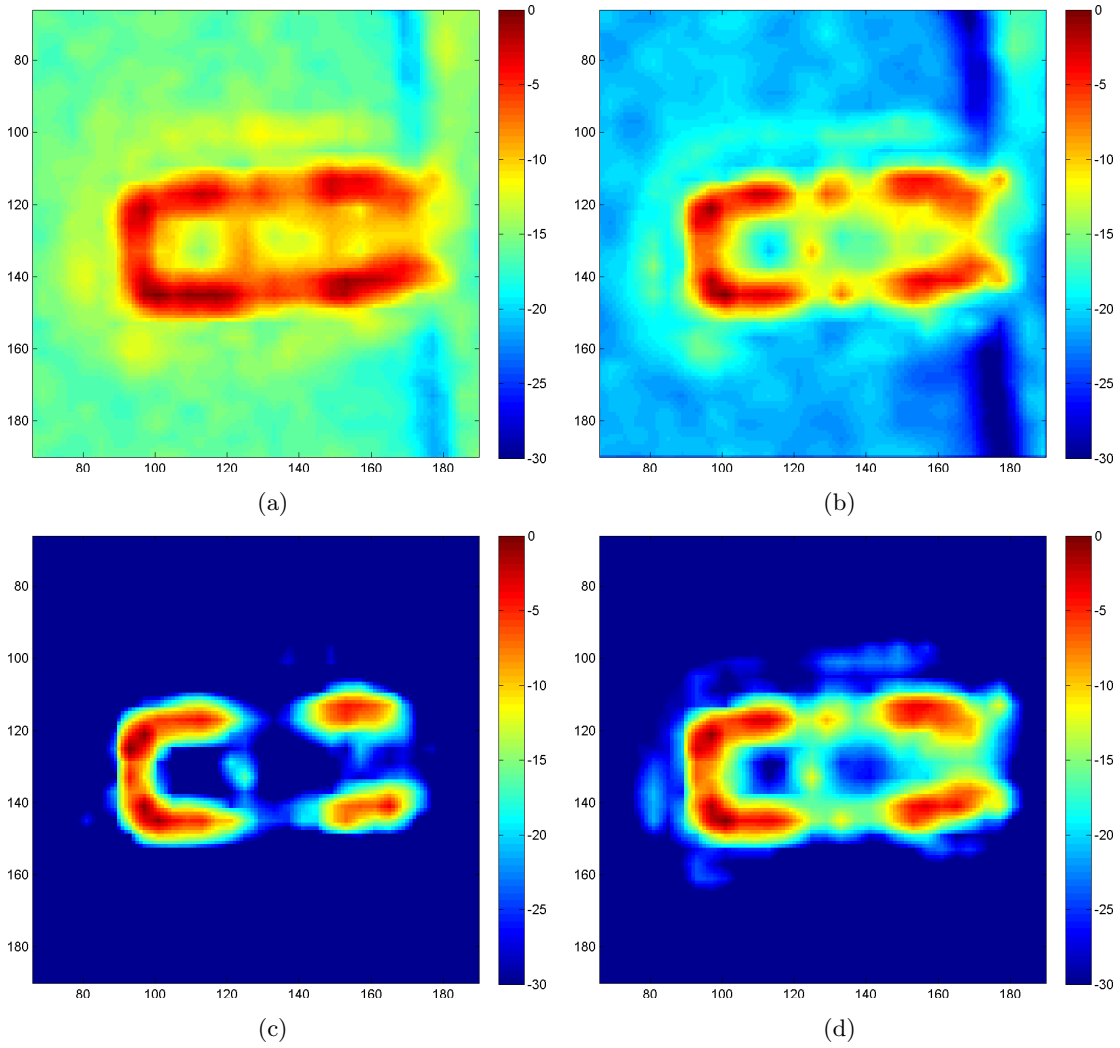

Fig. 7.4: Ford Taurus 2D processing results #2: (a) Backprojected reference image, (b) Resultant image using weightings of $\omega_m = 0.00100$ and $\omega_g = 0.00100$, (c) Resultant image using weightings of $\omega_m = 0.00500$ and $\omega_g = 0.00500$, (d) Resultant image using weightings of $\omega_m = 0.00200$ and $\omega_g = 0.00200$.

the spatial smoothness term into the image formation processing, as opposed to a post-process. The enhancement of point features and smoothing is very difficult to achieve together in a post processing step only.

The results shown in Figure 7.5 utilize a model fidelity term, a sparsity term, a spatial term and an aspect term in the cost function on the same target scene. This problem formulation is detailed in Section 6.4.4.

The parameters employed for the processing weighting for each image is provided in

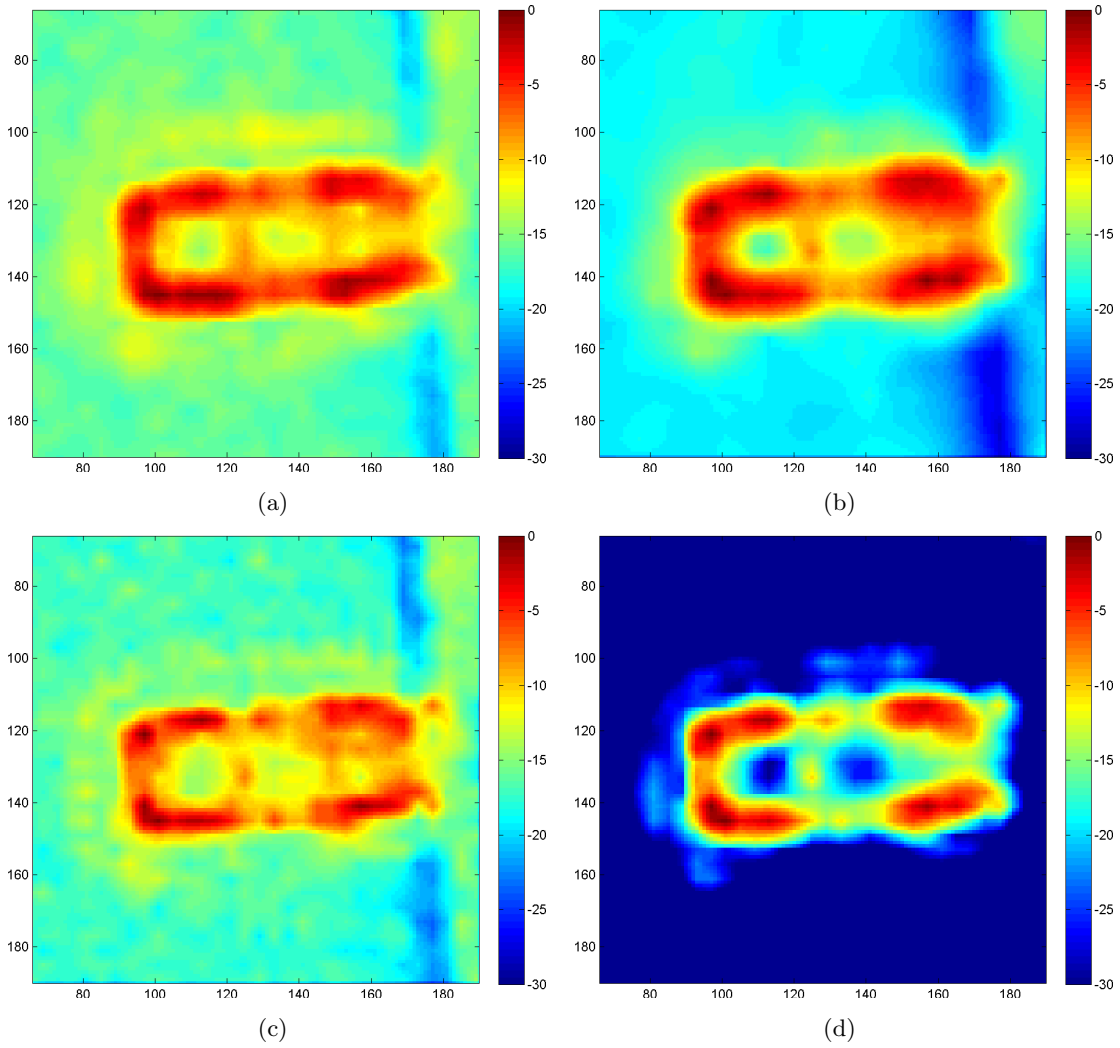

Fig. 7.5: Ford Taurus 2D processing results #3: (a) Backprojected reference image; (b) Resultant image using weightings of $\omega_m = 0.00050$, $\omega_g = 0.00100$, and $\omega_f = 0.01000$; (c) Resultant image using weightings of $\omega_m = 0.00010$, $\omega_g = 0.00001$, and $\omega_f = 0.00100$; (d) Resultant image using weightings of $\omega_m = 0.0010$, $\omega_g = 0.00100$, and $\omega_f = 0.00100$.

the caption of Figure 7.5. The driver and passenger side mirrors can be seen in the middle of the car in Figure 7.4(d), but they are not readily seen in the other images. These driver and passenger side mirrors exhibit a glint when viewed from the appropriate broadside aspect angle. The scene smoothness is increased in Figure 7.5(b). Figure 7.5(d) encourages sparsity more significantly and the image is correspondingly sparse, but in Figure 7.5(c) sparsity, and spatial smoothness are slightly encouraged with a more significant emphasis on aspect.

Many diverse results can be encouraged by changing the parameter weightings and a few examples have been shown for the Ford Taurus 2D target in this section. The model-based processing results are not extremely compelling, in general, for this particular 2D target. However, several examples do show promise for improved resolution of point-responses, improved scene dynamic range, and increased overall scene spatial smoothness. It was demonstrated that incorporating an aspect term can enhance or suppress actual physical features. Unfortunately, many of the characteristics do have a strong dependence on the particular parameter settings used.

7.1.2 2D Parking Lot

The next target of interest is a larger scene that incorporates a significant fraction of the GOTCHA parking lot shown in Figure 7.6 highlighted in a yellow-dashed box. The larger 2D scene is selected in order to compare diverse targets and scene objects together, instead of individually as previously done in Section 7.1.1.

The scene includes several vehicles, a tractor, and a forklift along with diverse parking lot features. The reference image processed with backprojected image is shown in Figure 7.7 and is used as the reference image for the following results.

The first results only incorporate a magnitude constraint and are given in Figure 7.8. The scene reconstruction is very sparse and only the dominant features are visible due to the large emphasis on sparsity, but the results accentuate many point response features found on the tractor compared to traditional backprojection processing, which could be relevant for ATR algorithms.

The next results, shown in Figure 7.9, are processed similiarly to the previous results but with a smaller emphasis on sparsity applied. The point responses features are still super-resolved compared to the backprojected results in Figure 7.7. Many of the scene features are now visible when a less emphasis is given to sparsity, but unfortunately, the backprojected results in Figure 7.7 has a smoother spatial appearance than the model-based results in Figure 7.9.

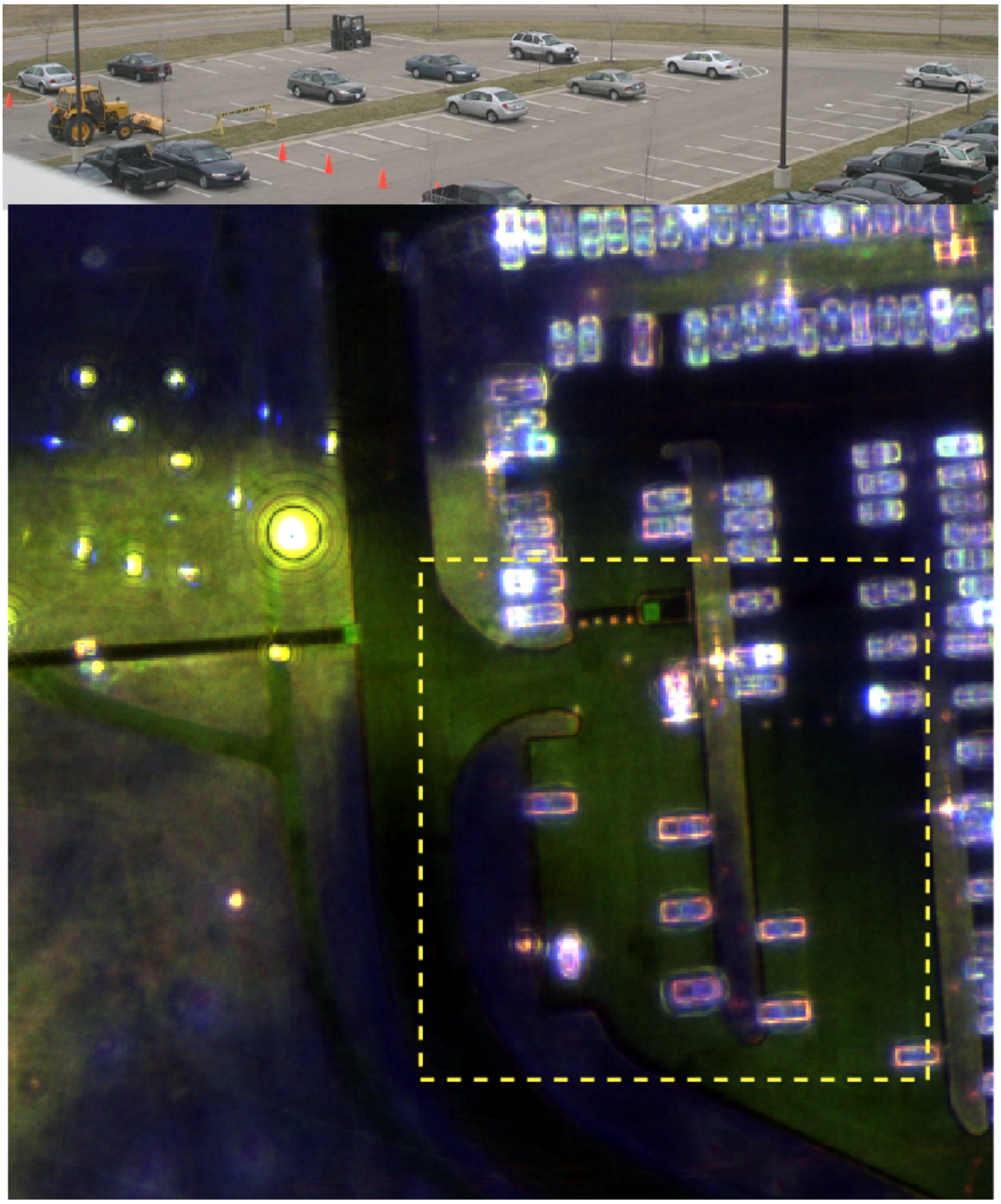

Fig. 7.6: Gotcha 2D scene overview.

The final results for this scene incorporate a spatial smoothness constraint and a sparsity constraint. The results are shown in Figure 7.10. The results still have enhanced point features like the previous results, but the addition of the spatial constraint has produced an

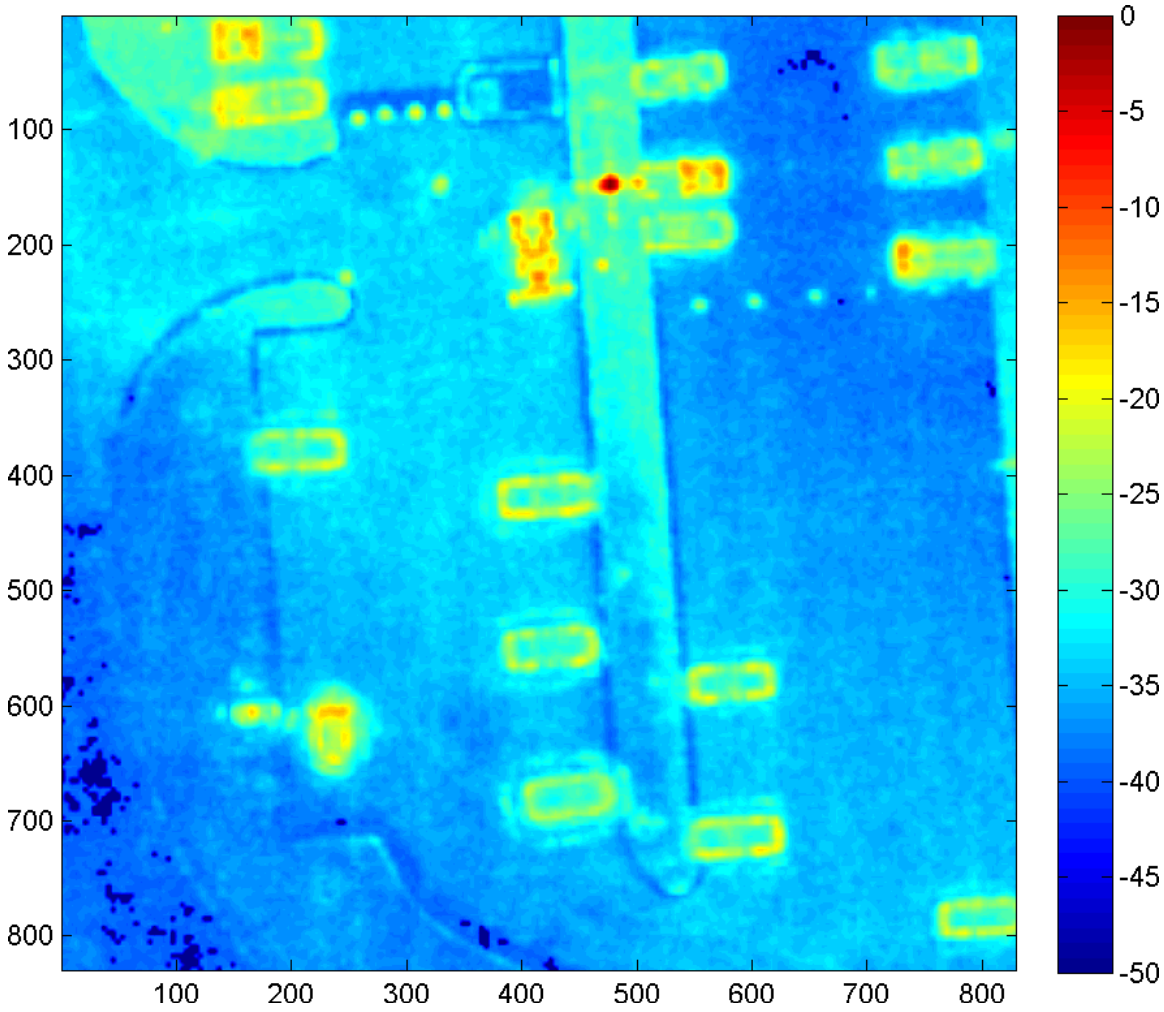

Fig. 7.7: GOTCHA 2D medium scene backprojected results.

image that is spatially smoother than the reference image with enhanced point responses.

7.2 Results for 3D Scenes

The real objective of this research was for 3D scene reconstruction. The GOTCHA data set has a very sparse vertical aperture, since 8 circles where collected. The sparse vertical aperture can be used to generate 3D scene reconstruction. Unfortunately, the sparse sampling causes severe side-lobe features in the vertical dimension. The work here relies on modeling the side-lobes to improve results, and leverages prior information about the scene by incorporating regularization terms that promote solutions that are smooth

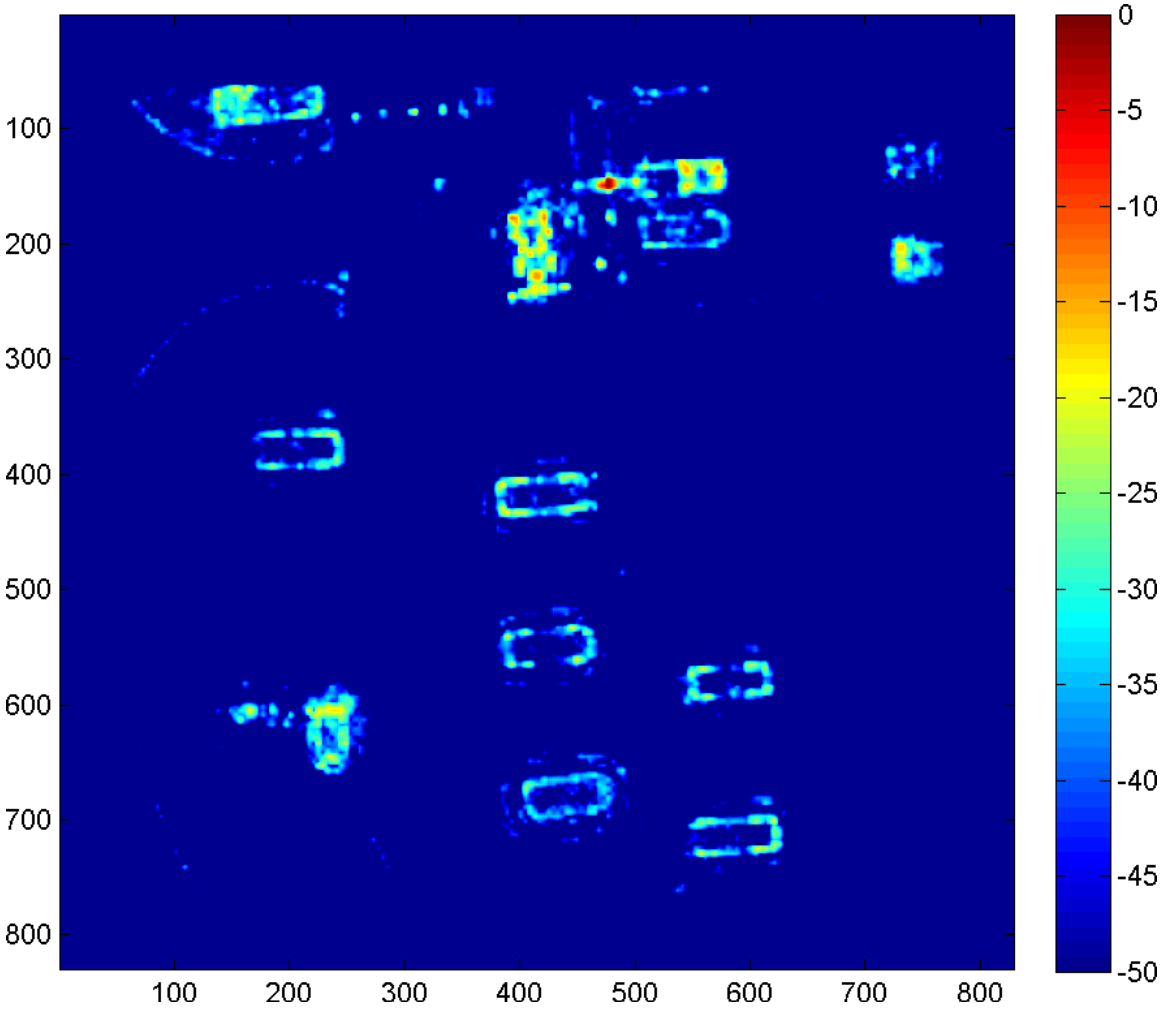

Fig. 7.8: GOTCHA 2D medium scene processing results #1 with $\omega_m = 0.00100$.

spatially and in aspect.

Two different 3D targets will be considered in this section. The first is the same Ford Taurus that was previously processed, but now the processing will be done in 3D instead of 2D. The second target selected is the tractor. All the images presented have been up-sampled by 3 in each dimension. That means each voxel is up sampled by nine for improved image interpretation.

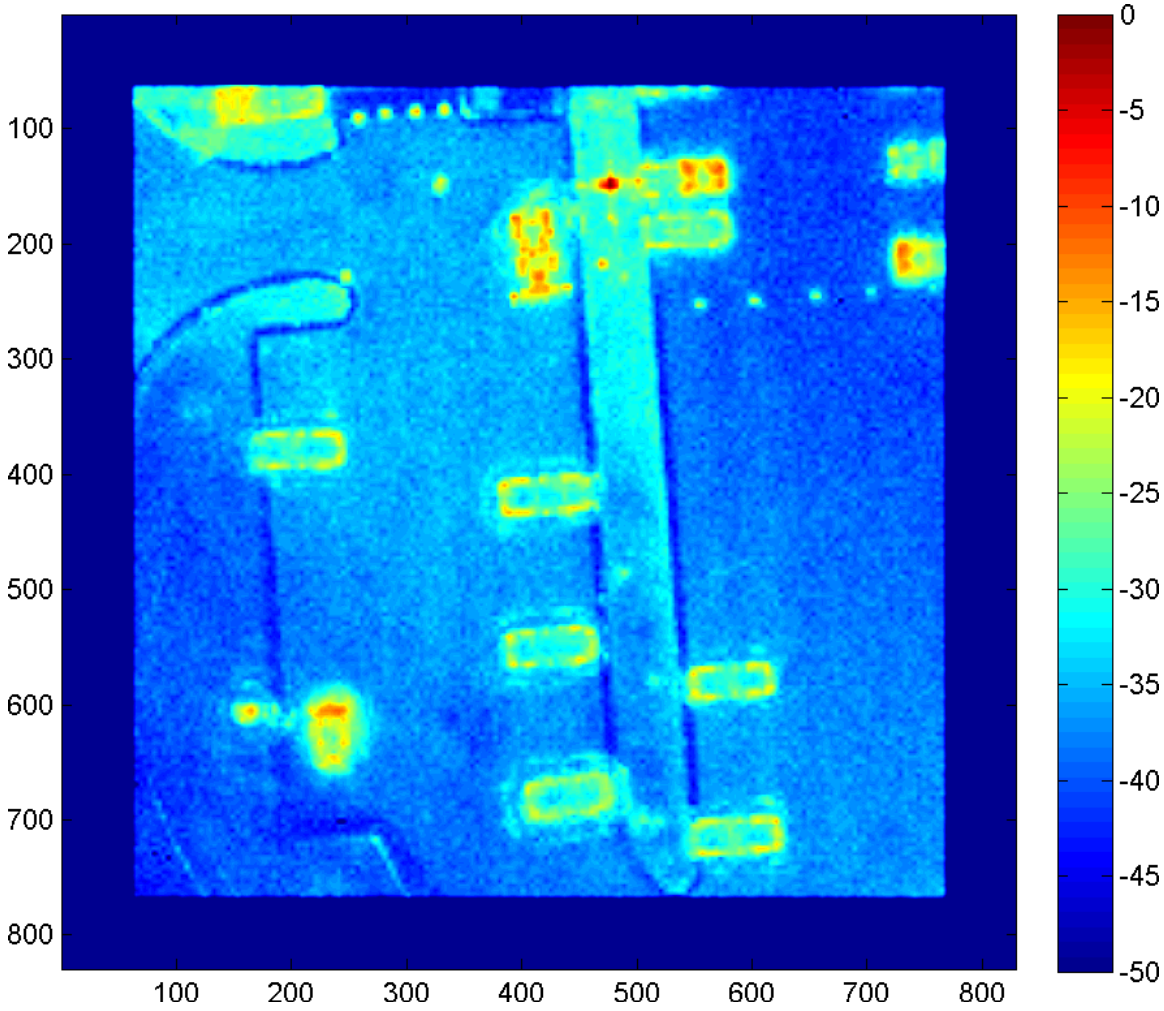

Fig. 7.9: GOTCHA 2D medium scene processing results #2 with $\omega_m = 0.00010$.

7.2.1 3D Ford Taurus

The Ford Taurus used in the GOTCHA data collect is shown in Figure 7.11 for reference and comparison. The image is provided in the GOTCHA documentation.

The reference backprojected image is shown in Figure 7.12. The image is viewed from two diverse aspect angles to provide perspective. The first view is shown from an azimuth angle of 3° degrees and an elevation angle of 44° degrees. This corresponds with the angle that the radar illuminated the target. The second view is from an azimuth angle of 12° degrees and an elevation angle of 14° degrees, which corresponds to an angle most people are used to seeing when viewing vehicles. The imagery is displayed in a power log-scale

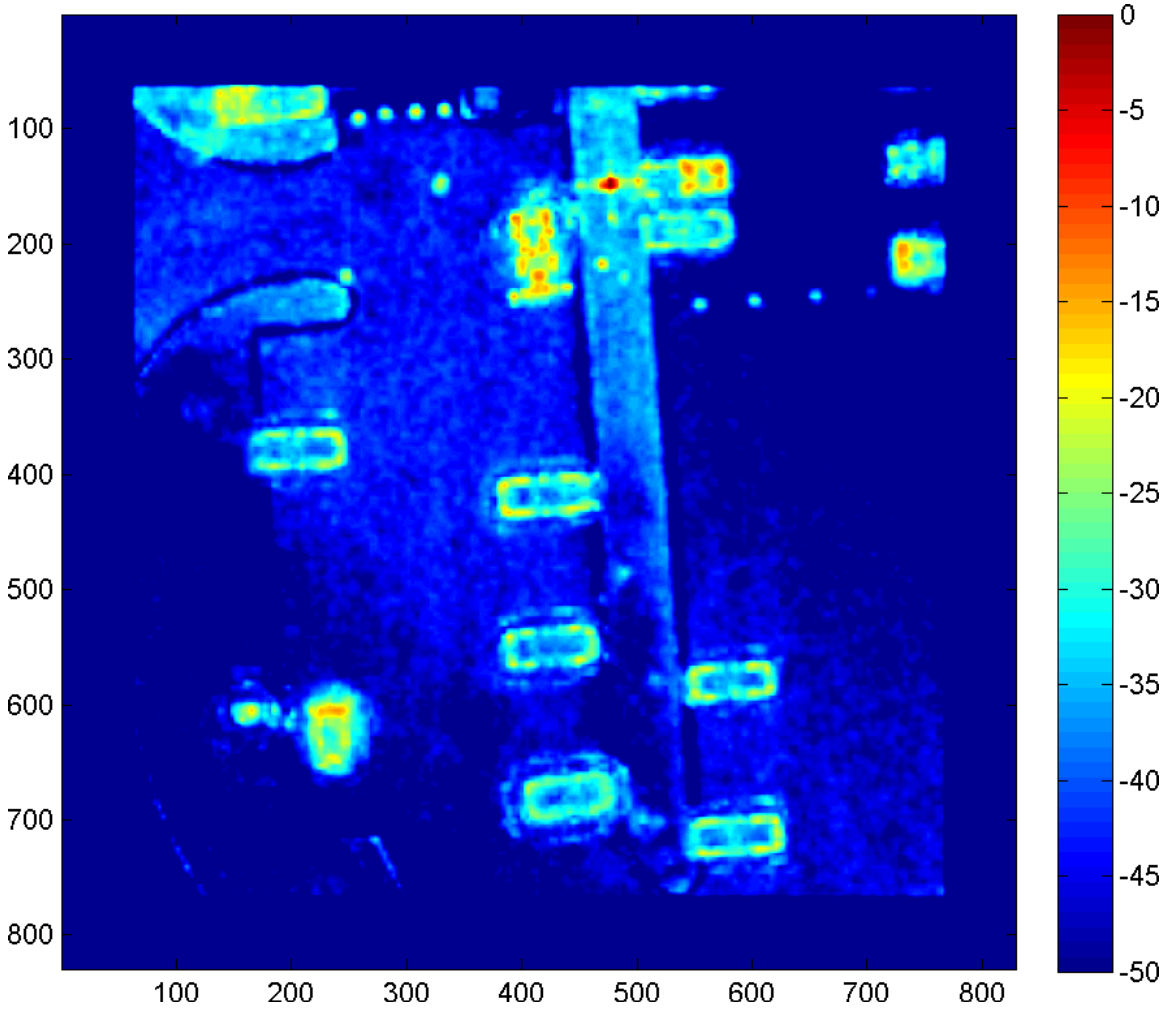

Fig. 7.10: GOTCHA 2D medium scene processing results #3 $\omega_m = 0.00030$ and $\omega_m = 0.00010$.

with a dynamic range of -20dB.

The first results are processed incorporating a sparsity and spatial regularization term of $\omega_m = 0.00050$ and $\omega_g = 0.00010$. The results are shown in Figure 7.13. One very interesting feature of these results is that the subtle feature of the curb in front of the vehicle is still visible. If common threshholding methods were applied to the reference image, such features would disappear and be lost, but the model-based processing actually retains subtle features. The severe blurring caused by the side-lobes is mitigated also by model-based processing. Unfortunately, there remains some artifacts seen above the car in two distinct places, but for overall interpretability the images show extensive promise.

Fig. 7.11: Ford Taurus.

The second results for the 3D Ford Taurus scene incorporate a sparsity, an aspect, and a smoothness regularization term in the optimization problem. The corresponding weights are $\omega_m = 0.00050$, $\omega_f = 0.00010$, and $\omega_g = 0.00500$, respectively. The results are shown in Figure 7.14. The inclusion of the aspect term promotes aspect consistent solutions, and the increased emphasis on the spatial smoothness generates an image where the outline of the vehicle is readily apparent. The image is visually much more appealing and potentially could have more application to ATR algorithms.

The final results for the 3D Ford Taurus scene are shown in Figure 7.15. The results incorporate a sparsity, an aspect, and a smoothness regularization term again, but with different weighting values. The weighting values are $\omega_m = 0.00050$, $\omega_f = 0.00050$, and $\omega_g = 0.00010$ respectively. The spatial term is not emphasized nearly as much as in Figure 7.14, which results in an image that exhibits sparse characteristics. The aspect weighting is increased also promoting persistent features.

7.2.2 3D Tractor

The final target analyzed is the tractor. The tractor has many bright features and the side-lobe artifacts from those bright features make it very difficult to visualize the results in the backprojected image. The images are visualized from two perspectives again. The first

perspective is from -110° degrees azimuth and 44° degrees elevation. This corresponds to the angle from which the SAR sensor generated the tractor image. The second perspective is -105° degrees azimuth and 12° degrees elevation, which is more characteristic of the angles humans would view a tractor. A high resolution optical image, provided with the GOTCHA documentation is shown in Figure 7.16.

The initial 3D backprojected results are shown in Figure 7.17 for a reference. The coarse outline of a tractor can be seen, but many of the details are not distinguishable. A threshhold can be applied to the image, but unfortunately this retains only the strongest glint features and neglects many suppressed features which are critical for identification.

The first example of model-based results are shown in Figure 7.18. This particular example incorporated sparsity, aspect and spatial regularization terms in the cost function with the values of $\omega_m = 0.00020$, $\omega_f = 0.00010$, $\omega_g = 0.00010$. The results show a drastically improved target image, but there still remains side-lobe artifacts.

The next model-based results are shown in Figure 7.19. These results deemphasized sparsity, but increased the emphasis on aspect and spatial smoothness. The resultant image is a lot more distinguishable in this case, especially when viewed from the same angle as the radar. A lot of the side-lobe artifacts have been removed but many of the features have become more distinguishable. Many of the subtle and dominant features still remain.

The last model-based processing result for the tractor is given in Figure 7.20. This processing instance used common regularization weightings terms for sparsity, aspect and spatial smoothness. The resultant image does look different than the rest, but is much improved over the backprojected reference imagery shown in Figure 7.17.

7.3 Summary Results

This chapter shows four total target results. The first two results were 2D targets. The first was a 2D Ford Taurus processed with different parameter weightings, which are specified in Section 7.1.1. The results shown did seem to have several positive effects, but overall the interpretability of the image was similar. The second 2D target was a large scene and that was shown in Section 7.1.2. The larger scene did seem to illustrate more

concisely some improvements. The scene dynamic range was increased, and point targets were sharpened while the scene smoothness was often improved. These effects could be employed to enhanced desirable targets and suppress targets that are not of interest, but in the 2D case, the additional processing incurred, for most practical scenarios, might not merit the slight benefit that was noted.

The 3D results illustrated the benefit of the advanced model-image formation processing. Visually targets were much more interpretable. The side-lobe artifacts were suppressed and the overall target features were much more recognizable. For those familiar with compressive sensing, this is not completely surprising. The fact that the model-based processing approach incorporated the 3D impulse response along with a sparsity constraint would lead one to believe that improved 3D point responses could be achieved possibly.

However, what was surprising, was how the resultant image could be positively influenced by the weighting provided to the aspect and spatial smoothness regularization term. The aspect term provided a nice ability to suppress, or enhance glint features and it allowed the ability to enhance or suppress spatially fluid features in the case of the spatial smoothness.

The model-based image formation approach showed robustness also since no detailed information about the GOTCHA sensor was available to incorporate into the model. This is not surprising, since the l_1-norm was utilized for all the regularization terms. In summary, the ability to resolve 3D scenes showed remarkable improvement on actual SAR data by the model-based processing formulation proposed in this work.

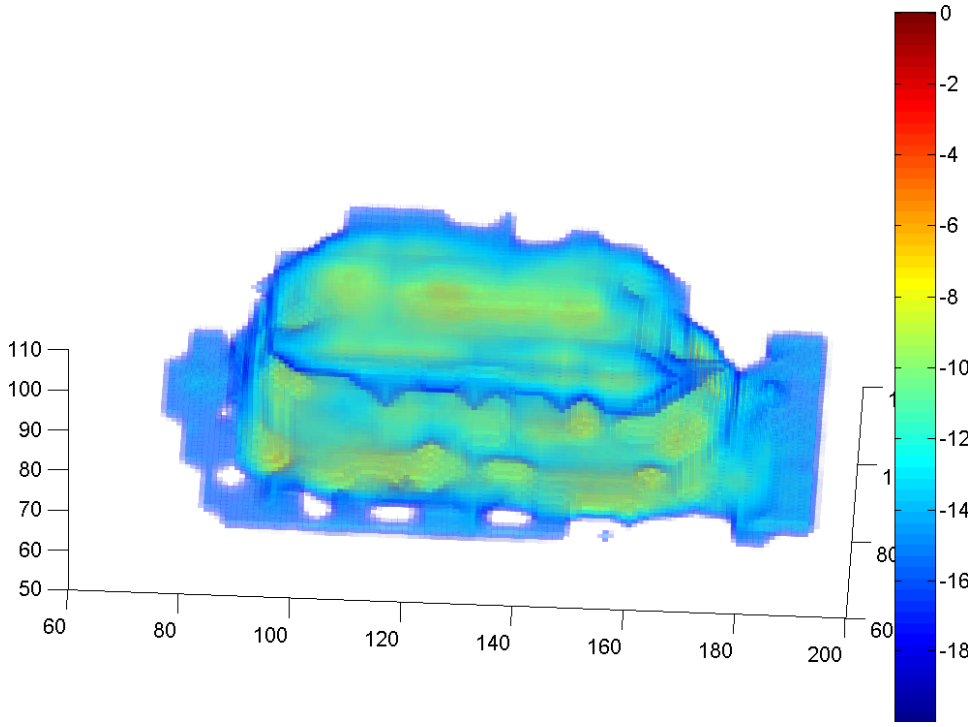

(a)

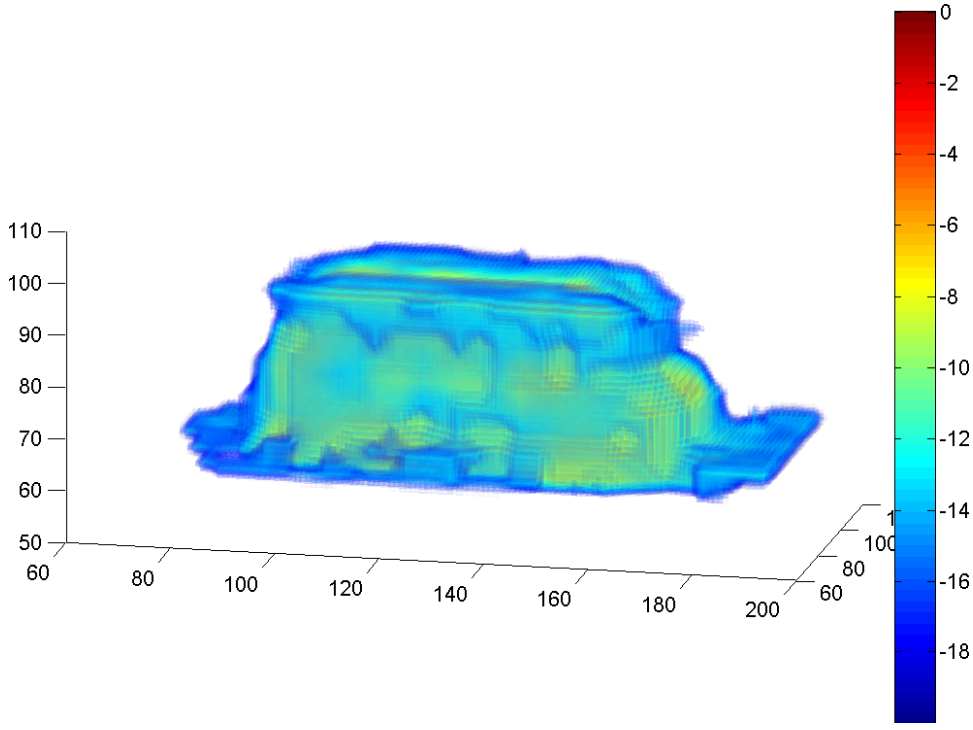

(b)

Fig. 7.12: Ford Taurus 3D backprojected results: (a) Viewing angle of 3° azimuth and 44° elevation, (b) Viewing angle of 12° azimuth and 14° elevation.

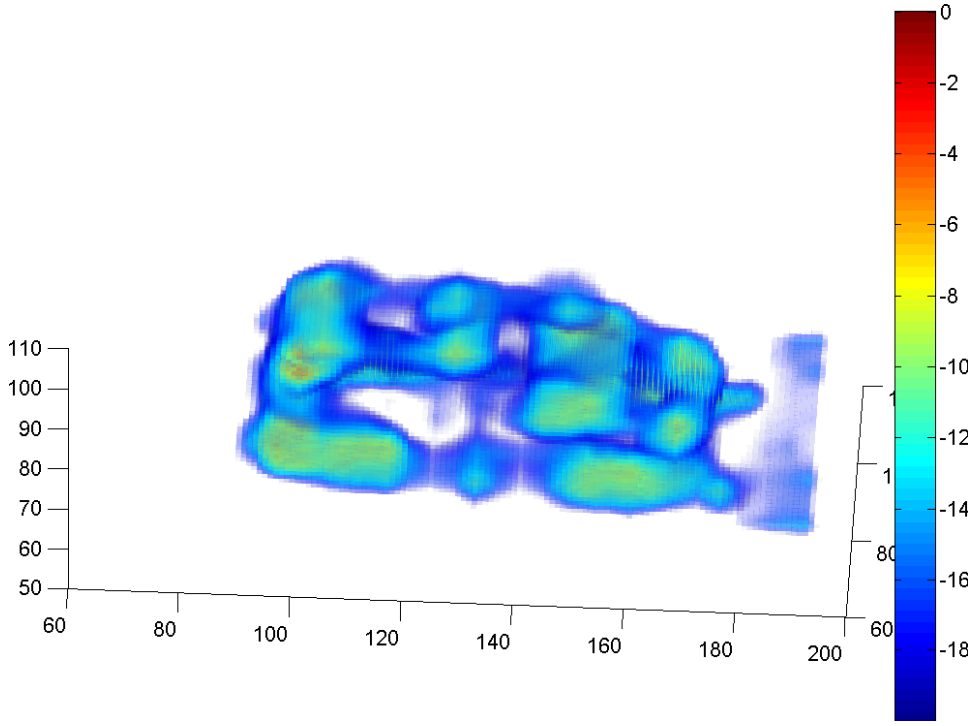

(a)

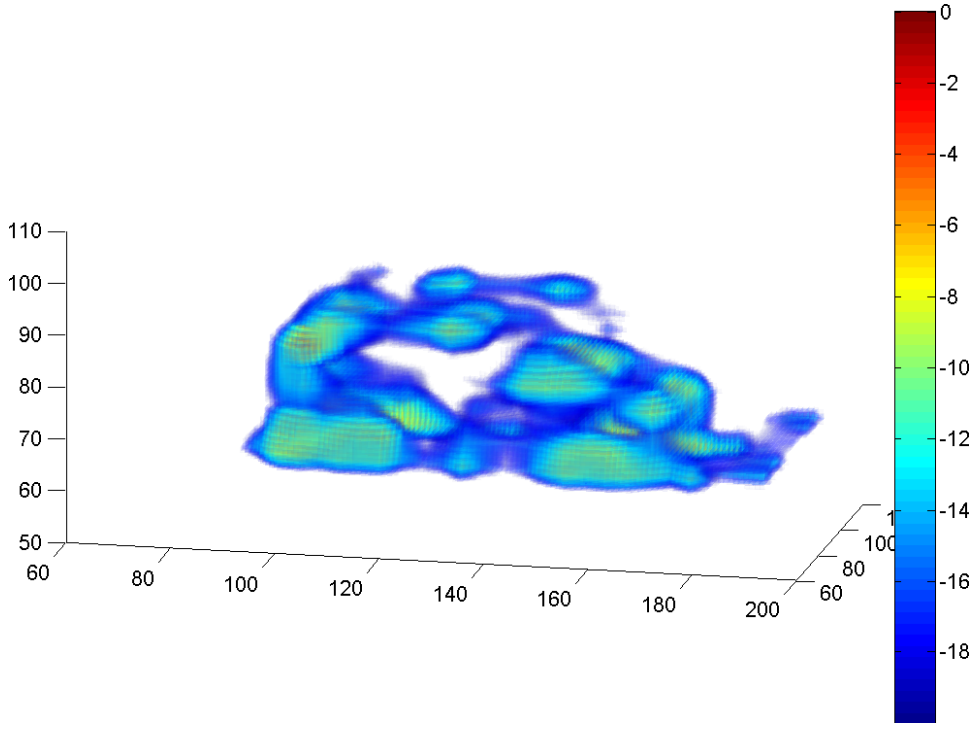

(b)

Fig. 7.13: Ford Taurus 3D processing results #1 with $\omega_m = 0.00050$ and $\omega_g = 0.00050$: (a) Viewing angle of 3° azimuth and 44° elevation, (b) Viewing angle of 12° azimuth and 14° elevation.

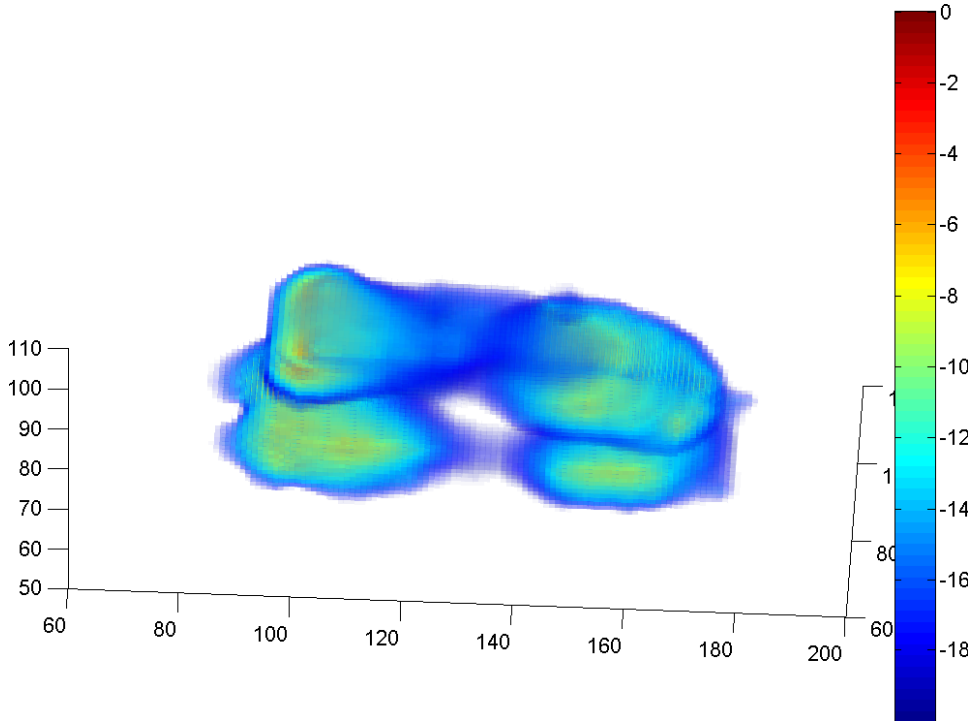

(a)

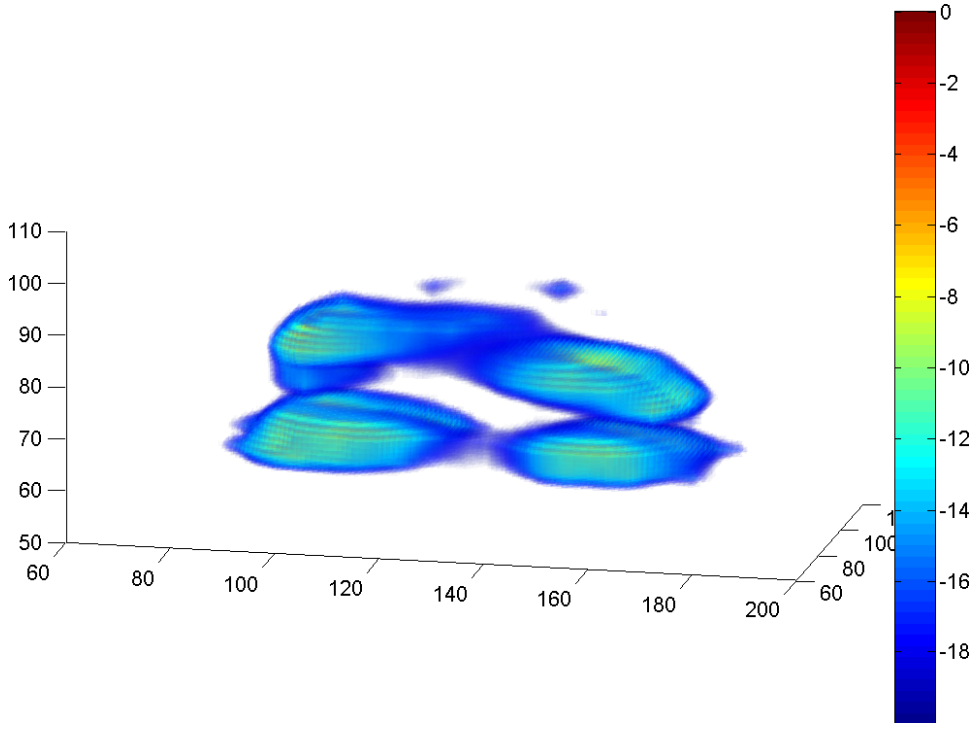

(b)

Fig. 7.14: Ford Taurus 3D processing results #2 with $\omega_m = 0.00050$, $\omega_f = 0.00010$, and $\omega_g = 0.00500$: (a) Viewing angle of 3° azimuth and 44° elevation, (b) Viewing angle of 12° azimuth and 14° elevation.

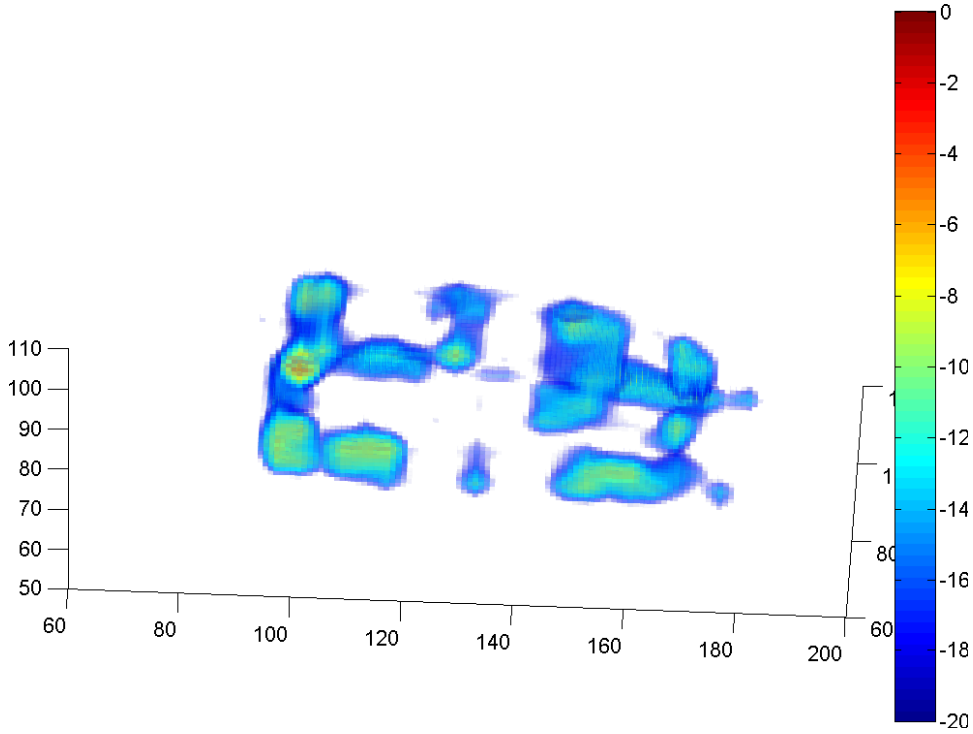

(a)

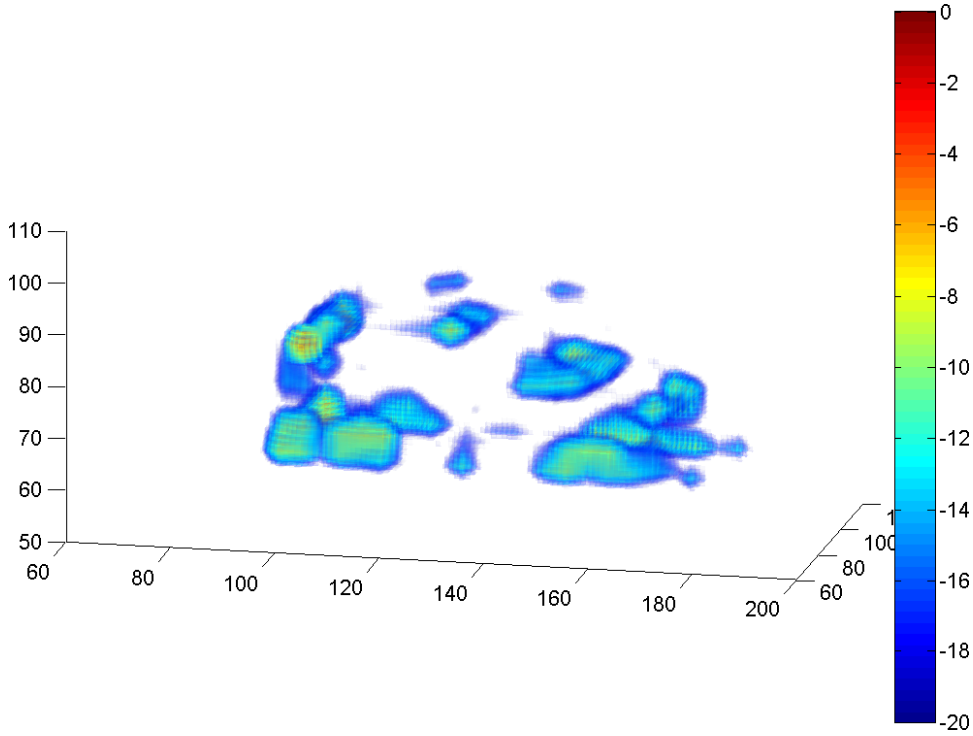

(b)

Fig. 7.15: Ford Taurus 3D processing results #3 with $\omega_m = 0.00050$, $\omega_f = 0.00050$, and $\omega_g = 0.00010$: (a) Viewing angle of 3° azimuth and 44° elevation, (b) Viewing angle of 12° azimuth and 14° elevation.

Fig. 7.16: GOTCHA tractor.

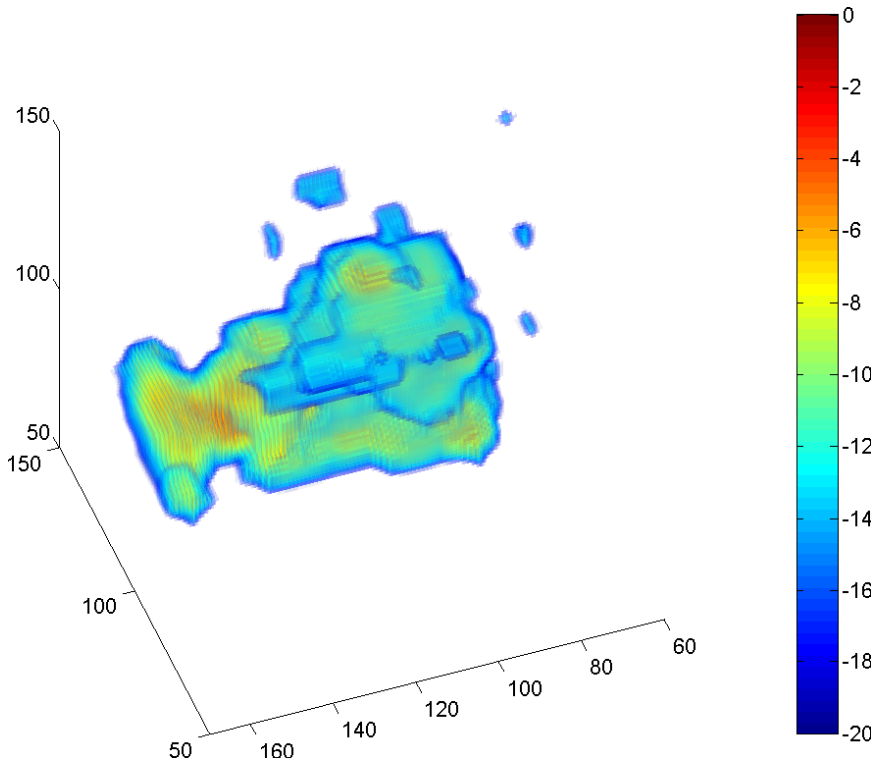

(a)

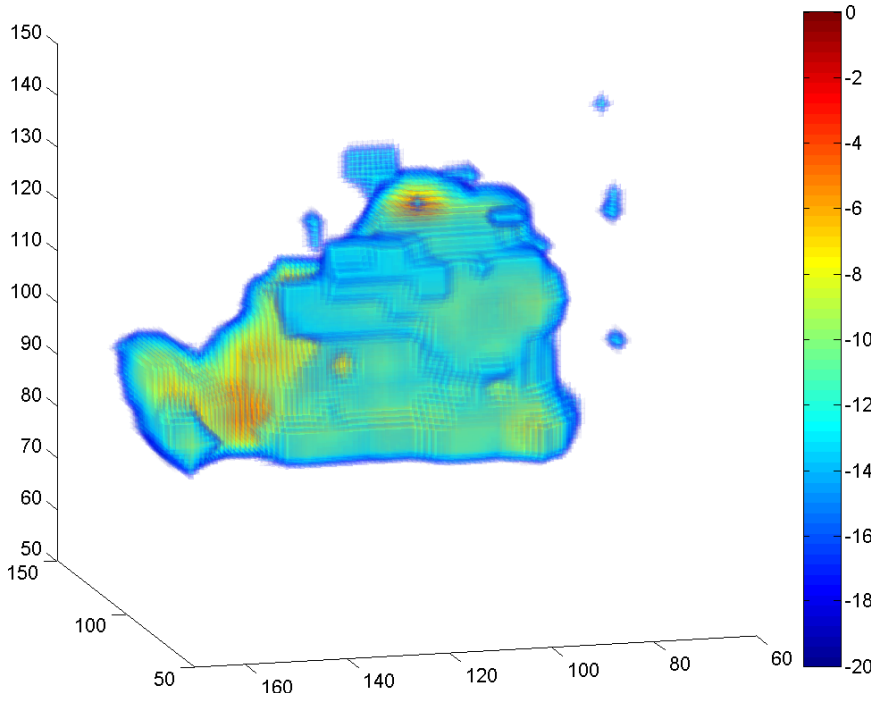

(b)

Fig. 7.17: Tractor 3D backprojected results: (a) Viewing angle of -110° azimuth and 44° elevation, (b) Viewing angle of -105° azimuth and 12° elevation.

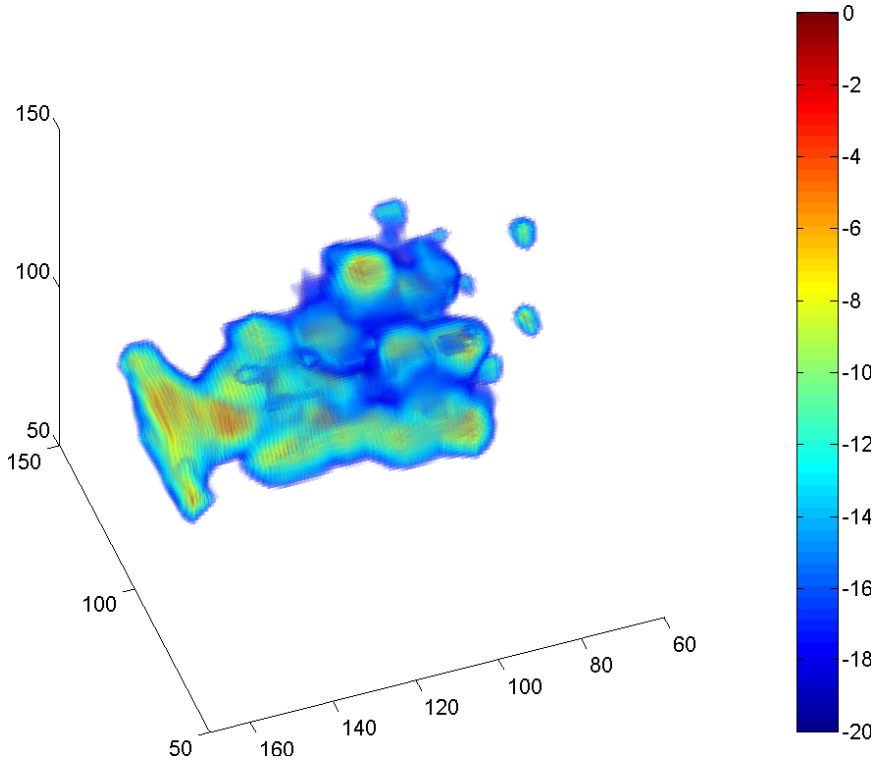

(a)

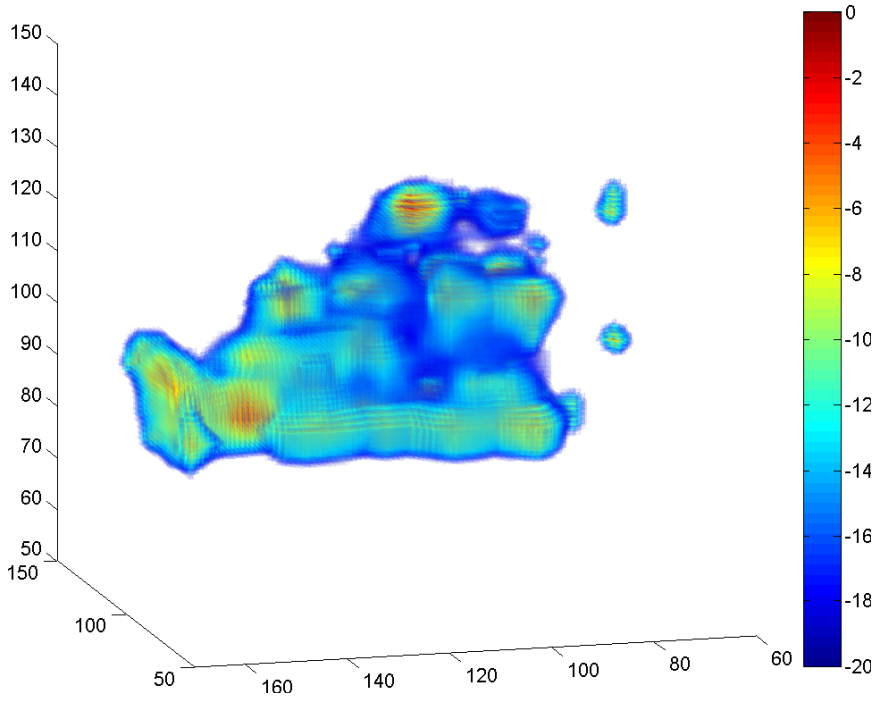

(b)

Fig. 7.18: Tractor 3D processing results #1 with $\omega_m = 0.00020$, $\omega_f = 0.00010$, and $\omega_g = 0.00010$: (a) Viewing angle of -110° azimuth and 44° elevation, (b) Viewing angle of -105° azimuth and 12° elevation.

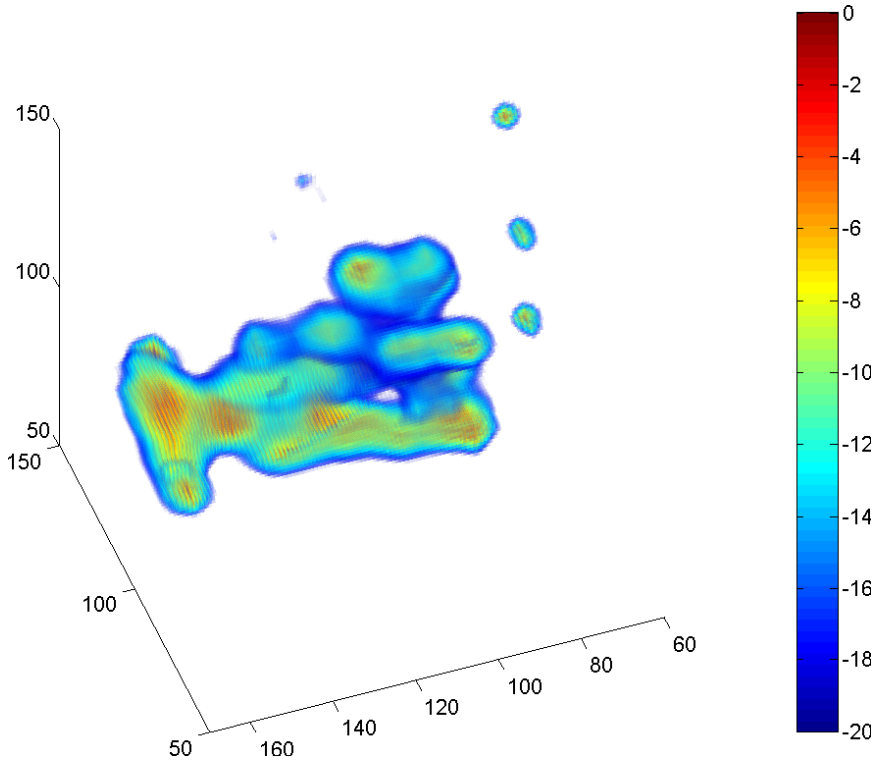

(a)

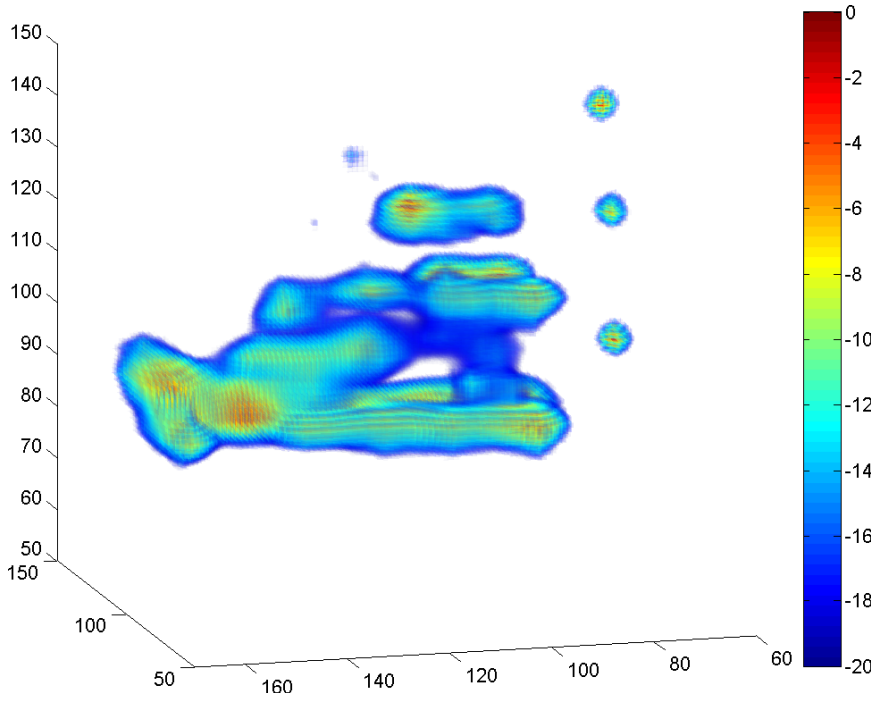

(b)

Fig. 7.19: Tractor 3D processing results #2 with $\omega_m = 0.00010$, $\omega_f = 0.00050$, and $\omega_g = 0.00050$: (a) Viewing angle of -110° azimuth and 44° elevation, (b) Viewing angle of -105° azimuth and 12° elevation.

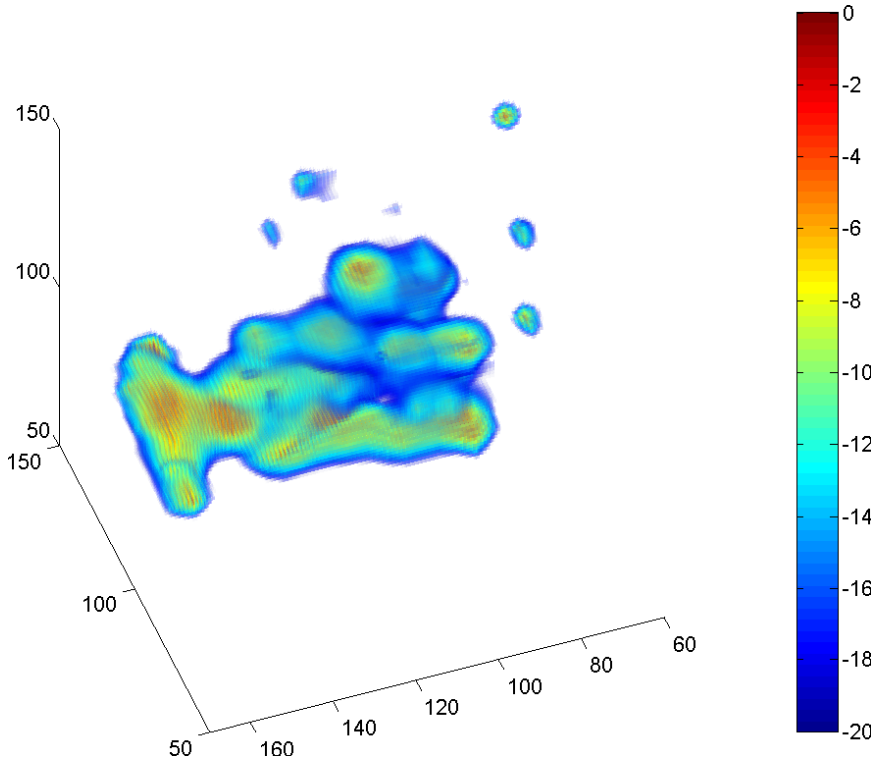

(a)

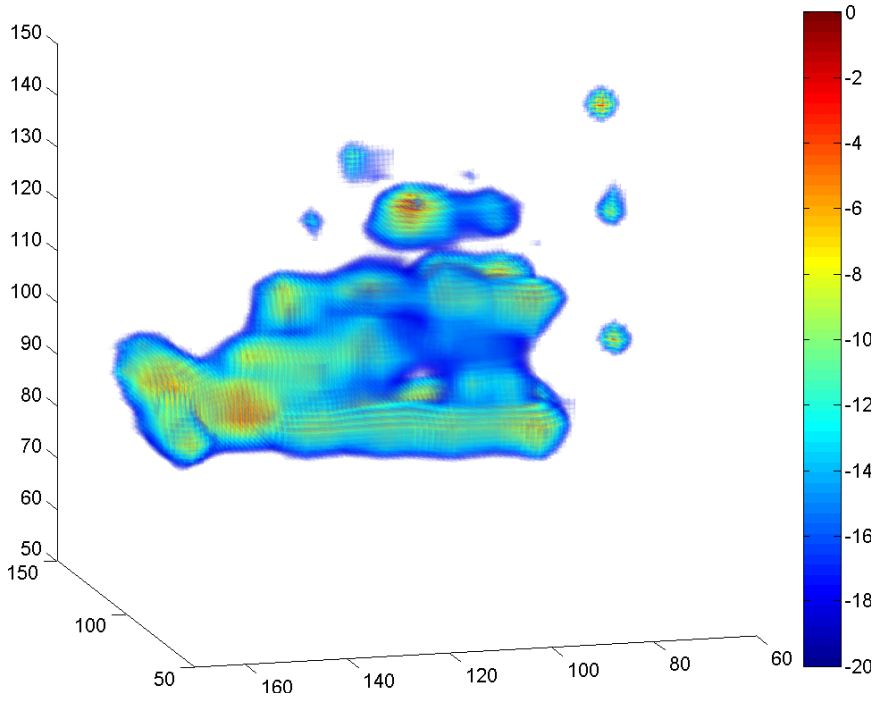

(b)

Fig. 7.20: Tractor 3D processing results #3 with $\omega_m = 0.00020$, $\omega_f = 0.00020$, and $\omega_g = 0.00020$: (a) Viewing angle of -110° azimuth and 44° elevation, (b) Viewing angle of -105° azimuth and 12° elevation.

Chapter 8

Conclusion

This section will outline the contributions this work has provided for advanced SAR image formation. Several closely related extensions of this work will be discussed. And, based on the results of this effort, several natural extensions of this work will be proposed for future research endeavors.

8.1 Summary of Work

The results demonstrated on actual SAR data in the previous section graphically illustrate the contribution this work provides for image reconstruction. The demonstrations focused on 2D scenes and 3D scenes. Both 2D and 3D scenes demonstrated the ability to enhance particular target features. The ability to accentuate point responses, vary aspect and, or spatial responses was readily apparent.

The 3D scenes demonstrated the most drastic improvement for overall scene interpretability. In practice, almost all SAR scenes have a sparse vertical aperture due to practical collection restrictions. It is prohibitive in cost and time to sample SAR scenes at dense elevation and azimuth angles. This effort demonstrated that improved 3D interpretability could be achieved on SAR scenes that had sparsely sampled vertical apertures. The improved results employed convex model-based processing. Visual interpretation for 3D scenes was drastically improved compared to 3D scenes formed by backprojection processing, which is currently the "gold standard."

The improved results were accomplished by leveraging a model and incorporating several regularization terms. The regularization terms emphasized sparsity, spatial, and aspect magnitude into the image formation process. The results demonstrated the ability to suppress and, or, enhance target features. It was shown that spatially smooth features, point

responses, or particular aspect responses could be enhanced (or suppressed) by appropriately weighting the corresponding regularization terms. Unfortunately, the additional processing cost is expensive. But with the increase in distributed processing, and Moore's law, the increased processing cost can be reduced.

While other researches have previously incorporated similar constraints, this work was the first to formulate the problem as a SOCP and demonstrate 3D results on actual SAR data. The SOCP formulation allows for global optimal solutions to be found, since SOCPs are naturally a convex problem formulation. The SOCP formulation also allows for commercial solvers to be employed which have many benefits such as excellent robustness and continued support.

The spatial and aspect magnitude regularization terms provide the unique ability to incorporate prior knowledge into the image formation process on a per-pixel basis. This allows for knowledge-aided-image-formation (KAIF) where pixels could be classified and then appropriately processed.

Many considerations were given to reduce the data volume in this work. The data volume becomes intractable for 3D model-based SAR processing quickly. The spatial domain was chosen to model the signal due to the compact sparse IPR representation. The desire to model the signals in the spatial domain required generating efficient code for simulating the impulse response and image formation so that the time-lines were practical. Significant emphasis was placed on this effort. Furthermore, data reduction is required by advanced model-based image-reconstruction algorithms intrinsically.

The approach developed in this work incorporated prior knowledge into the image formation process. The prior knowledge was based on sparsity, aspect, and magnitude correlation seen in actual measured SAR data. This insight could be directly applied to many related sparse SAR problems. Any SAR image formation problem where there is a sparsely sampled SAR signal is an excellent candidate. The sparsely sampled SAR signal could be sparsely sampled in the vertical or azimuth aperture. Or it could be sparsely sampled in the range, or frequency domain. The results found here provide the impetus to

explore these other related sparsely sampled SAR problems.

8.2 Future Work

SAR provides an abundant opportunity for practitioners and researches inherently, but there are several areas related to this effort that are prominent and worth mentioning specifically.

Regularization problems in general require hand-tweaking the parameter weighting. Improved parameter estimation [74] would avoid the iterative, hand-tweaking processing currently done with many regularization problems. This would increase practical utility drastically since this time-consuming, tedious step could be avoided since scene dependant features can drastically effect the ideal weighting of the regularization terms.

An understanding of the required model-fit would answer the question of what is a tolerable error, and what is an intolerable error. The answer has a direct impact on practical implementation of this approach since it influences the complexity in general.

The ability to incorporate spatial and magnitude filters into the image formation process appears to provide potential advantages for KAIF. An experimental study of target types and their corresponding magnitude RCS correlation in aspect and spatially could help provide measurable datum. Such measured datum could help illuminate the possible utility of such an approach for the measured targets. And the datum could also help provide the foundational knowledge needed to understand how to optimally design the aspect and spatial magnitude filters for the measured targets.

The incorporation of a model for image reconstruction shows significant value. The incorporation of model-based processing into other SAR problems such as single-channel (or maybe multiple-channel) GMTI could potentially provide benefit. For example, the model could "explain" static targets and be used to cancel clutter improving (or make possible) single-channel GMTI detection.

The advanced model-based image formation was applied to SAR data that was sparsely sampled in the vertical aperture. But the SAR data could be sparsely sampled in frequency, aspect, or any domain. The advanced model-based image formation incorporating

spatial and aspect magnitude would naturally extend to such data. For example, a random compressive sensing approach could be employed that sampled below the Nyquist PRF randomly. The resultant reconstructed image could be generated incorporating sparsity, spatial smoothness, and aspect smoothness in varying combinations.

In bistatic or passive SAR configurations [21] there could often be aspect diversity leading to sparsely sampled signals. Applications of the advanced model-based processing to bistatic and passive SAR application could provide improved results. The diverse aspect sampling, inherent in such configurations, could potentially benefit from the anisotropic model and the ability to incorporate magnitude aspect filters.

Modern SAR systems have the ability to be cognitively agile and adaptive systems. A cognitive SAR system would exhibit diversity in multiple domains. Expanding the advanced model-based image formation processing to such systems could provide insight regarding optimal use.

For example, the ambiguity function is often employed as the tool used to measure the waveform effectiveness [75, 76]. Model-based processing illustrates how the SIPR matrix rank could provide a different metric, when the objective is static scene resolvability. Augmenting the SIPR matrices rank would, theoretically, allow for improved scene resolvability. The SIPR matrix rank could be increased by diverse sampling geometries, and waveforms. This contrasts the many efforts to produce the ideal "thumbtack" response.

In model-based processing, appropriately modeled, side-lobes are accounted for with a tight system model. A tight system model means that the simulated IPR response accurately portrays the actual IPR generated by the SAR system. When this is the case, traditional practices like range and azimuth windowing are unnecessary and detrimental since windowing reduces the SIPR rank. Windowing could have a positive effect since it would make the SIPR matrix more diagonally dominant. A diagonally dominant SIPR matrix would provide robustness if or when model mismatch is present. More research could be done understanding the trade-space when maximizing the SIPR rank is the objective metric, and the corresponding effects of model mismatch regarding overall robustness.

References

[1] M. Preisis and N. J. Stacy, "Coherent change detection: Theoretical description and experimetnal results," Defense Science and Technology Organisation, Tech. Rep. 1851, 2006.

[2] J. Ward, "Space-Time Adaptive Processing for Airborne Radar," MIT Lincoln Laboratory, Tech. Rep. 1015, 13 Dec. 1994.

[3] J. R. Guerci, *Space-Time Adaptive Processing for Radar.* Norwood, MA: Artech House, 2003.

[4] C. V. Jakowatz, Jr., D. E. Wahl, P. H. Eichel, D. C. Ghiglia, and P. A. Thompson, *Spotlight-Mode Synthetic Aperture Radar: A Signal Processing Approach.* New York, NY: Kluwer Academic Publishers, 1996.

[5] W. G. Carrara, R. S. Goodman, and R. M. Majewski, *Spotlight Synthetic Aperture Radar: Signal Processing Algorithms.* Norwood, MA: Artech House, 1995.

[6] J. C. Curlander and R. N. McDonough, *Synthetic Aperture Radar Systems and Signal Processing.* Hoboken, NJ: John Wiley and Sons, Inc., 1991.

[7] C. D. Austin, E. Ertin, and R. L. Moses, "Sparse multipass 3D SAR imaging: applications to the GOTCHA data set," *Proc. SPIE*, vol. 7337, pp. 733 703–733 703–12, 2009. [Online]. Available: http://dx.doi.org/10.1117/12.820323

[8] E. Ertin, C. D. Austin, S. Sharma, R. L. Moses, and L. C. Potter, "GOTCHA experience report: three-dimensional SAR imaging with complete circular apertures," *Proc. SPIE*, vol. 6568, pp. 656 802–656 802–12, 2007. [Online]. Available: http://dx.doi.org/10.1117/12.723245

[9] M. Ferrara, J. A. Jackson, and C. Austin, "Enhancement of multi-pass 3D circular SAR images using sparse reconstruction techniques," *Proc. SPIE*, vol. 7337, pp. 733 702–733 702–10, 2009. [Online]. Available: http://dx.doi.org/10.1117/12.820256

[10] W.-Q. Wang, "MIMO SAR imaging: Potential and challenges," *Aerospace and Electronic Systems Magazine, IEEE*, vol. 28, no. 8, pp. 18–23, 2013.

[11] D. Reale, G. Fornaro, A. Pauciullo, X. Zhu, N. Adam, and R. Bamler, "Advanced techniques and new high resolution SAR sensors for monitoring urban areas," *Geoscience and Remote Sensing Symposium (IGARSS), 2010 IEEE International*, pp. 1800–1803, July 2010.

[12] E. Ertin, R. L. Moses, and L. C. Potter, "Interferometric Methods for 3-D Target Reconstruction with Multi-Pass Circular SAR," *Synthetic Aperture Radar (EUSAR), 2008 7th European Conference on*, pp. 1–4, June 2008.

[13] E. Candes and M. Wakin, "An Introduction To Compressive Sampling," *Signal Processing Magazine, IEEE*, vol. 25, no. 2, pp. 21–30, March 2008.

[14] R. Baraniuk, E. Candes, R. Nowak, and M. Vetterli, "Compressive Sampling [From the Guest Editors]," *Signal Processing Magazine, IEEE*, vol. 25, no. 2, pp. 12–13, March 2008.

[15] R. Baraniuk and P. Steeghs, "Compressive Radar Imaging," *Radar Conference, 2007 IEEE*, pp. 128–133, April 2007.

[16] S. Boyd and L. Vandenberghe, *Convex Optimization*. Cambridge, United Kingdom: Cambridge University Press, 2010.

[17] J. B. Billingsley, *Low-Angle Radar Land Clutter*. Norwich, NY: William Andrew Publishing, 2002.

[18] M. Skolnik, *Radar Handbook Third Edition*. New York, NY: McGraw-Hill, 2008.

[19] M. A. Richards, *Fundamentals of Radar Signal processing*. New York, NY: McGraw-Hill, 2005.

[20] N. J. Willis and H. D. Griffiths, *Advances in Bistatic Radar*. Edison, NJ: SciTech Publishing, 2007.

[21] M. Rodriguez-Cassola, S. Baumgartner, G. Krieger, and A. Moreira, "Bistatic TerraSAR-X/F-SAR Spaceborne x2013;Airborne SAR Experiment: Description, Data Processing, and Results," *Geoscience and Remote Sensing, IEEE Transactions on*, vol. 48, no. 2, pp. 781–794, Feb 2010.

[22] A. Papandreou-Suppappola, A. Nehorai, and R. Calderbank, "Waveform-Agile Sensing and Processing [From the Guest Editors]," *Signal Processing Magazine, IEEE*, vol. 26, no. 1, pp. 10–11, Jan 2009.

[23] R. Calderbank, S. Howard, and B. Moran, "Waveform Diversity in Radar Signal Processing," *Signal Processing Magazine, IEEE*, vol. 26, no. 1, pp. 32–41, Jan 2009.

[24] D. Cochran, S. Suvorova, S. Howard, and B. Moran, "Waveform Libraries," *Signal Processing Magazine, IEEE*, vol. 26, no. 1, pp. 12–21, Jan 2009.

[25] M. Bell, "Information theory and radar waveform design," *Information Theory, IEEE Transactions on*, vol. 39, no. 5, pp. 1578–1597, Sep 1993.

[26] J. A. Gubner, *Probability and Random Processes for Electrical and Computer Engineers*. Cambridge, NY: Cambridge University Press, 2006.

[27] A. V. Oppenheim and R. W. Schaffer, *Discrete-Time Signal Processing*. Upper Saddle River, NJ: Pearson, 2010.

[28] R. Raney, "A New And Fundamental Fourier Transform Pair," *Geoscience and Remote Sensing Symposium, 1992. IGARSS '92. International*, vol. 1, pp. 106–107, May 1992.

[29] I. G. Cumming and F. H. Wong, *Digital Processing of Synthetic Aperture Radar Data: Algorithms And Implementation.* Norwood, MA: Artech House, 2004.

[30] A. Yegulalp, "Fast backprojection algorithm for synthetic aperture radar," *Radar Conference, 1999. The Record of the 1999 IEEE*, pp. 60–65, 1999.

[31] L. M. H. Ulander, P.-O. Froelind, A. Gustavsson, D. Murdin, and G. Stenstroem, "Fast Factorized Back-Projection for Bistatic SAR Processing," *Synthetic Aperture Radar (EUSAR), 2010 8th European Conference on*, pp. 1–4, June 2010.

[32] L. A. Gorham and L. J. Moore, "SAR image formation toolbox for MATLAB," *Proc. SPIE*, vol. 7699, pp. 769 906–769 906–13, 2010. [Online]. Available: http://dx.doi.org/10.1117/12.855375

[33] M. Soumekh, *Synthetic Aperture Radar Signal Processing.* New York, NY: John Wiley and Sons, 1999.

[34] C. A. Balanis, *Antenna Theory Analysis and Design Third Edition.* Hoboken, NJ: John Wiley and Sons, 2005.

[35] C. H. Casteel, L. A. Gorham, M. J. Minardi, S. M. Scarborough, K. D. Naidu, and U. Majumder, "A challenge problem for 2D/3D imaging of targets from a volumentric data set in an urban environment," *Algorithms for Synthetic Aperture Radar Imagery XIV*, vol. 6568, no. 1, 2007.

[36] J.-S. Lee and E. Potter, *Polarimetric Radar Imaging from Basics to Application.* Boca Raton, FL: CRC Press, 2009.

[37] R. J. Sullivan, *Radar Foundations for Imaging and Advanced Concepts.* Raleigh, NC: Scitech Publishing Inc., 2004.

[38] J. B. Keller, "Geometrical Theory of Diffraction," *J. Opt. Soc. Am.*, vol. 52, no. 2, pp. 116–130, Feb 1962. [Online]. Available: http://www.opticsinfobase.org/abstract.cfm?URI=josa-52-2-116

[39] L. Potter, D.-M. Chiang, R. Carriere, and M. Gerry, "A GTD-based parametric model for radar scattering," *Antennas and Propagation, IEEE Transactions on*, vol. 43, no. 10, pp. 1058–1067, Oct 1995.

[40] C. A. Balanis, *Advanced Engineering Electromagnetics.* John Wiley and Sons, 1989.

[41] V. C. Chen and H. Ling, *Time-Frequency Transforms for Radar Imaging and Signal Analysis.* Norwood, MA: Artech House, 2002.

[42] L. N. Ridenour, *Radar System Engineering.* McGraw-Hill Book Company, 1947.

[43] Mark A. Richards. (2008) Generating swerling random sequences. [Online]. Available: http://users.ece.gatech.edu/mrichard/Generating%20Swerling%20Random%20Sequences.pdf

[44] B. P. Lathi, *Signal Processing and Linear Systems.* Carmichael, CA: Berkeley-Cambridge Press, 1998.

[45] K. E. Dungan, L. A. Gorham, and L. J. Moore, "SAR digital spotlight implementation in MATLAB," *Proc. SPIE*, vol. 8746, pp. 87 460A–87 460A–11, 2013. [Online]. Available: http://dx.doi.org/10.1117/12.2020884

[46] S. M. Kay, *Fundamentals of Statistical Signal Processing Estimation Theory.* Upper Saddle River, NJ: Prentice Hall, 1993.

[47] G. Strang, *Linear Algebra and its Applications, Fourth Edition.* Belmount, CA: Cengage Learning, Inc., 2006.

[48] S. DeGraaf, "SAR imaging via modern 2-D spectral estimation methods," *Image Processing, IEEE Transactions on*, vol. 7, no. 5, pp. 729–761, May 1998.

[49] M. Cetin and W. Karl, "Feature-enhanced synthetic aperture radar image formation based on nonquadratic regularization," *Image Processing, IEEE Transactions on*, vol. 10, no. 4, pp. 623 –631, Apr 2001.

[50] J. Munson, D.C. and J. Sanz, "Image reconstruction from frequency-offset Fourier data," *Proceedings of the IEEE*, vol. 72, no. 6, pp. 661 – 669, June 1984.

[51] D. Geman and C. Yang, "Nonlinear image recovery with half-quadratic regularization," *Image Processing, IEEE Transactions on*, vol. 4, no. 7, pp. 932–946, 1995.

[52] L. Potter, E. Ertin, J. Parker, and M. Cetin, "Sparsity and Compressed Sensing in Radar Imaging," *Proceedings of the IEEE*, vol. 98, no. 6, pp. 1006–1020, 2010.

[53] R. C. Gonzalez and R. E. Woods, *Digital Image Processing Third Edition.* Upper Saddle River, NJ: Pearson, 2008.

[54] K. R. Varshney, M. Cetin, J. W. Fisher III, and A. S. Willsky, "Joint image formation and anisotropy characterization in wide-angle SAR," *Proc. SPIE*, vol. 6237, pp. 62 370D–62 370D–12, 2006. [Online]. Available: http://dx.doi.org/10.1117/12.663974

[55] E. Ertin, "Manifold Learning Methods for Wide-angle SAR ATR," *2013 International Conference on Radar*, pp. 500–504, Sept 2013.

[56] R. L. Moses, L. C. Potter, and M. Cetin, "Wide-angle sar imaging," *Proc. SPIE*, vol. 5427, pp. 164–175, 2004. [Online]. Available: http://dx.doi.org/10.1117/12.544935

[57] K. Dungan and J. Nehrbass, "Wide-area wide-angle SAR focusing," *Aerospace and Electronic Systems Magazine, IEEE*, vol. 29, no. 1, pp. 21–28, Jan 2014.

[58] O. L. Moses and L. C. Potter, "Noncoherent 2D and 3D SAR reconstruction from wide-angle measurements," *in 13th Annual Adaptive Sensor Array Processing Workshop, MIT Lincoln Laboratory*, 2005.

[59] M. Cetin and R. L. Moses, "SAR imaging from partial-aperture data with frequency-band omissions," *Algorithms for Synthetic Aperture Radar Imagery XII*, vol. 5808, no. 1, pp. 32–43, 2005. [Online]. Available: http://link.aip.org/link/?PSI/5808/32/1

[60] I. Stojanovic, M. Cetin, and W. C. Karl, "Joint space aspect reconstruction of wide-angle SAR exploiting sparsity," *Algorithms for Synthetic Aperture Radar Imagery XV*, vol. 6970, no. 1, p. 697005, 2008. [Online]. Available: http://link.aip.org/link/?PSI/6970/697005/1

[61] Dattorro, *Convex Optimization And Euclidean Distance Geometry.* Palo Alto, CA: MeBoo Publishing, 2005.

[62] E. van den Berg and M. P. Friedlander, "Probing the Pareto frontier for basis pursuit solutions," *SIAM Journal on Scientific Computing*, vol. 31, no. 2, pp. 890–912, 2008. [Online]. Available: http://link.aip.org/link/?SCE/31/890

[63] M. S. Lobo, L. Vandenberghe, S. Boyd, and H. Lebret, "Applications of second-order cone programming," *Linear Algebra and its Applications*, vol. 284, no. 13, pp. 193 – 228, 1998, international Linear Algebra Society (ILAS) Symposium on Fast Algorithms for Control, Signals and Image Processing. [Online]. Available: http://www.sciencedirect.com/science/article/pii/S0024379598100320

[64] F. Alizadeh, F. Alizadeh, D. Goldfarb, and D. Goldfarb, "Second-Order Cone Programming," *Mathematical Programming*, vol. 95, pp. 3–51, 2001.

[65] A. Antoniou and W.-S. Lu, *Practical Optimization: Algorithms and Engineering Applications.* New York, NY: Springer, 2007.

[66] D. Malioutov, M. Cetin, and A. Willsky, "A sparse signal reconstruction perspective for source localization with sensor arrays," *IEEE Transactions on Signal Processing*, vol. 53, no. 8, pp. 3010–3022, 2005.

[67] X. Zhang, L. Gou, B. Hou, and L. Jiao, "Gaussian process classification using automatic relevance determination for sar target recognition," *Proc. SPIE*, vol. 7830, pp. 78 300R–78 300R–7, 2010. [Online]. Available: http://dx.doi.org/10.1117/12.864845

[68] O. Batu and M. Cetin, "Parameter Selection in Sparsity-Driven SAR Imaging," *IEEE Transactions on Aerospace and Electronic Systems*, vol. 47, no. 4, pp. 3040–3050, 2011.

[69] M. Grant and S. Boyd, "CVX: Matlab Software for Disciplined Convex Programming, version 2.0 beta," http://cvxr.com/cvx, Sep. 2013.

[70] J. Sturm, "Using SeDuMi 1.02, a MATLAB toolbox for optimization over symmetric cones," *Optimization Methods and Software*, vol. 11–12, pp. 625–653, 1999, version 1.05 available from `http://fewcal.kub.nl/sturm`.

[71] I. Gurobi Optimization, "Gurobi optimizer reference manual," 2014. [Online]. Available: http://www.gurobi.com

[72] M. ApS, "The mosek optimization toolbox for matlab manual version 7.0 (revision 94)," 2014. [Online]. Available: http://www.mosek.com

[73] N. Onhon and M. Cetin, "A Sparsity-Driven Approach for Joint SAR Imaging and Phase Error Correction," *IEEE Transactions on Image Processing*, vol. 21, no. 4, pp. 2075–2088, April.

[74] O. Batu and M. Cetin, "Hyper-parameter selection in non-quadratic regularization-based radar image formation," *Proc. SPIE*, vol. 6970, pp. 697 009–697 009–12, 2008. [Online]. Available: http://dx.doi.org/10.1117/12.782341

[75] N. Levanon and E. Mozeson, *Radar Signals.* Hoboken, NJ: John Wiley and Sons, 2004.

[76] J. Li and P. Stoica, *MIMO Radar Signal Processing.* Hoboken, NJ: John Wiley and Sons, 2008.

Vita

Chad P. Knight

Education

- Ph.D., Electrical Engineering, Utah State University 2014 (expected)
- M.E., Electrical Engineering, Utah State University 2004
- B.S., Electrical Engineering, Utah State University 2004

Professional Experience

- SAR Engineer, Space Dynamics Laboratory, North Logan, UT, 2007-Present
- Electrical Engineer, Space Dynamics Laboratory, North Logan, UT, 2004-2007
- Student Software Developer and Tester, Space Dynamics Laboratory, North Logan, UT, 2000-2004

Published Journal Articles

Published Conference Papers

- Model-based 3D Reconstruction, Chad Knight, Jacob Gunther, and Todd Moon, in *Algorithms for Synthetic Aperture Radar Imagery XXI (SPIE)*, 2014
- Anisotropic Model-Based SAR Processing, Chad Knight, Jacob Gunther, and Todd Moon, in *Radar Sensor Technology XVII (SPIE)*, 2013

- Compact, autonomous, multi-mission synthetic aperture radar, Thomas J. Walls, Michael L. Wilson, Chad Knight, David Madsen, Mark Jensen, Scott A. Anderson, Mide Addario, in *Radar Sensor Technology XVII (SPIE)*, 2013

- Breaking the isotropic scattering assumption in wide-beam stripmap SAR imaging, Chad Knight, Jacob Gunther, and Todd Moon, in *Signals, Systems and Computers (ASILOMAR)*, 2012

- Analysis of RASAR Field Test Performance and Tactical Imagery, Thomas J. Walls, Michael L. Wilson, Mark Jensen, Chad Knight, David Madsen, Brad Petersen, Scott A. Anderson, Mike Addario, Doug Colclough in *MSS Tri-Servie Symposium*, June 2012

- Applications of Compact, Tactical Synthetic Aperture Radars,, Thomas J. Walls, Michael L. Wilson, Chad Knight, David Madsen, Mark Jensen, Scott A. Anderson, Darin Partridge, Mike Addario, Doug Colclough in *MSS Passive Sensors*, 2012

- Real-time Autonomous, Synthetic Aperture Radar, Thomas J. Walls, Michael L. Wilson, Mark Jensen, Chad Knight, David Madsen, Brad Petersen, Scott A. Anderson, Mike Addario, Doug Colclough in *MSS Tri-Servie Symposium*, June 2011

- Applications of Ultra-wide Beam Synthetic Aperture Radar for Thin Target Detection, T.J. Walls, M. L. Wilson, C. Knight, S. Jaroszewski and L.R. Moyer, in *MSS Tri-service Radar Converence*, July 2010

Awards

- Space Dynamics Fellowship, 2009-2013

- Space Dynamics Outstanding Performance Awards, 2005, 2006-2, 2007, 2009, 2012

- USU Graduate Student Assitant 2003-2004